ISSN 1949-8470 (online)

World Journal of *Radiology*

World J Radiol 2015 December 28; 7(12): 421-537

Published by Baishideng Publishing Group Inc

W J R
World Journal of
Radiology

A peer-reviewed, online, open-access journal of Radiology

Editorial Board

2014-2017

The *World Journal of Radiology* Editorial Board consists of 365 members, representing a team of worldwide experts in radiology. They are from 36 countries, including Afghanistan (1), Argentina (2), Australia (5), Austria (7), Belgium (2), Brazil (8), Canada (6), Chile (1), China (43), Croatia (1), Denmark (4), Egypt (6), France (5), Germany (22), Greece (10), India (12), Iran (6), Ireland (2), Israel (3), Italy (47), Japan (13), Netherlands (1), New Zealand (1), Pakistan (1), Poland (2), Portugal (1), Serbia (1), Singapore (3), Slovakia (1), South Korea (18), Spain (4), Sweden (2), Switzerland (4), Thailand (1), Turkey (26), United Kingdom (11), and United States (82).

EDITORS-IN-CHIEF

Kai U Juergens, *Bremen*
Edwin JR van Beek, *Edinburgh*
Thomas J Vogl, *Frankfurt*

GUEST EDITORIAL BOARD MEMBERS

Wing P Chan, *Taipei*
Chung-Huei Hsu, *Taipei*
Chin-Chang Huang, *Taipei*
Tsong-Long Hwang, *Taoyuan*
Jung-Lung Hsu, *Taipei*
Chia-Hung Kao, *Taichung*
Yu-Ting Kuo, *Tainan*
Hon-Man Liu, *Taipei*
Hui-Lung Liang, *Kaohsiung*
Chun Chung Lui, *Kaohsiung*
Sen-Wen Teng, *Taipei*
Yung-Liang (William) Wan, *Taoyuan*

MEMBERS OF THE EDITORIAL BOARD

Afghanistan

Takao Hiraki, *Okayama*

Argentina

Patricia Carrascosa, *Vicente Lopez*
Maria C Ziadi, *Rosario*

Australia

Lourens Bester, *Sydney*
Gemma A Figtree, *Sydney*
Stuart M Grieve, *Sydney*
Wai-Kit Lee, *Fitzroy*
Prabhakar Ramachandran, *Melbourne*

Austria

Herwig R Cerwenka, *Graz*
Gudrun M Feuchtner, *Innsbruck*
Benjamin Henninger, *Innsbruck*
Rupert Lanzenberger, *Vienna*
Shu-Ren Li, *Vienna*
Veronika Schopf, *Vienna*
Tobias De Zordo, *Innsbruck*

Belgium

Steve Majerus, *Liege*
Kathelijne Peremans, *Merelbeke*

Brazil

Clerio F Azevedo, *Rio de Janeiro*
Patrícia P Alfredo, *São Paulo*
Eduardo FC Fleury, *São Paulo*
Edward Araujo Júnior, *São Paulo*
Wellington P Martins, *Ribeirao Preto*
Ricardo A Mesquita, *Belo Horizonte*
Vera MC Salemi, *São Paulo*
Claudia Szobot, *Porto Alegre*
Lilian YI Yamaga, *São Paulo*

Canada

Marie Arsalidou, *Toronto*
Otman A Basir, *Waterloo*
Tarik Zine Belhocine, *Toronto*
James Chow, *Toronto*
Tae K Kim, *Toronto*
Anastasia Oikonomou, *Toronto*

China

Hong-Wei Chen, *Wuxi*
Feng Chen, *Hangzhou*
Jian-Ping Chu, *Guangzhou*
Guo-Guang Fan, *Shenyang*
Bu-Lang Gao, *Shijiazhuang*
Qi-Yong Gong, *Chengdu*
Ying Han, *Beijing*
Xian-Li Lv, *Beijing*
Yi-Zhuo Li, *Guangzhou*
Xiang-Xi Meng, *Harbin*
Yun Peng, *Beijing*
Jun Shen, *Guangzhou*
Ze-Zhou Song, *Hangzhou*
Wai Kwong Tang, *Hong Kong*
Gang-Hua Tang, *Guangzhou*
Jie Tian, *Beijing*
Lu-Hua Wang, *Beijing*
Xiao-bing Wang, *Xi'an*
Yi-Gen Wu, *Nanjing*
Kai Wu, *Guangzhou*
Hui-Xiong Xu, *Shanghai*
Zuo-Zhang Yang, *Kunming*
Xiao-Dan Ye, *Shanghai*
David T Yew, *Hong Kong*
Ting-He Yu, *Chongqing*
Zheng Yuan, *Shanghai*
Min-Ming Zhang, *Hangzhou*
Yudong Zhang, *Nanjing*
Dong Zhang, *ChongQing*
Wen-Bin Zeng, *Changsha*

Yue-Qi Zhu, *Shanghai*

Croatia

Goran Kusec, Osijek

Denmark

Poul E Andersen, *Odense*
Lars J Petersen, *Aalborg*
Thomas Z Ramsoy, *Frederiksberg*
Morten Ziebell, *Copenhagen*

Egypt

Mohamed F Bazeed, *Mansoura*
Mohamed Abou El-Ghar, *Mansoura*
Reem HA Mohamed, *Cairo*
Mohamed R Nouh, *Alexandria*
Ahmed AKA Razek, *Mansoura*
Ashraf A Zytoon, *Shebin El-Koom*

France

Sabine F Bensamoun, *Compiègne*
Romaric Loffroy, *Dijon*
Stephanie Nougaret, *Montpellier*
Hassane Oudadesse, *Rennes*
Vincent Vinh-Hung, *Fort-de-France*

Germany

Henryk Barthel, *Leipzig*
Peter Bannas, *Hamburg*
Martin Beeres, *Frankfurt*
Ilja F Ciernik, *Dessau*
A Dimitrakopoulou-Strauss, *Heidelberg*
Peter A Fasching, *Erlanegn*
Andreas G Schreyer, *Regensburg*
Philipp Heusch, *Duesseldorf*
Sonja M Kirchhoff, *Munich*
Sebastian Ley, *Munich*
Adel Maataoui, *Frankfurt am Main*
Stephan M Meckel, *Freiburg*
Hans W Muller, *Duesseldorf*
Kay Raum, *Berlin*
Dirk Rades, *Luebeck*
Marc-Ulrich Regier, *Hamburg*
Alexey Surov, *Halle*
Martin Walter, *Magdeburg*
Axel Wetter, *Essen*
Christoph Zilkens, *Düsseldorf*

Greece

Panagiotis Antoniou, *Thessaloniki*
Nikos Efthimiou, *Athens*
Dimitris Karnabatidis, *Patras*
George Latsios, *Athens*
Stylianos Megremis, *Iraklion*
Alexander D Rapidis, *Athens*
Kiki Theodorou, *Larissa*
Ioannis A Tsalafoutas, *Athens*
Evanthia E Tripoliti, *Ioannina*
Athina C Tsili, *Ioannina*

India

Ritesh Agarwal, *Chandigarh*
Chandan J Das, *New Delhi*
Prathamesh V Joshi, *Mumbai*
Naveen Kalra, *Chandigarh*
Chandrasekharan Kesavadas, *Trivandrum*
Jyoti Kumar, *New Delhi*
Atin Kumar, *New Delhi*
Kaushala P Mishra, *Allahabad*
Daya N Sharma, *New Delhi*
Binit Sureka, *New Delhi*
Sanjay Sharma, *New Delhi*
Raja R Yadav, *Allahabad*

Iran

Majid Assadi, *Bushehr*
SeyedReza Najafizadeh, *Tehran*
Mohammad Ali Oghabian, *Tehran*
Amir Reza Radmard, *Tehran*
Ramin Sadeghi, *Mashhad*
Hadi Rokni Yazdi, *Tehran*

Ireland

Tadhg Gleeson, *Wexford*
Frederik JAI Vernimmen, *Cork*

Israel

Dafna Ben Bashat, *Tel Aviv*
Amit Gefen, *Tel Aviv*
Tamar Sella, *Jerusalem*

Italy

Adriano Alippi, *Rome*
Dante Amelio, *Trento*
Michele Anzidei, *Rome*
Filippo F Angileri, *Messinas*
Stefano Arcangeli, *Rome*
Roberto Azzoni, *San Donato milanese*
Tommaso V Bartolotta, *Palermo*
Tommaso Bartalena, *Imola*
Livia Bernardin, *San Bonifacio*
Federico Boschi, *Verona*
Sergio Casciaro, *Lecce*
Emanuele Casciani, *Rome*
Musa M Can, *Napoli*
Alberto Cuocolo, *Napoli*
Michele Ferrara, *Coppito*
Mauro Feola, *Fossano*
Giampiero Francica, *Castel Volturno*
Luigi De Gennaro, *Rome*
Giulio Giovannetti, *Pisa*
Francesca Iacobellis, *Napoli*
Formato Invernizzi, *Monza Brianza*
Francesco Lassandro, *Naples*
Lorenzo Livi, *Florence*
Pier P Mainenti, *Napoli*
Laura Marzetti, *Chieti*
Giuseppe Malinverni, *Crescentino*
Enrica Milanesi, *Turin*
Giovanni Morana, *Treviso*
Lorenzo Monti, *Milan*
Silvia D Morbelli, *Genoa*
Barbara Palumbo, *Perugia*
Cecilia Parazzini, *Milan*
Stefano Pergolizzi, *Messina*
Antonio Pinto, *Naples*
Camillo Porcaro, *Rome*
Carlo C Quattrocchi, *Rome*
Alberto Rebonato, *Perugia*
Giuseppe Rizzo, *Rome*
Roberto De Rosa, *Naples*
Domenico Rubello, *Rovigo*
Andrea Salvati, *Bari*
Sergio Sartori, *Ferrara*
Luca M Sconfienza, *Milano*
Giovanni Storto, *Rionero*
Nicola Sverzellati, *Parma*
Alberto S Tagliafico, *Genova*
Nicola Troisi, *Florence*

Japan

Yasuhiko Hori, *Chiba*
Hidetoshi Ikeda, *Koriyama*
Masahito Kawabori, *Sapporo*
Tamotsu Kamishima, *Sapporo*
Hiro Kiyosue, *Yufu*
Yasunori Minami, *Osaka-sayama*
Yasuhiro Morimoto, *Kitakyushu*
Satoru Murata, *Tokyo*
Shigeki Nagamachi, *Miyazaki*
Hiroshi Onishi, *Yamanashi*
Morio Sato, *Wakayama Shi*
Yoshito Tsushima, *Maebashi*
Masahiro Yanagawa, *Suita*

Netherlands

Willem Jan van Rooij, *Tilburg*

New Zealand

W Howell Round, *Hamilton*

Pakistan

Wazir Muhammad, *Abbottabad*

Poland

Maciej S Baglaj, *Wroclaw*

Piotr Czauderna, *Gdansk*

Portugal

Joao Manuel RS Tavares, *Porto*

Serbia

Olivera Ciraj-Bjelac, *Belgrade*

Singapore

Gopinathan Anil, *Singapore*
Terence KB Teo, *Singapore*
Cher Heng Tan, *Singapore*

Slovakia

Stefan Sivak, *Martin*

South Korea

Ki Seok Choo, *Busan*
Seung Hong Choi, *Seoul*
Dae-Seob Choi, *Jinju*
Hong-Seok Jang, *Seoul*
Yong Jeong, *Daejeon*
Chan Kyo Kim, *Seoul*
Se Hyung Kim, *Seoul*
Joong-Seok Kim, *Seoul*
Sang Eun Kim, *Seongnam*
Sung Joon Kwon, *Seoul*
Jeong Min Lee, *Seoul*
In Sook Lee, *Busan*
Noh Park, *Goyang*
Chang Min Park, *Seoul*
Sung Bin Park, *Seoul*
Deuk Jae Sung, *Seoul*
Choongsoo Shin, *Seoul*
Kwon-Ha Yoon, *Iksan*

Spain

Miguel A De Gregorio, *Zaragoza*
Antonio Luna, *Jaén*
Enrique Marco de Lucas, *Santander*
Fernando Ruiz Santiago, *Granada*

Sweden

Dmitry Grishenkov, *Stockholm*
Tie-Qiang Li, *Stockholm*

Switzerland

Nicolau Beckmann, *Basel*
Christian Boy, *Bern*
Giorgio Treglia, *Bellinzona*

Stephan Ulmer, *Kiel*

Thailand

Sirianong Namwongprom, *Chiang Mai*

Turkey

Kubilay Aydin, *Istanbul*
Ramazan Akdemir, *Sakarya*
Serhat Avcu, *Ankara*
Ayse Aralasmak, *Istanbul*
Oktay Algin, *Ankara*
Nevbahar Akcar, *Meselik*
Bilal Battal, *Ankara*
Zulkif Bozgeyik, *Elazig*
Nazan Ciledag, Aakara
Fuldem Y Donmez, *Ankara*
Gulgun Engin, *Istanbul*
Ahmet Y Goktay, *Izmir*
Oguzhan G Gumustas, *Bursa*
Kaan Gunduz, *Ankara*
Pelin Ozcan Kara, *Mersin*
Kivanc Kamburoglu, *Ankara*
Ozgur Kilickesmez, *Istanbul*
Furuzan Numan, *Istanbul*
Cem Onal, *Adana*
Ozgur Oztekin, *Izmir*
Seda Ozbek (Boruban), *Konya*
Selda Sarikaya, *Zonguldak*
Figen Taser, *Kutahya*
Baran Tokar, *Eskisehir*
Ender Uysal, *Istanbul*
Ensar Yekeler, *Istanbul*

United Kingdom

Indran Davagnanam, *London*
M DC Valdés Hernández, *Edinburgh*
Alan Jackson, *Manchester*
Suneil Jain, *Belfast*
Long R Jiao, *London*
Miltiadis Krokidis, *Cambridge*
Pradesh Kumar, *Liverpool*
Peter D Kuzmich, *Derby*
Georgios Plataniotis, *Brighton*
Vanessa Sluming, *Liverpool*

United States

Garima Agrawal, *Saint Louis*
James R Brasic, *Baltimore*
Rajendra D Badgaiyan, *Buffalo*
Ulas Bagci, *Bethesda*
Anat Biegon, *Stony Brook*
Ramon Casanova, *Winston Salem*
Wenli Cai, *Boston*
Zheng Chang, *Durham*
Corey J Chakarun, *Long Beach*
Kai Chen, *Los Angeles*
Hyun-Soon Chong, *Chicago*
Marco Cura, *Dallas*
Ravi R Desai, *Bensalem*
Delia DeBuc, *Miami*
Carlo N De Cecco, *Charleston*
Timm-Michael L Dickfeld, *Baltimore*
Subba R Digumarthy, *Boston*
Huy M Do, *Stanford*
Todd A Faasse, *Grand Rapids*
Salomao Faintuch, *Boston*
Girish M Fatterpekar, *New York*
Dhakshinamoorthy Ganeshan, *Houston*
Robert J Griffin, *Little Rock*
Andrew J Gunn, *Boston*
Sandeep S Hedgire, *Boston*
Timothy J Hoffman, *Columbia*
Mai-Lan Ho, *San Francisco*
Juebin Huang, *Jackson*
Abid Irshad, *Charleston*
Matilde Inglese, *New York*
El-Sayed H Ibrahim, *Jacksonville*
Paul R Julsrud, *Rochester*
Pamela T Johnson, *Baltimore*
Ming-Hung Kao, *Tempe*
Sunil Krishnan, *Houston*
Richard A Komoroski, *Cincinnati*
Sandi A Kwee, *Honolulu*
King Kim, *Ft. Lauderdale*
Guozheng Liu, *Worcester*
Yiyan Liu, *Newark*
Venkatesh Mani, *New York*
Lian-Sheng Ma, *Pleasanton*
Rachna Madan, *Boston*
Zeyad A Metwalli, *Houston*
Yilong Ma, *Manhasset*
Hui Mao, *Atlanta*
Feroze B Mohamed, *Philadelphia*
Gul Moonis, *Boston*
John L Nosher, *New Brunswick*
Rahmi Oklu, *Boston*
Aytekin Oto, *Chicago*
Bishnuhari Paudyal, *Philadelphia*
Rajul Pandya, *Youngstown*
Chong-Xian Pan, *Sacramento*
Jay J Pillai, *Baltimore*
Neal Prakash, *Duarte*
Reza Rahbar, *Boston*
Ali S Raja, *Boston*
Gustavo J Rodriguez, *El Paso*
David J Sahn, *Portlsand*
Steven Schild, *Scottsdale*
Ali R Sepahdari, *Los Angeles*
Li Shen, *Indianapolis*
JP Sheehan, *Charlottesville*
Atul B Shinagare, *Boston*
Sarabjeet Singh, *Boston*
Charles J Smith, *Columbia*
Kenji Suzuki, *Chicago*
Monvadi Srichai-Parsia, *Washington*
Sree H Tirumani, *Boston*
Hebert A Vargas, *New York*
Sachit Verma, *Philadelphia*
Yoichi Watanabe, *Minneapolis*
Li Wang, *Chapel Hill*
Carol C Wu, *Boston*
Shoujun Xu, *Houston*
Min Yao, *Cleveland*
Xiaofeng Yang, *Atlanta*
Qingbao Yu, *Albuquerque*
Aifeng Zhang, *Chicago*
Chao Zhou, *Bethlehem*
Hongming Zhuang, *Philadelphia*

WJR

World Journal of
Radiology

Contents

Monthly Volume 7 Number 12 December 28, 2015

EDITORIAL

421 Future of cardiac computed tomography
De Cecco CN, Schoepf UJ

DIAGNOSTIC ADVANCES

424 Various diffusion magnetic resonance imaging techniques for pancreatic cancer
Tang MY, Zhang XM, Chen TW, Huang XH

REVIEW

438 Middle cerebellar peduncles: Magnetic resonance imaging and pathophysiologic correlate
Morales H, Tomsick T

448 Magnetic resonance imaging of the spinal marrow: Basic understanding of the normal marrow pattern and its variant
Nouh MR, Eid AF

459 Multi-detector computed tomography imaging of large airway pathology: A pictorial review
Jugpal TS, Garg A, Sethi GR, Daga MK, Kumar J

MINIREVIEWS

475 Amyloid positron emission tomography and cognitive reserve
Bauckneht M, Picco A, Nobili F, Morbelli S

484 Three-dimensional imaging of the uterus: The value of the coronal plane
Wong L, White N, Ramkrishna J, Araujo Júnior E, Meagher S, Da Silva Costa F

ORIGINAL ARTICLE

Retrospective Study

494 Recovery of serum testosterone following neoadjuvant and adjuvant androgen deprivation therapy in men treated with prostate brachytherapy
Tsumura H, Satoh T, Ishiyama H, Hirano S, Tabata K, Kurosaka S, Matsumoto K, Fujita T, Kitano M, Baba S, Hayakawa K, Iwamura M

501 Common bile duct diameter in an asymptomatic population: A magnetic resonance imaging study
Peng R, Zhang L, Zhang XM, Chen TW, Yang L, Huang XH, Zhang ZM

Observational Study

509 Combined value of apparent diffusion coefficient-standardized uptake value max in evaluation of post-treated locally advanced rectal cancer

Ippolito D, Fior D, Trattenero C, De Ponti E, Drago S, Guerra L, Franzesi CT, Sironi S

Prospective Study

521 Cavernosal nerve functionality evaluation after magnetic resonance imaging-guided transurethral ultrasound treatment of the prostate

Sammet S, Partanen A, Yousuf A, Sammet CL, Ward EV, Wardrip C, Niekrasz M, Antic T, Razmaria A, Farahani K, Sokka S, Karczmar G, Oto A

SYSTEMATIC REVIEWS

531 Classifications of mandibular canal branching: A review of literature

Castro MAA, Lagravere-Vich MO, Amaral TMP, Abreu MHG, Mesquita RA

Contents

World Journal of Radiology
Volume 7 Number 12 December 28, 2015

ABOUT COVER

Editorial Board Member of *World Journal of Radiology*, Gopinathan Anil, DNB, MD, Doctor, Department of Diagnostic Imaging, National University Hospital and Yong Loo Lin School of Medicine, Singapore 119074, Singapore

AIM AND SCOPE

World Journal of Radiology (*World J Radiol*, *WJR*, online ISSN 1949-8470, DOI: 10.4329) is a peer-reviewed open access academic journal that aims to guide clinical practice and improve diagnostic and therapeutic skills of clinicians.

WJR covers topics concerning diagnostic radiology, radiation oncology, radiologic physics, neuroradiology, nuclear radiology, pediatric radiology, vascular/interventional radiology, medical imaging achieved by various modalities and related methods analysis. The current columns of *WJR* include editorial, frontier, diagnostic advances, therapeutics advances, field of vision, mini-reviews, review, topic highlight, medical ethics, original articles, case report, clinical case conference (clinicopathological conference), and autobiography.

We encourage authors to submit their manuscripts to *WJR*. We will give priority to manuscripts that are supported by major national and international foundations and those that are of great basic and clinical significance.

INDEXING/ABSTRACTING

World Journal of Radiology is now indexed in PubMed Central, PubMed, Digital Object Identifier, and Directory of Open Access Journals.

FLYLEAF

I-III Editorial Board

EDITORS FOR THIS ISSUE

Responsible Assistant Editor: *Xiang Li*
Responsible Electronic Editor: *Huan-Liang Wu*
Proofing Editor-in-Chief: *Lian-Sheng Ma*
Responsible Science Editor: *Jin-Xin Kong*
Proofing Editorial Office Director: *Xiu-Xia Song*

NAME OF JOURNAL
World Journal of Radiology

ISSN
ISSN 1949-8470 (online)

LAUNCH DATE
December 31, 2009

FREQUENCY
Monthly

EDITORS-IN-CHIEF
Kai U Juergens, MD, Associate Professor, MRT und PET/CT, Nuklearmedizin Bremen Mitte, ZEMODI - Zentrum für morphologische und molekulare Diagnostik, Bremen 28177, Germany

Edwin JR van Beek, MD, PhD, Professor, Clinical Research Imaging Centre and Department of Medical Radiology, University of Edinburgh, Edinburgh EH16 4TJ, United Kingdom

Thomas J Vogl, MD, Professor, Reader in Health Technology Assessment, Department of Diagnostic and Interventional Radiology, Johann Wolfgang Goethe University of Frankfurt, Frankfurt 60590, Germany

EDITORIAL OFFICE
Jin-Lei Wang, Director
Xiu-Xia Song, Vice Director
World Journal of Radiology
Room 903, Building D, Ocean International Center,
No. 62 Dongsihuan Zhonglu, Chaoyang District,
Beijing 100025, China
Telephone: +86-10-59080039
Fax: +86-10-85381893
E-mail: editorialoffice@wjgnet.com
Help Desk: http://www.wjgnet.com/esps/helpdesk.aspx
http://www.wjgnet.com

PUBLISHER
Baishideng Publishing Group Inc
8226 Regency Drive,
Pleasanton, CA 94588, USA
Telephone: +1-925-223-8242
Fax: +1-925-223-8243
E-mail: bpgoffice@wjgnet.com
Help Desk: http://www.wjgnet.com/esps/helpdesk.aspx
http://www.wjgnet.com

PUBLICATION DATE
December 28, 2015

INSTRUCTIONS TO AUTHORS
Full instructions are available online at http://www.wjgnet.com/1949-8470/g_info_20100316162358.htm.

ONLINE SUBMISSION
http://www.wjgnet.com/esps/

W J R World Journal of Radiology

Submit a Manuscript: http://www.wjgnet.com/esps/
Help Desk: http://www.wjgnet.com/esps/helpdesk.aspx
DOI: 10.4329/wjr.v7.i12.421

World J Radiol 2015 December 28; 7(12): 421-423
ISSN 1949-8470 (online)

EDITORIAL

Future of cardiac computed tomography

Carlo N De Cecco, U Joseph Schoepf

Carlo N De Cecco, U Joseph Schoepf, Division of Cardiovascular Imaging, Department of Radiology and Radiological Science, Medical University of South Carolina, Charleston, SC 29425, United States

U Joseph Schoepf, Division of Cardiology, Department of Medicine, Medical University of South Carolina, Charleston, SC 29425, United States

Author contributions: Both authors contributed to this manuscript.

Conflict-of-interest statement: Dr. Schoepf is a consultant for and/or receives research support from Bayer, Bracco, GE and Siemens. The other authors have no conflicts of interest to disclose.

Correspondence to: Carlo N De Cecco, MD, PhD, Division of Cardiovascular Imaging, Department of Radiology and Radiological Sciences, Medical University of South Carolina, 25 Courtenay Drive, MSC 226, Charleston, SC 29425,
United States. dececco@musc.edu
Telephone: +1-843-8763185
Fax: +1-843-8763157

Received: June 8, 2015
Peer-review started: June 10, 2015
First decision: August 4, 2015
Revised: September 17, 2015
Accepted: October 16, 2015
Article in press: October 19, 2015
Published online: December 28, 2015

Abstract

Coronary computed tomography angiography (CCTA) has become an integral tool in the noninvasive diagnostic workup of patients with suspected coronary artery disease in both elective and emergency settings. Today, it represents a mature technique providing accurate, non-invasive morphological assessment of the coronary arteries and atherosclerotic plaque burden. Iterative reconstruction algorithms, low kV imaging, and single-heart beat acquisitions hold promise to further reduce dose requirements and improve the safety and robustness of the technique in several circumstances including imaging of heavily calcified vessels, patients with morbid obesity or irregular heart rates, and assessment in the emergency setting. However, it has become clear over recent years that cardiac radiologists need to take further steps towards the development and integration of functional imaging with morphological CCTA assessment to truly provide a comprehensive evaluation of the heart. Computed tomography myocardial perfusion imaging, including both dynamic and static dual-energy approaches, has demonstrated the ability to directly assess and quantify myocardial ischemia with simultaneous CCTA acquisition with a reasonable contrast medium volume and radiation dose delivered to the patient. In order to promote CCTA in the clinical and research environments, radiologists should prepare to embrace the change from morphological to functional imaging, furnishing all the necessary resources and information to referring clinicians.

Key words: Coronary computed tomography angiography; Coronary computed myocardial perfusion imaging; Functional imaging; Coronary artery disease; Dynamic imaging; Dual energy coronary computed

Core tip: Coronary computed tomography angiography (CCTA) represents a mature technique providing accurate, non-invasive morphological assessment of the coronary arteries and atherosclerotic plaque burden. Computed tomography myocardial perfusion imaging, including both dynamic and static dual-energy approaches, has demonstrated the ability to directly assess and quantify myocardial ischemia with simultaneous CCTA acquisition. In order to promote CCTA in the clinical and research environments, radiologists should prepare to embrace the change from morphological to functional imaging.

De Cecco CN, Schoepf UJ. Future of cardiac computed tomography. *World J Radiol* 2015; 7(12): 421-423 Available from: URL: http://www.wjgnet.com/1949-8470/full/v7/i12/421.htm DOI: http://dx.doi.org/10.4329/wjr.v7.i12.421

In recent years, coronary computed tomography angiography (CCTA) has transitioned through the experimental and clinical validation stages to become an integral tool in the noninvasive diagnostic workup of patients with suspected coronary artery disease in both elective and emergency settings. Today, it represents a mature technique providing accurate, non-invasive morphological assessment of the coronary arteries and atherosclerotic plaque burden with a pooled sensitivity and specificity of 98% and 89%, respectively[1]. Technical innovations are continuously improving diagnostic performance and decreasing the radiation dose and contrast medium volume necessary for this test. Iterative reconstruction algorithms, low kV imaging, and single-heart beat acquisitions hold promise to further reduce dose requirements and improve the safety and robustness of the technique in several circumstances including imaging of heavily calcified vessels, patients with morbid obesity or irregular heart rates, and assessment in the emergency setting. In parallel with the growth of CCTA, the cardiac radiologist has evolved from the role of a general thoracic radiologist with limited knowledge of cardiac pathophysiology to a specialist with vast expertise in cardiac disease and cutting edge imaging applications.

However, it has become clear over recent years that cardiac radiologists need to take further steps towards the development and integration of functional imaging with morphological CCTA assessment to truly provide a comprehensive evaluation of the heart. In fact, a growing body of evidence has shown that a purely anatomical evaluation of coronary stenosis does not adequately predict hemodynamic relevance and is thus suboptimal for guiding patient management, including the major FAME and COURAGE trials which validated the impact of functional tests in coronary revascularization[2,3]. In response to this limitation, innovative computed tomography (CT) technology has allowed the derivation of functional data in addition to morphological assessment, providing comprehensive appraisal of both the anatomical and functional aspects of coronary heart disease with a single modality.

CT myocardial perfusion imaging, including both dynamic and static dual-energy approaches, has demonstrated the ability to directly assess and quantify myocardial ischemia with simultaneous CCTA acquisition with a reasonable contrast medium volume and radiation dose delivered to the patient as long as the scanner technology is recent enough to meet such high technological requirements[4]. The administration of a pharmacological stressor, including adenosine, regadenoson, dobutamine, or dipyridamole, to induce a hyperemic myocardium, could represent a potential challenge from a radiological point of view. However, as demonstrated in our department, a trained team composed of a radiologist, technologist, and nurse with the support of cardiologists or anesthesiologists can safely handle the administration of these drugs, especially in the case of regadenoson, a selective A2A receptor agonist with limited side effects and convenient administration.

In clinical settings where appropriate CT technology is not available or stress perfusion acquisitions cannot be easily performed, other options are available for the assessment of cardiac function[5]. CT-based fractional flow reserve (FFR) allows the assessment of flow-limiting stenosis directly from CCTA datasets, without the use of stress agents, additional image acquisitions or contrast medium injections. However, CT-based FFR calculations require the use of dedicated third party off-site post-processing software, significantly increasing the cost and reporting time. In-house dedicated software is under development which could drastically increase the clinical availability and utilization of this technique. Other less advanced solutions in the diagnosis of significant coronary stenosis, including the lesion length/minimal luminal diameter or corrected coronary attenuation (CCO) can be directly calculated from the CCTA dataset without the need for any dedicated software and with sufficient efficacy[6].

What role, then, should we expect CCTA to play in the standard clinical cardiovascular workup? As CT technology continues to increase the potential for functional assessment in CCTA, we believe the future of cardiac CT is bright.

The volume of CCTA examinations has increased exponentially over the last decade as the technique grew from a niche method performed in the research environment to a routinely used diagnostic test offered in most diagnostic imaging centers. As old scanners are replaced with more advanced versions, an increasing number of hospitals and private diagnostic centers will offer CCTA and it stands to reason that clinician demand will increase. In addition, the aforementioned technological improvements will bring CT-based functional analysis to clinical practice, echoing the rise of morphological CCTA assessment.

In order to promote CCTA in the clinical and research environments, radiologists should prepare to embrace the change from morphological to functional imaging, furnishing all the necessary resources and information to referring clinicians. We are confident in the continued development of this well-established but rapidly growing field and that any challenges to come will continue to promote the role of comprehensively trained cardiac radiologists aware of their pivotal role in cardiac disease management.

REFERENCES

1 **De Cecco CN**, Meinel FG, Chiaramida SA, Costello P, Bamberg F, Schoepf UJ. Coronary artery computed tomography scanning. *Circulation* 2014; **129**: 1341-1345 [PMID: 24664217 DOI: 10.1161/CIRCULATIONAHA.113.002835]

2 **Pijls NH**, Fearon WF, Tonino PA, Siebert U, Ikeno F, Bornschein B, van't Veer M, Klauss V, Manoharan G, Engstrøm T, Oldroyd KG, Ver Lee PN, MacCarthy PA, De Bruyne B. Fractional flow reserve versus angiography for guiding percutaneous coronary intervention in patients with multivessel coronary artery disease: 2-year follow-up of the FAME (Fractional Flow Reserve Versus Angiography for Multivessel Evaluation) study. *J Am Coll Cardiol* 2010; **56**: 177-184 [PMID: 20537493 DOI: 10.1016/j.jacc.2010.04.012]

3 **Shaw LJ**, Berman DS, Maron DJ, Mancini GB, Hayes SW, Hartigan PM, Weintraub WS, O'Rourke RA, Dada M, Spertus JA, Chaitman BR, Friedman J, Slomka P, Heller GV, Germano G, Gosselin G, Berger P, Kostuk WJ, Schwartz RG, Knudtson M, Veledar E, Bates ER, McCallister B, Teo KK, Boden WE. Optimal medical therapy with or without percutaneous coronary intervention to reduce ischemic burden: results from the Clinical Outcomes Utilizing Revascularization and Aggressive Drug Evaluation (COURAGE) trial nuclear substudy. *Circulation* 2008; **117**: 1283-1291 [PMID: 18268144 DOI: 10.1161/CIRCULATIONAHA.107.743963]

4 **Cannaò PM**, Schoepf UJ, Muscogiuri G, Wichmann JL, Fuller SR, Secchi F, Varga-Szemes A, De Cecco CN. Technical prerequisites and imaging protocols for dynamic and dual energy myocardial perfusion imaging. *Eur J Radiol* 2015; **84**: 2401-2410 [PMID: 25779223 DOI: 10.1016/j.ejrad.2015.02.010]

5 **De Cecco CN**, Varga-Szemes A, Meinel FG, Renker M, Schoepf UJ. Beyond stenosis detection: computed tomography approaches for determining the functional relevance of coronary artery disease. *Radiol Clin North Am* 2015; **53**: 317-334 [PMID: 25726997 DOI: 10.1016/j.rcl.2014.11.009]

6 **Wang R**, Renker M, Schoepf UJ, Wichmann JL, Fuller SR, Rier JD, Bayer RR, Steinberg DH, De Cecco CN, Baumann S. Diagnostic value of quantitative stenosis predictors with coronary CT angiography compared to invasive fractional flow reserve. *Eur J Radiol* 2015; **84**: 1509-1515 [PMID: 26022519 DOI: 10.1016/j.ejrad.2015.05.010]

P- Reviewer: Choe YH, Dogan OF **S- Editor**: Ji FF **L- Editor**: A **E- Editor**: Wu HL

W J R World Journal of Radiology

Submit a Manuscript: http://www.wjgnet.com/esps/
Help Desk: http://www.wjgnet.com/esps/helpdesk.aspx
DOI: 10.4329/wjr.v7.i12.424

World J Radiol 2015 December 28; 7(12): 424-437
ISSN 1949-8470 (online)

DIAGNOSTIC ADVANCES

Various diffusion magnetic resonance imaging techniques for pancreatic cancer

Meng-Yue Tang, Xiao-Ming Zhang, Tian-Wu Chen, Xiao-Hua Huang

Meng-Yue Tang, Xiao-Ming Zhang, Tian-Wu Chen, Xiao-Hua Huang, Sichuan Key Laboratory of Medical Imaging, Department of Radiology, Affiliated Hospital of North Sichuan Medical College, Nanchong 637000, Sichuan Province, China

Author contributions: Tang MY, Zhang XM and Chen TW designed research; Tang MY and Huang XH performed research; Tang MY and Zhang XM contributed analytic tools; Tang MY, Zhang XM and Huang XH analyzed data; Tang MY, Zhang XM, Chen TW and Huang XH wrote the paper.

Supported by National Nature Science Foundation of China, No. 81271643.

Conflict-of-interest statement: Authors declare that there is no conflict of interests regarding the publication of this article.

Correspondence to: Xiao-Ming Zhang, MD, PhD, Professor, Head, Sichuan Key Laboratory of Medical Imaging, Department of Radiology, Affiliated Hospital of North Sichuan Medical College, Wenhua Road 63, Nanchong 637000, Sichuan Province, China. cjr.zhxm@vip.163.com
Telephone: +86-817-2262218
Fax: +86-817-2222856

Received: May 15, 2015
Peer-review started: May 20, 2015
First decision: September 8, 2015
Revised: September 15, 2015
Accepted: November 13, 2015
Article in press: November 17, 2015
Published online: December 28, 2015

Abstract

Pancreatic cancer is one of the most common malignant tumors and remains a treatment-refractory cancer with a poor prognosis. Currently, the diagnosis of pancreatic neoplasm depends mainly on imaging and which methods are conducive to detecting small lesions. Compared to the other techniques, magnetic resonance imaging (MRI) has irreplaceable advantages and can provide valuable information unattainable with other noninvasive or minimally invasive imaging techniques. Advances in MR hardware and pulse sequence design have particularly improved the quality and robustness of MRI of the pancreas. Diffusion MR imaging serves as one of the common functional MRI techniques and is the only technique that can be used to reflect the diffusion movement of water molecules *in vivo*. It is generally known that diffusion properties depend on the characterization of intrinsic features of tissue microdynamics and microstructure. With the improvement of the diffusion models, diffusion MR imaging techniques are increasingly varied, from the simplest and most commonly used technique to the more complex. In this review, the various diffusion MRI techniques for pancreatic cancer are discussed, including conventional diffusion weighted imaging (DWI), multi-b DWI based on intra-voxel incoherent motion theory, diffusion tensor imaging and diffusion kurtosis imaging. The principles, main parameters, advantages and limitations of these techniques, as well as future directions for pancreatic diffusion imaging are also discussed.

Key words: Pancreatic cancer; Magnetic resonance imaging; Diffusion; Diffusion weighted imaging; Diffusion tensor imaging; Diffusion kurtosis imaging

Core tip: Magnetic resonance imaging (MRI) has irreplaceable advantages and can provide valuable information unattainable with other noninvasive or minimally invasive imaging techniques. Diffusion MR imaging serves as one of the common functional MRI

techniques and is the only technique that can be used to reflect the diffusion movement of water molecules *in vivo*. In this review, the various diffusion MR imaging techniques for pancreatic cancer will be discussed, including conventional diffusion weighted imaging (DWI), multi-b DWI based on intra-voxel incoherent motion theory, diffusion tensor imaging and diffusion kurtosis imaging.

Tang MY, Zhang XM, Chen TW, Huang XH. Various diffusion magnetic resonance imaging techniques for pancreatic cancer. *World J Radiol* 2015; 7(12): 424-437 Available from: URL: http://www.wjgnet.com/1949-8470/full/v7/i12/424.htm DOI: http://dx.doi.org/10.4329/wjr.v7.i12.424

INTRODUCTION

Pancreatic cancer is one of the most common malignant tumors with a poor prognosis, of which the 5-year survival rate range is no more than 5%[1] and as low as 0.4% to 2%[2,3]. It is reported that there has been little improvement in survival rate over the past 30 years[4]. Because the pancreas is deep-seated, there is a lack of apparent symptoms in early pancreatic cancer. In most cases, the tumor is diagnosed at an advanced stage, at which point, it does not benefit from radical surgery[2]. The management of pancreatic cancer is still encountered as a significant and unresolved therapeutic challenge.

Currently, the diagnosis of pancreatic neoplasm depends mainly on the imaging, and which methods can be conducive to detecting small lesions. Despite the continuing advances in diagnostic techniques, the early precise diagnosis of pancreatic cancer remains unsatisfactory. Early detection followed by surgical resection offers hope for a cure and is the key to improving pancreatic cancer survival[5]. Unfortunately, only 20% of patients are resectable at the time of diagnosis[6]. Computed tomography (CT), Magnetic resonance imaging (MRI), transabdominal and endoscopic ultrasonography (US and EUS) and endoscopic retrograde cholangiopancreatography (ERCP) also play an important role in the diagnosis of pancreatic cancer[7-10]. Among them, MRI has irreplaceable advantages, especially, the advances in MR hardware and pulse sequence design that have improved the quality and robustness of MRI of the pancreas. Today, MRI is an indispensable tool for pancreatic disorders and can provide valuable information unattainable with other noninvasive or minimally invasive imaging techniques[11-13].

With the rapid development of the MRI, diffusion MR imaging, which is based on the microscopic mobility of water molecules in the tissues without contrast administration, is a promising technique that is widely applied in clinical practice. Diffusion MR imaging is also the only available method that can measure the diffusion properties of tissues noninvasively and quantitatively[14,15], such as the diffusion weighted imaging (DWI), and has been helpful for the detection and characterization of pancreatic conditions[16,17]. The DWI technique serves as an excellent adjunct to routine abdominal MR imaging[13], is noninvasive in contrast to EUS and ERCP, and does not employ ionizing radiation like CT[18].

The changes in the composition and/or cellularity of tissues influences the random thermal diffusion of water molecules[19]. Compared to normal pancreatic tissue, pancreatic cancer has a higher cell density, relatively smaller extracellular space and a different blood supply. Thus, the diffusion of molecules in the cancer would be different from that in the normal pancreatic tissue. DWI, one of the functional MRI techniques based on water molecule movement, can depict this change in diffusion and can quantitatively measure the parameters that can represent these diffusion properties. Thus, DWI can reflect biologic abnormalities at an early stage[20].

In this review, the various diffusion MR imaging techniques for pancreatic cancer will be discussed, including DWI, multi-b DWI based on intra-voxel incoherent motion (IVIM) theory, diffusion tensor imaging (DTI) and diffusion kurtosis imaging (DKI). The principles, main parameters, advantages and limitations of each technique and the future directions for pancreatic diffusion imaging will also be discussed.

DWI FOR PANCREATIC CANCER

Conventional DWI

Single-shot spin-echo echo-planar (SE-EPI) sequence is the most widely applied in the DW MR imaging (Figure 1). Conventional DWI uses the 2 motion-probing bipolar gradients in 3 directions (x, y, z) and acquires the signal from the 3 directions. The final DW image is derived from the fusion of the 3 images. DWI exploits the random motion of water molecules in biologic tissues. The water molecules diffuse in 3 different compartments: The intracellular, the intravascular, and the interstitial compartment. The diffusion of water molecules depends on the interactions with cell membranes, tissue compartments, and intracellular content[21]. Consequently, the diffusion of water in tissues reflects, to various degrees, a combination of tissue cellularity, tortuosity of extracellular spaces, integrity of cell membranes, and viscosity of fluids[22].

DWI was originally described for the central nervous system[23,24], which is particularly good for the diagnosis of ischemic stroke. In recent years, DWI has presented promising results in the diagnosis of some illnesses of the lower abdomen, such as those of the prostate[25,26]. DWI of the upper abdomen has been a technical challenge due to respiration, bowel peristalsis, blood flow and long acquisition times[18]. The implementation of ultrafast imaging techniques, such as parallel imaging, has made DWI (a combination of pulses and strong gradients) of the upper abdomen

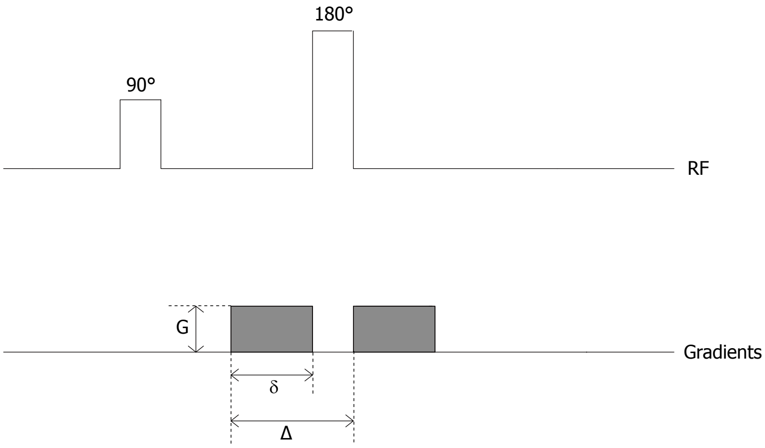

Figure 1 Diffusion weighted imaging sequence. Diffusion weighted imaging (DWI) applies the two motion-probing bipolar gradients on either side of the refocusing 180°pulse. The degree of diffusion weighting depends on the G (the amplitude of the gradients), δ (their duration) and Δ (the interval between gradients). This factor is quantitatively expressed by a parameter b, where $b = \gamma^2 G^2 \delta^2 (\Delta - \delta/3)$ and γ is a constant of the gyromagnetic ratio. Assuming that the water molecules in tissues are motionless, the effects of the two motion-probing bipolar gradients can cancel each other. Thus, for the free molecular diffusion of water molecules, the displacement can be depicted by the DWI. RF: Radio frequency.

a feasible option. It has also been found to be useful in the differentiation of malignancy from benign liver lesions[27,28].

The three main parameters in the DWI are D value, b value and apparent diffusion coefficient (ADC) value. The D value is the diffusion parameter representing the free molecular diffusion and is defined as the average displacement by molecules in a certain direction, per unit of time. The D value can be affected by a variety of physiological factors, including respiration, perfusion, pulse and movement. The b value is referred to as the gradient factor, which can reflect the effect of the diffusion gradient. In the conventional DWI, the various b values can be selected. The low b value is applied more in water molecules with rapid movement or long diffusion distance, but the high b value is applied more in water molecules with slow movement or a short diffusion distance. Thus, the high b value is good for reducing the effect of the movement of water molecules due to perfusion[29].

In vivo, there are many factors that can affect the diffusion movement of water molecules, including the b value, D value and T2 shine-through effect. The T2 shine- through effect occurs when tissue with a long T2 relaxation time is characterized by hyperintensity on DWI. The ADC results in standardizing by considering the above factors and would be used to reflect the state of diffusion of water molecules *in vivo*.

DWI, which can be used for the qualitative and quantitative assessment of tissue diffusivity, can be routinely applied in clinical practice[16]. Recent studies indicate that DWI is also promising in pancreatic imaging[30-34]. These popular research studies also reflect the value of DWI in the diagnosis of pancreatic cancer. Moreover, compared to the other techniques, the sensitivity and specificity for the diagnosis of pancreatic cancer is valuable. Kartalis *et al*[18] conducted research on the value of DWI for pancreatic cancer, and their results showed that the qualitative DWI of pancreatic cancer has an accuracy of 96%; further, DWI has been shown to have high sensitivity (92%) and specificity (97%), consistent with the findings of Ichikawa *et al*[30] (96.2% and 98.6%, respectively). Furthermore, a recent study shows that the addition of DWI to conventional MR imaging improves the sensitivity of cancer detection[35]. The sensitivity of DWI was close to that of dynamic gadolinium-enhanced MRI (97.7%), with a higher specificity (85.1%)[36]. Compared to the multidetector CT, positron emission tomography with CT and transabdominal ultrasound, the sensitivity and specificity of DWI are higher[18,37,38]. Although the sensitivity of EUS can reach 100%, it is invasive and has only 50% specificity[39]. Thus, it does not have wide application in clinical practice.

DWI can provide information regarding the cellular density and properties of the extracellular matrix[40,41]. The ADC values seem to reflect not only the underlying tissue microstructure but also the undirected movement of particles in thecapillaries[42]. The ADC value has been shown to be able to serve as a marker of cellularity[41,43]. The ADC value in the normal pancreas has been reported to range from 1.0 to 2.0 × 10^{-3} mm^2/s[44]. Many studies have shown that the ADC value of pancreatic cancer is lower than that of the normal pancreas[13,31,45-52]. There are three reasons that may explain these results[53]. First, tumor cell growth is rapid with high cellularity. Second, tumor cell atypia and the richness of organelles are positively correlated in the pancreatic tumor cells, and the nucleus and organelles are bulkier than that of normal pancreas cells. Thus, to some extent, tumor cell growth may limit the diffusion of water molecules. Third, the decrease of extracellular space from dense cellularity and extracellular fibrosis may also account for the restricted water diffusion[13,20,54-56]. However, Wang *et al*[54] reported that there is no significant difference in the ADC value between the normal pancreas and pancreatic cancer. These different results were most likely due to the application of different DWI experimental protocols and processing means[57]. The most important factor is the choice of b value. Kim *et al*[58] conducted research to determine the effect of the magnitude of b values on the ADC. Their results showed that the calculated ADC value could be affected by the magnitude of the maximum b value and that the higher the maximum b value, the lower the ADC value.

Additionally, the diverse differentiation of pancreatic cancer can be differentiated using DWI. For example, poorly differentiated adenocarcinoma had significantly lower ADCs than those of well/moderately differentiated adenocarcinomas[59].

Recently, DWI techniques have been shown not to be uniform, this controversial conclusion needs further study and differences in the sequence parameters and b values chosen may affect the ADC results. Future prospective studies are required to better determine the most appropriate use of the b value of pancreatic disease. Comparing different b values in a larger series of patients with malignant lesions would probably be of value; the quantification of the ADC of various lesions will be more accurate is feasible b values are used. The ADC values may have considerable overlap between the benign and malignant lesions, indicating that qualitative DWI seems to be more accurate than the quantitative analysis and can be used as an accurate method for the detection of pancreatic cancer[18].

Multi-b DWI based on IVIM theory

The rapid development of DWI monoexponential and biexponential models, of which the theoretical basis of the techniques is that the diffusion of water molecules is characterized by a normal distribution, has been applied to abdominal imaging using DWI. The monoexponential model is the most commonly used in daily practice. However, the biexponential model, which is based on the IVIM theory that was introduced as a technique to reflect both perfusion and diffusion by Le Bihan *et al*[20] can account for separating tissue diffusivity and tissue microcapillary perfusion. The unique feature of the multi-b DWI based on IVIM is the application of the multiple b value (Figures 2-4), which can be used in biexponential models to calculate the IVIM-derived parameters.

Monoexponential models are based on an assumption that the diffusion occurs in a free and unrestricted environment in biologic tissue, that is to say, the distribution of displacements obeys Gaussian law. Biexponential models reflect a combination of tissue perfusion and tissue diffusivity effects. It is now generally accepted that when the b value is relatively low (0-200 s/mm^2), the signal of ADC contains two parts; one is the diffusion of water molecules, and the other is the perfusion of water molecules in the capillary in local microcirculation. Further, the effect of perfusion is more sensitive. When the b value is relatively high (200-1000 s/mm^2), the attenuation of signal due to the effect of perfusion is slight, at this point, the signal of DWI only approximately reflects the diffusion of water molecules[60]. This is a basic principle of conventional DWI and is the reason that the high b value was selected.

IVIM can accurately describe the relationship between signal attenuation and b values in the DWI and relatively obtain the parameters that present the effect of diffusion and perfusion in tissue.

Standard ADC value (or conventional ADC value) can be obtained from IVIM. Additionally, there are three main parameters in the IVIM, including D value, D* value and f value (perfusion fraction). D value is the true diffusion coefficient, also called the structural diffusion constant D value or slow ADC value, which reflects the tissue microstructure[48] and is the actual diffusion effect of water molecules. The D* value, also referred as the pseudo diffusion coefficient, perfusion-related coefficient or fast ADC value, is the diffusion parameter due to the perfusion effect of the incoherent microcirculation within the voxel[61]. The diffusion and perfusion can affect the signal intensity attenuation on DWI, and the proportion of the perfusion effect is defined as the perfusion fraction (Figure 4).

Diffusion-based IVIM has recently gained interest as a method to detect and characterize pancreatic lesions, and multi-b DWI based on IVIM theory shows very promising results and should be further investigated[48,62]. The f values were reported to make a contribution to distinguishing between normal pancreatic parenchyma and pancreatic neoplasm[45,49,50,63,64], and the f value proved to be the superior DWI-derived parameter for the differentiation of mass-forming pancreatitis and pancreatic carcinoma[50].

Many studies indicated that the IVIM-derived parameter's f value was a superior parameter for differentiating pancreatic tumors from the normal pancreas compared to the conventional ADC values and that the f value is lower in pancreatic cancer[48,51]. Lemke *et al*[63] conducted research to study the vascular contribution to the measured ADC value and to validate the IVIM theory; their results showed that the perfusion fraction f in the blood-suppressed pancreatic tissue decreased, possibly because the normal pancreas has a rich blood supply and will lead to a high f value. However, pancreatic cancer can destroy the normal pancreatic tissue and the vessel, and the decrease of vessel density may lead to the decreased f value, even if research shows that the f value in the IVIM-approach proved to be the best parameter for the differentiation between the normal pancreas and pancreatic cancer[48,51].

Compared to the f value, there is relatively less research on D value and D* value in pancreatic tumors. The structural diffusion constant D value reflects the tissue microstructure. The value of the D value for pancreatic cancer is controversial. Lemke *et al*[48] found that the D value showed no significant difference in pancreatic carcinoma and the healthy pancreas. Concia

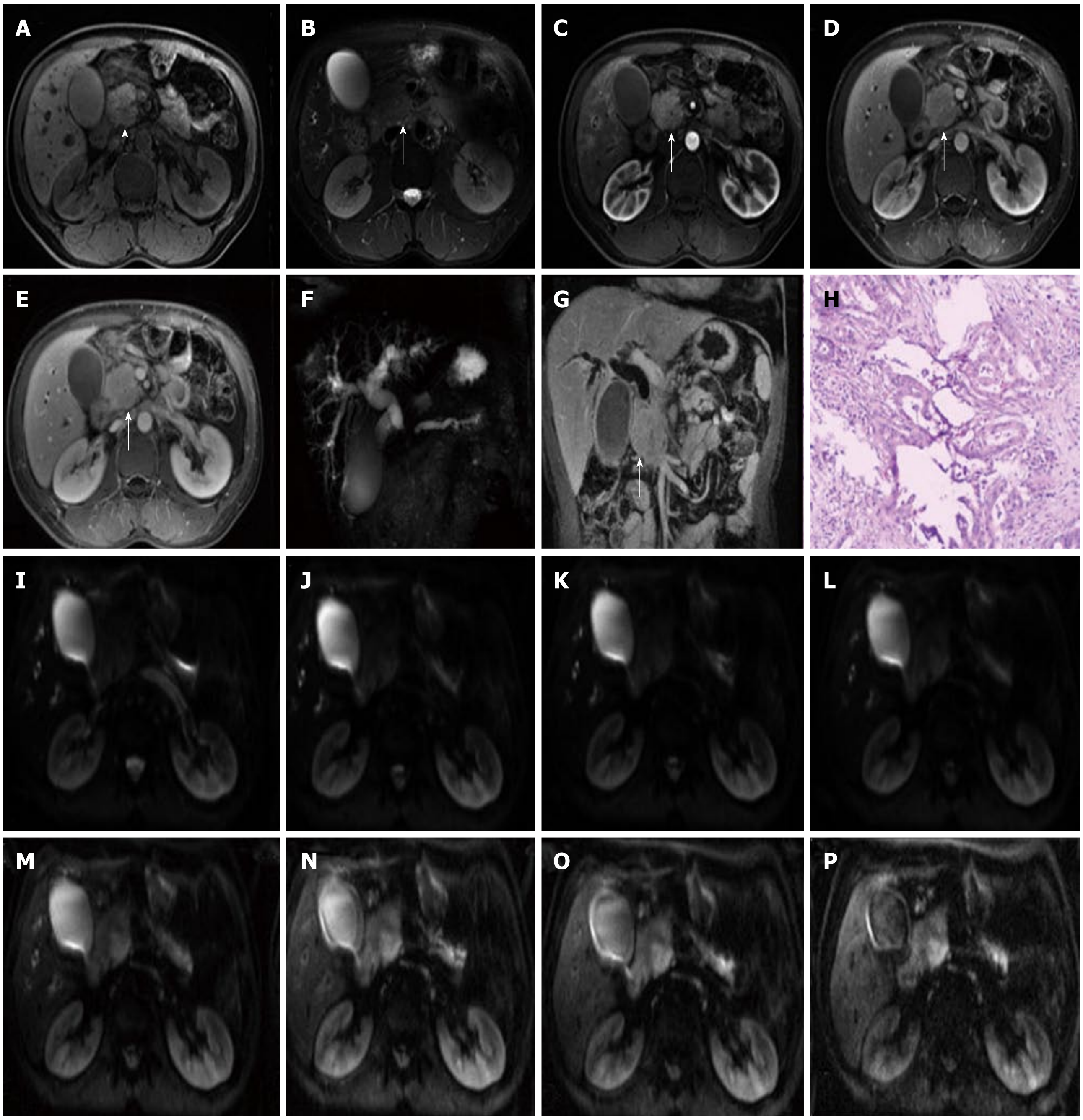

Figure 2 Images in a 47-year-old man with pancreatic moderately differentiated adenocarcinoma in the head of the pancreas (white arrows). A: Axial T1-weighted fat-suppressed gradient-echo MR image; B: Axial T2-weighted fat-suppressed fast spin-echo MR image; C-E and G: Axial and coronal slab three-dimensional liver acquisition with volume acceleration dynamic contrast-enhanced; F: MRCP shows the biliary obstruction; H: The pathology of the lesion is shown as pancreatic moderately differentiated adenocarcinoma; I-P: Multi-b DWI imaging (b = 0, 50, 100, 300, 500, 800, 1000 and 1500). MR: Magnetic resonance; DWI: Diffusion weighted imaging; MRCP: Magnetic resonance cholangiopancreatography.

et al[49] found that the D′ value (D value was estimated by D′ value) hardly differed in neuroendocrine pancreatic tumors and chronic pancreatitis. Klauss *et al*[50] reported that the D value cannot distinguish pancreatic carcinoma from mass-forming chronic pancreatitis. Klauss *et al*[42] reported that D value correlates with the histopathological grade of fibrosis in pancreatic lesions, which is the most characteristic histopathological feature of pancreatic carcinoma, compared with healthy pancreatic tissue, and concluded that D value can be used to monitor novel therapy approaches that inhibit the formation of fibrosis. In 2014, Hwang *et al*[65] reported that the D value may be a better marker of cellularity than ADC. Until now, this was the only research on the D* value in pancreatic cancer. In 2014, Kang *et al*[51] used IVIM-derived parameters for the differentiation of common pancreatic tumors and concluded that the D* value and f values were more useful parameters in the differentiation of pancreatic adenocarcinomas from neuroendocrine tumors than were the ADC and D values.

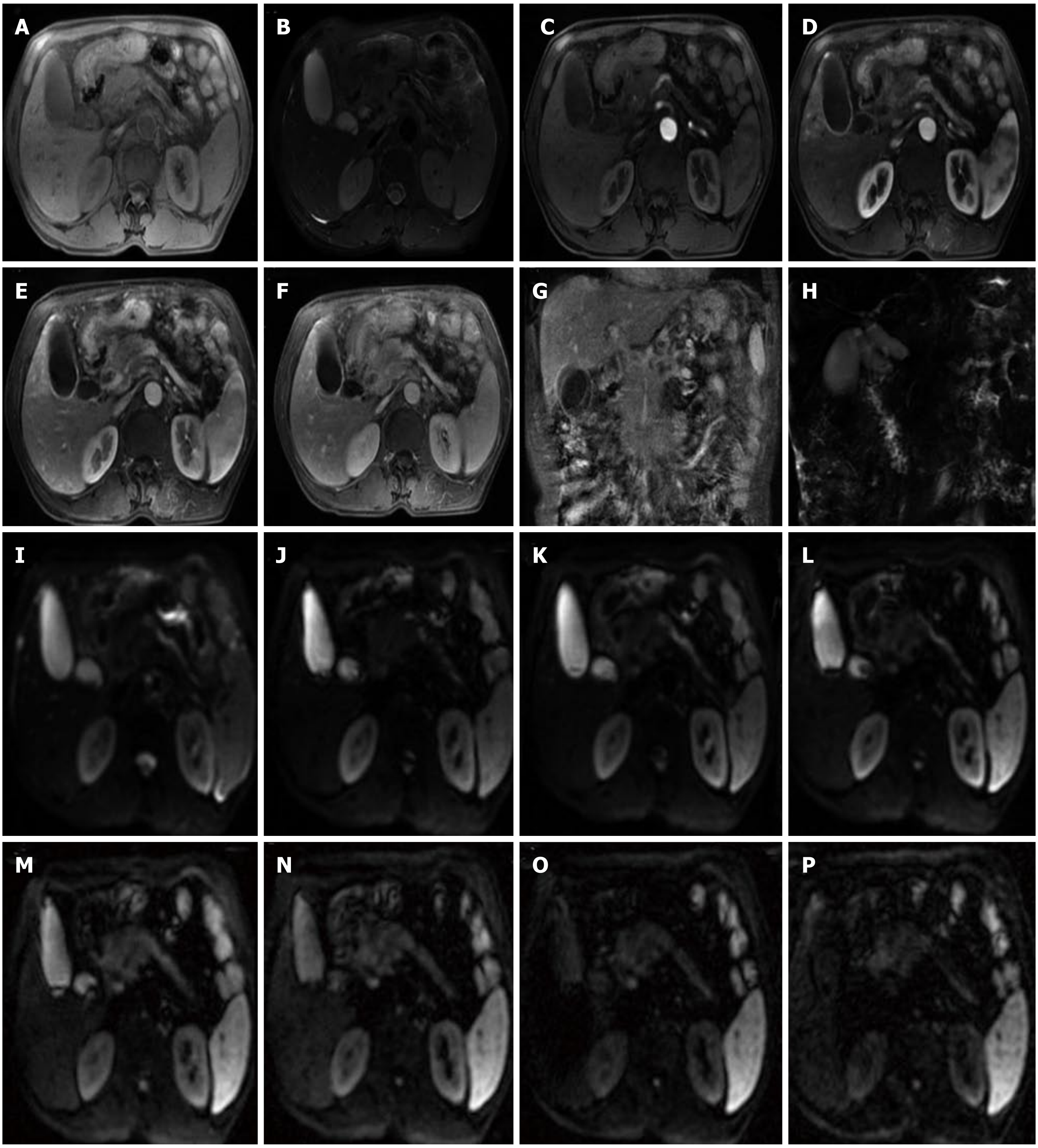

Figure 3 Images in a 63-year-old man with a focal lesion in the head of the pancreas. MR imaging suggests that it is a malignancy. A: Axial T1-weighted fat-suppressed gradient-echo MR image; B: Axial T2-weighted fat-suppressed fast spin-echo MR image; C-G: Axial and coronal slab three-dimensional liver acquisition with volume acceleration dynamic contrast-enhanced; H: MRCP shows the biliary obstruction; I-P: Multi-b DWI imaging (b = 0, 50, 100, 300, 500, 800, 1000 and 1500). MR: Magnetic resonance; DWI: Diffusion weighted imaging; MRCP: Magnetic resonance cholangiopancreatography.

DTI FOR PANCREATIC CANCER

The sequence of DTI is similar to that of the DWI, and both are a SE-EPI sequence. The DTI also applies the two motion-probing bipolar gradients on either side of the refocusing 180° pulse. The difference or the unique feature is that the DTI acquires images from multiple directions. Thus, in clinical practice, a minimum of 6 non-collinear images is needed, but 12 or more images are often collected to increase the accuracy of the measure (Figure 5, Figure 6Q and R).

The DTI based on the diffusion of water molecules is anisotropic, which can be illustrated by the fact that the diffusion can be greater in one direction than in other directions and is termed "anisotropic" due to some factors, such as cell membranes, fibers, and myelin[66].

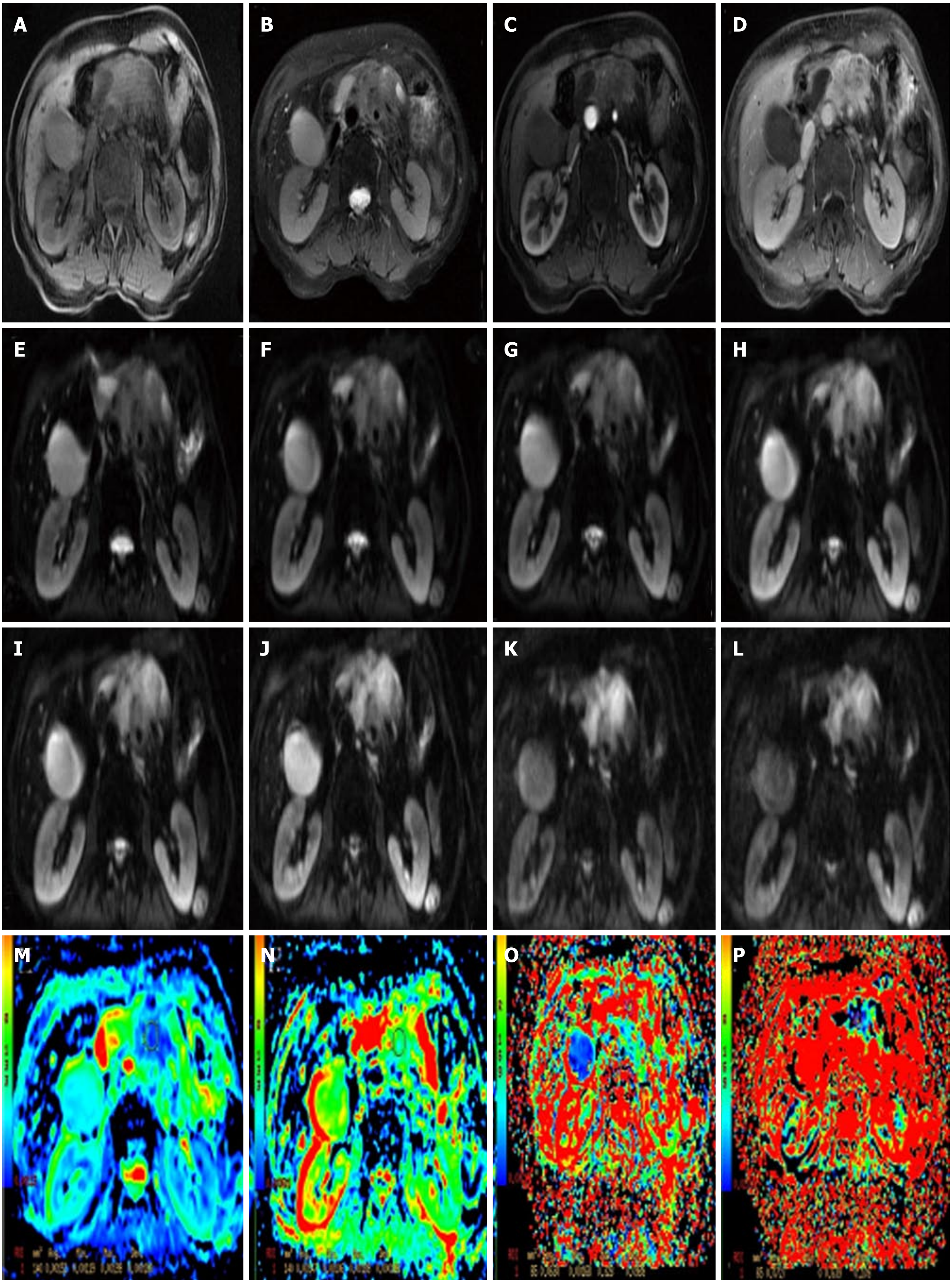

Figure 4 Images in a 65-year-old woman with a focal lesion in the neck of the pancreas. Magnetic resonance (MR) imaging suggests that it is a malignancy. A: Axial T1-weighted fat-suppressed gradient-echo MR image; B: Axial T2-weighted fat-suppressed fast spin-echo MR image; C and D: Axial slab three-dimensional liver acquisition with volume acceleration dynamic contrast-enhanced; E-L: Multi-b DWI (b = 0, 50, 100, 300, 500, 800, 1000 and 1500); M-P: Standard ADC = 1.52 × 10^{-3} mm^2/s, slow ADC = 1.39 × 10^{-3} mm^2/s, fast ADC = 63 × 10^{-3} mm^2/s and f = 7.2% generated by the post-processing from the multi-b DWI. DWI: Diffusion weighted imaging; ADC: Apparent diffusion coefficient.

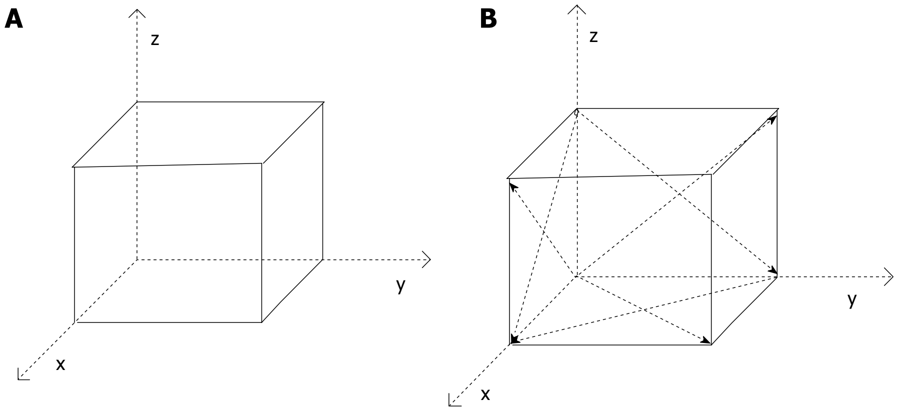

Figure 5 Conventional diffusion weighted imaging (A): The bipolar gradients in three directions; the diffusion tensor imaging bipolar gradients in the six non-collinear directions (solid black arrows) (B).

Conversely, without barriers, the random Brownian movement of water molecules is uniform in all directions or "isotropic". In general, DWI experiments yield an average ADC over three orthogonal directions, ignoring the anisotropy of tissue in the diffusion process[11,67]. Though the DTI model also assumes the diffusion distribution to be Gaussian, the same as the DWI, the DTI can measure the magnitude and directionality of water diffusion in tissue quantitatively[66]. The "tensor" in DTI refers to a mathematical construct for representing the magnitude of directional water diffusion in a three-dimensional volume[17].

DTI can not only reveal the degree of the restriction of water molecules in the diffusion movement but can also evaluate the different direction of diffusion. In a recently popular model, the DTI can provide some details on the microstructure of tissues that are not available in conventional imaging[68-70]. The major advantages of DTI are that it can assess the directionality of the diffusion of water molecules in biological tissue[71]. Thus, the DTI can evaluate more comprehensively and accurately the diffusion movement of water molecules in tissue. DTI also provides another non-invasive characterization of tissue microstructural properties *in vivo*[68].

DTI can demonstrate the subtle abnormalities of some diseases, and degrees of anisotropy have been reported to correlate with the microstructural changes in neural tissues[72,73] and even the peripheral nervous system[70]. DTI is also applied in myocardial infarction[74], prostate cancer[75,76], kidneys[77], liver[78], breast cancer[79], to name just a few. Indeed, it was reported that DTI would provide significant characterization of tissue microstructure and pathophysiology[80-82]. Each voxel in a DTI data set contains vector information that reflects the directionality and magnitude of diffusion in the underlying tissue.

There are five main parameters in the DTI, including mean diffusivity (MD), three eigenvalues $\lambda1$, $\lambda2$, $\lambda3$, and fractional anisotropy (FA). MD is the average of the ADC in all directions and can represent the degree of diffusion. In theory, MD more truly reflects the water molecules' diffusion ability than ADC, but in clinical practice, the mean diffusivity is expressed as ADC. The FA represents the fraction of the magnitude of tensor that is due to anisotropic water diffusion[83]. That is to say, FA represents the diversity of diffusion direction, which is calculated by the three above eigenvalues[84].

In 2014, Nissan *et al*[57] used the DTI for patients with pancreatic-ductal-adenocacinoma, and their results indicated that the parameters of DTI ($\lambda1$, $\lambda2$, $\lambda3$ and the ADC value) were lower than the values of the corresponding diffusion coefficients in the distal normal pancreatic tissue of the patients[57]; this outcome suggested that the fast diffusion component is dominated by the microcapillary perfusion process[63]. The results were consistent with those of previous DWI studies reporting lower ADC values in pancreatic cancer attributed to their higher cellularity[45-47].

DKI FOR PANCREATIC CANCER

The high b value is the most important feature of the DKI (Figure 6S and T). The DWI and IVIM are based on an assumption that the diffusion of water molecules obeys the normal distribution *in vivo*. However, Wu *et al*[85] reported that in biological tissue, complex cellular microstructures make water diffusion a highly hindered or restricted process, especially at high b values, where the distribution of displacements does not obey a Gaussian distribution. DKI was recently reported to be an extension to the Gaussian DT model[14], and it has become more popular in recent years.

DKI uses the same pulse sequences as that of conventional DWI, but with b values that are somewhat larger than those usually selected[86]. DKI is a straightforward extension of DTI, which requires only minor changes in data acquisition and processing[87,88]. The theory of DKI is based on the above principles, which describes the non-Gaussian diffusion behavior in tissues[14]. The literature has even reported that the DKI parameters, such as the radial or axial kurtosis, are more sensitive to brain physiology changes than the well-known DTI parameters in some white and gray matter structures[14]. In the white and gray matter structures,

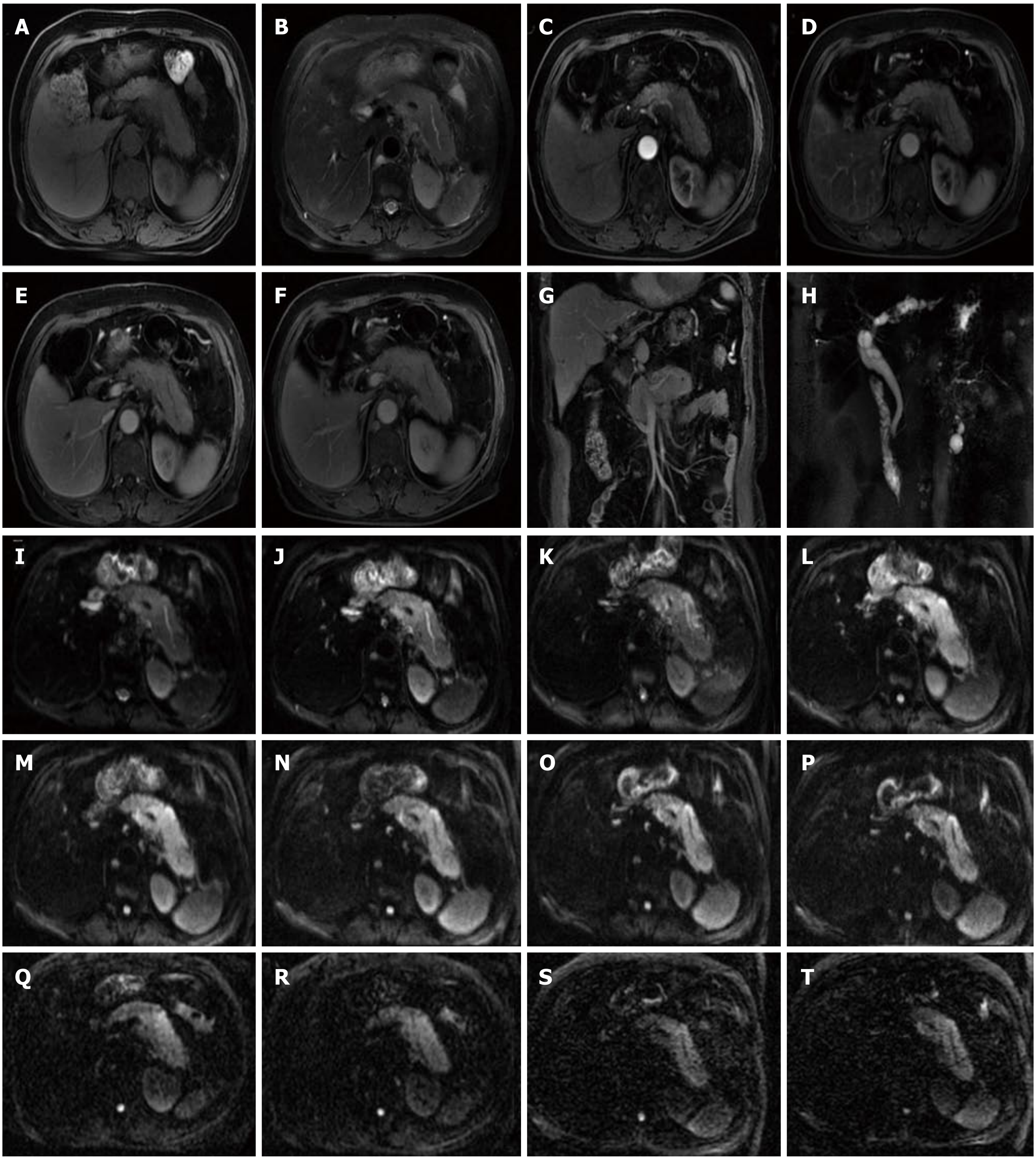

Figure 6 Images in a 52-year-old man with a focal lesion in the body and tail of the pancreas. MR imaging suggests that it is a malignancy. A: Axial T1-weighted fat-suppressed gradient-echo MR image; B: Axial T2-weighted fat-suppressed fast spin-echo MR image; C-G: Axial and coronal slab three-dimensional liver acquisition with volume acceleration dynamic contrast-enhanced; H: MRCP shows the dilated main pancreatic duct in the body and tail of pancreas; I-P: Multi-b DWI imaging (b = 0, 50, 100, 300, 500, 800, 1000 and 1500); Q and R: DTI (b = 500 and 800) using 30 diffusion gradients directions; S and T: DKI (b = 1500 and 2000) using 30 diffusion gradients directions. MR: Magnetic resonance; DWI: Diffusion weighted imaging; DKI: Diffusion kurtosis imaging; MRCP: Magnetic resonance cholangiopancreatography.

the DKI shows a better detection and characterization of various changes[89]. Hence, the DKI, which can measure the kurtosis excess of that distribution, allows for a more accurate description of the diffusion properties of neural tissues than the DTI model[87].

In the model, DKI can obtain the parameters that can also be derived from DWI and DTI, such as ADC and FA. Its main parameter is the mean kurtosis (MK). MK is a complex micro parameter that is associated with the complexity of the tissue structure. The high MK represents the more complex tissue structure[14].

There is less research on DKI for pancreatic cancer. However, in 2012, Rosenkrantz *et al*[90] used DKI in prostate cancer, and their preliminary findings suggest an increased value for DKI compared with that of standard DWI in prostate cancer assessment. In theory, the pancreatic cancer occurs with tumor cell invasion and the proliferation of interstitial cells and connective tissue. The change in the tissue structure leads to the change of MK value.

ADVANTAGES AND LIMITATIONS FOR THESE DIFFUSION MR IMAGING FOR PANCREATIC CANCER

In pancreatic cancer, tumor cell growth will lead to changes in cellularity, tumor cell atypia, organelles, and extracellular space. All of these factors can change the water molecules' movement and restrict water diffusion. Extending the diffusion MR imaging, the diffusion of water molecules can be described more accurately and comprehensively. The conventional DWI can reflect the diffusion in one direction. The multi-b value DWI is based on the IVIM theory, which is generated by the blood flow in the tortuous microcirculation of the normal pancreatic tissue[51] and thus can reflect both perfusion and diffusion. The DTI can measure the magnitude and directionality of water diffusion in tissue quantitatively. DKI describes the non-Gaussian diffusion behavior in tissues.

However, we should be aware of the limitations of this technique: (1) Generally, in daily work, abdominal MRI suffers from interference and motional artifacts due to breathing[91,92]; (2) The gradient eddy currents in the EPI protocols can lead to the B0 field inhomogeneity and susceptibility differences[93,94]. Using a dielectric pad and a bellows belt for respiratory triggering can reduce geometrical distortions. DWI has been mostly acquired using single-shot echo planar imaging (ss EPI) to minimize motion-induced artifacts[95]; and (3) the choice of b value can also limit the technique. Currently, the ADC of the pancreas still does not reach unanimity; some scholars think the ADC, which was derived from the low b value, presents only a small part of the diffusion movement, which leads to contamination of other forms of IVIM, such as perfusion in the capillary bed. The perfusion will affect the diffusion when the b value is low, even though it can characterize the anatomy and the details of the lesion[55]. Finally, low b values result in increased ADC values[19,20]. Conversely, Kim *et al*[58] indicated that the high b value can be useful in clinical practice. The high b value means that it needs a longer echo time (TE), implying that it will lead to decreasing the SNR and increasing artifacts. Poor image quality will affect observation[18]. Using a high b value, the ADC value may be closer to the real state. In clinical practice, the choice of b value is controversial. As a compromise, a b value of 500 s/mm^2 was chosen[18]; however, the higher b value of 1000 s/mm^2 has been reported as good for malignant abdominal tumors[96] and the detection of pancreatic adenocarcinoma[32,96]. The choice of b value to minimize motion artifacts and to improve the SNR in pancreas is very important. Higher b values may be more sensitive to reflect true diffusion[30,97]. In clinical practice, taking the two factors into the consideration, a feasible b value can be selected depending on your purpose of study.

CONCLUSION

The proposed method may hold great promise for the non-invasive, non-contrast-enhanced imaging of pancreas lesions and may eventually become a screening tool for pancreatic cancer. MR is well suited to the quantitative and non-invasive measurement of diffusion. Diffusion MR imaging techniques are increasingly varied, from the simplest and most commonly used techniques to the more complex, such as from DWI to DKI. The diffusion MR imaging for pancreatic cancer revealed valuable advantages, such as high sensitivity and specificity. Moreover, diffusion MR imaging can aid in differentiating the different type of differentiation. These techniques go beyond traditional macrostructural volumetric methods and provide valuable information about underlying tissue integrity and organization at the microstructural and biochemical levels.

At present, a major issue with diffusion MR imaging is the lack of standardization of the protocol[98]. The IVIM-derived parameters in pancreatic cancer are controversial. For example, it is unknown how fibrosis affects diffusion parameters[42,52]. Further studies evaluating the behavior of IVIM-derived parameters in the diagnosis and treatment of pancreatic cancer are needed for standardization. One important point to bear in mind in future studies is that larger sample sizes, including imaging and histopathological workup are needed. The clinical report of utilization of the DTI and DKI in pancreatic cancer is still rare, and the potential of DTI to reveal the complex microstructure and physiology of the pancreas and detect pathological changes has not been investigated. Much work remains in solving the challenges inherent to tractography, which may certainly be a very promising technique that may be likely to contribute greatly to our understanding of nerve invasion.

In addition to the use of advanced DTI or DKI for pancreatic cancer, future advancements will come from continued study. Further standard diffusion MR imaging can benefit the accurate detection and staging of pancreatic cancer and provide the imaging evidence for clinical treatment.

REFERENCES

1 **Vincent A**, Herman J, Schulick R, Hruban RH, Goggins M. Pancreatic cancer. *Lancet* 2011; **378**: 607-620 [PMID: 21620466 DOI: 10.1016/S0140-6736(10)62307-0]

2 **Krechler T**, Horejs J, Ulrych J, Zeman M, Macásek J, Dusková J, Zák A. Current status of pancreatic cancer diagnosis. *Cas Lek Cesk*

2011; **150**: 587-593 [PMID: 22292339]

3 **Singh M**, Maitra A. Precursor lesions of pancreatic cancer: molecular pathology and clinical implications. *Pancreatology* 2007; **7**: 9-19 [PMID: 17449961 DOI: 10.1159/000101873]

4 **Siegel R**, Naishadham D, Jemal A. Cancer statistics, 2012. *CA Cancer J Clin* 2012; **62**: 10-29 [PMID: 22237781 DOI: 10.3322/caac.20138]

5 **Chari ST**, Kelly K, Hollingsworth MA, Thayer SP, Ahlquist DA, Andersen DK, Batra SK, Brentnall TA, Canto M, Cleeter DF, Firpo MA, Gambhir SS, Go VL, Hines OJ, Kenner BJ, Klimstra DS, Lerch MM, Levy MJ, Maitra A, Mulvihill SJ, Petersen GM, Rhim AD, Simeone DM, Srivastava S, Tanaka M, Vinik AI, Wong D. Early detection of sporadic pancreatic cancer: summative review. *Pancreas* 2015; **44**: 693-712 [PMID: 25931254 DOI: 10.1097/MPA.0000000000000368]

6 **Amedei A**, Niccolai E, Prisco D. Pancreatic cancer: role of the immune system in cancer progression and vaccine-based immunotherapy. *Hum Vaccin Immunother* 2014; **10**: 3354-3368 [PMID: 25483688 DOI: 10.4161/hv.34392]

7 **Li D**, Xie K, Wolff R, Abbruzzese JL. Pancreatic cancer. *Lancet* 2004; **363**: 1049-1057 [PMID: 15051286 DOI: 10.1016/S0140-6736(04)15841-8]

8 **Klimstra DS**, Pitman MB, Hruban RH. An algorithmic approach to the diagnosis of pancreatic neoplasms. *Arch Pathol Lab Med* 2009; **133**: 454-464 [PMID: 19260750 DOI: 10.1043/1543-2165-133.3.454]

9 **Jang SK**, Kim JH, Joo I, Jeon JH, Shin KS, Han JK, Choi BI. Differential diagnosis of pancreatic cancer from other solid tumours arising from the periampullary area on MDCT. *Eur Radiol* 2015; **25**: 2880-2888 [PMID: 25916385 DOI: 10.1007/s00330-015-3721-4]

10 **Putzer D**, Jaschke W. Radiological evaluation of focal pancreatic lesions. *Dig Dis* 2015; **33**: 91-98 [PMID: 25531502 DOI: 10.1159/000366045]

11 **Heyn C**, Sue-Chue-Lam D, Jhaveri K, Haider MA. MRI of the pancreas: problem solving tool. *J Magn Reson Imaging* 2012; **36**: 1037-1051 [PMID: 23090915 DOI: 10.1002/jmri.23708]

12 **de la Santa LG**, Retortillo JA, Miguel AC, Klein LM. Radiology of pancreatic neoplasms: An update. *World J Gastrointest Oncol* 2014; **6**: 330-343 [PMID: 25232458 DOI: 10.4251/wjgo.v6.i9.330]

13 **O'Neill E**, Hammond N, Miller FH. MR imaging of the pancreas. *Radiol Clin North Am* 2014; **52**: 757-777 [PMID: 24889170 DOI: 10.1016/j.rcl.2014.02.006]

14 **Poot DH**, den Dekker AJ, Achten E, Verhoye M, Sijbers J. Optimal experimental design for diffusion kurtosis imaging. *IEEE Trans Med Imaging* 2010; **29**: 819-829 [PMID: 20199917 DOI: 10.1109/TMI.2009.2037915]

15 **Yao X**, Kuang T, Wu L, Feng H, Liu H, Cheng W, Rao S, Wang H, Zeng M. Optimization of MR diffusion-weighted imaging acquisitions for pancreatic cancer at 3.0T. *Magn Reson Imaging* 2014; **32**: 875-879 [PMID: 24848293 DOI: 10.1016/j.mri.2014.04.011]

16 **Barral M**, Taouli B, Guiu B, Koh DM, Luciani A, Manfredi R, Vilgrain V, Hoeffel C, Kanematsu M, Soyer P. Diffusion-weighted MR imaging of the pancreas: current status and recommendations. *Radiology* 2015; **274**: 45-63 [PMID: 25531479 DOI: 10.1148/radiol.14130778]

17 **Moseley M**, Bammer R, Illes J. Diffusion-tensor imaging of cognitive performance. *Brain Cogn* 2002; **50**: 396-413 [PMID: 12480486]

18 **Kartalis N**, Lindholm TL, Aspelin P, Permert J, Albiin N. Diffusion-weighted magnetic resonance imaging of pancreas tumours. *Eur Radiol* 2009; **19**: 1981-1990 [PMID: 19308414 DOI: 10.1007/s00330-009-1384-8]

19 **Ma C**, Li YJ, Pan CS, Wang H, Wang J, Chen SY, Lu JP. High resolution diffusion weighted magnetic resonance imaging of the pancreas using reduced field of view single-shot echo-planar imaging at 3 T. *Magn Reson Imaging* 2014; **32**: 125-131 [PMID: 24231348 DOI: 10.1016/j.mri.2013.10.005]

20 **Le Bihan D**, Breton E, Lallemand D, Aubin ML, Vignaud J, Laval-Jeantet M. Separation of diffusion and perfusion in intravoxel incoherent motion MR imaging. *Radiology* 1988; **168**: 497-505 [PMID: 3393671]

21 **Qayyum A**. Diffusion-weighted imaging in the abdomen and pelvis: concepts and applications. *Radiographics* 2009; **29**: 1797-1810 [PMID: 19959522 DOI: 10.1148/rg.296095521]

22 **Koh DM**, Collins DJ, Orton MR. Intravoxel incoherent motion in body diffusion-weighted MRI: reality and challenges. *AJR Am J Roentgenol* 2011; **196**: 1351-1361 [PMID: 21606299 DOI: 10.2214/AJR.10.5515]

23 **Le Bihan D**, Breton E, Lallemand D, Grenier P, Cabanis E, Laval-Jeantet M. MR imaging of intravoxel incoherent motions: application to diffusion and perfusion in neurologic disorders. *Radiology* 1986; **161**: 401-407 [PMID: 3763909 DOI: 10.1148/radiology.161.2.3763909]

24 **Robertson RL**, Glasier CM. Diffusion-weighted imaging of the brain in infants and children. *Pediatr Radiol* 2007; **37**: 749-768 [PMID: 17589837 DOI: 10.1007/s00247-007-0515-0]

25 **Morgan VA**, Kyriazi S, Ashley SE, DeSouza NM. Evaluation of the potential of diffusion-weighted imaging in prostate cancer detection. *Acta Radiol* 2007; **48**: 695-703 [PMID: 17611881 DOI: 10.1080/02841850701349257]

26 **Bittencourt LK**, Hausmann D, Sabaneeff N, Gasparetto EL, Barentsz JO. Multiparametric magnetic resonance imaging of the prostate: current concepts. *Radiol Bras* 2014; **47**: 292-300 [PMID: 25741104 DOI: 10.1590/0100-3984.2013.1863]

27 **Bruegel M**, Holzapfel K, Gaa J, Woertler K, Waldt S, Kiefer B, Stemmer A, Ganter C, Rummeny EJ. Characterization of focal liver lesions by ADC measurements using a respiratory triggered diffusion-weighted single-shot echo-planar MR imaging technique. *Eur Radiol* 2008; **18**: 477-485 [PMID: 17960390 DOI: 10.1007/s00330-007-0785-9]

28 **Gourtsoyianni S**, Papanikolaou N, Yarmenitis S, Maris T, Karantanas A, Gourtsoyiannis N. Respiratory gated diffusion-weighted imaging of the liver: value of apparent diffusion coefficient measurements in the differentiation between most commonly encountered benign and malignant focal liver lesions. *Eur Radiol* 2008; **18**: 486-492 [PMID: 17994317 DOI: 10.1007/s00330-007-0798-4]

29 **Szafer A**, Zhong J, Gore JC. Theoretical model for water diffusion in tissues. *Magn Reson Med* 1995; **33**: 697-712 [PMID: 7596275 DOI: 10.1002/mrm.1910330516]

30 **Ichikawa T**, Erturk SM, Motosugi U, Sou H, Iino H, Araki T, Fujii H. High-b value diffusion-weighted MRI for detecting pancreatic adenocarcinoma: preliminary results. *AJR Am J Roentgenol* 2007; **188**: 409-414 [PMID: 17242249 DOI: 10.2214/AJR.05.1918]

31 **Matsuki M**, Inada Y, Nakai G, Tatsugami F, Tanikake M, Narabayashi I, Masuda D, Arisaka Y, Takaori K, Tanigawa N. Diffusion-weighed MR imaging of pancreatic carcinoma. *Abdom Imaging* 2007; **32**: 481-483 [PMID: 17431713 DOI: 10.1007/s00261-007-9192-6]

32 **Takeuchi M**, Matsuzaki K, Kubo H, Nishitani H. High-b-value diffusion-weighted magnetic resonance imaging of pancreatic cancer and mass-forming chronic pancreatitis: preliminary results. *Acta Radiol* 2008; **49**: 383-386 [PMID: 18415779 DOI: 10.1080/02841850801895381]

33 **Jang KM**, Kim SH, Min JH, Lee SJ, Kang TW, Lim S, Choi D. Value of diffusion-weighted MRI for differentiating malignant from benign intraductal papillary mucinous neoplasms of the pancreas. *AJR Am J Roentgenol* 2014; **203**: 992-1000 [PMID: 25341136 DOI: 10.2214/AJR.13.11980]

34 **Lee NK**, Kim S, Kim DU, Seo HI, Kim HS, Jo HJ, Kim TU. Diffusion-weighted magnetic resonance imaging for non-neoplastic conditions in the hepatobiliary and pancreatic regions: pearls and potential pitfalls in imaging interpretation. *Abdom Imaging* 2015; **40**: 643-662 [PMID: 25216848 DOI: 10.1007/s00261-014-0235-5]

35 **Park MJ**, Kim YK, Choi SY, Rhim H, Lee WJ, Choi D. Preoperative detection of small pancreatic carcinoma: value of adding diffusion-weighted imaging to conventional MR imaging for improving confidence level. *Radiology* 2014; **273**: 433-443 [PMID:

24991989 DOI: 10.1148/radiol.14132563]

36 **Birchard KR**, Semelka RC, Hyslop WB, Brown A, Armao D, Firat Z, Vaidean G. Suspected pancreatic cancer: evaluation by dynamic gadolinium-enhanced 3D gradient-echo MRI. *AJR Am J Roentgenol* 2005; **185**: 700-703 [PMID: 16120921 DOI: 10.2214/ajr.185.3.01850700]

37 **Fletcher JG**, Wiersema MJ, Farrell MA, Fidler JL, Burgart LJ, Koyama T, Johnson CD, Stephens DH, Ward EM, Harmsen WS. Pancreatic malignancy: value of arterial, pancreatic, and hepatic phase imaging with multi-detector row CT. *Radiology* 2003; **229**: 81-90 [PMID: 14519871 DOI: 10.1148/radiol.2291020582]

38 **Farma JM**, Santillan AA, Melis M, Walters J, Belinc D, Chen DT, Eikman EA, Malafa M. PET/CT fusion scan enhances CT staging in patients with pancreatic neoplasms. *Ann Surg Oncol* 2008; **15**: 2465-2471 [PMID: 18551347 DOI: 10.1245/s10434-008-9992-0]

39 **Agarwal B**, Abu-Hamda E, Molke KL, Correa AM, Ho L. Endoscopic ultrasound-guided fine needle aspiration and multidetector spiral CT in the diagnosis of pancreatic cancer. *Am J Gastroenterol* 2004; **99**: 844-850 [PMID: 15128348 DOI: 10.1111/j.1572-0241.2004.04177.x]

40 **Charles-Edwards EM**, deSouza NM. Diffusion-weighted magnetic resonance imaging and its application to cancer. *Cancer Imaging* 2006; **6**: 135-143 [PMID: 17015238 DOI: 10.1102/1470-7330.2006.0021]

41 **Thoeny HC**, Ross BD. Predicting and monitoring cancer treatment response with diffusion-weighted MRI. *J Magn Reson Imaging* 2010; **32**: 2-16 [PMID: 20575076 DOI: 10.1002/jmri.22167]

42 **Klauss M**, Gaida MM, Lemke A, Grünberg K, Simon D, Wente MN, Delorme S, Kauczor HU, Grenacher L, Stieltjes B. Fibrosis and pancreatic lesions: counterintuitive behavior of the diffusion imaging-derived structural diffusion coefficient d. *Invest Radiol* 2013; **48**: 129-133 [PMID: 23296083 DOI: 10.1097/RLI.0b013e31827ac0f1]

43 **Schnapauff D**, Zeile M, Niederhagen MB, Fleige B, Tunn PU, Hamm B, Dudeck O. Diffusion-weighted echo-planar magnetic resonance imaging for the assessment of tumor cellularity in patients with soft-tissue sarcomas. *J Magn Reson Imaging* 2009; **29**: 1355-1359 [PMID: 19472392 DOI: 10.1002/jmri.21755]

44 **Herrmann J**, Schoennagel BP, Roesch M, Busch JD, Derlin T, Doh LK, Petersen KU, Graessner J, Adam G, Habermann CR. Diffusion-weighted imaging of the healthy pancreas: ADC values are age and gender dependent. *J Magn Reson Imaging* 2013; **37**: 886-891 [PMID: 23086728 DOI: 10.1002/jmri.23871]

45 **Lee SS**, Byun JH, Park BJ, Park SH, Kim N, Park B, Kim JK, Lee MG. Quantitative analysis of diffusion-weighted magnetic resonance imaging of the pancreas: usefulness in characterizing solid pancreatic masses. *J Magn Reson Imaging* 2008; **28**: 928-936 [PMID: 18821618 DOI: 10.1002/jmri.21508]

46 **Fattahi R**, Balci NC, Perman WH, Hsueh EC, Alkaade S, Havlioglu N, Burton FR. Pancreatic diffusion-weighted imaging (DWI): comparison between mass-forming focal pancreatitis (FP), pancreatic cancer (PC), and normal pancreas. *J Magn Reson Imaging* 2009; **29**: 350-356 [PMID: 19161187 DOI: 10.1002/jmri.21651]

47 **Fukukura Y**, Takumi K, Kamimura K, Shindo T, Kumagae Y, Tateyama A, Nakajo M. Pancreatic adenocarcinoma: variability of diffusion-weighted MR imaging findings. *Radiology* 2012; **263**: 732-740 [PMID: 22623694 DOI: 10.1148/radiol.120111222]

48 **Lemke A**, Laun FB, Klauss M, Re TJ, Simon D, Delorme S, Schad LR, Stieltjes B. Differentiation of pancreas carcinoma from healthy pancreatic tissue using multiple b-values: comparison of apparent diffusion coefficient and intravoxel incoherent motion derived parameters. *Invest Radiol* 2009; **44**: 769-775 [PMID: 19838121 DOI: 10.1097/RLI.0b013e3181b62271]

49 **Concia M**, Sprinkart AM, Penner AH, Brossart P, Gieseke J, Schild HH, Willinek WA, Mürtz P. Diffusion-weighted magnetic resonance imaging of the pancreas: diagnostic benefit from an intravoxel incoherent motion model-based 3 b-value analysis. *Invest Radiol* 2014; **49**: 93-100 [PMID: 24089021 DOI: 10.1097/RLI.0b013e3182a71cc3]

50 **Klauss M**, Lemke A, Grünberg K, Simon D, Re TJ, Wente MN, Laun FB, Kauczor HU, Delorme S, Grenacher L, Stieltjes B. Intravoxel incoherent motion MRI for the differentiation between mass forming chronic pancreatitis and pancreatic carcinoma. *Invest Radiol* 2011; **46**: 57-63 [PMID: 21139505 DOI: 10.1097/RLI.0b013e3181fb3bf2]

51 **Kang KM**, Lee JM, Yoon JH, Kiefer B, Han JK, Choi BI. Intravoxel incoherent motion diffusion-weighted MR imaging for characterization of focal pancreatic lesions. *Radiology* 2014; **270**: 444-453 [PMID: 24126370 DOI: 10.1148/radiol.13122712]

52 **Muraoka N**, Uematsu H, Kimura H, Imamura Y, Fujiwara Y, Murakami M, Yamaguchi A, Itoh H. Apparent diffusion coefficient in pancreatic cancer: characterization and histopathological correlations. *J Magn Reson Imaging* 2008; **27**: 1302-1308 [PMID: 18504750 DOI: 10.1002/jmri.21340]

53 **Sakuma H**, Nomura Y, Takeda K, Tagami T, Nakagawa T, Tamagawa Y, Ishii Y, Tsukamoto T. Adult and neonatal human brain: diffusional anisotropy and myelination with diffusion-weighted MR imaging. *Radiology* 1991; **180**: 229-233 [PMID: 2052700 DOI: 10.1148/radiology.180.1.2052700]

54 **Wang Y**, Chen ZE, Nikolaidis P, McCarthy RJ, Merrick L, Sternick LA, Horowitz JM, Yaghmai V, Miller FH. Diffusion-weighted magnetic resonance imaging of pancreatic adenocarcinomas: association with histopathology and tumor grade. *J Magn Reson Imaging* 2011; **33**: 136-142 [PMID: 21182131 DOI: 10.1002/jmri.22414]

55 **Padhani AR**, Liu G, Koh DM, Chenevert TL, Thoeny HC, Takahara T, Dzik-Jurasz A, Ross BD, Van Cauteren M, Collins D, Hammoud DA, Rustin GJ, Taouli B, Choyke PL. Diffusion-weighted magnetic resonance imaging as a cancer biomarker: consensus and recommendations. *Neoplasia* 2009; **11**: 102-125 [PMID: 19186405 DOI: 10.1593/neo.81328]

56 **Wang Y**, Chen ZE, Yaghmai V, Nikolaidis P, McCarthy RJ, Merrick L, Miller FH. Diffusion-weighted MR imaging in pancreatic endocrine tumors correlated with histopathologic characteristics. *J Magn Reson Imaging* 2011; **33**: 1071-1079 [PMID: 21509863 DOI: 10.1002/jmri.22541]

57 **Nissan N**, Golan T, Furman-Haran E, Apter S, Inbar Y, Ariche A, Bar-Zakay B, Goldes Y, Schvimer M, Grobgeld D, Degani H. Diffusion tensor magnetic resonance imaging of the pancreas. *PLoS One* 2014; **9**: e115783 [PMID: 25549366 DOI: 10.1371/journal.pone.0115783]

58 **Kim T**, Murakami T, Takahashi S, Hori M, Tsuda K, Nakamura H. Diffusion-weighted single-shot echoplanar MR imaging for liver disease. *AJR Am J Roentgenol* 1999; **173**: 393-398 [PMID: 10430143 DOI: 10.2214/ajr.173.2.10430143]

59 **Wang Y**, Miller FH, Chen ZE, Merrick L, Mortele KJ, Hoff FL, Hammond NA, Yaghmai V, Nikolaidis P. Diffusion-weighted MR imaging of solid and cystic lesions of the pancreas. *Radiographics* 2011; **31**: E47-E64 [PMID: 21721197 DOI: 10.1148/rg.313105174]

60 **Luciani A**, Vignaud A, Cavet M, Nhieu JT, Mallat A, Ruel L, Laurent A, Deux JF, Brugieres P, Rahmouni A. Liver cirrhosis: intravoxel incoherent motion MR imaging--pilot study. *Radiology* 2008; **249**: 891-899 [PMID: 19011186 DOI: 10.1148/radiol.2493080080]

61 **Zhang JL**, Sigmund EE, Chandarana H, Rusinek H, Chen Q, Vivier PH, Taouli B, Lee VS. Variability of renal apparent diffusion coefficients: limitations of the monoexponential model for diffusion quantification. *Radiology* 2010; **254**: 783-792 [PMID: 20089719 DOI: 10.1148/radiol.09090891]

62 **Grünberg K**, Grenacher L, Klauss M. Diffusion-weighted imaging of the pancreas. *Radiologe* 2011; **51**: 186-194 [PMID: 21305263 DOI: 10.1007/s00117-010-2059-9]

63 **Lemke A**, Laun FB, Simon D, Stieltjes B, Schad LR. An in vivo verification of the intravoxel incoherent motion effect in diffusion-weighted imaging of the abdomen. *Magn Reson Med* 2010; **64**: 1580-1585 [PMID: 20665824 DOI: 10.1002/mrm.22565]

64 **Re TJ**, Lemke A, Klauss M, Laun FB, Simon D, Grünberg K, Delorme S, Grenacher L, Manfredi R, Mucelli RP, Stieltjes B. Enhancing pancreatic adenocarcinoma delineation in diffusion derived intravoxel incoherent motion f-maps through automatic vessel and

duct segmentation. *Magn Reson Med* 2011; **66**: 1327-1332 [PMID: 21437979 DOI: 10.1002/mrm.22931]

65 **Hwang EJ**, Lee JM, Yoon JH, Kim JH, Han JK, Choi BI, Lee KB, Jang JY, Kim SW, Nickel MD, Kiefer B. Intravoxel incoherent motion diffusion-weighted imaging of pancreatic neuroendocrine tumors: prediction of the histologic grade using pure diffusion coefficient and tumor size. *Invest Radiol* 2014; **49**: 396-402 [PMID: 24500090 DOI: 10.1097/RLI.0000000000000028]

66 **Wozniak JR**, Lim KO. Advances in white matter imaging: a review of in vivo magnetic resonance methodologies and their applicability to the study of development and aging. *Neurosci Biobehav Rev* 2006; **30**: 762-774 [PMID: 16890990 DOI: 10.1016/j.neubiorev.2006.06.003]

67 **Fukuda Y**, Ohashi I, Hanafusa K, Nakagawa T, Ohtani S, An-naka Y, Hayashi T, Shibuya H. Anisotropic diffusion in kidney: apparent diffusion coefficient measurements for clinical use. *J Magn Reson Imaging* 2000; **11**: 156-160 [PMID: 10713948 DOI: 10.1002/(SICI)1522-2586(200002)11: 2<156: : AID-JMRI12>3.0.CO; 2-8]

68 **Basser PJ**, Pierpaoli C. Microstructural and physiological features of tissues elucidated by quantitative-diffusion-tensor MRI. *J Magn Reson B* 1996; **111**: 209-219 [PMID: 8661285 DOI: 10.1006/jmrb.1996.0086]

69 **Le Bihan D**, Mangin JF, Poupon C, Clark CA, Pappata S, Molko N, Chabriat H. Diffusion tensor imaging: concepts and applications. *J Magn Reson Imaging* 2001; **13**: 534-546 [PMID: 11276097 DOI: 10.1002/jmri.1076]

70 **Hagmann P**, Jonasson L, Maeder P, Thiran JP, Wedeen VJ, Meuli R. Understanding diffusion MR imaging techniques: from scalar diffusion-weighted imaging to diffusion tensor imaging and beyond. *Radiographics* 2006; **26** Suppl 1: S205-S223 [PMID: 17050517 DOI: 10.1148/rg.26si065510]

71 **Basser PJ**, Mattiello J, LeBihan D. MR diffusion tensor spectroscopy and imaging. *Biophys J* 1994; **66**: 259-267 [PMID: 8130344 DOI: 10.1016/S0006-3495(94)80775-1]

72 **Vandermosten M**, Boets B, Wouters J, Ghesquière P. A qualitative and quantitative review of diffusion tensor imaging studies in reading and dyslexia. *Neurosci Biobehav Rev* 2012; **36**: 1532-1552 [PMID: 22516793 DOI: 10.1016/j.neubiorev.2012.04.002]

73 **Kuswanto CN**, Teh I, Lee TS, Sim K. Diffusion tensor imaging findings of white matter changes in first episode schizophrenia: a systematic review. *Clin Psychopharmacol Neurosci* 2012; **10**: 13-24 [PMID: 23429992 DOI: 10.9758/cpn.2012.10.1.13]

74 **Wu MT**, Tseng WY, Su MY, Liu CP, Chiou KR, Wedeen VJ, Reese TG, Yang CF. Diffusion tensor magnetic resonance imaging mapping the fiber architecture remodeling in human myocardium after infarction: correlation with viability and wall motion. *Circulation* 2006; **114**: 1036-1045 [PMID: 16940196 DOI: 10.1161/CIRCULATIONAHA.105.545863]

75 **Uribe CF**, Jones EC, Chang SD, Goldenberg SL, Reinsberg SA, Kozlowski P. In vivo 3T and ex vivo 7T diffusion tensor imaging of prostate cancer: Correlation with histology. *Magn Reson Imaging* 2015; **33**: 577-583 [PMID: 25721995 DOI: 10.1016/j.mri.2015.02.022]

76 **Li L**, Margolis DJ, Deng M, Cai J, Yuan L, Feng Z, Min X, Hu Z, Hu D, Liu J, Wang L. Correlation of gleason scores with magnetic resonance diffusion tensor imaging in peripheral zone prostate cancer. *J Magn Reson Imaging* 2015; **42**: 460-467 [PMID: 25469909 DOI: 10.1002/jmri.24813]

77 **Sigmund EE**, Vivier PH, Sui D, Lamparello NA, Tantillo K, Mikheev A, Rusinek H, Babb JS, Storey P, Lee VS, Chandarana H. Intravoxel incoherent motion and diffusion-tensor imaging in renal tissue under hydration and furosemide flow challenges. *Radiology* 2012; **263**: 758-769 [PMID: 22523327 DOI: 10.1148/radiol.12111327]

78 **Taouli B**, Chouli M, Martin AJ, Qayyum A, Coakley FV, Vilgrain V. Chronic hepatitis: role of diffusion-weighted imaging and diffusion tensor imaging for the diagnosis of liver fibrosis and inflammation. *J Magn Reson Imaging* 2008; **28**: 89-95 [PMID: 18581382 DOI: 10.1002/jmri.21227]

79 **Nissan N**, Furman-Haran E, Shapiro-Feinberg M, Grobgeld D, Degani H. Diffusion-tensor MR imaging of the breast: hormonal regulation. *Radiology* 2014; **271**: 672-680 [PMID: 24533873 DOI: 10.1148/radiol.14132084]

80 **Cauley KA**, Filippi CG. Diffusion-tensor imaging of small nerve bundles: cranial nerves, peripheral nerves, distal spinal cord, and lumbar nerve roots--clinical applications. *AJR Am J Roentgenol* 2013; **201**: W326-W335 [PMID: 23883249 DOI: 10.2214/AJR.12.9230]

81 **Jambawalikar S**, Baum J, Button T, Li H, Geronimo V, Gould ES. Diffusion tensor imaging of peripheral nerves. *Skeletal Radiol* 2010; **39**: 1073-1079 [PMID: 20593175 DOI: 10.1007/s00256-010-0974-5]

82 **Lee JW**, Kim JH, Kang HS, Lee JS, Choi JY, Yeom JS, Kim HJ, Chung HW. Optimization of acquisition parameters of diffusion-tensor magnetic resonance imaging in the spinal cord. *Invest Radiol* 2006; **41**: 553-559 [PMID: 16772848 DOI: 10.1097/01.rli.0000221325.03899.48]

83 **Masutani Y**, Aoki S, Abe O, Hayashi N, Otomo K. MR diffusion tensor imaging: recent advance and new techniques for diffusion tensor visualization. *Eur J Radiol* 2003; **46**: 53-66 [PMID: 12648802 DOI: 10.1016/S0720-048X(02)00328-5]

84 **Basser PJ**, Pierpaoli C. Microstructural and physiological features of tissues elucidated by quantitative-diffusion-tensor MRI. 1996. *J Magn Reson* 2011; **213**: 560-570 [PMID: 22152371 DOI: 10.1016/j.jmr.2011.09.022]

85 **Wu EX**, Cheung MM. MR diffusion kurtosis imaging for neural tissue characterization. *NMR Biomed* 2010; **23**: 836-848 [PMID: 20623793 DOI: 10.1002/nbm.1506]

86 **Huang Y**, Chen X, Zhang Z, Yan L, Pan D, Liang C, Liu Z. MRI quantification of non-Gaussian water diffusion in normal human kidney: a diffusional kurtosis imaging study. *NMR Biomed* 2015; **28**: 154-161 [PMID: 25392938 DOI: 10.1002/nbm.3235]

87 **Jensen JH**, Helpern JA, Ramani A, Lu H, Kaczynski K. Diffusional kurtosis imaging: the quantification of non-gaussian water diffusion by means of magnetic resonance imaging. *Magn Reson Med* 2005; **53**: 1432-1440 [PMID: 15906300 DOI: 10.1002/mrm.20508]

88 **Lu H**, Jensen JH, Ramani A, Helpern JA. Three-dimensional characterization of non-gaussian water diffusion in humans using diffusion kurtosis imaging. *NMR Biomed* 2006; **19**: 236-247 [PMID: 16521095 DOI: 10.1002/nbm.1020]

89 **Cheung MM**, Hui ES, Chan KC, Helpern JA, Qi L, Wu EX. Does diffusion kurtosis imaging lead to better neural tissue characterization? A rodent brain maturation study. *Neuroimage* 2009; **45**: 386-392 [PMID: 19150655 DOI: 10.1016/j.neuroimage.2008.12.018]

90 **Rosenkrantz AB**, Sigmund EE, Johnson G, Babb JS, Mussi TC, Melamed J, Taneja SS, Lee VS, Jensen JH. Prostate cancer: feasibility and preliminary experience of a diffusional kurtosis model for detection and assessment of aggressiveness of peripheral zone cancer. *Radiology* 2012; **264**: 126-135 [PMID: 22550312 DOI: 10.1148/radiol.12112290]

91 **Dietrich O**, Reiser MF, Schoenberg SO. Artifacts in 3-T MRI: physical background and reduction strategies. *Eur J Radiol* 2008; **65**: 29-35 [PMID: 18162353]

92 **Riffel P**, Michaely HJ, Morelli JN, Pfeuffer J, Attenberger UI, Schoenberg SO, Haneder S. Zoomed EPI-DWI of the pancreas using two-dimensional spatially-selective radiofrequency excitation pulses. *PLoS One* 2014; **9**: e89468 [PMID: 24594702 DOI: 10.1371/journal.pone.0089468]

93 **Dietrich O**, Biffar A, Baur-Melnyk A, Reiser MF. Technical aspects of MR diffusion imaging of the body. *Eur J Radiol* 2010; **76**: 314-322 [PMID: 20299172 DOI: 10.1016/j.ejrad.2010.02.018]

94 **Jones DK**, Cercignani M. Twenty-five pitfalls in the analysis of diffusion MRI data. *NMR Biomed* 2010; **23**: 803-820 [PMID: 20886566 DOI: 10.1002/nbm.1543]

95 **Yamada I**, Aung W, Himeno Y, Nakagawa T, Shibuya H. Diffusion coefficients in abdominal organs and hepatic lesions: evaluation with intravoxel incoherent motion echo-planar MR imaging. *Radiology* 1999; **210**: 617-623 [PMID: 10207458 DOI: 10.1148/

radiology.210.3.r99fe17617]

96 **Tsushima Y**, Takano A, Taketomi-Takahashi A, Endo K. Body diffusion-weighted MR imaging using high b-value for malignant tumor screening: usefulness and necessity of referring to T2-weighted images and creating fusion images. *Acad Radiol* 2007; **14**: 643-650 [PMID: 17502253 DOI: 10.1016/j.acra.2007.02.006]

97 **Huang WC**, Sheng J, Chen SY, Lu JP. Differentiation between pancreatic carcinoma and mass-forming chronic pancreatitis: usefulness of high b value diffusion-weighted imaging. *J Dig Dis* 2011; **12**: 401-408 [PMID: 21955434 DOI: 10.1111/j.1751-2980.2011.00517.x]

98 **Sandrasegaran K**. Functional MR imaging of the abdomen. *Radiol Clin North Am* 2014; **52**: 883-903 [PMID: 24889176 DOI: 10.1016/j.rcl.2014.02.018]

P- Reviewer: Hayano K, Sugimura H **S- Editor**: Gong ZM
L- Editor: A **E- Editor**: Wu HL

World Journal of
Radiology

Submit a Manuscript: http://www.wjgnet.com/esps/
Help Desk: http://www.wjgnet.com/esps/helpdesk.aspx
DOI: 10.4329/wjr.v7.i12.438

World J Radiol 2015 December 28; 7(12): 438-447
ISSN 1949-8470 (online)

REVIEW

Middle cerebellar peduncles: Magnetic resonance imaging and pathophysiologic correlate

Humberto Morales, Thomas Tomsick

Humberto Morales, Thomas Tomsick, Department of Neuroradiology, University of Cincinnati Medical Center, Cincinnati, OH 45267-0761, United States

Author contributions: All authors equally contributed to this paper.

Conflict-of-interest statement: The authors declare no source of funding or conflict of interest pertinent to this submitted manuscript.

Correspondence to: Humberto Morales, MD, Assistant Professor of Radiology, Department of Neuroradiology, University of Cincinnati Medical Center, 234 Goodman Street, Cincinnati, OH 45267-0761,
United States. moralehc@ucmail.uc.edu
Telephone: +1-513-5841584
Fax: +1-513-5849100

Received: July 22, 2015
Peer-review started: July 24, 2015
First decision: August 25, 2015
Revised: September 5, 2015
Accepted: October 23, 2015
Article in press: October 27, 2015
Published online: December 28, 2015

Abstract

We describe common and less common diseases that can cause magnetic resonance signal abnormalities of middle cerebellar peduncles (MCP), offering a systematic approach correlating imaging findings with clinical clues and pathologic mechanisms. Myelin abnormalities, different types of edema or neurodegenerative processes, can cause areas of abnormal T2 signal, variable enhancement, and patterns of diffusivity of MCP. Pathologies such as demyelinating disorders or certain neurodegenerative entities (*e.g.*, multiple system atrophy or fragile X-associated tremor-ataxia syndrome) appear to have predilection for MCP. Careful evaluation of concomitant imaging findings in the brain or brainstem; and focused correlation with key clinical findings such as immunosuppression for progressive multifocal leukoencephalopahty; hypertension, post-transplant status or high dose chemotherapy for posterior reversible encephalopathy; electrolyte disorders for myelinolysis or suspected toxic-drug related encephalopathy; would yield an appropriate and accurate differential diagnosis in the majority of cases.

Key words: Middle cerebellar peduncle; Brachium pontis; Magnetic resonance imaging; Multiple sclerosis; Progressive multifocal leukoencephalopathy; Posterior reversible encephalopathy; Toxic encephalopathy

Core tip: Though a few prior reviews have described pathologic processes involving the middle cerebellar peduncles (MCP), our paper offers not only an updated approach to include diffusion tensor imaging but also important correlations of imaging findings with anatomy, pathophysiologic insights and key clinical scenarios. Overall, this concise and comprehensive review is expected to help the readers not only to improve their approach to cases with MCP involvement, but also to increase awareness and understanding of pathologic processes increasingly seen in neuroimaging such as progressive multifocal leukoencephalopahty, posterior reversible encephalopathy and toxic encephalopathies.

Morales H, Tomsick T. Middle cerebellar peduncles: Magnetic resonance imaging and pathophysiologic correlate. *World J Radiol* 2015; 7(12): 438-447 Available from: URL: http://www.wjgnet.com/1949-8470/full/v7/i12/438.htm DOI: http://dx.doi.org/10.4329/wjr.v7.i12.438

INTRODUCTION

Pathologic processes can have predilection for specific anatomic locations. Our purpose is to describe not only common and less common entities, but also pathologic mechanisms causing magnetic resonance (MR) signal abnormalities of middle cerebellar peduncles (MCP). We provide a systematic approach narrowing differential diagnosis to help radiologists and clinicians.

ANATOMY AND CLINICAL CORRELATION

The MCP are the main afferent pathway to the cerebellum. MCP are composed by white matter fibers originated from the contralateral pontine nuclei (Figure 1). The pontine nuclei are intermediary gray matter scattered in the basis pons and part of the cortico-ponto-cerebellar pathway (closed loop communication between the cerebellum and pre-central /prefrontal cortex that control not only the action of motor tasks but also planning and initiation of movements)[1]. The cerebellum has a high ratio of afferent/efferent pathways (40:1); with the small superior cerebellar peduncles (SCP) as the only efferent fibers, connecting the dentate nuclei to the cortex through the dentate-rubro-thalamic tracts (Figure 1C). In general, the cerebellar pathways decussate twice, one at the level of the pons (crossing pontine fibers) and other at the level of the inferior colliculi in the tegmentum (decussation of the SCP). Thus, clinical signs (*e.g.*, limb ataxia) are ipsilateral to MCP lesion. Difficulty walking (cerebellar ataxia), difficulty speaking (scanning speech) and in some cases vertigo and facial weakness are common clinical manifestation of MCP lesion.

INSIGHTS INTO PATHOLOGIC MECHANISMS

It is not surprising that demyelinating processes affect the MCP, composed of axons, oligodendrocytes and scattered glial cells. Demyelination can occur in the setting of immune-related entities such as MS or acute disseminated encephalomyelitis (ADEM), and is usually accompanied by perivascular inflammatory infiltrates (with areas of enhancement on MRI in some cases) (Figure 2). Demyelination can also occur secondary to infectious processes such as progressive multifocal leukoencephalopathy (PML) (Figures 3 and 4) or metabolic abnormalities such as osmotic demyelination syndrome (ODS) (Figure 5), usually not accompanied by inflammatory changes (enhancement is not a characteristic feature on MR imaging). Vasogenic edema due to dys-regulation of small arteries can also cause increased T2 signal in the MCP, as is the case in posterior reversible encephalopathy (PRES) (Figure 6). However, the vascular dys-regulation and leaking edema might also be due to toxic states such as cyclosporine-related encephalopathy. Cytotoxic edema is characteristic of ischemia/infarction, a rare event in the MCP (Figure 7). Intra-myelinic edema appears to be the cause of areas of abnormal white matter signal in different entities. The edema can predominate between the myelin sheaths (potential extracellular space) or result from swelling of the oligodendrocytes, myelin sheaths or axons (intracellular compartment)[2]. This type of edema might or might not be reversible and is the main pathologic mechanism in some toxic or myelinolytic states (Figure 8). White matter vacuolization/spongyform degeneration causes abnormal T2 signal in other toxic states (*e.g.*, chronic heroin inhalation). Damage to the axons (due to loss of antegrade or retrograde input) with subsequent myelin breakdown and end-stage gliosis/volume loss is the mechanism for wallerian degeneration (WD) (Figure 9). Myelin breakdown and white matter damage in leukodystrophies (LD) is caused by biochemical defects that interfere with myelin formation, maintenance, turnover, and catabolism (known as dysmyelination), leading to increased T2 signal and in some cases abnormal enhancement (*e.g.*, adrenoleukodystrophy) (Figure 10). Neurodegenerative processes affecting MCP have distinct mechanisms; in general, there is preferential loss of Purkinje cells, or gray matter nuclei in the brain stem in diseases such as multiple system atrophy (MSA-C, cerebellar variant), fragile X-associated tremor-ataxia syndrome (FXTAS) or some spino-cerebellar ataxias, leading to axonal loss and degeneration of the associated MCP fibers (Figure 11). Neoplastic processes are unusual in the MCP, though lymphoma or glial neoplasms can also involve them. Rare infectious or inflammatory pathologies, such as Lyme disease, Listeria rhombencephalitis, Whipple disease, neurosarcoid, vasculitis (*e.g.*, Bechet's), and the recently described CLIPPERS (chronic lymphocytic inflammation with pontine perivascular enhancement responsive to steroids) might also extend to MCP with variable imaging findings (usually enhancement accompany areas of increased T2 signal). Rarely, vascular malformations (Figure 12) can involve the MCP, in which case the recognition of their typical features is not challenging ("pop-corn" appearance for a cavernoma, or prominent flow voids for arteriovenous malformations).

PATHOLOGIC ENTITIES AND IMAGING FINDINGS

Demyelination

Cerebellar symptoms and signs are commonly seen in 50%-80% of multiple sclerosis (MS) patients. On

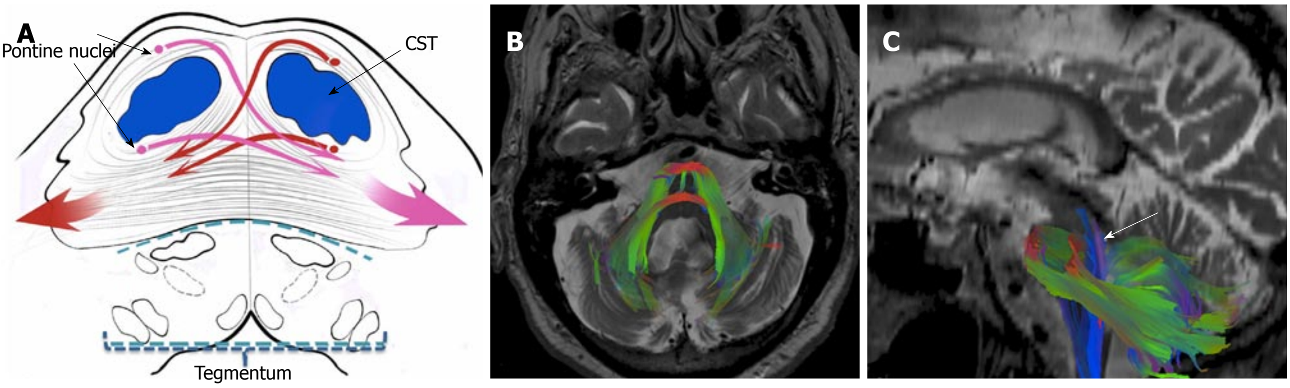

Figure 1 Anatomy of the middle cerebellar peduncles. A: Diagram shows the pontine crossing fibers (PCF) (red and pink long arrows) originating from the contralateral pontine nuclei and conforming the middle cerebellar peduncles (MCP) (only afferent fibers constitute MCP); B and C: Diffusion tensor imaging (DTI) tractography after seed ROIs placed in the bilateral MCP. Note the representation of the PCF (red on B). Here, we can envision the origin of well described signs on conventional T2 sequences such as the "hot cross bun sign" or "trident sign" where there is involvement of the PCF or central pons and sparing of the corticospinal tracts (CST) and tegmentum. Sagittal DTI (C) including the main efferent pathway (purple ascending fibers, arrow) through the pontine tegmentum and superior cerebellar peduncles which constitutes part of the dentate-rubro-thalamic tract. (DTI was acquired on a GE-3T Magnet, b = 0 and 1000 s/mm^2 with 25 directions; Brain Lab Software was used to fuse T2-WI with DTI acquisition; and tractography was performed using a tensor deflection algorithm). ROIs: Regions of interest.

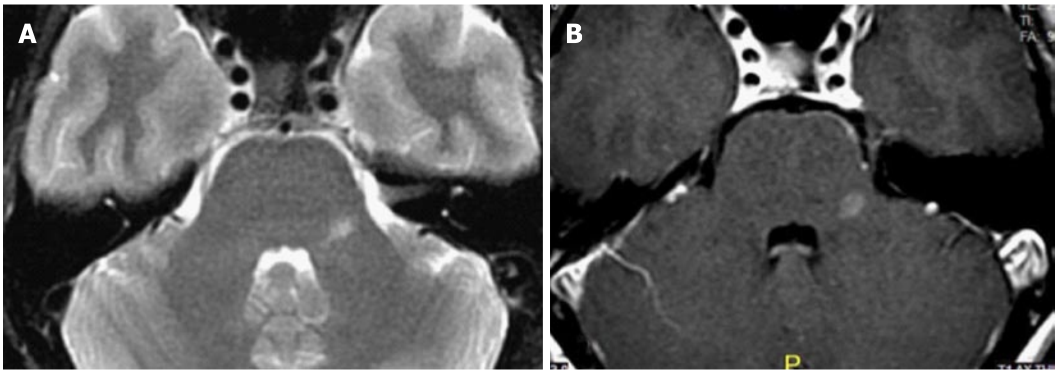

Figure 2 Multiple sclerosis. A 40-year-old female with 2 mo history of left facial pain/numbness and difficulty talking (scanning speech). Axial T2 (A) and axial post-contrast MR (B) images show isolated lesion in the left MCP. Due to suspicion for demyelinating disease MRI of the spine and CSF analysis was recommended. Additional lesion found in the thoracic cord (not shown) and CSF led to the diagnosis of MS. MCP: Middle cerebellar peduncles; CSF: Cerebrospinal fluid; MRI: Magnetic resonance imaging; MS: Multiple sclerosis.

conventional MRI, reported frequency of brainstem lesions and cerebellar lesions is 68% and 49%-88% respectively[3].

Multifocal areas of demyelination, some times areas of cavitation characterize progressive multifocal leucoencephalopathy (PML), with scanty if any inflammatory-lymphocytic infiltrates. Posterior fossa involvement of JC virus (PML) has been reported in 58% of cases[4], when present there is MCP involvement in 64%-100% of cases[5]. There is increased recognition of the common involvement of posterior fossa by PML, with reported cases of isolated/restricted posterior fossa compromise[6,7]. PML usually progresses relentlessly over a few months, resulting in increasing neurologic impairment, dementia, and eventually death. Treatment of the cause of the underlying immunosuppression can lead to remission of PML. However, white matter sequelae are seen in most cases[8] (Figure 3). White matter lesions on PML should not enhance; if so, an infectious process, inflammatory reaction or neoplastic process should be considered.

Reconstitution of the immune system (*e.g.*, in the treatment of AIDS with highly active antiretroviral therapy) occasionally causes a paradoxical inflammatory response in the CNS, also known as IRIS (immune reconstitution inflammatory syndrome). This response might or might not be associated with an infectious agent, as in the case of PML-IRIS (Figure 4). Enhancement is present in these cases.

Vascular/toxic

Involvement of the brainstem by posterior reversible encephalopathy (PRES) has been reported in 18% of cases[9]. Isolated involvement of the brainstem or basal ganglia (no cortical or subcortical edema) can be seen in 4% of cases (central variant of PRES)[10]. In fact, there is increased awareness of "atypical distribution patterns" of PRES; thus, involvement involvement of the brainstem and MCP can actually be more common than expected (Figure 6)[11].

Toxic/metabolic

ODS is a metabolic induced demyelination characteristically involving the central pons secondary to rapid

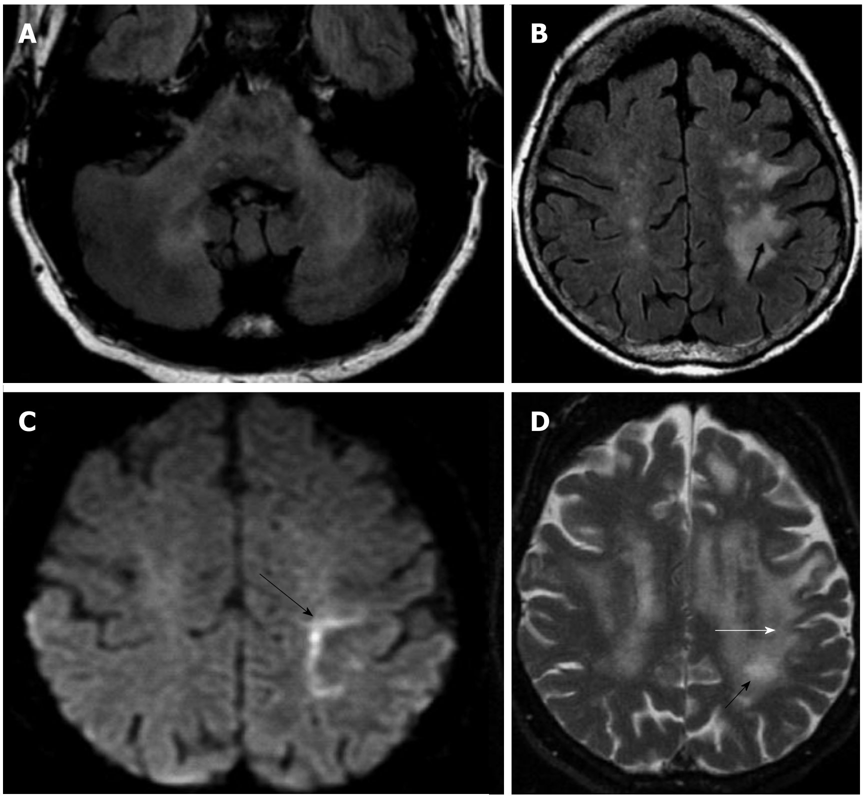

Figure 3 Progressive multifocal leucoencephalopathy. HIV patient with + JC virus on PCR-CSF. Bilateral involvement of MCP on axial FLAIR (A); with no enhancement (not shown); Axial FLAIR (B) and axial DWI (C) images show asymmetric confluent areas of increased signal in the subcortical WM with involvement of the u-fibers (arrow) and linear "edge" on DWI (arrow on C) consistent with advancing demyelinated edge; D: Three months f/u images better depict involvement of u-fibers (white arrow) as well as progression of WM disease with formation of small central cavitation/micro cyst, characteristic of PML (black arrow). PML: Progressive multifocal leucoencephalopathy; MCP: Middle cerebellar peduncles; CSF: Cerebrospinal fluid; DWI: Diffusion weighted-imaging; PCR: Polymerase chain reaction; HIV: Human immunodeficiency virus.

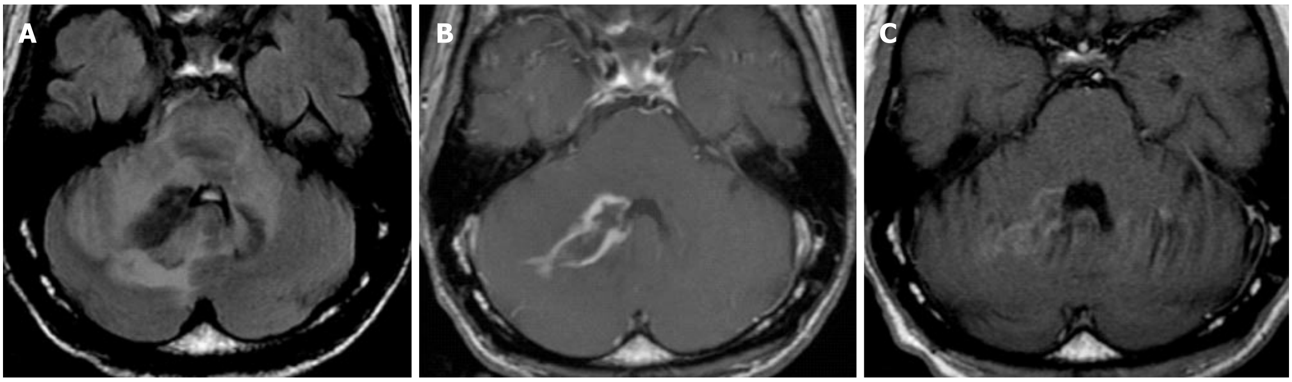

Figure 4 Immune reconstitution inflammatory syndrome and progressive multifocal leukoencephalopathy. HIV + JC virus, irregular antiretroviral therapy, with confusion and right sided weakness. Axial FLAIR (A) and axial post contrast (B) show abnormal signal in the bilateral MCP, greater on the right with associated enhancement; Axial post contrast (C) 2 mo after treatment with steroids and antiretroviral therapy show significant improvement of abnormal enhancement. IRIS might or might not be associated with an infectious process, in this case the abnormal enhancement in a patient with positive JC virus lead to the suspicious of a superimposed neoplastic process (lymphoma), other fungal or bacterial infection. Ultimately, the response to steroid gives the diagnosis of IRIS. IRIS: Immune reconstitution inflammatory syndrome; MCP: Middle cerebellar peduncles; HIV: Human immunodeficiency virus.

correction of hyponatremia (other disorders of the serum electrolyte such as hypernatremia could also cause it). The mechanism of demyelination is poorly understood. On imaging, there is usually preservation of the periphery of the pons and typically preservation of the corticospinal tracts ("trident sign") (Figure 5).

Toxic/drug induced involvement of the MCP has been reported after heroin inhalation ("chasing the dragon"). The initial stage is characterized by diffuse leukoencephalopathy, presumably caused by excitotoxicity and in some cases difficult to distinguish from hypoxic-ischemic injury (though cortical involvement is also expected in the latter, potentially a characteristic to differentiate them) (Figure 8). This stage can be reversible or lead to a chronic form or spongiform leukoencephalopathy (typically involve the posterior brain

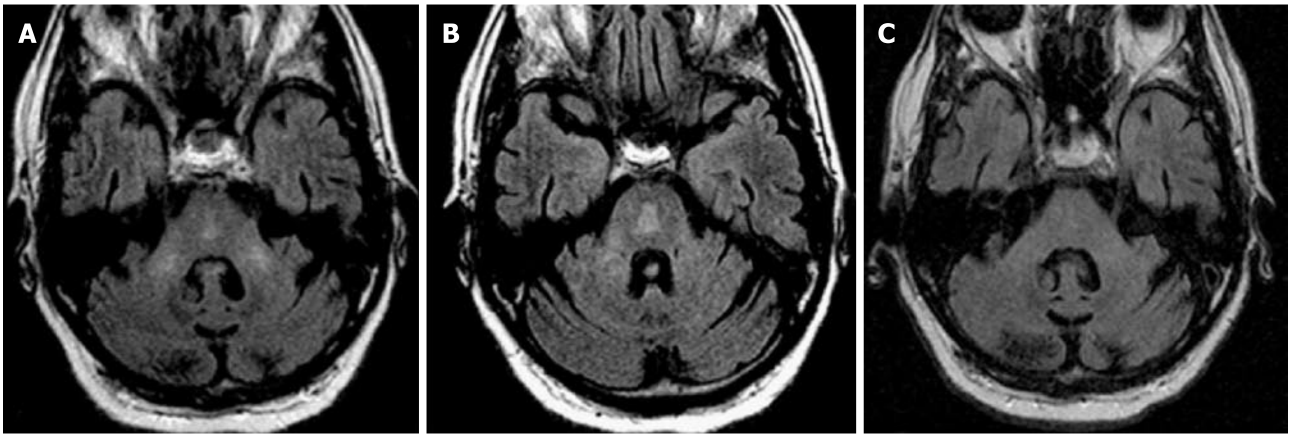

Figure 5 Osmotic demyelination syndrome. History of ethanol abuse and rapid correction of hyponatremia. A and B: Axial FLAIR images at two different levels of the pons show abnormal signal in the bilateral MCP as well as abnormal signal in the central pons with subtle "trident" appearance; C: Three months f/u demonstrate resolution of abnormal signal in the MCP and pons. ODS characteristically involve the central pons with sparing of the corticospinal tract, peripheral pons and tegmentum. In some acute cases, restricted diffusion is possible, differing from ischemic insult, which extends to the periphery of the pons with sparing of the midline (see Figure 9B). ODS: Osmotic demyelination syndrome; MCP: Middle cerebellar peduncles.

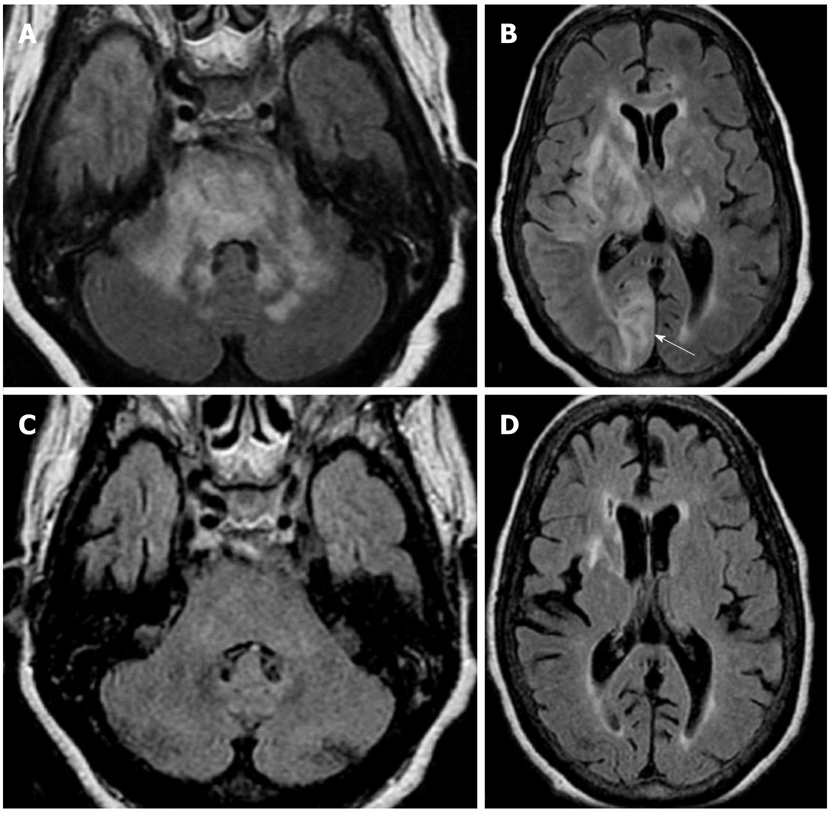

Figure 6 Posterior reversible encephalopathy. A and B: Axial FLAIR images in an hypertense encephalopathic patient show symmetric bilateral areas of abnormal signal in the MCP and pons. Concomitant involvement of supratentorial subcortical white matter in a "vasogenic type pattern" as well as cortical involvement (arrow on B) was noted; C and D: Three months f/u after control of hypertensive crisis show almost complete resolution of abnormal signal in MCP, pons and supratentorial regions to include the basal ganglia/thalami. Given the asymmetric distribution of supratentorial lesions, PML could be included in the differential. However, cortical involvement is not characteristic for PML. This case could be considered "atypical PRES" and proved by resolution of abnormal white matter disease (compare with Figure 3 where no resolution is noted). PRES: Posterior reversible encephalopathy; MCP: Middle cerebellar peduncles; PML: Progressive multifocal leucoencephalopathy.

white matter, midbrain and bilateral MCP)[12]. Other toxic-drug-induced abnormalities, such as toluene or methotrexate toxicity, involving the cerebellum and MCP have also been reported[13-15].

Preferential neuronal loss/volume loss of the putamen and caudate characterizes Wilson's disease, in some cases with late spongiform white matter changes[8]. In the midbrain, abnormal signal in the tegmentum lead to the well described "panda sign". Early work by King *et al*[16] described 32% of cases with MCP involvement. It appears that signal changes on T2 are less conspicuous in long-standing disease[16]

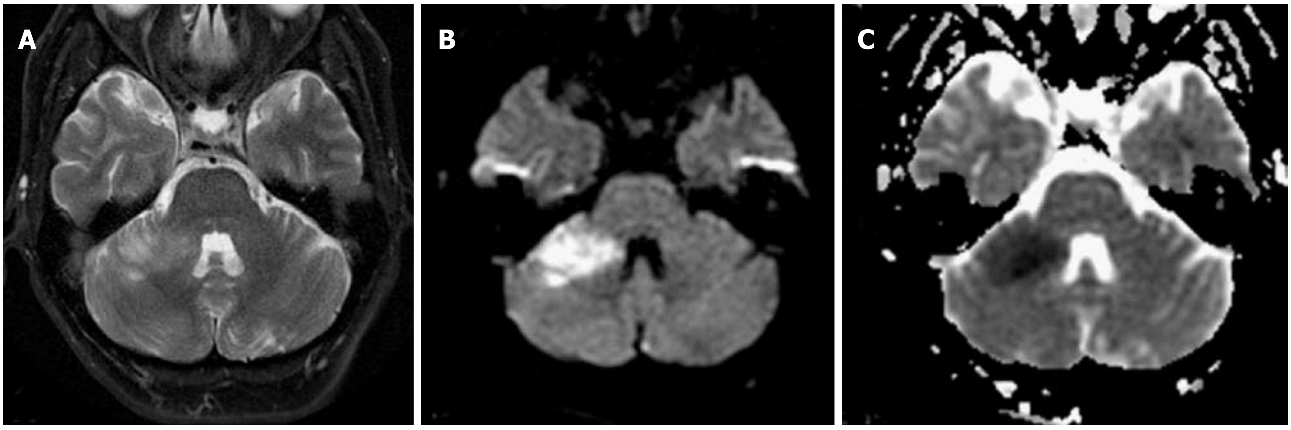

Figure 7 Anterior inferior cerebellar artery infarct. Patient with acute cerebellar ataxia and right-sided weakness. Axial T2 (A), DWI (B) and ADC maps (C) show well-defined area of high T2 signal and restricted diffusion consistent with ischemia. DWI: Diffusion weighted-imaging.

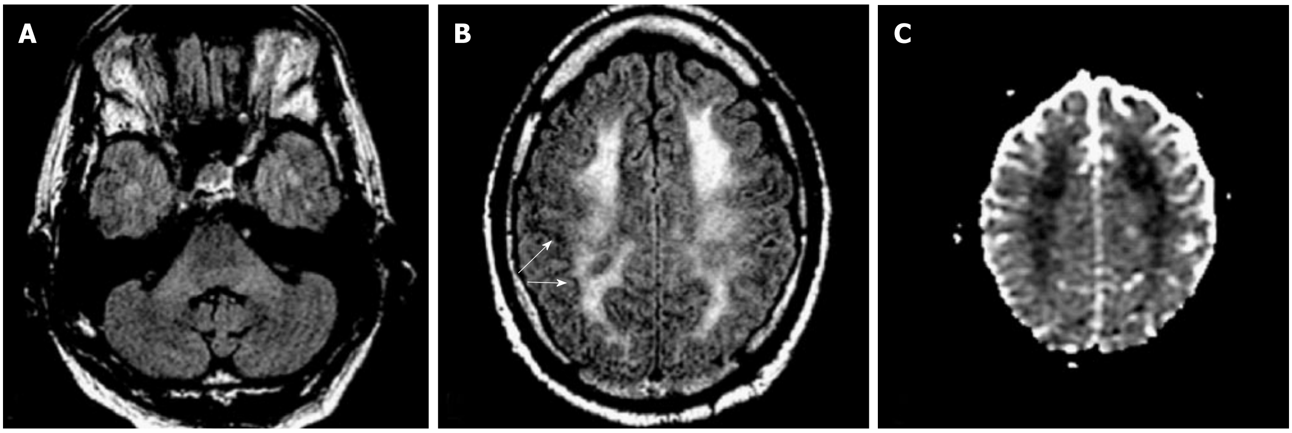

Figure 8 Acute heroin induced leukoencephalopathy ("chasing the dragon"). Twenty-year-old patient found down, history of recent heroin inhalation. A: Axial FLAIR shows subtle increased signal of MCP; Axial FLAIR (B) and ADC maps (C) show concomitant diffuse and confluent increased white matter signal and restricted diffusion with overall sparing of the subcortical u-fibers (arrows on B) and cortex. Though difficult to differentiate from hypoxic-ischemic event, the cortical sparing is more common in toxic leukoencephalopathies. Restricted diffusion has been described not only in the acute stage of toxic heroin inhalation, but in other hypoxic-toxic-metabolic states and could represent acute intramyelinic or excitotoxic edema, in some cases reversible. Evolution could lead to a chronic "chasing the dragon", spongiform leukoencephalopathy, where the posterior white matter, pons and MCP are typically involved. MCP: Middle cerebellar peduncles.

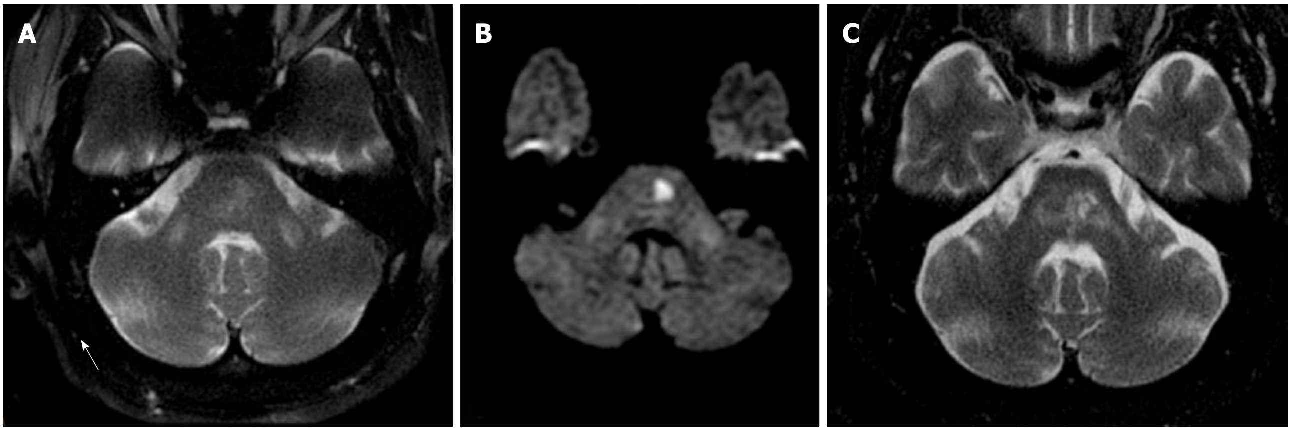

Figure 9 Wallerian degeneration of middle cerebellar peduncles. Axial T2 (A) and DWI (B) images show symmetric areas of abnormal signal in bilateral MCP as well as focal area of restricted diffusion in the left pons (note the characteristic spare of the midline due to occlusion of para-median branches of basilar artery); Axial T2 (C), 3 years f/u, shows evolution of lacunar infarction in the pons with resolution of abnormal signal in the right MCP and persistent abnormal signal and development of volume loss in the left MCP. Findings are consistent with WD of the MCP, with "acute" early changes in the bilateral MCP and subsequent left greater than right involvement on follow up (ipsilateral to infarct). WD: Wallerian degeneration; MCP: Middle cerebellar peduncles.

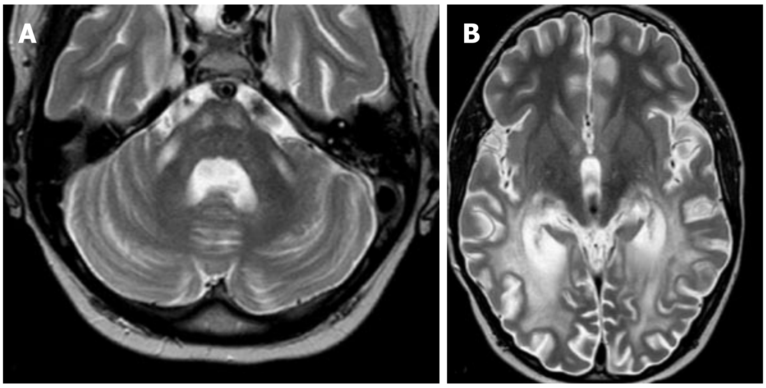

Figure 10 Adrenoleukodystrophy. A: Axial T2 image shows symmetric increased T2 signal in the MCP and bilateral corticospinal tracts; B: Axial T2 show concomitant symmetric and confluent white matter abnormal signal in bilateral occipito-parietal regions, typical for ADL. Note the preservation of subcortical u-fibers. Images courtesy of Dr. Lily Wang. ADL: Adrenoleukodystrophy; MCP: Middle cerebellar peduncles.

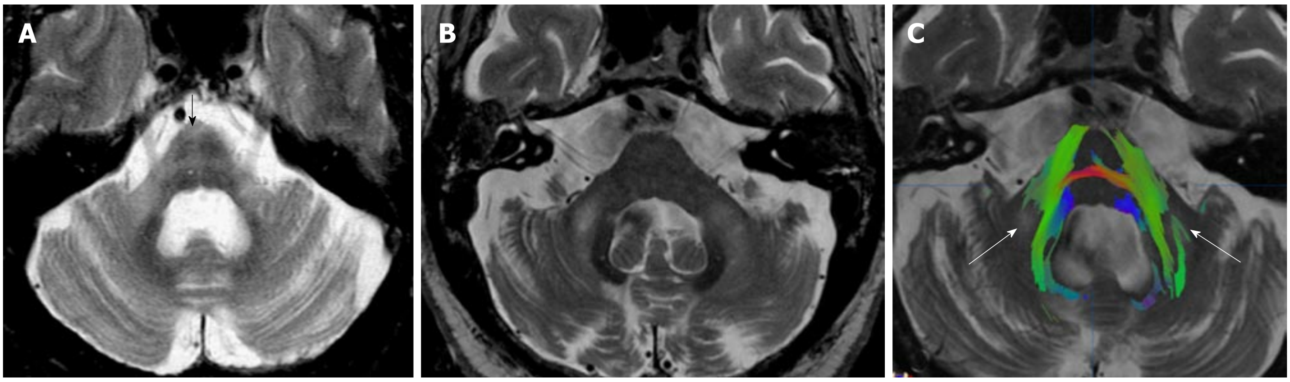

Figure 11 Multiple system atrophy C type and fragile-X associated tremor-ataxia syndrome. Axial T2 (A) in a patient with MSA-C show typical atrophy of the pons and MCP with degeneration of the pontine crossing fibers ("hot cross bun" sign, black arrow). There is also associated increased T2 signal of the MCP bilaterally. Axial T2 (B) and diffusion tensor imaging (DTI) tractography (C) in a patient with FXTAS show cerebellar volume loss and associated increased T2 signal and volume loss of MCP. Due to decreased fractional anisotropy (white arrows on C) there is lack of fibers in the areas of abnormal T2 signal. (DTI acquisition technique similar than Figure 1, please see figure for details). Image (B) courtesy of Dr. Andrew Duker. FXTAS: Fragile-X associated tremor-ataxia syndrome; MSA-C: Multiple system atrophy C type; MCP: Middle cerebellar peduncles.

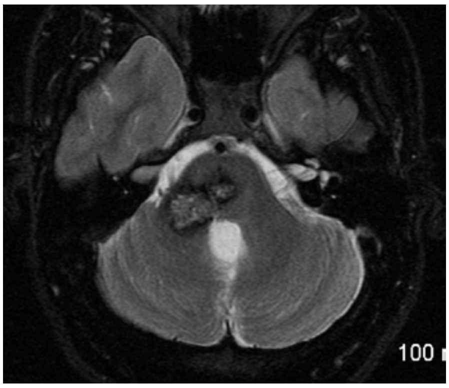

Figure 12 Cavernoma of middle cerebellar peduncle. Axial T2-WI shows contiguous lesions involving the pons and right MCP, with a typical mixed speckled hyper-intense and hypo-intense center and peripheral halo of hypo-intensity due to chronic hemosiderin deposition. MCP: Middle cerebellar peduncles.

and present in early or "active" forms of the disease; in some cases with concomitant restricted diffusion[17]. In our experience involvement of the MCP by Wilson's is not a common finding.

Vascular/ischemic

MCP is supplied by the anterior inferior cerebellar artery (AICA) and in lesser degree by the superior cerebellar artery. Isolated AICA infarction (thromboembolic or secondary to severe atherosclerotic disease of basilar artery and branches) is an uncommon event. When it occurs, characteristic restricted diffusion is seen in the involved cerebellar peduncle (Figure 7).

WD in the MCP can occur in the setting of pontine ischemia or hemorrhage (Figure 9). Increased T2 signal caused by gliosis would correspond to the third of four stages in the evolution of WD, as described by Kuhn *et al*[18]. This stage should occur 10-14 wk after axonal injury/loss of antegrade input. Interestedly, increased signal on diffusion weighted-imaging (DWI) in the cortico-spinal tract (CST) have been reported in approximately 20% of cases of MCA/ACA infarcts as early as 72 h[19]. Similarly, restricted diffusion in the CST has been reported at 48 h after MCA ischemia in the pediatric population[20] and in the bilateral MCP at 3-4 wk after acute pontine insult[21-24]. In all cases the changes are attributed to early WD. Certainly, they represent different phases in the development of WD and should not be misinterpreted as ischemic insults.

Degenerative

MSA is a sporadic neurodegenerative disorder characterized clinically by any combination of parkinsonian, autonomic, cerebellar or pyramidal signs. The abundant presence of glial cytoplasmic inclusions in all clinical subtypes of MSA led to the recognition that Shy-Drager syndrome, striatonigral degeneration, and sporadic olivopontocerebellar atrophy are one disease characterized by neuronal multisystem degeneration with unique oligodendroglial inclusion pathology[25].

Preferential neuronal loss of the cerebellum, pons and olivary nucleus with subsequent MCP degeneration characterizes the MSA-C subtype (where cerebellar ataxia is the main motor feature)[8]. Abnormal T2 signal of MCP has been reported in 43% of cases of MSA-C[26]. Concomitant volume loss is the rule (Figure 11A)[27].

FXTAS is a genetic disorder with overexpression of the fragile-X mental retardation 1 gene (*FMR1*); it is most common in males and associated with progressive ataxia as the individual age. Though there are abnormal inclusions in the neurons and cortical atrophy, there is predominant loss of Purkinje cells with cerebellar axonal degeneration[8,28]. Interestedly, in some series, as much as 82% of cases demonstrated increased T2 signal in the MCP (Figure 11B) (called as the "MCP sign", which as we described here, is not an specific sign)[28].

LD

LD are inherited metabolic disorders in which biochemical defects interfere with myelin formation. Usually, LD are associated with peroxisomal (*e.g.*, adrenoleukodystrophy) or lysosomal defects (*e.g.*, metachromatic LD). LD can affect the MCP. However, there is concomitant, usually symmetric involvement of the supratentorial white matter, with sparing of subcortical u-fibers (Figure 10). Few LD, such as Canavan's or Pelizaeus-Merzbacher disase, compromise the subcortical u-fibers[8].

Infectious

ADEM or rhombencephalitis can affect MCP. In most cases, the cause of ADEM or rhombencephalitis is not known; however an association with recent systemic infectious process or vaccination is described. Most common associated virus is varicella, mumps, measles, rubella or rotavirus. Rarely, bacterial infections such as Lyme disease, Listeria or Whipple can affect the posterior fossa and compromise the MCP[29,30].

DWI AND DIFFUSION TENSOR IMAGING

As discussed, other conditions besides ischemic/cytotoxic edema can cause restriction diffusion (*e.g.*, intra-myelinic edema) (Figure 8). Some acute toxic states can show white matter restricted diffusion[31,32]. In fact, the signal changes in these conditions could be reversible[32]. Early WD and early stages of metabolic diseases such as Wilson's disease can also be associated with areas of restricted diffusion[17,20,21,33]. Overall, the mechanism of restricted diffusion in the "non-ischemic" cases is debatable. In addition to the mentioned intra-myelinic edema; acute white matter vacuolization or other types of excitotoxic edema could be postulated.

The use of diffusion tensor imaging (DTI) for prediction of neurologic deficits or for differential diagnosis is in continuous research. Fractional anisotropy (FA) measurements by DTI have proved involvement of the cerebellar peduncles by MS (even in the absence of T2 signal changes). Decreased FA in the MCP of MS patients as compared with controls is also correlated with motor deficits[34]. Decreased FA early in the course of WD appears to predict neurologic deficits[35]. DTI in the MCP has also been used to differentiate neurodegenerative diseases such as MSA-C from other cerebellar degenerative ataxias or Parkinson-like syndromes (Figure 11C)[36].

OTHER ADVANCED IMAGING TECHNIQUES

MR spectroscopy (MRS) evaluates the biochemical signature in normal and abnormal brain parenchyma. Multiple metabolites to include N-acetyl-aspartate (NAA - marker of neuronal tissue), choline (Cho - membrane turnover), myo-Inositol (glial tissue), lipids (necrosis) and lactate (hypoxia) are altered in different pathologic processes. Very few studies of MRS in the MCP have assessed changes in neurodegenerative diseases, particularly MSA-C[37]. They demonstrated decreased NAA in correlation with known decreased of neuronal/axonal tissue. In demyelinating processes, in addition to decreased NAA, an increase in Cho can also be demonstrated particularly in cases of acute demyelination (usually attributed to active myelin breakdown or increased macrophages in acute demyelinating plaques)[7,38,39]. In other pathophysiologic processes, such as ischemia, an increase in lactate might be expected[38,40].

MR perfusion is expecting to be altered in different pathologic processes involving the MCP. MR Perfusion, in conjunction with MRS and particularly DWI, is an important indicator of hypoxia, cell density and necrosis. Decreased perfusion on SPECT imaging has been demonstrated in MSA-C including the cerebellum and peduncles[41-43]. Demyelinating or ischemic processes usually show decreased perfusion as compared with other pathologic processes such as tumors[40,44,45].

Clinical clues

Given the improvement in the management of chronic infectious (*e.g.*, HIV) or immune-mediated diseases (*e.g.*, rituximab on MS or rheumatoid arthritis patients), patients in chronic immune-suppression states are not uncommon. In these populations, JC virus infection/reactivation (PML) should be high in the differential when confronting abnormal MCP signal. A post-transplant patient have also a particular risk for PRES and in less degree ODS. Other known associations for PRES includes not only hypertension but also high dose chemotherapy. Concomitant or recent history of fever should raise suspicion for infectious or post infectious process (ADEM or rombencephalitis). In the pediatric population, a leukodystrophy should be excluded. In a young encephalopathic patient, high suspicion for toxic/illicit drug use is warranted. Other toxic leukoencephalopathies, such as cyclosporine or methrotexate, should also be correlated clinically. After exclusion of relative common acquired causes of ataxia such as alcohol/anti-epileptic drugs (where cerebellar vermian atrophy predominates rather than MCP involvement), a progressive ataxic syndrome should raise suspicion for a degenerative process such as MSA-C or FXTAS (where areas of increased T2 signal in the MCP are common).

Imaging clues

As previously discussed, the involvement of the MCP or posterior fossa can be isolated (Figure 2). However, usually there is concomitant involvement of the pons or supratentorial white matter. The distribution and characteristic of the concomitant involvement can help in the differential. There is usually involvement of subcortical u-fibers in demyelinating diseases, particularly PML. To the contrary, the subcortical u-fibers are spared in other leukoencephalopathies such as toxic/metabolic entities or most LD[8]. Additionally, the involvement is usually symmetric in these cases. Vasogenic edema pattern with not only involvement of the subcortical white matter but also the adjacent cortex should rise suspicion for PRES. Restricted diffusion is characteristic of an acute ischemic process, however it can be the result of early WD, the acute phase of ODS or toxic leukoenchephalopathies. In these cases, restricted diffusion is usually bilateral. Volume loss characterizes not only neurodegenerative disorders such as MSA-C and FXTAS, but also the late stage of WD.

CONCLUSION

Pathologic entities such as demyelinating disorders and certain neurodegenerative diseases have predilection for the MCP. When approaching abnormal T2 signal in the MCP, entities such as MS, PML, PRES, and certain toxic/metabolic or neurodegenerative states should be entertained. Careful evaluation of concomitant imaging findings described, in conjunction with focused correlation with key clinical findings discussed; would yield an appropriate and accurate differential diagnosis in the majority of cases.

ACKWNOLEDGEMENTS

The authors would like to thanks Dr. Angelo Rutty, Perea Hospital - Puerto Rico, for his wonderful contribution with the anatomic drawing presented in Figure 1. Previously presented exhibit at the Annual Meeting of the American Society of Neuroradiology, Chicago, 2015.

REFERENCES

1 **Ramnani N**. The primate cortico-cerebellar system: anatomy and function. *Nat Rev Neurosci* 2006; **7**: 511-522 [PMID: 16791141 DOI: 10.1038/nrn1953]

2 **Moritani T**, Smoker WR, Sato Y, Numaguchi Y, Westesson PL. Diffusion-weighted imaging of acute excitotoxic brain injury. *AJNR Am J Neuroradiol* 2005; **26**: 216-228 [PMID: 15709116]

3 **Ormerod IE**, Miller DH, McDonald WI, du Boulay EP, Rudge P, Kendall BE, Moseley IF, Johnson G, Tofts PS, Halliday AM. The role of NMR imaging in the assessment of multiple sclerosis and isolated neurological lesions. A quantitative study. *Brain* 1987; **110** (Pt 6): 1579-1616 [PMID: 3427402]

4 **Post MJ**, Yiannoutsos C, Simpson D, Booss J, Clifford DB, Cohen B, McArthur JC, Hall CD. Progressive multifocal leukoencephalopathy in AIDS: are there any MR findings useful to patient management and predictive of patient survival? AIDS Clinical Trials Group, 243 Team. *AJNR Am J Neuroradiol* 1999; **20**: 1896-1906 [PMID: 10588116]

5 **Bag AK**, Curé JK, Chapman PR, Roberson GH, Shah R. JC virus infection of the brain. *AJNR Am J Neuroradiol* 2010; **31**: 1564-1576 [PMID: 20299430 DOI: 10.3174/ajnr.A2035]

6 **Gonçalves FG**, Lamb L, Del Carpio-O'Donovan R. Progressive multifocal leukoencephalopathy restricted to the posterior fossa in a patient with systemic lupus erythematosus. *Braz J Infect Dis* 2011; **15**: 609-612 [PMID: 22218525]

7 **Horger M**, Beschorner R, Beck R, Nägele T, Schulze M, Ernemann U, Heckl S. Common and uncommon imaging findings in progressive multifocal leukoencephalopathy (PML) with differential diagnostic considerations. *Clin Neurol Neurosurg* 2012; **114**: 1123-1130 [PMID: 22771304 DOI: 10.1016/j.clineuro.2012.06.018]

8 **Ellison D**, Love S, Chimelli L, Harding BN, Lowe J, Vinters HV. Neuropathology: A Reference Text of CNS Pathology (2nd edition). MOSBY, Elsevier Ltd, 2004: 879 [DOI: 10.1111/j.1365-2990.2004.00620.x]

9 **Bartynski WS**, Boardman JF. Distinct imaging patterns and lesion distribution in posterior reversible encephalopathy syndrome. *AJNR Am J Neuroradiol* 2007; **28**: 1320-1327 [PMID: 17698535 DOI: 10.3174/ajnr.A0549]

10 **McKinney AM**, Jagadeesan BD, Truwit CL. Central-variant posterior reversible encephalopathy syndrome: brainstem or basal ganglia involvement lacking cortical or subcortical cerebral edema. *AJR Am J Roentgenol* 2013; **201**: 631-638 [PMID: 23971457 DOI: 10.2214/AJR.12.9677]

11 **McKinney AM**, Short J, Truwit CL, McKinney ZJ, Kozak OS, SantaCruz KS, Teksam M. Posterior reversible encephalopathy syndrome: incidence of atypical regions of involvement and imaging findings. *AJR Am J Roentgenol* 2007; **189**: 904-912 [PMID: 17885064 DOI: 10.2214/AJR.07.2024]

12 **Geibprasert S**, Gallucci M, Krings T. Addictive illegal drugs: structural neuroimaging. *AJNR Am J Neuroradiol* 2010; **31**: 803-808 [PMID: 19875473 DOI: 10.3174/ajnr.A1811]

13 **Okamoto K**, Tokiguchi S, Furusawa T, Ishikawa K, Quardery AF, Shinbo S, Sasai K. MR features of diseases involving bilateral middle cerebellar peduncles. *AJNR Am J Neuroradiol* 2003; **24**: 1946-1954 [PMID: 14625215]

14 **Uchino A**, Sawada A, Takase Y, Kudo S. Symmetrical lesions of the middle cerebellar peduncle: MR imaging and differential diagnosis. *Magn Reson Med Sci* 2004; **3**: 133-140 [PMID: 16093630]

15 **Arora A**, Neema M, Stankiewicz J, Guss ZD, Guss JG, Prockop L, Bakshi R. Neuroimaging of toxic and metabolic disorders. *Semin Neurol* 2008; **28**: 495-510 [PMID: 18843577 DOI: 10.1055/s-0028-1083684]

16 **King AD**, Walshe JM, Kendall BE, Chinn RJ, Paley MN, Wilkinson ID, Halligan S, Hall-Craggs MA. Cranial MR imaging in Wilson'

s disease. *AJR Am J Roentgenol* 1996; **167**: 1579-1584 [PMID: 8956601 DOI: 10.2214/ajr.167.6.8956601]

17 **Sener RN**. Diffusion MR imaging changes associated with Wilson disease. *AJNR Am J Neuroradiol* 2003; **24**: 965-967 [PMID: 12748103]

18 **Kuhn MJ**, Johnson KA, Davis KR. Wallerian degeneration: evaluation with MR imaging. *Radiology* 1988; **168**: 199-202 [PMID: 3380957 DOI: 10.1148/radiology.168.1.3380957]

19 **Castillo M**, Mukherji SK. Early abnormalities related to postinfarction Wallerian degeneration: evaluation with MR diffusion-weighted imaging. *J Comput Assist Tomogr* 1999; **23**: 1004-1007 [PMID: 10589585]

20 **Bekiesinska-Figatowska M**, Duczkowski M, Madzik J, Uliasz M, Zawadka A, Baszczeska J. Diffusion-Weighted Imaging of the Early Phase of Wallerian Degeneration. A Report of two Pediatric Cases and Literature Review. *Neuroradiol J* 2012; **25**: 657-664 [PMID: 24029177]

21 **De Simone T**, Regna-Gladin C, Carriero MR, Farina L, Savoiardo M. Wallerian degeneration of the pontocerebellar fibers. *AJNR Am J Neuroradiol* 2005; **26**: 1062-1065 [PMID: 15891160]

22 **Fitzek C**, Fitzek S, Stoeter P. Bilateral Wallerian degeneration of the medial cerebellar peduncles after ponto-mesencephalic infarction. *Eur J Radiol* 2004; **49**: 198-203 [PMID: 14962648 DOI: 10.1016/S0720-048X(03)00132-3]

23 **Küker W**, Schmidt F, Heckl S, Nägele T, Herrlinger U. Bilateral Wallerian degeneration of the middle cerebellar peduncles due to paramedian pontine infarction: MRI findings. *Neuroradiology* 2004; **46**: 896-899 [PMID: 15526095 DOI: 10.1007/s00234-004-1287-y]

24 **Gala F**, Becker A, Pfeiffer M, Kollias S. Acute Wallerian degeneration of middle cerebellar peduncles due to basilar artery thrombosis. *Indian J Radiol Imaging* 2013; **23**: 164-167 [PMID: 24082483 DOI: 10.4103/0971-3026.116581]

25 **Wenning GK**, Colosimo C, Geser F, Poewe W. Multiple system atrophy. *Lancet Neurol* 2004; **3**: 93-103 [PMID: 14747001]

26 **Naka H**, Ohshita T, Murata Y, Imon Y, Mimori Y, Nakamura S. Characteristic MRI findings in multiple system atrophy: comparison of the three subtypes. *Neuroradiology* 2002; **44**: 204-209 [PMID: 11942373]

27 **Nicoletti G**, Fera F, Condino F, Auteri W, Gallo O, Pugliese P, Arabia G, Morgante L, Barone P, Zappia M, Quattrone A. MR imaging of middle cerebellar peduncle width: differentiation of multiple system atrophy from Parkinson disease. *Radiology* 2006; **239**: 825-830 [PMID: 16714464 DOI: 10.1148/radiol.2393050459]

28 **Tassone F**, Berry-Kravis EM, Fragile X-associated tremor ataxia syndrome (FXTAS). New York, London: Springer, 2010

29 **Guzmán-De-Villoria JA**, Ferreiro-Argüelles C, Fernández-García P. Differential diagnosis of T2 hyperintense brainstem lesions: Part 2. Diffuse lesions. *Semin Ultrasound CT MR* 2010; **31**: 260-274 [PMID: 20483393 DOI: 10.1053/j.sult.2010.03.002]

30 **Black DF**, Aksamit AJ, Morris JM. MR imaging of central nervous system Whipple disease: a 15-year review. *AJNR Am J Neuroradiol* 2010; **31**: 1493-1497 [PMID: 20395395 DOI: 10.3174/ajnr.A2089]

31 **Rollins N**, Winick N, Bash R, Booth T. Acute methotrexate neurotoxicity: findings on diffusion-weighted imaging and correlation with clinical outcome. *AJNR Am J Neuroradiol* 2004; **25**: 1688-1695 [PMID: 15569732]

32 **McKinney AM**, Kieffer SA, Paylor RT, SantaCruz KS, Kendi A, Lucato L. Acute toxic leukoencephalopathy: potential for reversibility clinically and on MRI with diffusion-weighted and FLAIR imaging. *AJR Am J Roentgenol* 2009; **193**: 192-206 [PMID: 19542414 DOI: 10.2214/AJR.08.1176]

33 **Musson R**, Romanowski C. Restricted diffusion in Wallerian degeneration of the middle cerebellar peduncles following pontine infarction. *Pol J Radiol* 2010; **75**: 38-43 [PMID: 22802803]

34 **Anderson VM**, Wheeler-Kingshott CA, Abdel-Aziz K, Miller DH, Toosy A, Thompson AJ, Ciccarelli O. A comprehensive assessment of cerebellar damage in multiple sclerosis using diffusion tractography and volumetric analysis. *Mult Scler* 2011; **17**: 1079-1087 [PMID: 21511688 DOI: 10.1177/1352458511403528]

35 **Liang Z**, Zeng J, Zhang C, Liu S, Ling X, Wang F, Ling L, Hou Q, Xing S, Pei Z. Progression of pathological changes in the middle cerebellar peduncle by diffusion tensor imaging correlates with lesser motor gains after pontine infarction. *Neurorehabil Neural Repair* 2009; **23**: 692-698 [PMID: 19244384 DOI: 10.1177/1545968308331142]

36 **Prakash N**, Hageman N, Hua X, Toga AW, Perlman SL, Salamon N. Patterns of fractional anisotropy changes in white matter of cerebellar peduncles distinguish spinocerebellar ataxia-1 from multiple system atrophy and other ataxia syndromes. *Neuroimage* 2009; **47** Suppl 2: T72-T81 [PMID: 19446636 DOI: 10.1016/j.neuroimage.2009.05.013]

37 **Terakawa H**, Abe K, Watanabe Y, Nakamura M, Fujita N, Hirabuki N, Yanagihara T. Proton magnetic resonance spectroscopy (1H MRS) in patients with sporadic cerebellar degeneration. *J Neuroimaging* 1999; **9**: 72-77 [PMID: 10208103]

38 **Oz G**, Alger JR, Barker PB, Bartha R, Bizzi A, Boesch C, Bolan PJ, Brindle KM, Cudalbu C, Dinçer A, Dydak U, Emir UE, Frahm J, González RG, Gruber S, Gruetter R, Gupta RK, Heerschap A, Henning A, Hetherington HP, Howe FA, Hüppi PS, Hurd RE, Kantarci K, Klomp DW, Kreis R, Kruiskamp MJ, Leach MO, Lin AP, Luijten PR, Marjańska M, Maudsley AA, Meyerhoff DJ, Mountford CE, Nelson SJ, Pamir MN, Pan JW, Peet AC, Poptani H, Posse S, Pouwels PJ, Ratai EM, Ross BD, Scheenen TW, Schuster C, Smith IC, Soher BJ, Tkáč I, Vigneron DB, Kauppinen RA. Clinical proton MR spectroscopy in central nervous system disorders. *Radiology* 2014; **270**: 658-679 [PMID: 24568703 DOI: 10.1148/radiol.13130531]

39 **Shah R**, Bag AK, Chapman PR, Curé JK. Imaging manifestations of progressive multifocal leukoencephalopathy. *Clin Radiol* 2010; **65**: 431-439 [PMID: 20451009 DOI: 10.1016/j.crad.2010.03.001]

40 **Chu WJ**, Mason GF, Pan JW, Hetherington HP, Liu HG, San Pedro EC, Mountz JM. Regional cerebral blood flow and magnetic resonance spectroscopic imaging findings in diaschisis from stroke. *Stroke* 2002; **33**: 1243-1248 [PMID: 11988598]

41 **Miyoshi F**, Kanasaki Y, Shinohara Y, Fujii S, Kaminou T, Tanabe Y, Ogawa T. Significance of combined use of MRI and perfusion SPECT for evaluation of multiple system atrophy, cerebellar type. *Acta Radiol* 2015 Aug 7; Epub ahead of print [PMID: 26253930 DOI: 10.1177/0284185115598810]

42 **Cilia R**, Marotta G, Benti R, Pezzoli G, Antonini A. Brain SPECT imaging in multiple system atrophy. *J Neural Transm* (Vienna) 2005; **112**: 1635-1645 [PMID: 16284908 DOI: 10.1007/s00702-005-0382-5]

43 **Matsuda H**, Imabayashi E, Kuji I, Seto A, Ito K, Kikuta D, Yamada M, Shimano Y, Sato N. Evaluation of both perfusion and atrophy in multiple system atrophy of the cerebellar type using brain SPECT alone. *BMC Med Imaging* 2010; **10**: 17 [PMID: 20701753 DOI: 10.1186/1471-2342-10-17]

44 **Song SS**. Advanced imaging in acute ischemic stroke. *Semin Neurol* 2013; **33**: 436-440 [PMID: 24504605 DOI: 10.1055/s-0033-1364214]

45 **Fayed-Miguel N**, Morales-Ramos H, Modrego-Pardo PJ. Magnetic resonance imaging with spectroscopy, perfusion and cerebral diffusion in the diagnosis of brain tumours. *Rev Neurol* 2006; **42**: 735-742 [PMID: 16775800]

P- Reviewer: Li YZ, Shen J, Sijens PE **S- Editor**: Ji FF
L- Editor: A **E- Editor**: Wu HL

World Journal of Radiology

Submit a Manuscript: http://www.wjgnet.com/esps/
Help Desk: http://www.wjgnet.com/esps/helpdesk.aspx
DOI: 10.4329/wjr.v7.i12.448

World J Radiol 2015 December 28; 7(12): 448-458
ISSN 1949-8470 (online)

REVIEW

Magnetic resonance imaging of the spinal marrow: Basic understanding of the normal marrow pattern and its variant

Mohamed Ragab Nouh, Ahmed Fathi Eid

Mohamed Ragab Nouh, Faculty of Medicine, Alexandria University, Alexandria 21563, Egypt

Ahmed Fathi Eid, National Guard hospital, Al Ehsa 31982, Eastern Provience, Saudi Arabia

Author contributions: Nouh MR had the idea of the manuscript, reviewed the literature, drafted the manuscript and supplied some of the figures; Eid AF supplied some of the figures, critically reviewed the manuscript; Both authors approved the manuscript in its current final form.

Conflict-of-interest statement: The authors declare no conflict of interest.

Correspondence to: Mohamed Ragab Nouh, MD, Assistant Professor of radiology and clinical imaging, Faculty of Medicine, Alexandria University, 1 Kolyat El-Teb Street, Mahata El-Ramel, Alexandria 21563, Egypt. mragab73@yahoo.com
Telephone: +20-111-6590365

Received: June 2, 2015
Peer-review started: June 5, 2015
First decision: August 8, 2015
Revised: September 29, 2015
Accepted: October 23, 2015
Article in press: October 27, 2015
Published online: December 28, 2015

Abstract

For now, magnetic resonance (MR) is the best noninvasive imaging modality to evaluate vertebral bone marrow thanks to its inherent soft-tissue contrast and non-ionizing nature. A daily challenging scenario for every radiologist interpreting MR of the vertebral column is discerning the diseased from normal marrow. This requires the radiologist to be acquainted with the used MR techniques to judge the spinal marrow as well as its normal MR variants. Conventional sequences used basically to image marrow include T1W, fat-suppressed T2W and short tau inversion recovery (STIR) imaging provides gross morphological data. Interestingly, using non-routine MR sequences; such as opposed phase, diffusion weighted, MR spectroscopy and contrasted-enhanced imaging; may elucidate the nature of bone marrow heterogeneities; by inferring cellular and chemical composition; and adding new functional prospects. Recalling the normal composition of bone marrow elements and the physiologic processes of spinal marrow conversion and reconversion eases basic understanding of spinal marrow imaging. Additionally, orientation with some common variants seen during spinal marrow MR imaging as hemangiomas and bone islands is a must. Moreover, awareness of the age-associated bone marrow changes as well as changes accompanying different variations of the subject's health state is essential for radiologists to avoid overrating normal MR marrow patterns as pathologic states and metigate unnecessary further work-up.

Key words: Magnetic resonance imaging; Normal; Spinal; Marrow; Variants

Core tip: Magnetic resonance (MR) remains the ideal noninvasive imaging modality to evaluate vertebral bone marrow. Radiologists have to be aware by age-associated bone marrow changes as well as changes accompanying different variations of the subject's health state. Moreover, acquaintation with the used MR techniques, their privileges and limitations, in evaluation of spinal marrow is a prime requirement for radiologist to discern the normal spinal marrow as well as its variants from diseased one.

Nouh MR, Eid AF. Magnetic resonance imaging of the spinal marrow: Basic understanding of the normal marrow pattern and its variant. *World J Radiol* 2015; 7(12): 448-458 Available from: URL: http://www.wjgnet.com/1949-8470/full/v7/i12/448.htm DOI: http://dx.doi.org/10.4329/wjr.v7.i12.448

INTRODUCTION

The spine is the largest store of bone marrow in the body[1,2]. Addressing bone marrow signal pattern is an integral part of the spinal magnetic resonance (MR) imaging evaluation. By far, magnetic resonance imaging (MRI) is the best imaging modality to depict bone marrow thanks to its inherent soft-tissue contrast and non-ionizing nature[3-5].

Bone marrow is a dynamic organ with continued changes occurring with increased age and increased hematopoietic needs in different environmental and health states[4,6]. Similarly, it is the target of a lot of pathologic processes that results in altered signal intensity or heterogenous signal pattern on MR imaging. A daily challenging scenario for every radiologist interpreting MR of the spine is to discern the diseased from normal marrow. This requires the radiologist to be acquainted with normal MR patterns of the spinal bone marrow, its chronological conversion, and its different common variants. This review starts with a brief discussion of the composition and physiology of the spinal marrow, followed by a concise discussion on the common MR sequences used to evaluate the spinal marrow. In the latter section the normal spinal marrow MR patterns and common variants are displayed.

Spinal bone marrow buildup and physiology

Imaging-wise, the spinal bone marrow is a mix of cellular elements enclosed within a cortical bone shell; the vertebral body. These cellular elements are enmeshed within the medullary bony trabeculae; predominantly vertically oriented; that provide both structural support and storage of minerals as calcium and phosphate; thicker in the lumbar region[2,5,6]. There are two types of bone marrow in the spine: the red marrow, named after its richness in hemoglobin in erythrocytes lineage and is richly vascular; and the yellow marrow, named after abundant carotenoid bodies in its fat cells and is scarily vascular[7]. Either marrow type, whether red or yellow, is composed of a blend of fat, water and proteins in different proportions (Table 1). The 3 components vary in volume with normal growth and in response to different stimuli. Hence, their proportions are the main determinants of spinal marrow MR signal characteristics[8-10]. The nutrition of spinal marrow is derived from ambient sinusoids branching from nutrient vessels piercing the vertebral cortices and drained *via* the Batson's venous plexus emerging from the posterior vertebral bodies' cortices. Nerves accompany this vascular network and few lymph nodes can be identified within the vertebral marrow[7]. The function of bone marrow is to provide different blood cell lineages involved in tissue nutrition, oxygenation and body's immune reactions[7].

Table 1 Vertebral bone marrow chemical composition and cellular buildup

Marrow phenotype	Chemical composition	Cellular components
Red marrow	40%-60% lipids 30%-40% water 10%-20% proteins	60% hematopoietic cells 40% fat cells
Yellow marrow	80% lipids 15% water 5% proteins	95% fat cells 5% hematopoietic cells

Spinal marrow conversion

At birth, the whole spinal marrow is metabolically active (hematopoietic/red marrow). This pattern gradually, and in orderly fashion, turns into a less metabolically active (fat/yellow) marrow with growing up. This temporal physiologic phenomenon is known as normal marrow conversion and concludes around age of 25-30 years[2,6,11,12]. As in other skeletal region, the pattern of spinal marrow conversion is centripetal starting in the subcortical and subendplates regions and going to the center of vertebral body[8]. At all times, both red and yellow marrow are spinal marrow cohabitant yet the prevalent type is used to address the type of marrow in focus[2,4,12]. Moreover, a peculiar character of the spinal marrow is the persistence of red marrow over all ages, especially in the lumbar region[1]. Consequently, heterogeneity of the spinal marrow is a normal phenomenon, especially in adolescence and middle age. Focal areas of red marrow may be a challenge to disclose its nature in some clinical scenarios and mandates making use of different MR pulse sequences to disclose its nature.

Spinal marrow reconversion

During lifetime, various physiologic and pathologic states require increased tissue demands for more oxygen and hemoglobin. The metabolically inactive fat marrow dynamically repopulates into the metabolically active red type, capable of responding to tissues' needs of oxygen in a process named marrow reconversion[5,6,13,14].

It could be in response to physiologic stimuli as in obesity, cigarette smokers and heavy training athletes; or pathologic conditions as chronic hemolytic anemias and marrow replacing disorders[2,13,14].

In contrast to the orderly fashion of normal marrow conversion, reconversion is a patchy and an asymmetrical process where areas of red marrow are embedded within the surrounding yellow marrow[15]. That is why recognition of this physiologic phenomenon is mandatory to rule out underlying myeloproliferative disorder on MR imaging.

MRI technique for the spinal marrow

Routine evaluation of spinal marrow will include spin echo T1 and T2W pulse sequences in the sagittal plane. Some institutes add short tau inversion recovery (STIR) sequences in the sagittal plane as a routine. The author's prefer to use the STIR in the coronal plane to discourse the neutral axis and its meningeal sleeves, especially in cervical and lumbar regions, abnormalities of the facets and sacroiliac joints and exploration of accidental extra-spinal pathologies not apparent on routine sagittal and axial planes. Any suspicious bone marrow lesion on the routine planes could be ascertained on this additional coronal STIR image. Axial planes will be advantageous in labeling presence of extra-medullary extensions and neural axis involvement by any marrow pathology.

Routine MR sequences for spinal bone marrow imaging

T1-weighted imaging: Both red and fat marrows contain lipid and water with various proportions. The red marrow appears as low signal due to its higher water content on T1W images yet it has to be higher than that of intervertebral discs and paraspinal muscles[16]. On the contrary, a high lipid content of yellow marrow returns high signal intensity comparable to that of subcutaneous fat on T1W images[16]. This makes T1W the money's worth sequence of MR screening of bone marrow[3,17,18].

T2-weighted imaging: The signal returning from both water and fat are high yet signal returning from red marrow is slightly lower than that of yellow marrow[19]. So, the ability of T2-sequence to differentiate marrow hyperplasia from marrow lesions is limited without the use of fat suppression especially on the fast spin echo (FSE) acquisitions[10,20]. This mandates the use of fat-suppression for better utility of T2 FSE used in clinical imaging of the spines. On fat suppression T2W sequences the red marrow will be of slightly higher signal than muscle while the yellow marrow has signal lower than it[6,10].

STIR sequence: It enhances the difference in longitudinal relaxation of fat and water on T1W imaging. A non-selective 180° inversion pulse applied at specified inversion time followed by refocusing 90 pulse can cancel any signal from fat and the returning signal will be of the non-fatty components, *e.g.,* water[10,21]. This enhances contrast of bone marrow lesions within the suppressed background. The main drawback of STIR imaging, that it suppresses any signal other than fat as hematomas and gadolinium enhancement[22].

Problem-solving MR sequences for spinal bone marrow imaging

Chemical-shift imaging: Chemical-shift or opposed phase imaging relies on the fact that water and fat have different resonance frequencies so that when they are resonating aligned their signal is summed (in-phase imaging) while when they are opposed (out-phase imaging) their signals are subtracted with subsequent signal drop[23]. As fat and water intermix in both types of marrow, the signal of red marrow will not significantly drop in out phase while that of yellow marrow will[23]. However, this is not absolute and a cut off value of 20% signal drop has postulated[24].

The main value of opposed phase imaging is to rule out neoplastic replacement of the marrow. Metastatic and infiltrative marrow neoplasia will destroy normal marrow and retain high water content with resultant high-signal on out-phase imaging[23]. This has proved beneficiary in differentiation neoplastic and osteoporotic fractures[25,26].

However, false negative results can rise from fat-containing metastasis (*e.g.,* from renal cell carcinoma) and false positive results can results from marrow fibrosis as well as susceptibility artifacts accompanying marrow hematomas and sclerotic metastasis[25,27]. This may necessitate marrow biopsy for histopathologic confirmation.

Diffusion-weighted imaging

Diffusion imaging addresses the free mobility of protons in a specific tissue[28]. This could be qualitative[29], *i.e.,* bull eying or quantitive[30] using the apparent diffusion coefficient (ADC). It is a sound fast sequence that can comprehend functional aspects of the examined tissues in addition to the available routine morphologic sequences. Normal marrow that is rich in protons will show free diffusion and high ADC values (*i.e.,* high signal intensity on both the diffusion image and ADC map)[31,32]. Contrarily, in metastatic lesions with densely packed cells and in cytotoxic edematous cells following trauma lower ADC values are seen (*i.e.,* high signal intensity on the diffusion image and low signal on ADC map)[31,32]. However, studies on the use of diffusion weighted imaging of the marrow are controversial and it should be interpreted in line with the routine marrow sequences[31,33].

Currently, common clinical musculoskeletal applications of diffusion weighted imaging of the spine are differencing osteoporotic fractures and neoplastic vertebral body collapse[34], differentiation of infective and degenerative sub-endplates changes[35] and follow-up treatment response of neoplastic marrow lesions[36].

Contrast-enhanced marrow imaging

Contrast enhancement is used to depict marrow lesions. The normal spinal marrow may show mild homogenous contrast enhancement in neonates and pediatrics due to abundant blood flow, prominent extravascular space and rich diverse cellularity[17,37]. This progressively become imperceptible as a function of age and increased fatty marrow content[38]. In normal adults spinal marrow doesn't show perceptible enhancement following administration of gadolinium based T1W agents[17,37,38].

Dynamic contrast studies of the spinal marrow had been used to diagnose and follow-up myelo-proli-

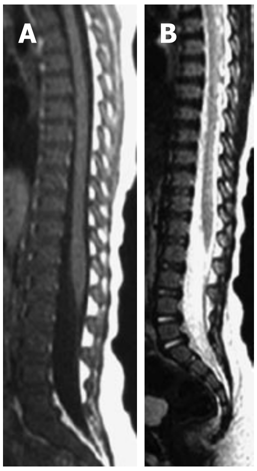

Figure 1 Sagittal T1W (A) and T2W (B) images of 2-year-old boy showing low-signal of the spinal marrow just barely brighter than intervertebral discs on T1W images due to richness in red marrow.

Figure 2 Sagittal T1W (A) and T2W (B) images of 25-year-old male showing linear high-signal of the normal fat marrow at the sub-endplate zones (white arrows) at LV2 through LV5 levels. Note also, linear focal fat depositions along the basi-vertebral veins posteriorly.

ferative disorders[39]. Following rapid IV gadolinium-based contrast agent administration, the changes in longitudinal relaxation of vertebral marrow are measured and signal time intensity curve is reproduced. Various parameters have been used like maximum intensity, slope of the curve and contrast washout[40]. Normal vertebral marrow shows decreased maximal enhancement, slope of enhancement and washout indices with increased age and fat marrow content[38,41]. However, dynamic contrast-enhanced studies have not been widely used in clinical practices.

Another less commonly used class of MR contrast agents affect the T2- or T2* imaging characteristics. Theses contrast agents, *e.g.*, ultra small particles iron oxides are engulfed by the hematopoietic cells of the normal bone marrow, produce local field inhomogeneities with resultant suppression of normal bone marrow[42]. This results in increased conspicuity of marrow lesion that will not take these agents. They are used to differentiate infiltrative marrow lesions from reactive marrow hyperplasia[43]. Also they can differentiate bone metastasis from infection[44].

Proton MR spectroscopy

MR spectroscopy is a non-invasive method of quantification of fat content of the marrow and evaluation of its chemical composition[45]. A single or multi-voxel method can used to asses one or more vertebral bodies and the fat content is expressed as a percentage (due to multiple lipid peaks) not an absolute value[46,47]. Previous reports emphasized age and sex related physiologic changes of the fat content of the spinal bone marrow[48,49].

However, it is not widely used clinically as same information could be achieved by the above used tools.

MRI appearance of the normal spinal bone marrow

As mentioned earlier, the bone marrow is a mix of red and yellow marrow supported by a trabecular marrow network. The trabecular marrow appears as a mesh of linear intermingled low signal intensities within both red and yellow marrow on all pulse sequences, especially prominent on the gradient recalled one. The trabecular marrow changes have little effects on the spinal marrow MR signal, if present.

Actually, the relative ratio of fat and water is the main determinant for the MR signal of spinal bone marrow as well as the used MR pulse sequence[1,4,5,9,13,50,51].

On T1W images, the vertebral fat marrow is high-signal intensity similar to subcutaneous fat in adults[2,5,6]. However, at birth all spinal marrow is of the red type with high water content resulting in low signal intensity of the vertebral bodies even relative to the intervertebral discs and muscles on T1W images (Figure 1)[14,52]. After that, gradual increased amount of fat cells, especially at the sub-endplates region and anterior part of the vertebral body (Figure 2), in the marrow results into the adulthood heterogenous vertebral marrow pattern (Figure 3)[52].

On T2W images, fatty marrow exhibits signal intensity near to that of the subcutaneous fat[2,6,10,17,18,53]. So use of fat suppression on fast/turbo spin echo T2 imaging is a must for better clinical utility of T2W sequence.

On fat-suppressed T2W and STIR images (Figure 3), the red marrow emits an intermediate signal slightly higher than adjacent paravertebral muscles against the black background of suppressed fatty marrow. However, it is far less intense compared to pathologic lesions with high cellular and water contents[10].

Following intravenous gadolinium-based contrast media administration, the red marrow; predominantly in children and young adolescents; shows appreciable visual enhancement and increased quantitive parameters on MR dynamic contrast studies inferring its abundant vascularity, well perfusion and increased metabolic activity. However, this SI increased has to be less than 35% by the age of 35 years[54]. On the other

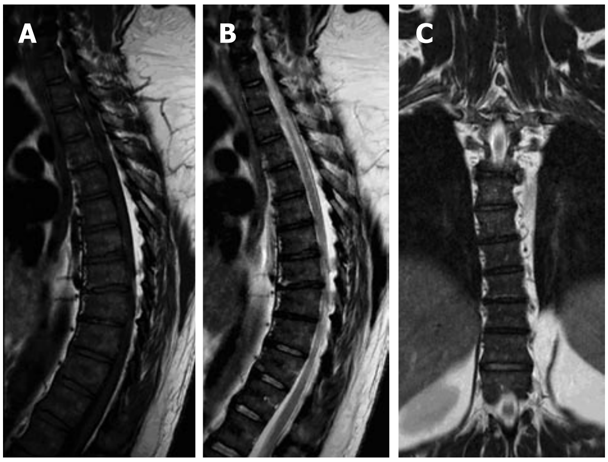

Figure 3 Sagittal T1W (A), T2W (B) and coronal STIR (C) images of the dorsal spines of a 60-year-old male with mild scoliotic deformity of the mid dorsal region. The figure shows heterogeneous vertebral marrow with predominantly T1W high-signal and T2W intermediate signal meanwhile, the whole marrow did not exhibit abnormal signal on STIR images. STIR: Short tau inversion recovery.

hand, this enhancement pattern is hardly perceptible in the fat marrow, in adults[37,38,55,56].

On chemical-shift imaging, the red marrow shows no remarkable signal drop on the out-phase image thanks to its near equal contents of both water and fat protons[57]. However, some signal drop may be seen in the yellow marrow (less than 20%) yet it is far less than malignant destructive processes[25].

On DWI, the normal red marrow shows intermediate signal that does not show lost signal on the corresponding ADC map.

Common variant of the normal spinal marrow on MR imaging

As bone marrow is a dynamic organ with the normal processeses of conversion and reconversion in response to various environmental and health stresses, and spines are the largest marrow reservoir of our body, heterogeneity of vertebral marrow MR signal is a common finding in daily clinical MR examinations. Additionally, this is more complicated by age- and sex-related variations as fat marrow is higher in men than women[49,58] and water content is higher in females child-bearing age[59].

In the same vertebral body of an adult, bone marrow is homogenously distributed with more abundance of the cellular red-marrow (50% of the spinal marrow by age of 70 years) near the endplates and anterior portion of the vertebral body while fat marrow is abundant around the basi-vertebral vein[2,60].

These spatial and sex-related changes are common between individuals of the same age group. However, it is important to recognize that these variations have to be homogenous between vertebral bodies of the same subject[54].

Spinal marrow heterogeneities' may be seen in all spinal regions but it is more common in the lumbar spines[1,6,9]. These changes could be in a focal or diffuse pattern, produced by either yellow or red marrow variant distributions[6,54,61,62].

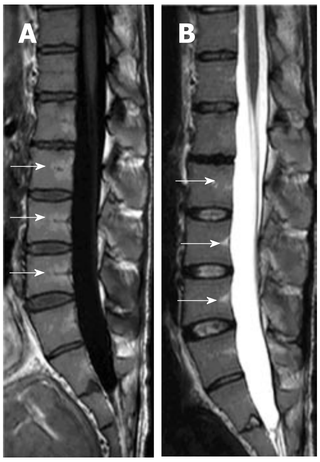

Figure 4 Sagittal T1W (A) and T2W (B) images of 24-year-old male showing linear high-signal intensities along the course of basi-vertebral veins with near ending of normal marrow conversion into the mature/fat type.

LOCALIZED NORMAL VARIANTS

Focal T1W hyper-intensities

Basi-vertebral vein fat: On T1W and T2W imaging, areas of focal fat deposition are commonly seen in the posterior elements of the vertebrae as well as areas of high vascularity with active processes of conversion and reconversion. This will include the sub-endplates and subcortical zones and around the basivertebral vein (Figure 4)[5,32,60].

Vertebral-end plate degenerative changes: Progressive degenerative changes of the vertebral endplates are not uncommon findings on spinal MR (Figure 5)[63]. Modic and colleagues described band-like sub-end plate marrow changes that exhibit water-like (low T1W and high T2W) MR signal for type-Ⅰ, fat-like (high T1W and T2W signals) for type-Ⅱ, and calcium-like (low T1W and T2W signals) for type-Ⅲ Modic changes[64]. Recognition of associated disc dehydration and presence of intra-discal gas precludes underling pathologies, *e.g.,* discitis.

Focal fatty marrow islands (Focal fatty metaplasia): A developmental variation of the bone marrow conversion process is the localized aggregates of areas of fat marrow. It can occur in any vertebral level yet it is a common variant in the lumbar spines (Figure 6) and lateral sacral ala of males than females; an area where sex-related marrow changes are important as age-related changes as proved by chemical-shift imaging and spectroscopic data[49,65]. It can take the eye of an inexperienced interpreter if seen in the turbo-spin echo

Figure 5 Sagittal T1W (A) and T2W (B) images of 53-year-old male showing LV4 lower end plate irregularities with subjacent Type-II Modic changes with high-T1W and T2W signal. Note adjacent LV4-5 disc desiccations.

T2W images. However, recognizing its high signal on T1W images and vanishing on fat-suppressed images will disclose its nature. Their corresponding radiographs and CT examinations will show preserved trabecular and cortical bone. They are not uncommon finding on daily spinal MR evaluations and should not raise clinical awkward.

HAEMANGIOMA

Histologically, hemangiomas are developmental vascular malformations consist of endothelial lined, thin-walled, blood-filled vessels and sinuses, containing and supported by fat and interspersed among the longitudinally oriented trabeculae of bones[66]. They are common in vertebral bodies than posterior elements. Hemangiomas are not exceedingly uncommon finding in MR studies of the spines. They are commonly asymptomatic and multiple. On T2W images as well as STIR images, typical hemangiomas have high-signal intensity due to slow flow in vascular channels[67]. Its benign nature is ascertained by corresponding high-signal intensity on T1W images due to its abundant fat content (Figure 7)[67]. Some atypical patterns of hemangioma may mimic more worrisome neoplastic lesions on MR imaging (Figure 8). Commonly, the intervening thickened trabeculae exhibits linear low-signal intensity on all pulse sequences[68]. Spinal hemangiomas shows variable patterns of enhancement and can be confused for serious bony lesions[69]. Radiography (Figure 8) and CT can help to solve such confusing situations by showing prominent trabeculae with the pathognomonic polka-dot sign (Figure 8) on axial images[70,71].

Focal T1W hypo-intensities

Vertebral enostosis*:* Enostosis (or bone island) is a common imaging finding on all imaging modalities assessing skeletal parts, especially the spine with an incidence of about 14%. It is thought as a benign osseous hamartoma of developmental origin[72]. It is composed of cortical bone layers embedded within the surrounding vertebral marrow cavity and it is usually endosteal surface based. It is common in the mid-dorsal and lumbar regions, although it can occur anywhere. It has low signal on all MR pulse sequences[72]. However, a previous report described a rare pattern of peripheral rim of high-signal intensity on STIR images making it difficult to differentiate from sclerotic metastasis[73]. However, correlation with radiography and CT will help to disclose the lesion’s nature.

Figure 6 Sagittal T1W (A) and T2W (B) images of 41-year-old female showing LV3 patch of high-signal intensity (unchanged on serial magnetic resonance follow-up; not shown) on both T1W and T2W with fuzzy margins, proved to focal fatty metaplasia. Note areas of low signal intensity under the anterior cortex of multiple adjacent vertebral bodies (short white arrows) corresponding to focal nodules of red marrow.

Focal nodular hyperplasia of the red marrow

Bone marrow hyperplasia is an abberance of normal marrow conversion-reconversion process with abundance of red marrow[74,75]. Mild regional forms can be seen in endurance athletes, obese subjects and heavy smokers[15,76]. A more pronounced form can show up in some hematologic disorders (*e.g.,* Hemolytic anemias) and malignancies as well as patients treated with granulocyte colony stimulating factors (GCSF) used to relive marrow suppression associated with chemotherapeutic regimens[77,78].

Rarely a localized focal form can be seen in the spinal (Figure 6) and pelvic marrow. On MR imaging these areas follow the signal criteria of normal red marrow, *i.e.,* low signal intensity on T1W images, intermediate or no signal increase on T2W, Fat-suppressed and STIR imaging. On gadolinium administration faint or no enhancement is observed. Sometimes, these focal lesions can show increased signal intensity on T2 FSE sequences. This is contradictory to high T2W signal and contrast enhancement seen in neoplastic cases[74,75,79].

Presences within areas rich in red marrow (subcortical and around basi-vertebral vein), elongated shape of the lesions, presence of central high-spot on T1W

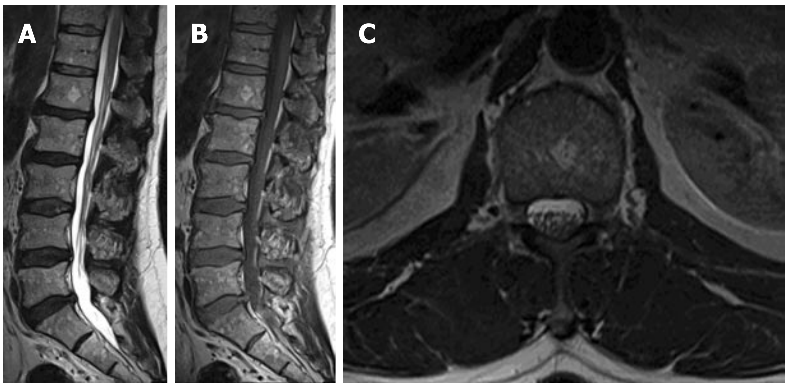

Figure 7 Sagittal T1W (A), T2W (B) and axial T2W images of 63-year-old osteoporotic female showing heterogeneous lumbar vertebral marrow signal with diffuse increased high-signal intensities due to higher fat content. There is a focal round patch of increased signal on both T1 and T2 weighting in LV1 body with small punctuate areas of low signal intensities; seen unchanged from previous 2 magnetic resonance examinations (not shown here) confirmed to be a small typical vertebral hemangioma.

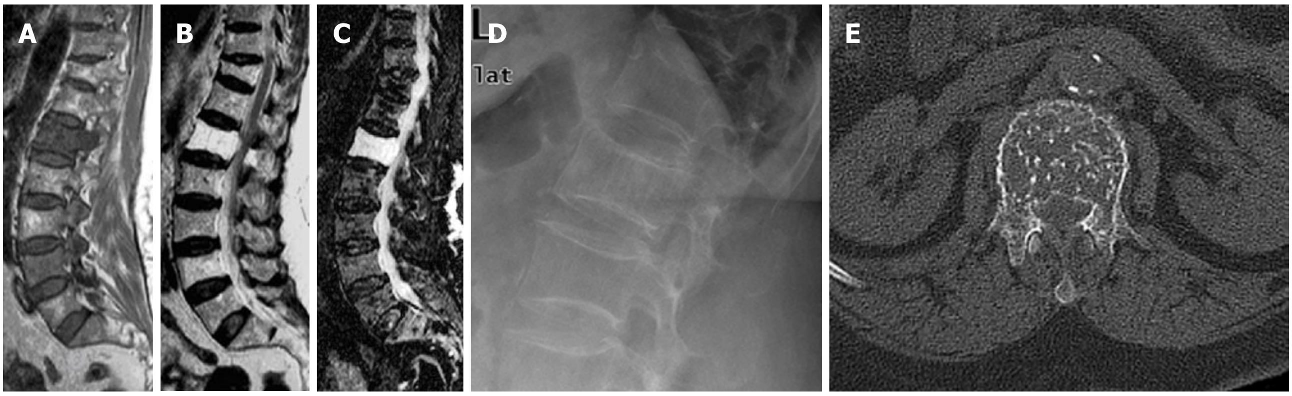

Figure 8 Sagittal T1W (A), T2W (B) and STIR (C) images of 65-year-old female showing L1 vertebral body atypical hemangioma with diffuse low signal intensity on T1W image and high-signal intensity on T2W and STIR images presented on a background of lumbar spondylotic changes. Note also, DV11 old porotic wedging. Companion imaging showed prominent trabecular pattern on focused radiography (D) and CT (E) of the LV1 with characteristic polka-dot sign. STIR: Short tau inversion recovery.

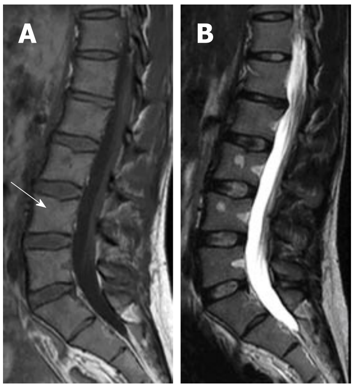

Figure 9 Sagittal T1W (A) and T2W (B) images of 33-year-old male showing focal geographic low signal intensity patches targeting LV3 and LV4 bodies centers as well as around basi-vertebral veins. These patches still of high-signal intensity on T2W image. Note, the central fat spot (white arrow) and fuzzy margins of LV4 lesion inferring benignity features are consistent with focal nodular marrow reconversion.

images (Figure 9), fuzzy margins are predictors of their benignity[1,3]. On corresponding radiographs and CT studies, radiolucency, geographic nature and absence of cortical disruption will ascertain their benign nature.

Benign notochordal cell tumors

Benign notochordal cell tumors are increasingly recognized intraosseous; presumably; benign lesions of notochordal remnants[80]. Its reported incidence in autopsies reaches 20% of clivus and vertebral bodies[81]. They are incidental finding on radiologic and histologic examinations and have to be distinguished from chordomas to save inadvertent extensive surgeries[82]. These lesions were found to emit homogenous low- to iso-signal intensity on T1W images and high-signal on T2W images with no enhancement on MR contrast studies[82,83]. Lesions that are sizable enough to be picked on CT and radiographs are sclerotic in nature. However, topographic features of the lesion, *i.e.*, intravertebral, preserved trabecular pattern and non-enhancement following MR contrast administration, are equally important to rule the possibility of chordoma; the extremely malignant spectrum of notchordal cell lineage[82,83]. A recent report described malignant, transformation into chordoma of L1 vertebral body supporting the postulation of a relation of the two entities[84]. MR imaging is the best modality to address and followup these lesions.

Diffuse normal variants

Diffuse hematopoietic marrow hyperplasia: Diffuse hematopoietic marrow hyperplasia is an exaggeration of the normal marrow reconversion discussed in an earlier section. It can occur in response to different physiologic stimuli as discussed before. Moreover, it is increasingly recognized in patients under chemo- and radio-therapeutic regimens whom are treated with GCSF to lessen the associated bone marrow suppression[85,86].

It can be confused with diffuse marrow infiltrative processes in the vertebral marrow thanks to both red and fat marrow cohabitation. As a rule of thumb, marrow hyperplasia exhibits a signal similar to that of red marrow. The vertebral hyperplastic marrow shows low signal on T1W images that may be even lower than adjacent intervertebral discs[1,6,13,14,87,88]. it may show mild to moderate enhancement following IV gadolinium administration[86]. However, the signal is relatively higher than paravertebral muscles on STIR and fat-saturated T2 imaging[1,6,13,14,87,88]. In chronic hemoglobinopathies, low signal may be seen on T2W images due to chronic hemosidine deposition[5]. Problem-solving MR sequences may be utilized in some difficult cases.

Fat conversion of the marrow

Under certain conditions, there may be premature conversion of red marrow into the fat type with increased MR signal compared to the age and sex matched subjects. This can be seen in subjects with hypercortisolism (whether endogenous or exogenous) and in some feeding disorders as anorexia nervosa[89]. This supposed to be mediated *via* hormonal effects on the preferential differentiation of bone marrow progenitor cells[90]. It has to be considered as a normal variation of the bone marrow for the health status of those subjects and not a pathologic marrow disease.

Serous conversion of the marrow

In conditions of severe systemic illness associated with loss body fat stores, *e.g.,* malignant cachexia, AIDS, anorexia nervosa or even following severe infections in pediatrics, a rare phenomenon of serous or gelatinous transformation of the bone marrow may commence in either diffuse or focal forms[91]. It starts in peripheral skelton yet it eventually reaches the axial skeleton. Pathologically; it is characterized by paucicellular marrow including both fat and hematopoietic cells which become embedded in hyaluronic acid-rich extracellular gelatinous substances[91,92]. These pathologic changes are recognized on MR as fat-poor marrow, which emits water-like signal on all pulse sequences, *i.e.*, low on T1W and high on T2W and STIR sequences[3,93]. Visual loss of normal fat stores of the subcutis and inter-tissues fascial spaces will raise this suspicion[93,94]. On 18FDG PET/CT it may show increased tracer uptake[95].

CONCLUSION

MR is the gold standard noninvasive imaging modality to evaluate vertebral bone marrow. Conventional sequences used basically to image marrow include T1W, fat-suppressed T2W and STIR imaging provides gross morphological data. Moreover, non-routine MR sequences may elucidate the nature of bone marrow heterogeneities; by inferring cellular and chemical composition; and adding new functional prospects. Awareness of the age-related bone marrow changes as well as changes accompanying different variations of the subject's health state is essential for radiologists. This will avoid overrating normal MR marrow patterns as pathologic states and avoid unnecessary further work-up.

ACKNOWLEDGMENTS

The authors would thank to Dr. Osamah Al Atyah, anesthesia and ICU Consultant, Hussein Al Ali Hospital, Al Ehsa, Saudi Arabia, for his critical linguistic revision of the final manuscript.

REFERENCES

1 **Alyas F**, Saifuddin A, Connell D. MR imaging evaluation of the bone marrow and marrow infiltrative disorders of the lumbar spine. *Magn Reson Imaging Clin N Am* 2007; **15**: 199-219, vi [PMID: 17599640]

2 **Murphy DT**, Moynagh MR, Eustace SJ, Kavanagh EC. Bone marrow. *Magn Reson Imaging Clin N Am* 2010; **18**: 727-735 [PMID: 21111977 DOI: 10.1016/j.mric.2010.07.003]

3 **Vande Berg BC**, Lecouvet FE, Michaux L, Ferrant A, Maldague B, Malghem J. Magnetic resonance imaging of the bone marrow in hematological malignancies. *Eur Radiol* 1998; **8**: 1335-1344 [PMID: 9853210 DOI: 10.1007/s003300050548]

4 **Strong PN**, Goerke J, Oberg SG, Kelly RB. beta-Bungarotoxin, a pre-synaptic toxin with enzymatic activity. *Proc Natl Acad Sci USA* 1976; **73**: 178-182 [PMID: 1749 DOI: 10.1007/s00256-007-0309-3]

5 **Tall MA**, Thompson AK, Vertinsky T, Palka PS. MR imaging of the spinal bone marrow. *Magn Reson Imaging Clin N Am* 2007; **15**: 175-198, vi [PMID: 17599639 DOI: 10.1016/j.mric.2007.01.001]

6 **Vande Berg BC**, Malghem J, Lecouvet FE, Maldague B. Magnetic resonance imaging of the normal bone marrow. *Skeletal Radiol* 1998; **27**: 471-483 [PMID: 9809875]

7 **Riley RS**, Williams D, Ross M, Zhao S, Chesney A, Clark BD, Ben-Ezra JM. Bone marrow aspirate and biopsy: a pathologist's perspective. II. interpretation of the bone marrow aspirate and biopsy. *J Clin Lab Anal* 2009; **23**: 259-307 [PMID: 19774631 DOI: 10.1002/jcla.20305]

8 **Vande Berg BC**, Malghem J, Lecouvet FE, Maldague B. Normal bone marrow: dynamic aspects in magnetic resonance imaging. *J Radiol* 2001; **82**: 127-135 [PMID: 11428207]

9 **Vande Berg BC**, Lecouvet FE, Galant C, Simoni P, Malghem J. Normal variants of the bone marrow at MR imaging of the spine. *Semin Musculoskelet Radiol* 2009; **13**: 87-96 [PMID: 19455471 DOI: 10.1055/s-0029-1220879]

10 **Shah LM**, Hanrahan CJ. MRI of spinal bone marrow: part I, techniques and normal age-related appearances. *AJR Am J Roentgenol* 2011; **197**: 1298-1308 [PMID: 22109283 DOI: 10.2214/AJR.11.7005]

11 **Kricun ME**. Red-yellow marrow conversion: its effect on the location of some solitary bone lesions. *Skeletal Radiol* 1985; **14**: 10-19 [PMID: 3895447]

12 **Rosen CJ**, Ackert-Bicknell C, Rodriguez JP, Pino AM. Marrow fat

and the bone microenvironment: developmental, functional, and pathological implications. *Crit Rev Eukaryot Gene Expr* 2009; **19**: 108-124 [DOI: 10.1615/CritRevEukarGeneExpr.v19.i2.20]

13 **Małkiewicz A**, Dziedzic M. Bone marrow reconversion - imaging of physiological changes in bone marrow. *Pol J Radiol* 2012; **77**: 45-50 [PMID: 23269936]

14 **Guillerman RP**. Marrow: red, yellow and bad. *Pediatr Radiol* 2013; **43** Suppl 1: S181-S192 [PMID: 23478934 DOI: 10.1007/s00247-012-2582-0]

15 **Poulton TB**, Murphy WD, Duerk JL, Chapek CC, Feiglin DH. Bone marrow reconversion in adults who are smokers: MR Imaging findings. *AJR Am J Roentgenol* 1993; **161**: 1217-1221 [PMID: 8249729]

16 **Carroll KW**, Feller JF, Tirman PF. Useful internal standards for distinguishing infiltrative marrow pathology from hematopoietic marrow at MRI. *J Magn Reson Imaging* 1997; **7**: 394-398 [PMID: 9090597]

17 **Vogler JB**, Murphy WA. Bone marrow imaging. *Radiology* 1988; **168**: 679-693 [PMID: 3043546]

18 **Long SS**, Yablon CM, Eisenberg RL. Bone marrow signal alteration in the spine and sacrum. *AJR Am J Roentgenol* 2010; **195**: W178-W200 [PMID: 20729415 DOI: 10.2214/AJR.09.4134]

19 **Levine CD**, Schweitzer ME, Ehrlich SM. Pelvic marrow in adults. *Skeletal Radiol* 1994; **23**: 343-347 [PMID: 7939832]

20 **Silva JR**, Hayashi D, Yonenaga T, Fukuda K, Genant HK, Lin C. MRI of bone marrow abnormalities in hematological malignancies. *Diagn Interv Radiol Ank Turk* 2013; **19**: 393-3999 [DOI: 10.5152/dir.2013.067]

21 **Mirowitz SA**, Apicella P, Reinus WR, Hammerman AM. MR imaging of bone marrow lesions: relative conspicuousness on T1-weighted, fat-suppressed T2-weighted, and STIR images. *AJR Am J Roentgenol* 1994; **162**: 215–221 [DOI: 10.2214/ajr.162.1.8273669]

22 **Bydder GM**, Steiner RE, Blumgart LH, Khenia S, Young IR. MR imaging of the liver using short TI inversion recovery sequences. *J Comput Assist Tomogr* 1985; **9**: 1084-1089 [PMID: 4056142]

23 **Disler DG**, McCauley TR, Ratner LM, Kesack CD, Cooper JA. In-phase and out-of-phase MR imaging of bone marrow: prediction of neoplasia based on the detection of coexistent fat and water. *AJR Am J Roentgenol* 1997; **169**: 1439-1447 [DOI: 10.2214/ajr.169.5.9353477]

24 **Zajick DC**, Morrison WB, Schweitzer ME, Parellada JA, Carrino JA. Benign and malignant processes: normal values and differentiation with chemical shift MR imaging in vertebral marrow. *Radiology* 2005; **237**: 590-596 [PMID: 16244268 DOI: 10.1148/radiol.2372040990]

25 **Erly WK**, Oh ES, Outwater EK. The utility of in-phase/opposed-phase imaging in differentiating malignancy from acute benign compression fractures of the spine. *AJNR Am J Neuroradiol* 2006; **27**: 1183-1188 [PMID: 16775260]

26 **Ragab Y**, Emad Y, Gheita T, Mansour M, Abou-Zeid A, Ferrari S, Rasker JJ. Differentiation of osteoporotic and neoplastic vertebral fractures by chemical shift {in-phase and out-of phase} MR imaging. *Eur J Radiol* 2009; **72**: 125-133 [PMID: 18672340 DOI: 10.1016/j.ejrad.2008.06.019]

27 **Swartz PG**, Roberts CC. Radiological reasoning: bone marrow changes on MRI. *AJR Am J Roentgenol* 2009; **193**: S1-4, Quiz S5-9 [PMID: 19696238 DOI: 10.2214/AJR.09.7069]

28 **Dietrich O**, Biffar A, Reiser MF, Baur-Melnyk A. Diffusion-weighted imaging of bone marrow. *Semin Musculoskelet Radiol* 2009; **13**: 134-144 [PMID: 19455476 DOI: 10.1055/s-0029-1220884]

29 **Lichy MP**, Aschoff P, Plathow C, Stemmer A, Horger W, Mueller-Horvat C, Steidle G, Horger M, Schafer J, Eschmann SM, Kiefer B, Claussen CD, Pfannenberg C, Schlemmer HP. Tumor detection by diffusion-weighted MRI and ADC-mapping--initial clinical experiences in comparison to PET-CT. *Invest Radiol* 2007; **42**: 605-613 [PMID: 17700275 DOI: 10.1097/RLI.0b013e31804ffd49]

30 **Costa FM**, Ferreira EC, Vianna EM. Diffusion-weighted magnetic resonance imaging for the evaluation of musculoskeletal tumors. *Magn Reson Imaging Clin N Am* 2011; **19**: 159-180 [PMID: 21129640 DOI: 10.1016/j.mric.2010.10.007]

31 **Baur A**, Huber A, Dürr HR, Nikolaou K, Stäbler A, Deimling M, Reiser M. Differentiation of benign osteoporotic and neoplastic vertebral compression fractures with a diffusion-weighted, steady-state free precession sequence. *Rofo* 2002; **174**: 70-75 [PMID: 11793288 DOI: 10.1055/s-2002-19534]

32 **Biffar A**, Baur-Melnyk A, Schmidt GP, Reiser MF, Dietrich O. Multiparameter MRI assessment of normal-appearing and diseased vertebral bone marrow. *Eur Radiol* 2010; **20**: 2679-2689 [DOI: 10.1016/j.ejrad.2010.03.011]

33 **Castillo M**, Arbelaez A, Smith JK, Fisher LL. Diffusion-weighted MR imaging offers no advantage over routine noncontrast MR imaging in the detection of vertebral metastases. *AJNR Am J Neuroradiol* 2000; **21**: 948-953 [PMID: 10815675]

34 **Karchevsky M**, Babb JS, Schweitzer ME. Can diffusion-weighted imaging be used to differentiate benign from pathologic fractures? A meta-analysis. *Skeletal Radiol* 2008; **37**: 791-795 [PMID: 18551290 DOI: 10.1007/s00256-008-0503-y]

35 **Eguchi Y**, Ohtori S, Yamashita M, Yamauchi K, Suzuki M, Orita S, Kamoda H, Arai G, Ishikawa T, Miyagi M, Ochiai N, Kishida S, Masuda Y, Ochi S, Kikawa T, Takaso M, Aoki Y, Inoue G, Toyone T, Takahashi K. Diffusion magnetic resonance imaging to differentiate degenerative from infectious endplate abnormalities in the lumbar spine. *Spine* (Phila Pa 1976) 2011; **36**: E198-E202 [PMID: 21099738 DOI: 10.1097/BRS.0b013e3181d5ff05]

36 **Padhani AR**, Koh DM, Collins DJ. Whole-body diffusion-weighted MR imaging in cancer: current status and research directions. *Radiology* 2011; **261**: 700-718 [PMID: 22095994 DOI: 10.1148/radiol.11110474]

37 **Baur A**, Stäbler A, Bartl R, Lamerz R, Scheidler J, Reiser M. MRI gadolinium enhancement of bone marrow: age-related changes in normals and in diffuse neoplastic infiltration. *Skeletal Radiol* 1997; **26**: 414-418 [PMID: 9259099]

38 **Montazel JL**, Divine M, Lepage E, Kobeiter H, Breil S, Rahmouni A. Normal Spinal Bone Marrow in Adults: Dynamic Gadolinium-enhanced MR Imaging1. *Radiol* 2003; **229**: 703-709 [DOI: 10.1148/radiol.2293020747]

39 **Rahmouni A**, Montazel JL, Divine M, Lepage E, Belhadj K, Gaulard P, Bouanane M, Golli M, Kobeiter H. Bone marrow with diffuse tumor infiltration in patients with lymphoproliferative diseases: dynamic gadolinium-enhanced MR imaging. *Radiology* 2003; **229**: 710-717 [PMID: 14593191 DOI: 10.1148/radiol.2293020748]

40 **Erlemann R**, Reiser M, Peters PE, Wuisman P, Niendorf HP, Kunze V. Time-dependent changes in signal intensity in neoplastic and inflammatory lesions of the musculoskeletal system following intravenous administration of Gd-DTPA. *Radiologe* 1988; **28**: 269-276 [PMID: 3399673]

41 **Griffith JF**, Yeung DK, Antonio GE, Lee FK, Hong AW, Wong SY, Lau EM, Leung PC. Vertebral bone mineral density, marrow perfusion, and fat content in healthy men and men with osteoporosis: dynamic contrast-enhanced MR imaging and MR spectroscopy. *Radiology* 2005; **236**: 945-951 [PMID: 16055699 DOI: 10.1148/radiol.2363041425]

42 **Simon GH**, Raatschen HJ, Wendland MF, von Vopelius-Feldt J, Fu Y, Chen MH, Daldrup-Link HE. Ultrasmall superparamagnetic iron-oxide-enhanced MR imaging of normal bone marrow in rodents: original research original research. *Acad Radiol* 2005; **12**: 1190-1197 [PMID: 16099684 DOI: 10.1016/j.acra.2005.05.014]

43 **Daldrup-Link HE**, Rummeny EJ, Ihssen B, Kienast J, Link TM. Iron-oxide-enhanced MR imaging of bone marrow in patients with non-Hodgkin's lymphoma: differentiation between tumor infiltration and hypercellular bone marrow. *Eur Radiol* 2002; **12**: 1557-1566 [PMID: 12042968 DOI: 10.1007/s00330-001-1270-5]

44 **Fukuda Y**, Ando K, Ishikura R, Kotoura N, Tsuda N, Kato N, Yoshiya S, Nakao N. Superparamagnetic iron oxide (SPIO) MRI contrast agent for bone marrow imaging: differentiating bone metastasis and osteomyelitis. *Magn Reson Med Sci* 2006; **5**: 191-196 [PMID: 17332709]

45 **Hu HH**, Kan HE. Quantitative proton MR techniques for measuring

fat. *NMR Biomed* 2013; **26**: 1609-1629 [PMID: 24123229 DOI: 10.1002/nbm.3025]

46 **Li X**, Kuo D, Schafer AL, Porzig A, Link TM, Black D, Schwartz AV. Quantification of vertebral bone marrow fat content using 3 Tesla MR spectroscopy: reproducibility, vertebral variation, and applications in osteoporosis. *J Magn Reson Imaging* 2011; **33**: 974-979 [PMID: 21448966 DOI: 10.1002/nbm.3025]

47 **Schwartz AV**, Sigurdsson S, Hue TF, Lang TF, Harris TB, Rosen CJ, Vittinghoff E, Siggeirsdottir K, Sigurdsson G, Oskarsdottir D, Shet K, Palermo L, Gudnason V, Li X. Vertebral bone marrow fat associated with lower trabecular BMD and prevalent vertebral fracture in older adults. *J Clin Endocrinol Metab* 2013; **98**: 2294-2300 [PMID: 23553860 DOI: 10.1210/jc.2012-3949]

48 **Jung CM**, Kugel H, Schulte O, Heindel W. [Proton-MR spectroscopy of the spinal bone marrow. An analysis of physiological signal behavior]. *Radiologe* 2000; **40**: 694-699 [PMID: 11006939]

49 **Kugel H**, Jung C, Schulte O, Heindel W. Age- and sex-specific differences in the 1H-spectrum of vertebral bone marrow. *J Magn Reson Imaging* 2001; **13**: 263-268 [PMID: 11169833]

50 **Panicek DM**, Schwartz LH. MR Imaging of Bone Marrow in Patients with Musculoskeletal Tumors. *Sarcoma* 1999; **3**: 37-41 [PMID: 18521263]

51 **Vanel D**, Dromain C, Tardivon A. MRI of bone marrow disorders. *Eur Radiol* 2000; **10**: 224-229 [PMID: 10663751]

52 **Foster K**, Chapman S, Johnson K. MRI of the marrow in the paediatric skeleton. *Clin Radiol* 2004; **59**: 651-673 [PMID: 15262540 DOI: 10.1016/j.crad.2004.02.001]

53 **Hilfiker P**, Zanetti M, Debatin JF, McKinnon G, Hodler J. Fast spin-echo inversion-recovery imaging versus fast T2-weighted spin-echo imaging in bone marrow abnormalities. *Invest Radiol* 1995; **30**: 110-114 [PMID: 7654279]

54 **Vande Berg BC**, Lecouvet FE, Galant C, Maldague BE, Malghem J. Normal variants and frequent marrow alterations that simulate bone marrow lesions at MR imaging. *Radiol Clin North Am* 2005; **43**: 761-770, ix [PMID: 15893536 DOI: 10.1016/j.rcl.2005.01.007]

55 **Bollow M**, Knauf W, Korfel A, Taupitz M, Schilling A, Wolf KJ, Hamm B. Initial experience with dynamic MR imaging in evaluation of normal bone marrow versus malignant bone marrow infiltrations in humans. *J Magn Reson Imaging* 1997; **7**: 241-250 [PMID: 9039623]

56 **Biffar A**, Dietrich O, Sourbron S, Duerr HR, Reiser MF, Baur-Melnyk A. Diffusion and perfusion imaging of bone marrow. *Eur J Radiol* 2010; **76**: 323-328 [PMID: 20381277 DOI: 10.1016/j.ejrad.2010.03.011]

57 **Blebea JS**, Houseni M, Torigian DA, Fan C, Mavi A, Zhuge Y, Iwanaga T, Mishra S, Udupa J, Zhuang J, Gopal R, Alavi A. Structural and functional imaging of normal bone marrow and evaluation of its age-related changes. *Semin Nucl Med* 2007; **37**: 185-194 [PMID: 17418151 DOI: 10.1053/j.semnuclmed.2007.01.002]

58 **Mitchell DG**, Rao VM, Dalinka M, Spritzer CE, Axel L, Gefter W, Kricun M, Steinberg ME, Kressel HY. Hematopoietic and fatty bone marrow distribution in the normal and ischemic hip: new observations with 1.5-T MR imaging. *Radiology* 1986; **161**: 199-202 [PMID: 3763867 DOI: 10.1148/radiology.161.1.3763867]

59 **Ishijima H**, Ishizaka H, Horikoshi H, Sakurai M. Water fraction of lumbar vertebral bone marrow estimated from chemical shift misregistration on MR imaging: normal variations with age and sex. *AJR Am J Roentgenol* 1996; **167**: 355-358 [PMID: 8686603 DOI: 10.2214/ajr.167.2.8686603]

60 **Ricci C**, Cova M, Kang YS, Yang A, Rahmouni A, Scott WW, Zerhouni EA. Normal age-related patterns of cellular and fatty bone marrow distribution in the axial skeleton: MR imaging study. *Radiology* 1990; **177**: 83-88 [PMID: 2399343 DOI: 10.1148/radiology.177.1.2399343]

61 **Hajek PC**, Baker LL, Goobar JE, Sartoris DJ, Hesselink JR, Haghighi P, Resnick D. Focal fat deposition in axial bone marrow: MR characteristics. *Radiology* 1987; **162**: 245-249 [PMID: 3786770 DOI: 10.1148/radiology.162.1.3786770S]

62 **Baur A**, Dietrich O, Reiser M. Diffusion-weighted imaging of bone marrow: current status. *Eur Radiol* 2003; **13**: 1699-1708 [PMID: 12759770 DOI: 10.1007/s00330-003-1873-0]

63 **Kuisma M**, Karppinen J, Niinimäki J, Kurunlahti M, Haapea M, Vanharanta H, Tervonen O. A three-year follow-up of lumbar spine endplate (Modic) changes. *Spine* (Phila Pa 1976) 2006; **31**: 1714-1718 [PMID: 16816768 DOI: 10.1097/01.brs.0000224167.18483.14]

64 **Modic MT**, Steinberg PM, Ross JS, Masaryk TJ, Carter JR. Degenerative disk disease: assessment of changes in vertebral body marrow with MR imaging. *Radiology* 1988; **166**: 193-199 [PMID: 3336678 DOI: 10.1148/radiology.166.1.3336678]

65 **Duda SH**, Laniado M, Schick F, Strayle M, Claussen CD. Normal bone marrow in the sacrum of young adults: differences between the sexes seen on chemical-shift MR imaging. *AJR Am J Roentgenol* 1995; **164**: 935-940 [PMID: 7726052 DOI: 10.2214/ajr.164.4.7726052]

66 **Hart JL**, Edgar MA, Gardner JM. Vascular tumors of bone. *Semin Diagn Pathol* 2014; **31**: 30-38 [PMID: 24680180 DOI: 10.1053/j.semdp.2014.01.003]

67 **Baudrez V**, Galant C, Vande Berg BC. Benign vertebral hemangioma: MR-histological correlation. *Skeletal Radiol* 2001; **30**: 442-446 [PMID: 11479749 DOI: 10.1007/s0025610300442]

68 **Ross JS**, Masaryk TJ, Modic MT, Carter JR, Mapstone T, Dengel FH. Vertebral hemangiomas: MR imaging. *Radiology* 1987; **165**: 165-169 [PMID: 3628764 DOI: 10.1148/radiology.165.1.3628764]

69 **Rodallec MH**, Feydy A, Larousserie F, Anract P, Campagna R, Babinet A, Zins M, Drapé JL. Diagnostic imaging of solitary tumors of the spine: what to do and say. *Radiographics* 2008; **28**: 1019-1041 [PMID: 18635627 DOI: 10.1148/rg.284075156]

70 **Laredo JD**, Reizine D, Bard M, Merland JJ. Vertebral hemangiomas: radiologic evaluation. *Radiology* 1986; **161**: 183-189 [PMID: 3763864 DOI: 10.1148/radiology.161.1.3763864]

71 **Persaud T**. The polka-dot sign. *Radiology* 2008; **246**: 980-981 [PMID: 18309021 DOI: 10.1148/radiol.2463050903]

72 **Murphey MD**, Andrews CL, Flemming DJ, Temple HT, Smith WS, Smirniotopoulos JG. From the archives of the AFIP. Primary tumors of the spine: radiologic pathologic correlation. *Radiographics* 1996; **16**: 1131-1158 [PMID: 8888395 DOI: 10.1148/radiographics.16.5.8888395]

73 Proceedings of UK Radiological Congress 1997. The British Institute of Radiology, 1997; 150. Available from: URL: http://www.birpublications.org/doi/abs/10.1259/conf-pukrc.1997 [DOI: 10.1259/conf-pukrc.1997]

74 **Bordalo-Rodrigues M**, Galant C, Lonneux M, Clause D, Vande Berg BC. Focal nodular hyperplasia of the hematopoietic marrow simulating vertebral metastasis on FDG positron emission tomography. *AJR Am J Roentgenol* 2003; **180**: 669-671 [PMID: 12591672 DOI: 10.2214/ajr.180.3.1800669]

75 **Detti B**. A Case of Focal Haematopoietic Hyperplasia of a Vertebral Body and Review of the Modern Literature. *J Nucl Med Radiat Ther* 2013; **4**: In press [DOI: 10.4172/2155-9619.1000151]

76 **Deutsch AL**, Mink JH, Rosenfelt FP, Waxman AD. Incidental detection of hematopoietic hyperplasia on routine knee MR imaging. *AJR Am J Roentgenol* 1989; **152**: 333-336 [PMID: 2783510 DOI: 10.2214/ajr.152.2.333]

77 **Hollinger EF**, Alibazoglu H, Ali A, Green A, Lamonica G. Hematopoietic cytokine-mediated FDG uptake simulates the appearance of diffuse metastatic disease on whole-body PET imaging. *Clin Nucl Med* 1998; **23**: 93-98 [PMID: 9481497 DOI: 10.1097/00003072-199802000-00007]

78 **Stäbler A**, Doma AB, Baur A, Krüger A, Reiser MF. Reactive bone marrow changes in infectious spondylitis: quantitative assessment with MR imaging. *Radiology* 2000; **217**: 863-868 [PMID: 11110955 DOI: 10.1148/radiology.217.3.r00dc23863]

79 **Steiner RM**, Mitchell DG, Rao VM, Schweitzer ME. Magnetic resonance imaging of diffuse bone marrow disease. *Radiol Clin North Am* 1993; **31**: 383-409 [PMID: 8446756]

80 **Amer HZ**, Hameed M. Intraosseous benign notochordal cell tumor. *Arch Pathol Lab Med* 2010; **134**: 283-288 [PMID: 20121620 DOI: 10.1043/1543-2165-134.2.283]

81 **Yamaguchi T**, Suzuki S, Ishiiwa H, Shimizu K, Ueda Y. Benign notochordal cell tumors: A comparative histological study of benign

notochordal cell tumors, classic chordomas, and notochordal vestiges of fetal intervertebral discs. *Am J Surg Pathol* 2004; **28**: 756-761 [PMID: 15166667]

82 **Yamaguchi T**, Iwata J, Sugihara S, McCarthy EF, Karita M, Murakami H, Kawahara N, Tsuchiya H, Tomita K. Distinguishing benign notochordal cell tumors from vertebral chordoma. *Skeletal Radiol* 2008; **37**: 291-299 [PMID: 18188556 DOI: 10.1007/s00256-007-0435-y]

83 **Nishiguchi T**, Mochizuki K, Ohsawa M, Inoue T, Kageyama K, Suzuki A, Takami T, Miki Y. Differentiating benign notochordal cell tumors from chordomas: radiographic features on MRI, CT, and tomography. *AJR Am J Roentgenol* 2011; **196**: 644-650 [PMID: 21343509 DOI: 10.2214/AJR.10.4460]

84 **Nishiguchi T**, Mochizuki K, Tsujio T, Nishita T, Inoue Y. Lumbar vertebral chordoma arising from an intraosseous benign notochordal cell tumour: radiological findings and histopathological description with a good clinical outcome. *Br J Radiol* 2010; **83**: e49-e53 [PMID: 20197427 DOI: 10.1259/bjr/63846600]

85 **Altehoefer C**, Bertz H, Ghanem NA, Langer M. Extent and time course of morphological changes of bone marrow induced by granulocyte-colony stimulating factor as assessed by magnetic resonance imaging of healthy blood stem cell donors. *J Magn Reson Imaging* 2001; **14**: 141-146 [PMID: 11477672]

86 **Ciray I**, Lindman H, Aström GK, Wanders A, Bergh J, Ahlström HK. Effect of granulocyte colony-stimulating factor (G-CSF)-supported chemotherapy on MR imaging of normal red bone marrow in breast cancer patients with focal bone metastases. *Acta Radiol* 2003; **44**: 472-484 [PMID: 14510752]

87 **Caldemeyer KS**, Smith RR, Harris A, Williams T, Huang Y, Eckert GJ, Slemenda CW. Hematopoietic bone marrow hyperplasia: correlation of spinal MR findings, hematologic parameters, and bone mineral density in endurance athletes. *Radiology* 1996; **198**: 503-508 [PMID: 8596857 DOI: 10.1148/radiology.198.2.8596857]

88 **Hanrahan CJ**, Shah LM. MRI of spinal bone marrow: part 2, T1-weighted imaging-based differential diagnosis. *AJR Am J Roentgenol* 2011; **197**: 1309-1321 [PMID: 22109284 DOI: 10.2214/AJR.11.7420]

89 **Geiser F**, Mürtz P, Lutterbey G, Träber F, Block W, Imbierowicz K, Schilling G, Schild H, Liedtke R. Magnetic resonance spectroscopic and relaxometric determination of bone marrow changes in anorexia nervosa. *Psychosom Med* 2001; **63**: 631-637 [PMID: 11485117 DOI: 10.1097/00006842-200107000-00016]

90 **Gimble JM**, Zvonic S, Floyd ZE, Kassem M, Nuttall ME. Playing with bone and fat. *J Cell Biochem* 2006; **98**: 251-266 [PMID: 16479589 DOI: 10.1002/jcb.20777]

91 **Jain R**, Singh ZN, Khurana N, Singh T. Gelatinous transformation of bone marrow: a study of 43 cases. *Indian J Pathol Microbiol* 2005; **48**: 1-3 [PMID: 16758772]

92 **Ecklund K**, Vajapeyam S, Feldman HA, Buzney CD, Mulkern RV, Kleinman PK. Bone marrow changes in adolescent girls with anorexia nervosa. *J Bone Miner Res* 2010; **25**: 298-304 [DOI: 10.1359/jbmr.090805]

93 **García AI**, Milinkovic A, Tomás X, Rios J, Pérez I, Vidal-Sicart S, Pomés J, Del Amo M, Mallolas J. MRI signal changes of the bone marrow in HIV-infected patients with lipodystrophy: correlation with clinical parameters. *Skeletal Radiol* 2011; **40**: 1295-1301 [PMID: 21479859 DOI: 10.1007/s00256-011-1147-x]

94 **Tins B**, Cassar-Pullicino V. Marrow changes in anorexia nervosa masking the presence of stress fractures on MR imaging. *Skeletal Radiol* 2006; **35**: 857-860 [DOI: 10.1007/s00256-005-0053-5]

95 **Chong A**, Song HC, Oh JR, Ha JM, Min JJ, Bom HS, Choi YD, Lee JS. Gelatinous degeneration of the bone marrow mimicking osseous metastasis on 18F-FDG PET/CT. *Clin Nucl Med* 2012; **37**: 798-800 [PMID: 22785516 DOI: 10.1097/RLU.0b013e31825ae455]

P- Reviewer: Anil G, Gao BL, Shen J, Sureka B **S- Editor**: Qiu S
L- Editor: A **E- Editor**: Wu HL

WJR World Journal of Radiology

Submit a Manuscript: http://www.wjgnet.com/esps/
Help Desk: http://www.wjgnet.com/esps/helpdesk.aspx
DOI: 10.4329/wjr.v7.i12.459

World J Radiol 2015 December 28; 7(12): 459-474
ISSN 1949-8470 (online)

REVIEW

Multi-detector computed tomography imaging of large airway pathology: A pictorial review

Tejeshwar Singh Jugpal, Anju Garg, Gulshan Rai Sethi, Mradul Kumar Daga, Jyoti Kumar

Tejeshwar Singh Jugpal, Anju Garg, Jyoti Kumar, Department of Radiodiagnosis, Maulana Azad Medical College and associated Lok Nayak Hospital, New Delhi 110002, India

Gulshan Rai Sethi, Department of Pediatrics, Maulana Azad Medical College and associated Lok Nayak Hospital, New Delhi 110002, India

Mradul Kumar Daga, Department of Medicine, Maulana Azad Medical College and associated Lok Nayak Hospital, New Delhi 110002, India

Author contributions: Jugpal TS substantially contributed towards the conception of study and drafting the article; Garg A and Kumar J analysed the data and critically revised to assess intellectual content in the article; Sethi GR and Daga MK contributed data for study.

Conflict-of-interest statement: Authors declare no conflict of interests for this article.

Correspondence to: **Jyoti Kumar, MD, Professor,** Department of Radiodiagnosis, Maulana Azad Medical College and associated Lok Nayak Hospital, New Delhi 110002, India. drjyotikumar@gmail.com
Telephone: +91-99-68604361

Received: May 24, 2015
Peer-review started: May 25, 2015
First decision: August 3, 2015
Revised: October 23, 2015
Accepted: November 13, 2015
Article in press: November 17, 2015
Published online: December 28, 2015

Abstract

The tracheobronchial tree is a musculo-cartilagenous framework which acts as a conduit to aerate the lungs and consequently the entire body. A large spectrum of pathological conditions can involve the trachea and bronchial airways. These may be congenital anomalies, infections, post-intubation airway injuries, foreign body aspiration or neoplasms involving the airway. Appropriate management of airway disease requires an early and accurate diagnosis. In this pictorial essay review, we will comprehensively describe the various airway pathologies and their imaging findings by multi-detector computed tomography.

Key words: Multi detector computed tomography; Trachea; Bronchial tree; Airway abnormality; Virtual bronchoscopy

Core tip: There is a wide range of lesions affecting the airway and patients with airway pathology usually present late during the course of disease. Multi-detector computed tomography (MDCT) has become the mainstay investigation modality as it provides detailed information about the airway and its surrounding structures with high spatial resolution. Therefore it is prudent to know the various pathology affecting airway and its appearance on MDCT.

Jugpal TS, Garg A, Sethi GR, Daga MK, Kumar J. Multi-detector computed tomography imaging of large airway pathology: A pictorial review. *World J Radiol* 2015; 7(12): 459-474 Available from: URL: http://www.wjgnet.com/1949-8470/full/v7/i12/459.htm DOI: http://dx.doi.org/10.4329/wjr.v7.i12.459

INTRODUCTION

The introduction of multi-detector computed tomography (MDCT) technology over the past decade has tremendously revolutionized imaging of airway[1,2]. Modern MDCT scanners have markedly increased the speed of data collection and cranio-caudal volume coverage enabling them to acquire thin-section, high spatial resolution images of the entire airway. These scanners can reconstruct images of varying slice thickness and in multiple planes from the acquired axial images[3-5].

The advancements in computer technology aid in processing the data sets acquired by the MDCT scanners to reconstruct the bronchial tree in three dimensions[6]. The developed computer software generates 3D view of the airway which provides clinically acceptable information with real time visualization of the entire tracheobronchial airway.

IMAGING TECHNIQUE

Thin slice axial images are acquired in a single breath hold. The imaging protocol that is used in our department for adults includes a tube voltage of 120 kV, tube current of 300 mA, 0.6 mm × 128 slices, a pitch of 1.5 with a matrix size of 512 × 512. For children, the tube voltage is reduced to 80 kV and tube current is altered to 110 mA.

Administration of contrast is generally not required for assessment of airway. However it is used in suspected cases of extraluminal compressive lesions to delineate the various mediastinal vascular structures and for suspected neoplastic etiology. Non-ionic iodinated contrast medium may be given using a dose of 1 mL/kg for adults and 1.5 mL/kg for children through peripheral venous access route.

Image reconstruction

The cross-sectional images are then transferred to a separate graphic computer. Reconstruction is done using standard visualization software. The acquired near isotropic data is used to generate multiplanar reformations (MPRs), minimum intensity projections (MinIPs) and volume rendered images for 3D reconstruction.

Two basic methods of 3D imaging are currently employed in airway reconstruction including external rendering and internal rendering. The external rendering of the airway shows its external surface and is also called computed tomography (CT) tracheobronchography. Internal rendering or virtual bronchoscopy (VB) allows navigation through the internal airway lumen of airway using the “fly through” virtual endoscopy CT software. The airway reconstructed by VB closely resemble those seen on conventional bronchoscopy[7-9]. However, VB can evaluate the airway distal to a high grade stenosis which is not possible on fiberoptic bronchoscopy.

NORMAL ANATOMY

Trachea

Trachea is a tubular structure extending from the level of the cricoid cartilage (6th cervical vertebral level) to the carina (5th thoracic vertebral level). Trachea is made up of multiple C shaped cartilages[10]. It measures 10 to 11 cm in length[10]. The trachea is divided into extra- and intra-thoracic parts. The extrathoracic part extends from the level of inferior border of cricoid upto the thoracic inlet. The intrathoracic portion extends from the thoracic inlet to the carina.The normal tracheal diameter in men ranges from 13 to 25 mm in the coronal dimension and 13 to 27 mm in the sagittal dimension[11,12]. In women, trachea is smaller and its dimension range from 10 to 21 mm in the coronal plane and 10 to 23 mm in the sagittal plane[11,12]. The posterior portion of the tracheal wall, lying between the open ends of the tracheal cartilages, is a thin fibromuscular membrane termed the posterior tracheal membrane. The cross section of trachea has marked variability in appearance, which may appear round, oval or horse shoe shaped. The posterior tracheal membrane may appear convex posteriorly, flat or convex anteriorly.

Carina

Trachea divides at the level of sternal angle (4th-5th dorsal vertebral levels) at the carina into the right and left mainstem bronchi[11]. The normal carinal angle ranges between 70°-100°.

Mainstem, lobar and segmental bronchi

The mainstem bronchi extend infero-laterally from the carina into the pulmonary hila. At the pulmonary hila, they branch further to form the bronchial tree within the pulmonary parenchyma. The mainstem bronchi divide into lobar bronchi. There are 3 lobar bronchi on rigth side and 2 on left side. The lobar bronchi further divides into segmental and subsegmental bronchi. There are approximately 23 generations of branching till the bronchi form the alveoli[13]. The segmental bronchi are accompanied by segmental arteries that form a broncho-pulmonary segment.

The bronchi on MDCT appear as small circular lucencies on axial scans. Bronchi that course obliquely to the axial plane are more difficult to evaluate on axial scans and therefore require MPRs images and MinIP images (Figure 1). VB also provides the intraluminal view (Figure 2).

PATHOLOGY

The pathological conditions affecting airway vary from innocuous to sinister. To add to the diagnostic dilemma, identification of tracheal disease is notoriously difficult. Patients become symptomatic very late in the natural history of diseases affecting the airway. Patients with tracheobronchial pathology can present with breathlessness, persistent cough, stridor, recurrent cyanotic episodes and haemoptysis in varying severity, depending upon the degree of airway involvement. These may cause sudden deterioration of the patient’s clinical condition. Therefore rapid and accurate diagnosis is imperative to reduce morbidity and mortality.

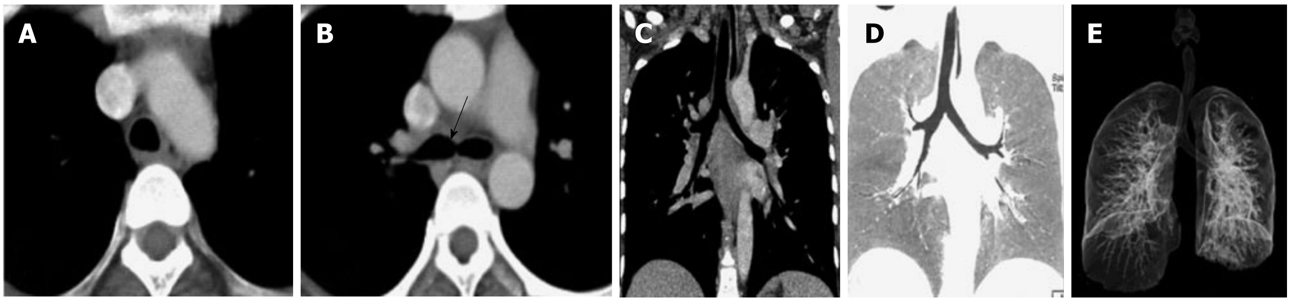

Figure 1 Normal arway. Axial image at the level of arch of aorta (A) shows a typical inverted U shaped trachea with thin fibromuscular membrane in posterior portion lying between open ends of tracheal cartilages. Axial image (B) at the level of carina (arrow) shows dichotomous branching of trachea at its distal end into right and left main bronchi. Coronal MPR image (C) shows trachea and mainstem bronchi as uniform tubular structures in midline within the mediastinum. Coronal reconstructed MinIP image (D) shows trachea and its bronchial branches as tubular air containing structures continuous from thoracic inlet till its divisions into the lung parenchyma. Volume rendered image (E) is the external rendered image showing 3-dimensional display of external surface of the airway and lung parenchyma. MPR: Multiplanar reformation; MinIP: Minimum intensity projection.

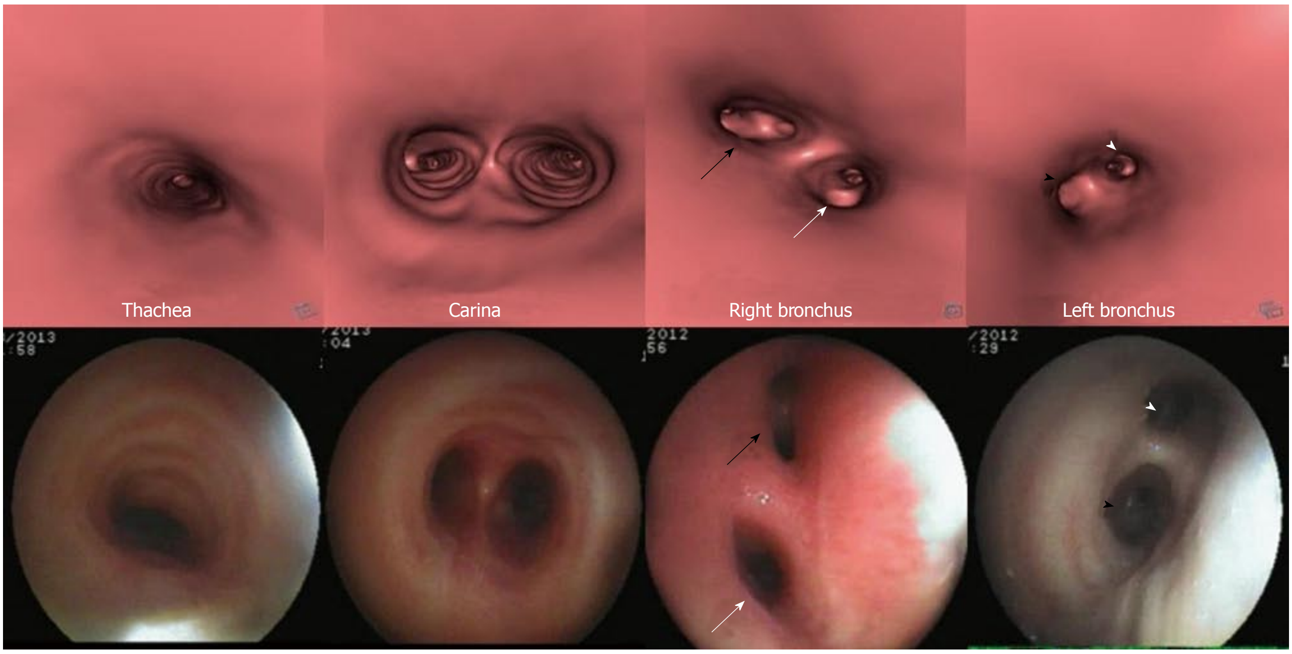

Figure 2 Virtual bronchoscopy of normal airway. Virtual bronchoscopy or internal rendered images reconstructed using dedicated "fly through" software at the level of trachea, carina, right and left main bronchus (top row) with corresponding appearance on fiberoptic bronchoscopy (bottom row). The division of right bronchus into upper lobe (white arrow) and bronchus intermedius (black arrow) and division of left main bronchus into upper (black arrowhead) and lower lobe bronchus (white arrowhead) is seen.

For descriptive purposes, the lesions affecting airway may be broadly classified as focal and diffuse lesions[14]. A lesion is characterized as focal when it affects a single short segment of airway, whereas it is characterized as diffuse if it involves either long segment of airway or when multiple lesions are detected.

FOCAL AIRWAY LESIONS

Intrinsic focal lesions

Tracheobronchial neoplasm: Tracheobronchial neoplasm is one of the commonest focal lesion involving the airway[15]. Tracheobronchial involvement by a malignant process can be both primary and secondary. Mostly airway is secondarily invaded by primary neoplasms arising from adjacent organs. Trachea is in close approximation with various organs in its extrathoracic and intrathoracic course. Therefore primary malignancy of adjacent organs like lung, esophagus or thyroid can invade the tracheobronchial tree.

Primary lung carcinoma is a disease with a very high mortality rate worldwide and commonly involves the airway. The main histopathological types include: adenocarcinoma, squamous cell carcinoma (SCC), small cell carcinoma and large cell carcinoma of which SCC and small cell carcinoma are most common types originating from the central airway[16,17]. SCC has an intraluminal growth pattern that can cause airway obstruction leading to pulmonary atelectasis or lobar collapse (Figure 3)[16]. Bronchial obstruction is much less common with small cell carcinoma than with SCC. The most common imaging finding seen in small cell

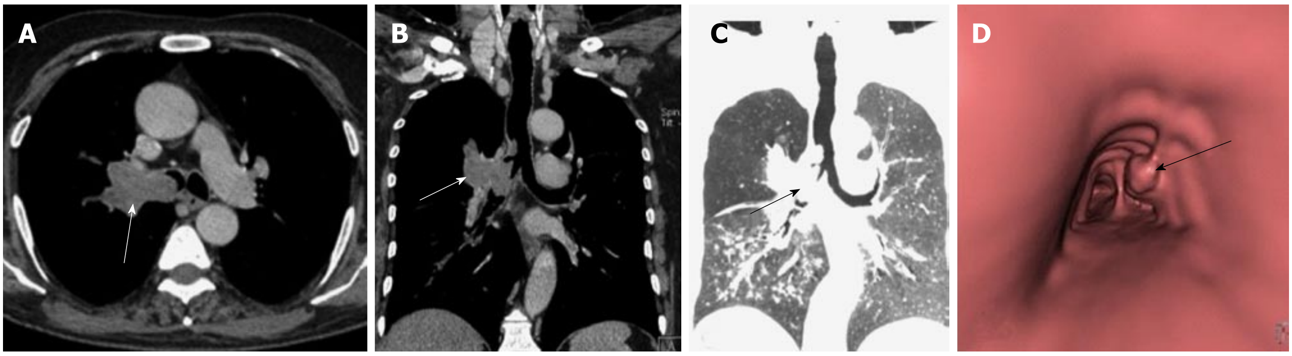

Figure 3 Squamous cell lung carcinoma. Contrast enhanced axial (A) and coronal MPR (B) images show enhancing soft tissue mass in right perihilar region with intraluminal extension of growth into the right mainstem bronchus and lower trachea (arrow). Coronal MinIP image (C) shows attenuation of right mainstem bronchus with a polypoidal growth extending into lower trachea (arrow). Virtual bronchoscopy (D) shows an irregular polypoidal intraluminal mass in lower trachea (arrow). MPR: Multiplanar reformation; MinIP: Minimum intensity projection.

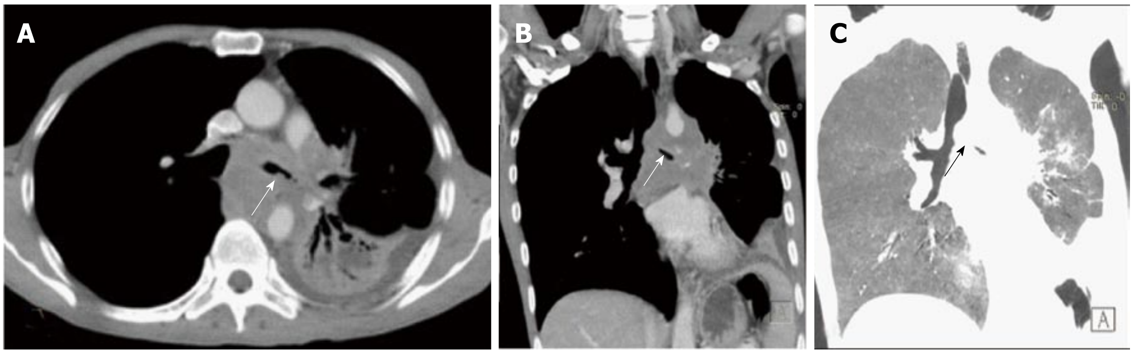

Figure 4 Small cell lung cancer. Axial (A) and coronal MPR (B) images show heterogeneously enhancing mass lesion encasing and attenuating left main bronchus and its lower division with mediastinal invasion and associated collapse-consolidation of left lower lobe. Coronal MinIP image (C) shows attenuated left main bronchus (arrow). MPR: Multiplanar reformation; MinIP: Minimum intensity projection.

carcinoma is that of extensive hilar or mediastinal lymphadenopathy (Figure 4)[18].

Primary tracheal neoplasm can also occur but are very rare. Majority of the primary tracheal neoplasms in adults are malignant with common histopathological patterns comprising of SCC, adenoid cystic carcinoma, carcinoid, mucoepidermoid carcinoma, and papilloma. SCC is the most common tracheal tumor and is more common in men[19]. It is highly associated with cigarette smoking and is histologically identical to lung SCC[14]. SCC appears as a polypoid intraluminal lesion generally in the lower third of trachea. It typically has irregular margins as it arises from the surface epithelium. It may invade mediastinum by direct extension or lymphatic spread (Figure 5)[20]. The second common cell type is adenoid cystic carcinoma (ACC) which occurs in younger patients with equal sex distribution. ACC arises within the submucosal glands and therefore has a smooth outline (Figure 6)[21]. The mucosal covering of the lesion rarely ulcerates in contrast to SCC. Lymphadenopathy and metastases are also uncommon[22].

Benign tumors of the airway include endobronchial carcinoid, hamartoma and papillomas. Endobronchial carcinoids are the most common airway tumors in adolescents and young adults. They generally arise within the central bronchi causing cough, hemoptysis, and airway obstruction[23]. They appear as an intensely enhancing endobronchial or hilar masses with post obstructive features like atelectasis or air trapping[23]. About one-fourth of these tumors can also show calcification on CT[24].

Respiratory papilloma is caused by human papilloma virus infection of the upper airway. The infection is usually acquired during birth or rarely through oro-genital sexual route. The tracheo-laryngeal form of papilloma is the commonest form and occurs in 2%-17% cases[25]. Respiratory papilloma is a benign endoluminal lesion that commonly involves larynx, trachea and the mainstem bronchi. It is a well circumscribed polypoid lesion which does not extend across the wall of trachea or bronchi (Figure 7)[25]. Respiratory papillomas can occur at multiple sites along the airway. VB can show the entire extent of the disease without the risk of downstream spread, which can be a problem with conventional bronchoscopy. Papillomas can cause airway obstruction and lead to post obstructive changes like atelectasis, pneumonia or pneumothorax. The most serious long term complication is malignant degeneration of papilloma to SCC[26].

MDCT acquired after contrast administration is currently the standard imaging modality to diagnose and stage central airway tumors. Axial images along

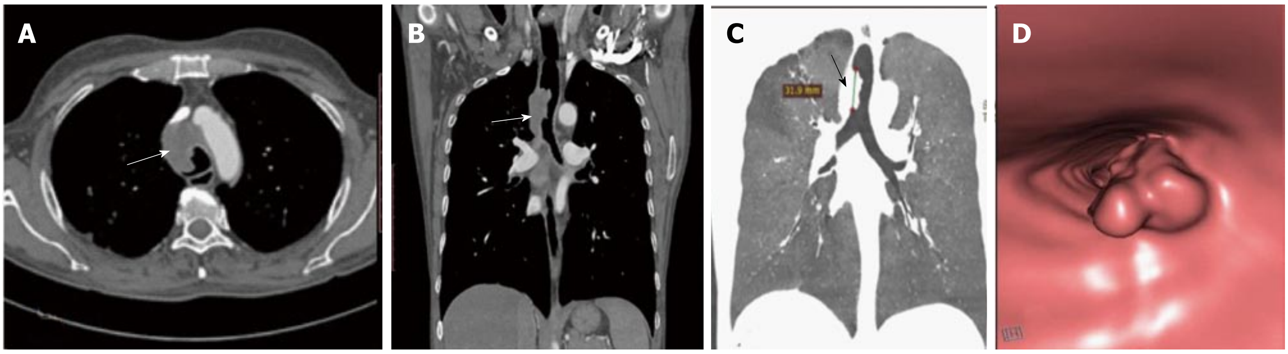

Figure 5 Squamous cell carcinoma of trachea. Axial (A) and coronal MPR (B) images show eccentric soft tissue mass with irregular surface involving trachea (arrow in B) with mediastinal extension (arrow in A). Coronal MinIP (C) shows partial attenuation of mid tracheal lumen involving a length of 3.19 cm (arrow). Virtual bronchoscopy (D) shows this mass lesion as irregular intraluminal growth along the right wall of trachea causing tracheal luminal narrowing. MPR: Multiplanar reformation; MinIP: Minimum intensity projection.

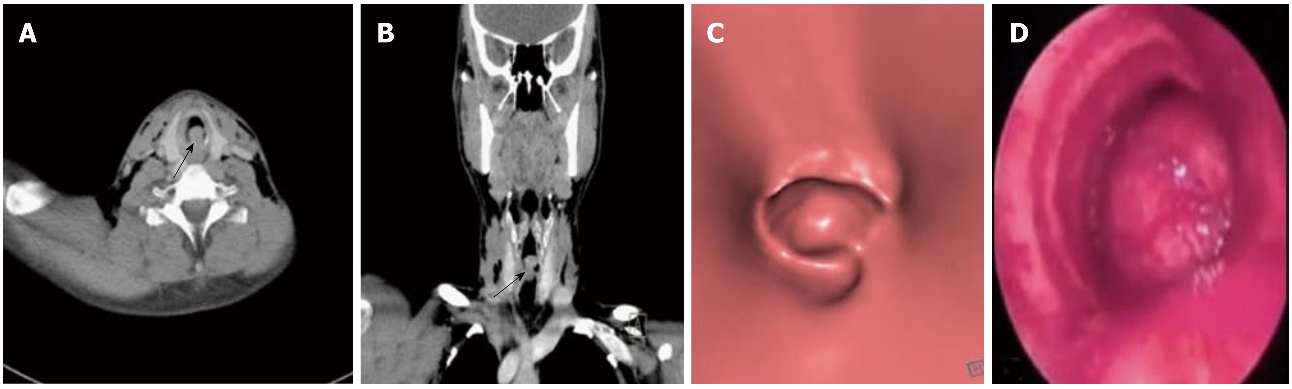

Figure 6 Adenoid cystic carcinoma of trachea. Axial (A) and coronal MPR (B) images show polypoidal mass with smooth outline within the trachea in subglottic region causing near complete attenuation of the airway (arrow). Virtual bronchoscopy (C) shows intraluminal smooth mass within trachea similar to that seen on conventional bronchoscopy (D). MPR: Multiplanar reformation.

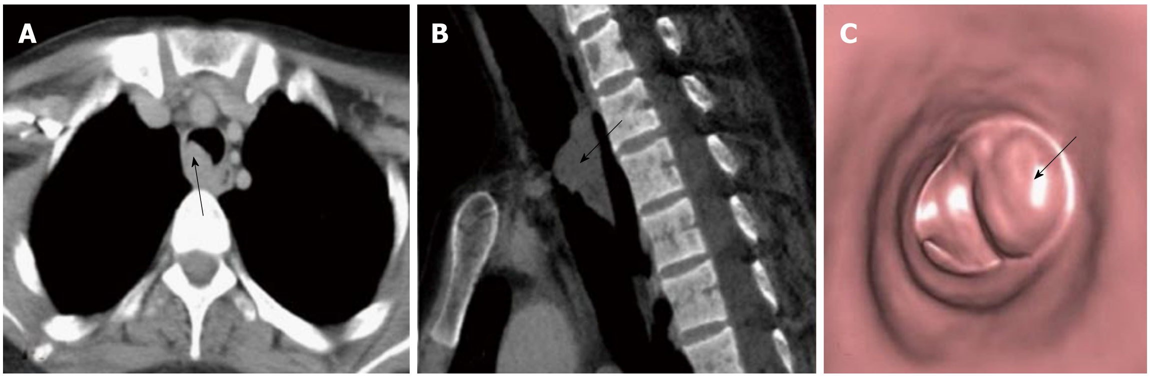

Figure 7 Respiratory papilloma. Axial (A) and sagittal MPR (B) images show a smooth polypoidal soft tissue mass arising from the postero-lateral wall of trachea (arrow). Virtual bronchoscopy (C) shows the intraluminal mass lesion with smooth surface (arrow). MPR: Multiplanar reformation.

with reconstructed MPR and 3D images provide comprehensive information about the involvement of airway by the tumor and its relationship with adjacent structures. MDCT can also detect associated lymph nodal spread and metastases (both intra-pulmonary and distant sites), thereby altering tumor staging. VB images provide an intraluminal view of the tumor involving the airway. These also score over conventional bronchoscopy due to their inability to evaluate the airway distal to a high grade narrowing or complete obstruction. This can have a significant impact on patient management as palliative stent placement in the airway can be offered to patients with proximal occlusive lesion and patent distal airway.

Post tracheostomy complications: Prolonged tracheal intubation and tracheostomy can cause airway complications. Tracheal stenosis is a frequently encoun-

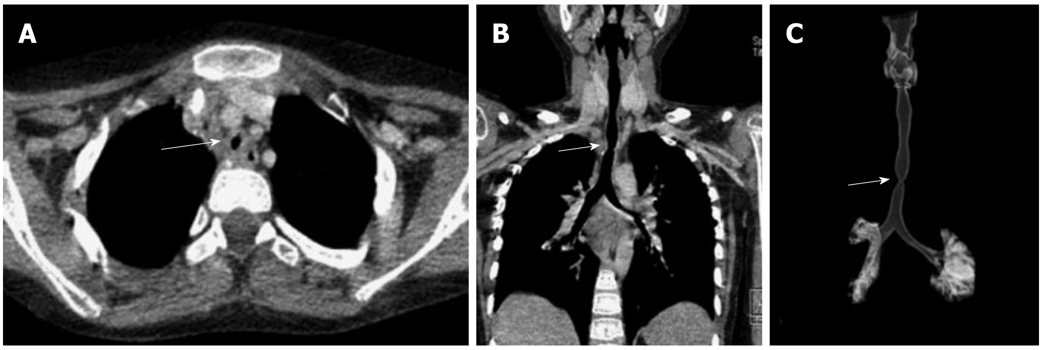

Figure 8 Post intubation tracheal stenosis. Axial (A), coronal MPR (B) and VRT (C) images show a focal short segment concentric narrowing of tracheal lumen giving an “hourglass” configuration better appreciated on coronal images. MPR: Multiplanar reformation; VRT: Volume rendering technique.

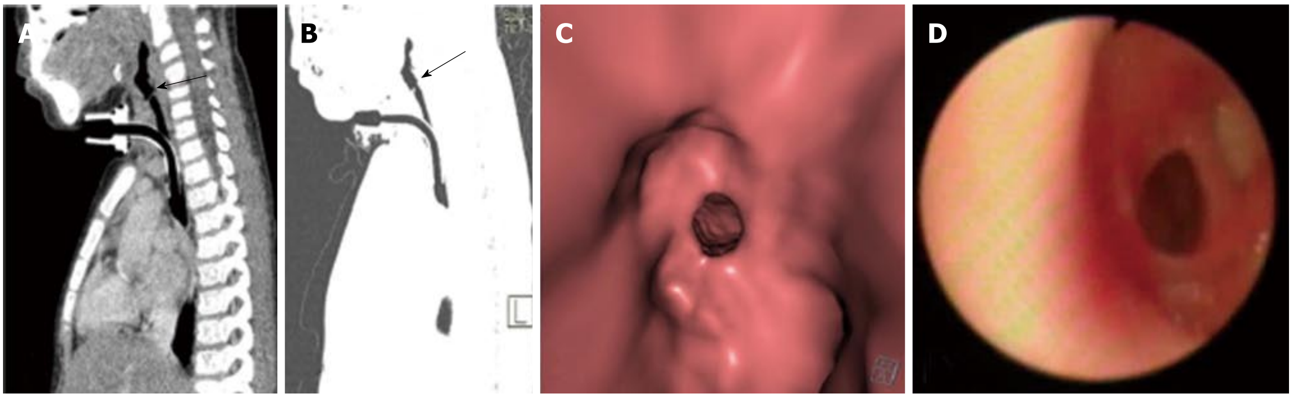

Figure 9 Tracheal membrane. Sagittal MPR (A) and sagittal MinIP (B) images show a partially occluding thin membrane in subglottic airway (arrow). Note made of tracheostomy tube insitu. Virtual bronchoscopy (C) shows circumferential membrane causing narrowing of airway lumen with similar finding confirmed on fiberoptic bronchoscopy. MPR: Multiplanar reformation; MinIP: Minimum intensity projection.

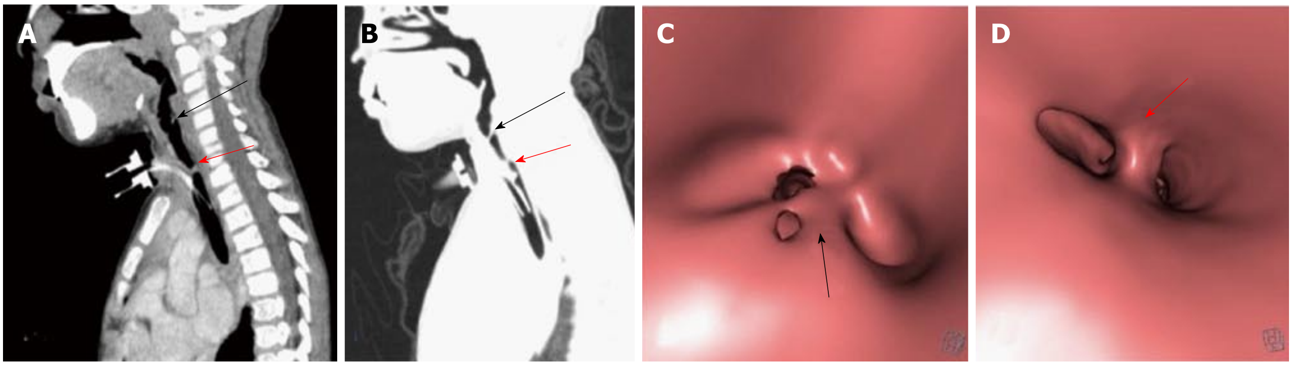

Figure 10 Post intubation mucosal synechiae. Sagittal MPR (A) and MinIP (B) images show thin membrane like adhesions within the airway at subglottic (black arrow) and upper tracheal (red arrow) levels extending across the airway lumen and compromising its patency suggestive of synechiae formation. The corresponding appearance of these synechiae are very well demonstrated on virtual bronchoscopy (C and D). MPR: Multiplanar reformation; MinIP: Minimum intensity projection.

tered entity in these patients. The stenosis generally occur at two sites: At the level of endotracheal tube cuff which is most common site and at the stoma site. The high pressure of the endotracheal tube balloon causes mucosal injury of tracheal wall. This leads to tissue scarring and ultimately tracheal stenosis.

The most common CT finding in post intubation stenosis is a localized area of narrowing of tracheal lumen[27,28]. This focal circumferential narrowing generally produces a characteristic hourglass configuration (Figure 8). Less common findings include a thin membrane projecting into the tracheal lumen (Figure 9). Due to mucosal injury there can also be formation of multiple mucosal synechiae compromising the tracheal lumen (Figure 10).

MDCT with multi planar reformats and VB provides information regarding the stenosis, *i.e.*, grade of stenosis, distance of stenotic segment from the vocal cord and length of the stenotic segment. These findings give a detailed road map to the surgeons before the

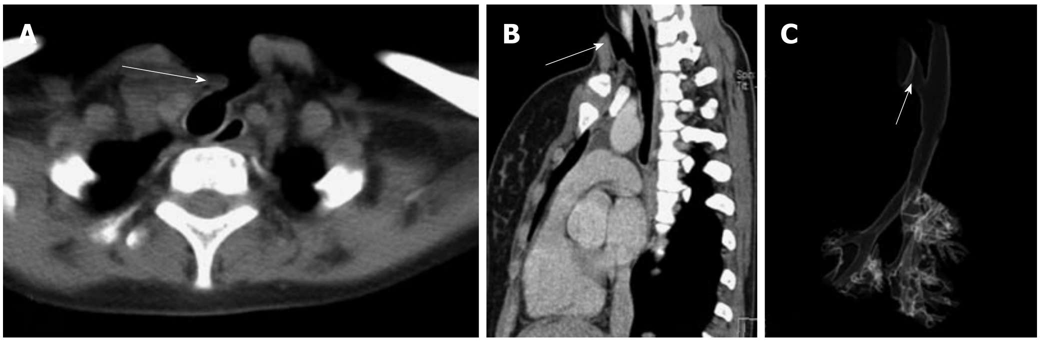

Figure 11 Post tracheostomy tracheo-cutaneous fistula. Axial (A) and oblique sagittal MPR (B) images show the fistula as an abnormal tract extending from antero-lateral wall of upper trachea to the skin surface (arrow). This fistulous tract is very well demonstrated on VRT image (C, arrow). MPR: Multiplanar reformation; VRT: Volume rendering technique.

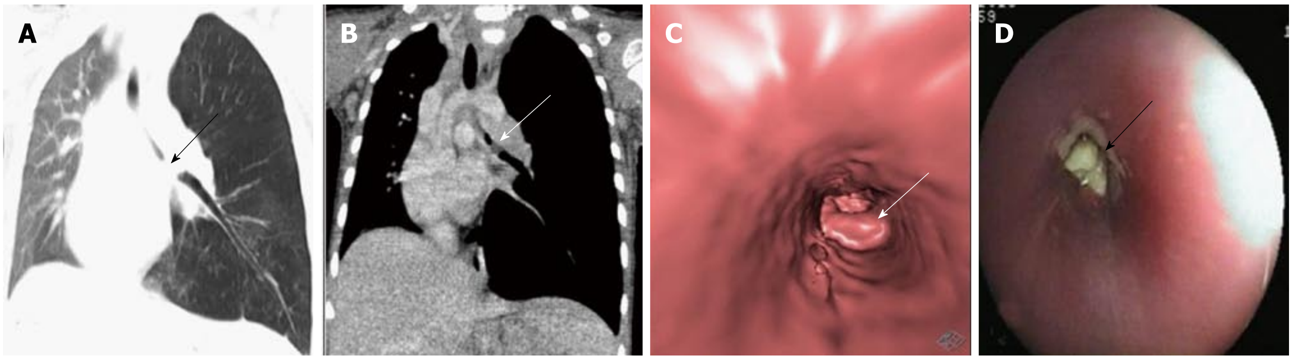

Figure 12 Foreign body aspiration. Coronal MPR images of thorax in lung settings (A) and mediastinal window settings (B) reveal soft tissue density attenuating left main bronchus (arrow) with associated hyperinflation of left lung. Virtual bronchoscopy (C) shows obstruction of left main bronchus with lobulated surface confirmed to be endobronchial foreign body (arrow) on conventional bronchoscopy (D). MPR: Multiplanar reformation.

patient is taken up for surgery. The MPR and volume rendering technique images are helpful in appreciating the vertical length of the lesion more precisely.

Other complication like diverticulum at the stoma site and tracheocutaneous fistula can also develop after tracheostomy. MDCT can accurately demonstrate the location, dimension and tract of the fistula which has an implication on the surgical management of these patients (Figure 11).

Foreign body aspiration: Foreign body aspiration is generally encountered in young children (aged between 6 mo to 5 years) and is a frequent cause of morbidity and mortality[29,30]. Foreign body aspiration is potentially life threatening if not recognised early and appropriately treated. Any child with acute stridor should always be evaluated for potential aspiration of foreign body. However, patients with chronically impacted foreign body are difficult to diagnose. They usually present with recurrent wheezing and radiographs if obtained may show pulmonary infiltrates, bronchiectatic changes or lung abscess[31]. Aspiration of organic vegetative objects is more dangerous as these swell with bronchial secretions and cause progressively increasing airway obstruction. Allergic and chemical bronchitis is also a frequent complication of aspiration of organic foreign body[32].

In suspected cases of foreign body aspiration, obtaining radiographs in both inspiratory and expiratory phases can be helpful. Decubitus view and fluoroscopic assessment can also be performed to look for features of airway obstruction like hyperinflation. However, radiographs are normal in around one-third of these cases and nearly 90% of these foreign bodies are radiolucent[33]. Therefore, the advantage of MDCT in evaluating these cases lies in the fact that it can detect both radioopaque and radiolucent foreign bodies (like plastic and organic food items). The aspirated radiolucent objects usually appear as non-enhancing soft tissue structure within the airway causing partial or complete airway obstruction (Figure 12). CT also help in identifying ancillary post obstructive findings like hyperinflation, lobar atelectasis or complete lung collapse (Figure 13)[34].

Broncholithiasis: The presence of calcific/ossific material within the bronchial lumen is called broncholithiasis. It is most commonly associated with erosion of the airway by a calcified lymph node caused by long-standing foci of granulomatous lymphadenitis like tubercular infection which can then extrude into the lumen of the bronchus. Other rarer causes include *in-situ* calcification of chronically aspirated foreign body

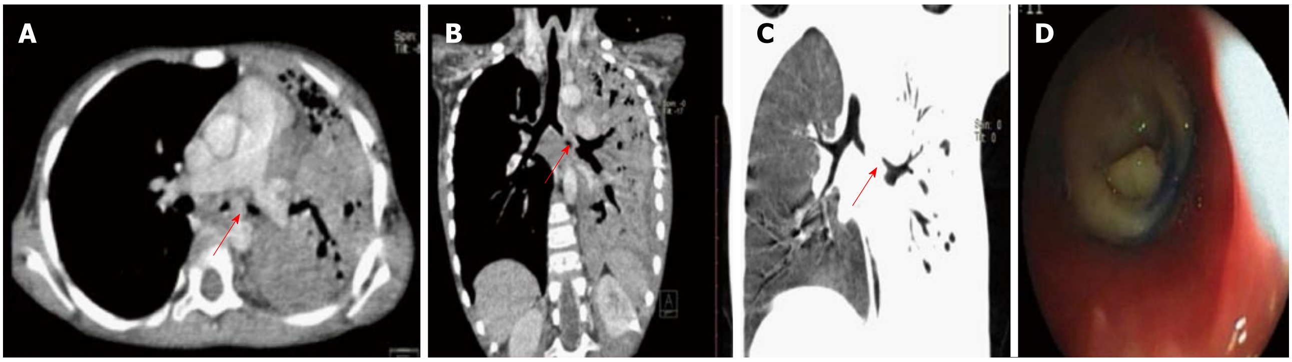

Figure 13 Chronic foreign body aspiration. Axial (A) and oblique coronal MPR (B) images reveal soft tissue density partially occluding the left main bronchus (arrow) with consolidation of left lung and associated bronchiectatic changes. Coronal MinIP image (C) shows attenuation of left main bronchus (arrow) with collapse of left lung. Endobronchial foreign body within left main bronchus was confirmed to be a small piece of plastic on conventional bronchoscopy (D). MPR: Multiplanar reformation; MinIP: Minimum intensity projection.

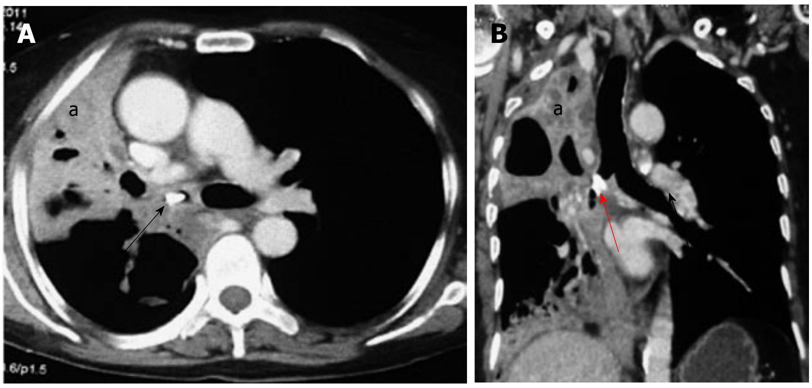

Figure 14 Broncholith. Axial (A) and coronal MPR (B) images show a hyperdense calcific density within the right main bronchus (arrow) with collapse-consolidation and bronchiectasis in the right lung (a). MPR: multiplanar reformation.

or even migration of calcified pleural plaque into the bronchus[35]. CT has high spatial resolution and superior ability to depict calcification. Therefore it provides useful information in the evaluation of suspected case of broncholithiasis. The presence of endobronchial or peribronchial calcified nodule is highly suggestive of broncholithiasis. It can also show features of bronchial obstruction like atelectasis, obstructive pneumonitis or bronchiectasis (Figure 14).

Tracheal wall pathology

Post traumatic tracheal rent: Tracheo-bronchial injuries are rare but they can occur in motor-vehicle accidents with trauma to the thoracic cavity. The injury predominantly involves the posterior membranous wall of intrathoracic trachea. The injury occurs due to sudden increase in the intra-airway pressure against a closed glottis at the time of injury[36].

MDCT depicts the site of injury as a focal or circumferential defect in tracheal wall, deformed tracheal contour or fistulous communication with adjacent structures (Figure 15)[36]. Other non-specific signs include pneumo-mediastinum, pneumo-thorax and non-resolving subcutaneous emphysema. Tracheo-bronchial injury is an emergency and early diagnosis with immediate surgical repair is necessary to reduce morbidity and mortality in such patients.

Tracheo-esophageal fistula: Esophageal atresia and tracheoesophageal fistula are a group of congenital anomalies involving the structures arising from primitive foregut. They occur due to an unknown intrauterine insult during the normal process of separation of primitive foregut into trachea and esophagus. (Figure 15)[37]. Tracheo-esophageal fistula can be an isolated anomaly or a part of VACTERL complex (vertebral, anal, cardiac, tracheal, esophageal, renal, and limb anomalies)[38].

However current usefulness of pre-operative CT in cases of tracheoesophageal fistula is controversial. It provides limited information about the fistulous tract as compared to endoscopy. Thus, the use of CT scan is not routinely recommended in the management of tracheoesophageal atresia.

Extrinsic focal lesions

Vascular compression: Anomalous mediastinal vessels (aorta and pulmonary arteries) are important causes of compression of the trachea. Although a majority of these patients are asymptomatic, vascular

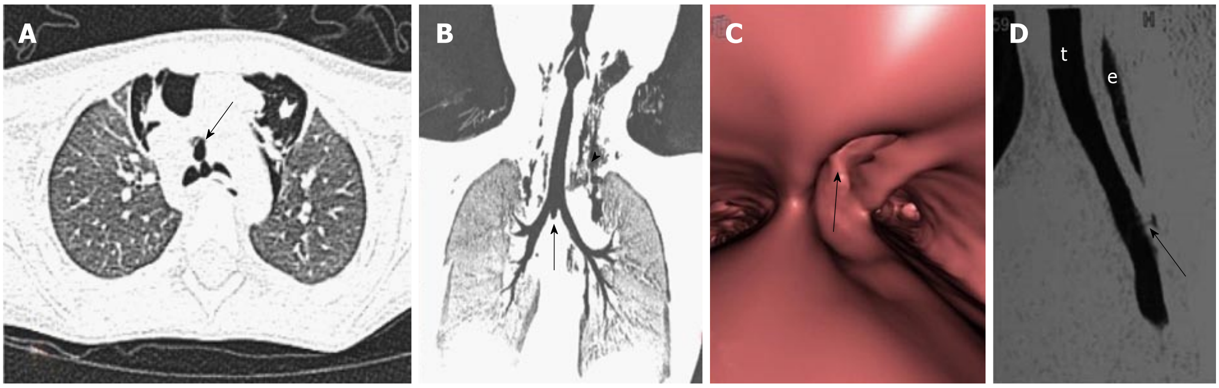

Figure 15 Airway wall pathology. Traumatic tracheal rent-Axial (A) and oblique coronal MinIP (B) images show a focal air containing outpouching at the level of carina in midline projecting antero-inferiorly (arrows). Virtual bronchoscopy (C) shows a focal defect within the wall of trachea at the level of carina (arrow). Note made of marked subcutaneous emphysema (arrowhead in B). Tracheo-esophageal fistula-sagittal MPR image (D) of another case shows a thin faint air containing tract (arrow) extending from esophagus (e) to trachea (t). MPR: Multiplanar reformation; MinIP: Minimum intensity projection.

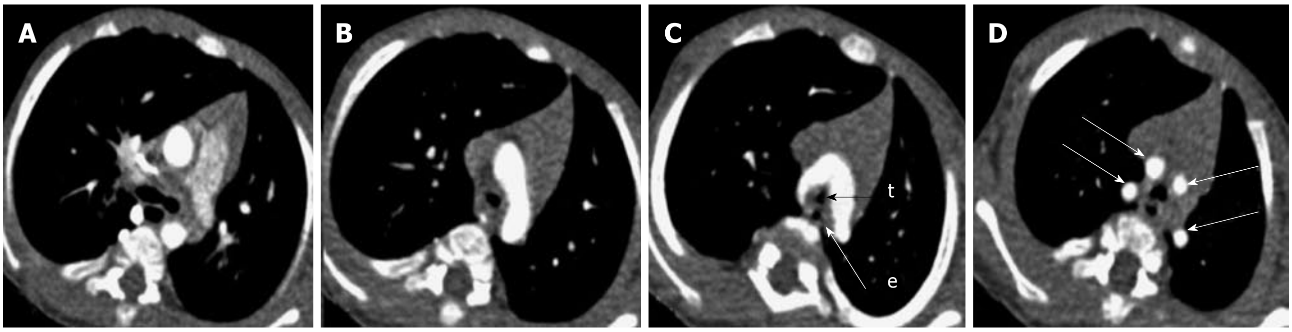

Figure 16 Double aortic arch. Serial axial images (A-D) of thorax (in caudo-cranial direction) reveal 2 aortic arches encircling and compressing trachea (t) and esophagus (e). Ipsilateral subclavian and common carotid arteries arise from each arch giving a characteristic "4-vessel sign" (arrows in D).

compression of the airway have been observed in 13%-26% of children who undergo bronchoscopy for persistent wheezing, stridor and apnea[39]. The vascular anomalies that present with airway compression include double aortic arch, anomalous course of innominate artery and pulmonary artery sling.

Double aortic arch is a vascular anomaly that occurs due to non regression of right aortic arch during intrauterine development. There is persistence of both right and left aortic arches, which form a vascular ring encircling and compressing esophagus and trachea. Each arch gives off two branches - the common carotid and subclavian arteries supplying ipsilateral sides of the body giving the characteristic "four vessel sign" (Figure 16). In most of the cases the right sided arch is higher and is larger in diameter. However they can also be in the same plane or the right sided arch may even be lower in location. Sometimes one of the arches may be replaced by a fibrous cord with absent luminal patency[40].

The innominate artery can sometimes have an anomalous course and originate at a point farther along the arch than is normal; when it does so, it winds around the anterior surface of the trachea as it courses upward and to the right. If this vessel is large and taut, it can compress the trachea to a serious degree (Figure 17).

Left pulmonary artery sling is a rare anomaly characterized by abnormal origin and course of left pulmonary artery. The left pulmonary artery has an anomalous origin from right pulmonary artery and courses between trachea and esophagus before entering the left hilum (Figure 18). It is thought to result from a failure of formation of the 6th aortic arch. Nearly half of the infants born with this condition present with symptoms of airway compression at birth. At one month of age, approximately 65% of the children develop stridor of varying degree[41].

Bronchogenic cyst: Bronchogenic cysts are intrathoracic cystic developmental lesions caused by abnormal antenatal budding of the tracheobronchial tree[42,43]. These are included under the broad spectrum of foregut duplication cysts that also includes neurenteric cysts and enteric cysts. Bronchogenic cysts are typically located in the middle mediastinum with subcarinal region being the most common site followed by right paratracheal location[44]. Rarely, they can also occur as intra-pulmonary lesions most of which are located in the lower lobes[44]. Small bronchogenic cysts are usually asymptomatic; however large lesions can cause mass effect on adjacent structures like the airway

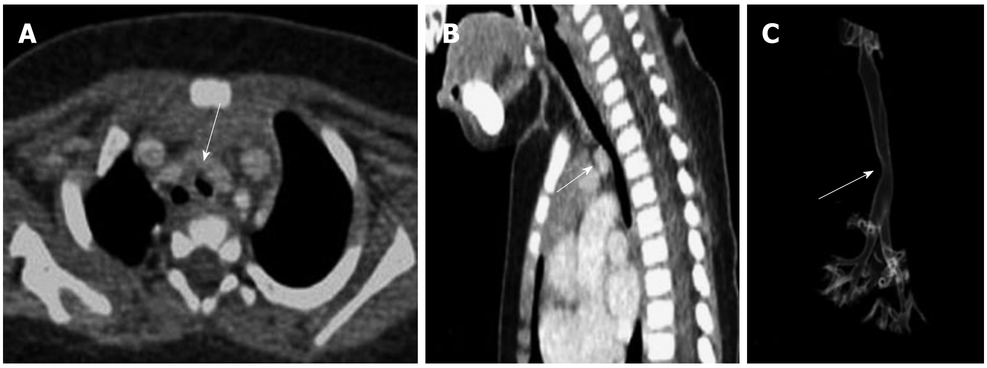

Figure 17 Innominate artery compression. Contrast enhanced axial (A) and sagittal MPR (B) images show extraluminal compression of trachea by anomalous course of innominate artery winding around the anterior wall of trachea (arrow). 3D VRT image (C) shows smooth indentation on the tracheal air column (arrow). MPR: Multiplanar reformation; VRT: Volume rendering technique.

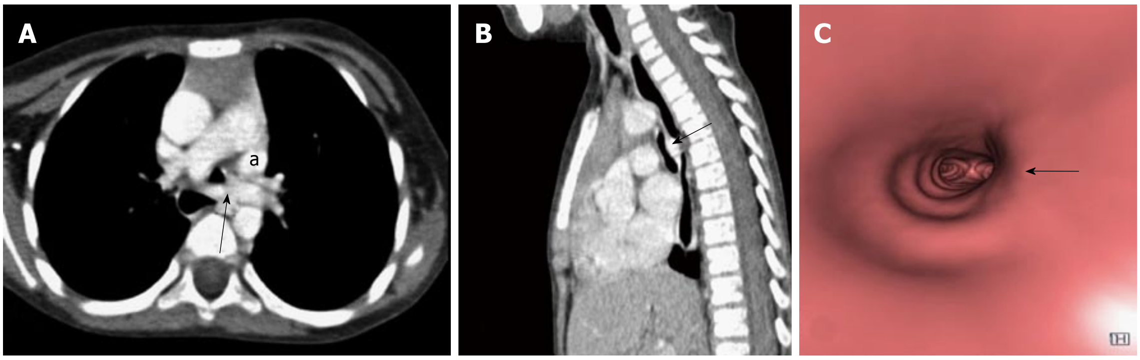

Figure 18 Left pulmonary artery sling. Contrast enhanced axial (A) and sagittal MPR (B) images reveal aberrant course of left pulmonary artery between trachea and esophagus (arrow) causing tracheal compression and vascular indentation on esophagus. Note made of left superior vena cava (a). Virtual bronchoscopy (C) shows an eccentric impression causing focal narrowing of the tracheal lumen (arrow). MPR: Multiplanar reformation.

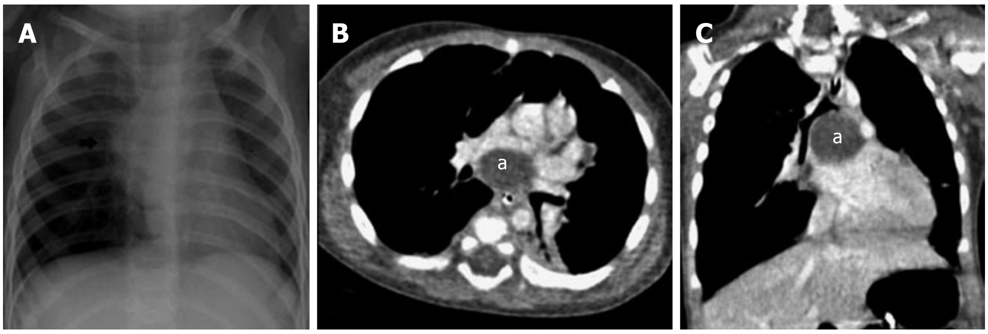

Figure 19 Subcarinal bronchogenic cyst. Frontal radiograph of chest (A) reveals mediastinal widening (arrow). Contrast enhanced axial (B) and coronal MPR (C) images reveal well defined non-enhancing homogenous fluid attenuation lesion in subcarinal location (a) narrowing the bronchial divisions with resultant subsegmental atelectasis in left lower lobe. MPR: Multiplanar reformation.

or esophagus causing respiratory distress and feeding difficulty respectively[43,44].

Bronchogenic cysts are usually single and show characteristic MDCT appearance of a well-circumscribed round or oval lesion with homogenous fluid attenuation (Figures 19 and 20). On contrast administration, they usually do not enhance or show minimal peripheral rim enhancement. The presence of thick walls, solid component, calcification or septations is unusual. If they cause substantial mass effect on adjacent airways post obstructive features like hyperinflation or lung collapse may also occur. Bronchogenic cysts can sometimes appear as an air containing cystic lesion if a fistulous communication develop with the airway (Figure 21).

Impacted esophageal foreign body: Foreign body ingestion with impaction within the oesophagus can rarely cause compression on the airway. Such cases are rarely encountered however may be seen especially in very young children who have a compliant airway which gets compressed extraluminally leading to airway compromise and post obstructive pulmonary changes

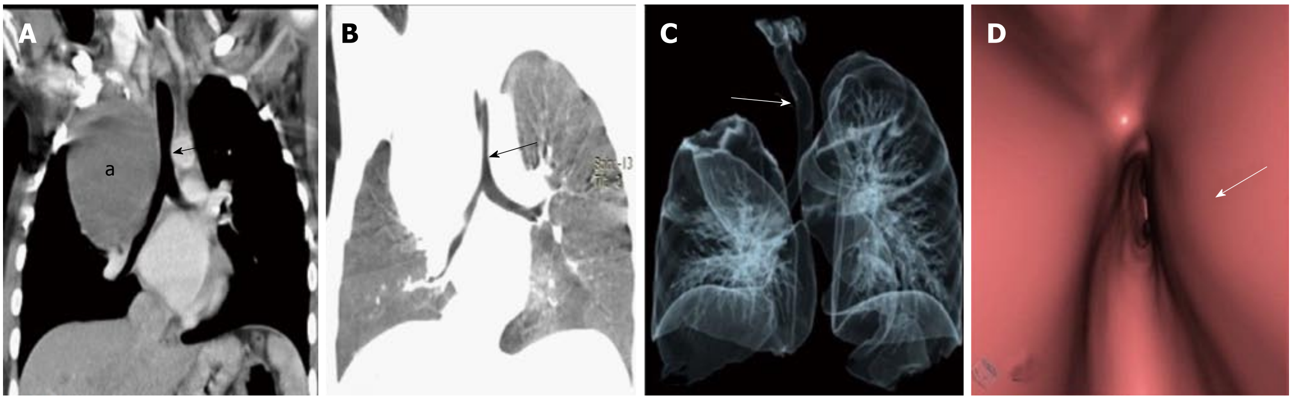

Figure 20 Paratracheal bronchogenic cyst. Coronal MPR image (A) shows large well defined non enhancing fluid attenuation lesion (a) in right paratracheal location with mass effect on adjacent trachea causing tracheal luminal attenuation (arrow). Coronal MinIP (B) and VRT (C) images show extrinsic mass effect on the airway (arrow) and right lung. Virtual bronchoscopy (D) clearly demonstrates the smooth extraluminal compression along the right wall of trachea causing luminal compromise. MPR: multiplanar reformation; MinIP: Minimum intensity projection; VRT: Volume rendering technique.

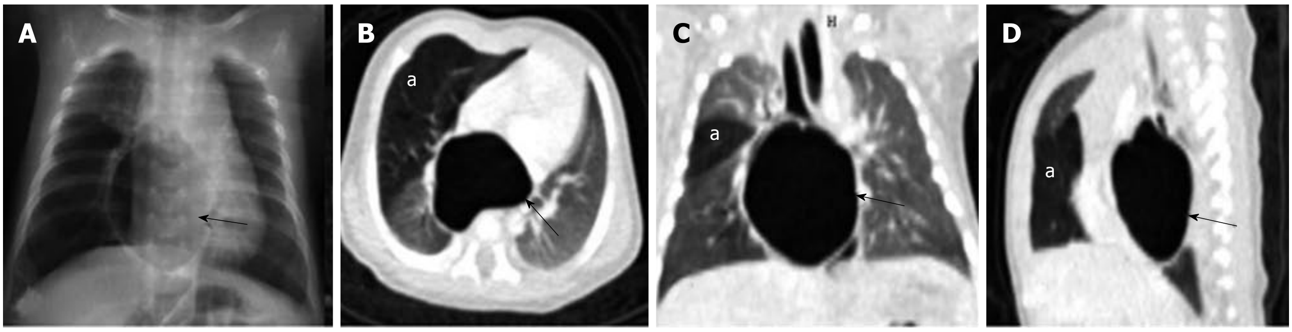

Figure 21 Bronchogenic cyst. Frontal radiograph of chest (A) shows a well-defined air filled cystic lesion in the retrocardiac location. Axial (B), coronal (C) and sagittal (D) MPR images show a large well defined homogenous air containing lesion (arrow) with carinal widening. The lesion is causing partial airway obstruction seen as air trapping in right middle lobe (a). MPR: Multiplanar reformation.

like atelectasis, consolidation and collapse (Figure 22)[45,46].

Lymphadenopathy: The mediastinum and pulmonary hila have a rich network of lymphatic tissues. These can enlarge due to various disease conditions including infective aetiologies like tuberculosis, histoplasmosis and malignant conditions like lymphoma and small cell lung cancer[47]. These may obstruct the airway to cause post obstructive pulmonary changes like atelectasis and collapse (Figure 23). Enlarged lymph nodes may also erode and infiltrate into the adjacent tracheal and bronchial wall leading to focal discontinuity of the airway wall (Figure 24). MDCT clearly depicts the cause of compression as enlarged lymph nodes and may also characterize primary pathology leading to lymphadenopathy.

DIFFUSE AIRWAY LESIONS

Saber-sheath trachea

Saber-sheath trachea is an abnormal morphological appearance of trachea seen in association with chronic obstructive pulmonary disease (COPD). It is seen almost exclusively in men and is characterized by reduced transverse and increased sagittal diameter of intrathoracic trachea (Figure 25). The sagittal-to-coronal diameter ratio is greater than 2[48]. The extra-thoracic trachea is not affected. Repeated injury to the airway from chronic coughing in patients with COPD is the probable cause. These changes initially begin at the thoracic inlet but can progress to involve the entire intrathoracic trachea over time. Other smoking-related conditions may be present such as emphysema and respiratory bronchiolitis[49].

Tracheo-bronchomegaly

This is also referred to as Mounier-Kuhn syndrome. There is dilatation of the central airway with the mucosa projecting between the cartilaginous rings forming multiple diverticulae. This gives a characteristic corrugated appearance of trachea and mainstem bronchi (Figure 26). This entity is seen in patients with recurrent respiratory infections in their 3rd and 4th decade resulting in thinning of the muscularis mucosa of airway[50]. Mounier-Kuhn syndrome is characterized by tracheal diameter of more than 3 cm and mainstem bronchi diameters of greater than 2.4 cm[50,51].

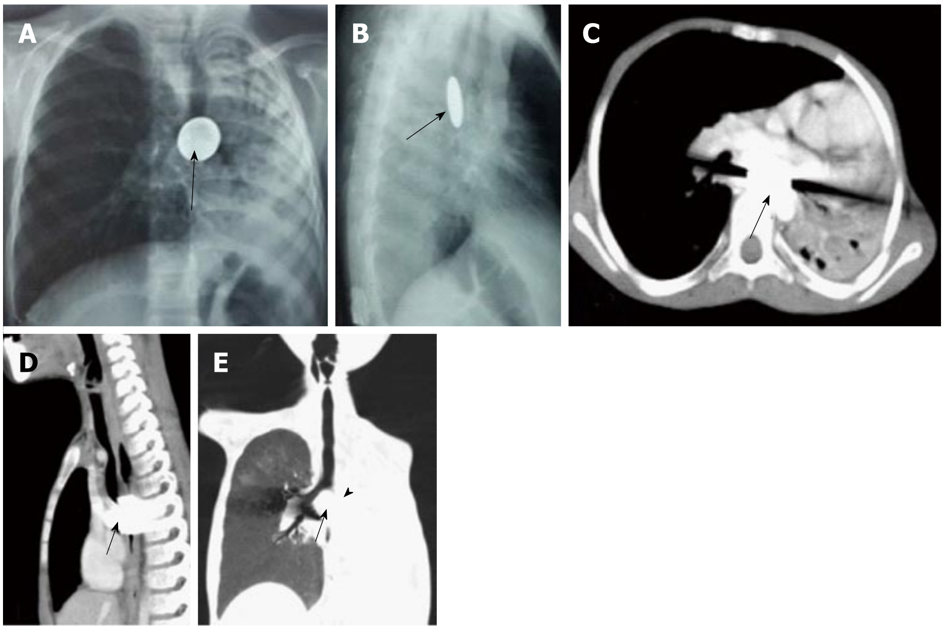

Figure 22 Impacted esophageal foreign body compressing airway. Frontal (A) and lateral (B) radiographs of chest reveal a well-defined round radio-opaque foreign body in the esophagus at the level of carina (arrows) with associated volume loss of left lung. Contrast enhanced axial (C) and sagittal (D) MPR images show a hyperdense foreign body giving streak artefacts impacted within the esophagus (arrow). Coronal MinIP image (E) shows near complete occlusion of left main bronchus (arrowhead) by the impacted esophageal foreign body (arrow) with collapse of left lung. MPR: Multiplanar reformation; MinIP: Minimum intensity projection.

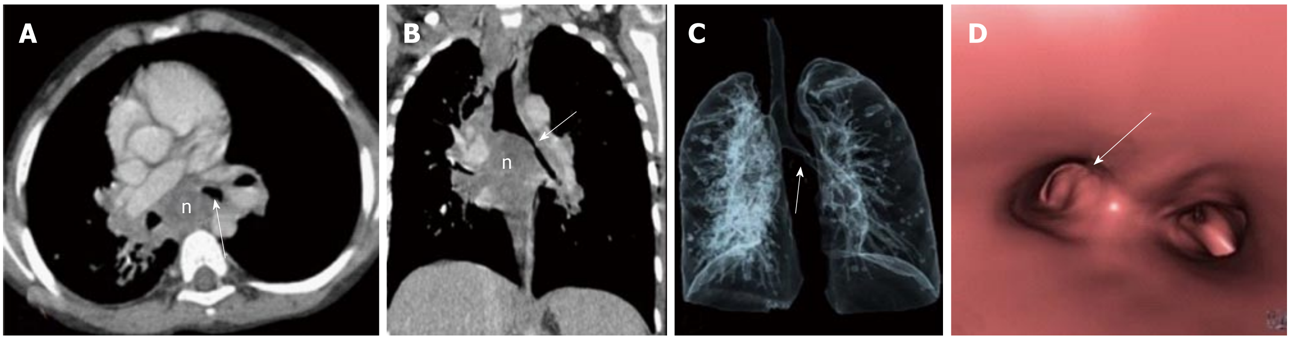

Figure 23 Enlarged tubercular lymph nodes compressing airway. Contrast enhanced axial (A) and coronal MPR (B) images show enlarged necrotic lymph nodal mass (n) in subcarinal station causing carinal widening and compression of left main bronchus (arrow). VRT (C) and virtual bronchoscopy (D) images also show compression of left main bronchus (arrow). MPR: Multiplanar reformation; VRT: Volume rendering technique.

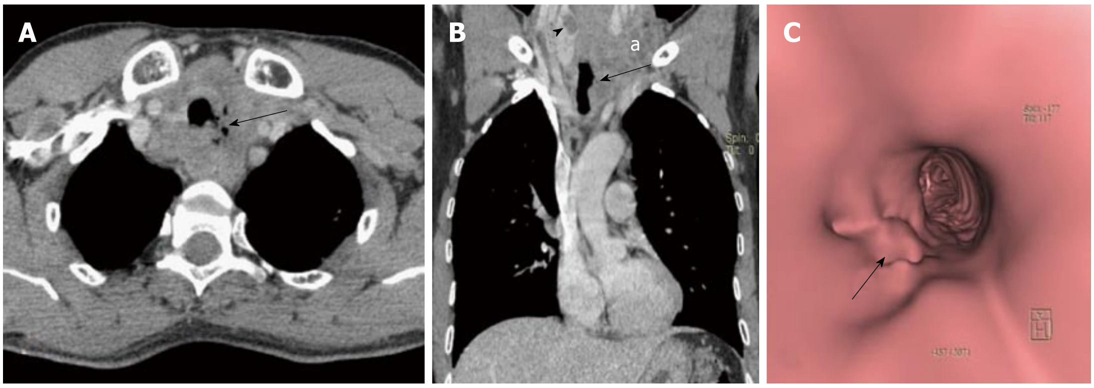

Figure 24 Paratracheal erosive malignant lymph nodes. Contrast enhanced axial (A) and coronal MPR (B) images show enlarged necrotic paratracheal lymph nodes eroding adjacent airway and showing foci of air within. There is a hypodense mass lesion (arrowhead in B) in right lobe of thyroid (patient was a known case of metastatic papillary thyroid carcinoma). Enlarged necrotic left lower jugular lymph nodes (a in B) also noted. Virtual bronchoscopy (C) shows focal area of irregularity along left lateral tracheal wall (arrow). MPR: Multiplanar reformation.

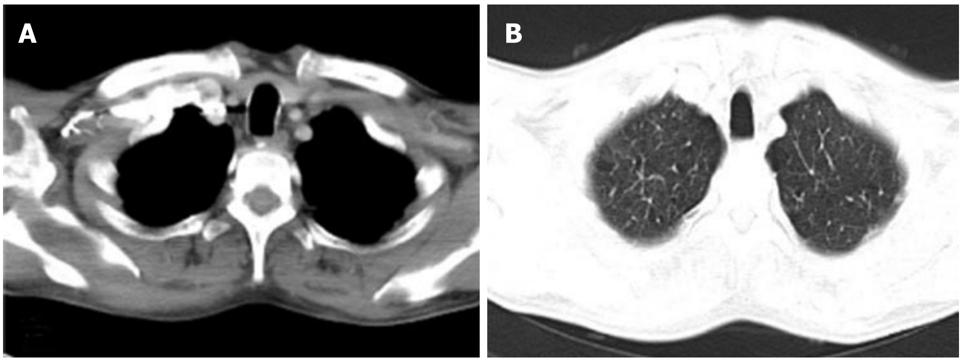

Figure 25 Saber-sheath trachea. In a 70-year old male with chronic obstructive pulmonary disease, axial images of thorax in mediastinal (A) and lung (B) window settings show increase in antero-posterior diameter of the trachea with narrowing of the transverse diameter. The sagittal to transverse diameter ratio measured 2.13:1.

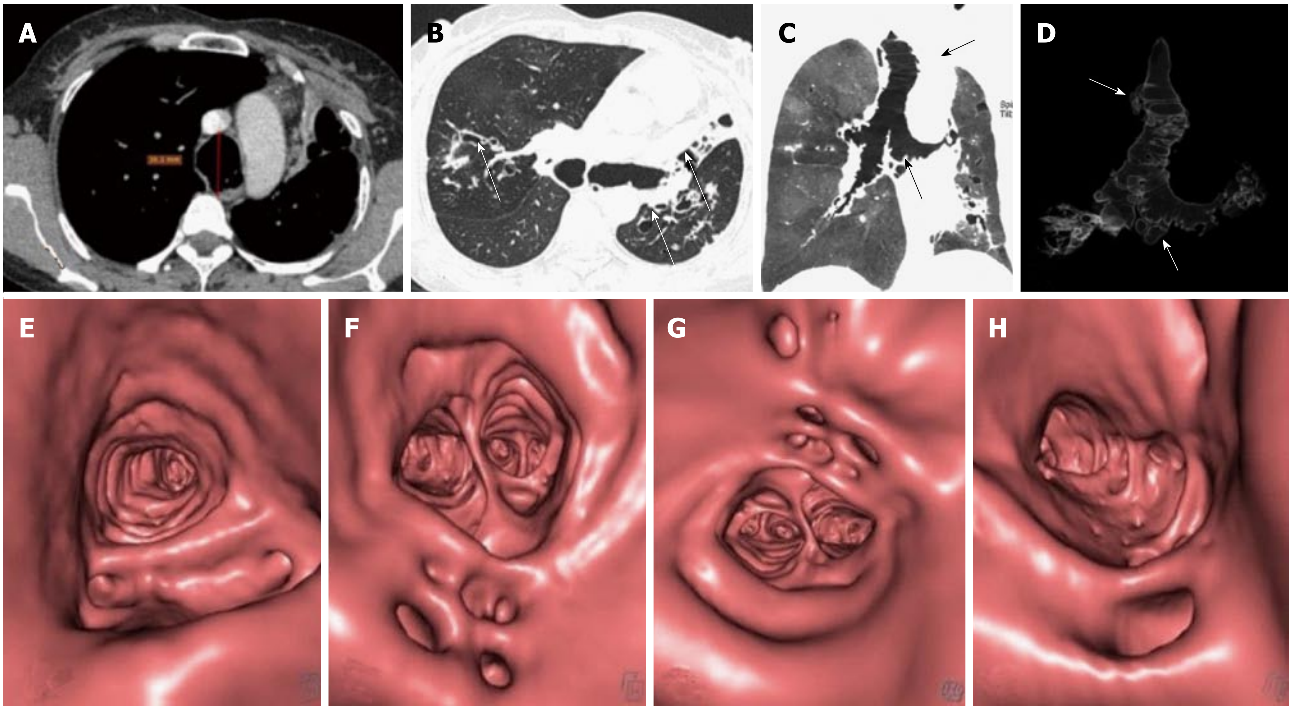

Figure 26 Mounier Kuhn syndrome. Axial images (A and B) show dilated trachea-AP diameter 3.6 cm at level of aortic arch (A) with dilated bronchi (B) and diverticula formation. Bronchiectasis is seen in bilateral upper and left lower lobes with collapse of lingula (arrow in B). Coronal MinIP (C) and VRT (D) images show tracheo-bronchomegaly with diffuse diverticulosis (arrows). Virtual bronchoscopy also shows diffusely scattered defects in the walls of upper trachea (E), carina (F), right (G) and left (H) main bronchi. MinIP: Minimum intensity projection; VRT: Volume rendering technique.

Tracheobronchopathia osteochondrodisplastica

Tracheobronchopathia osteochondroplastica is a rare, benign condition involving the trachea, and possibly major bronchi. The disease is characterised by diffuse nodularities, or polyps consisting of cartilaginous and/or osseous metaplastic tissue involving tracheal cartilagenous wall with sparing of membranous posterior wall (Figure 27)[52]. The nodules are 1 to 3 mm in diameter and may cause narrowing and rigidity of the trachea and bronchi. The majority of people remain asymptomatic throughout their lives unless severe airway stenosis develops, in which case patients may experience symptoms such as dyspnoea, hoarseness, persistent and often productive cough, haemoptysis and recurrent or slowly resolving pneumonia[53].

MISCELLANEOUS DEVELOPMENTAL ANOMALIES

Tracheal bronchus/displaced bronchus

The term tracheal bronchus was initially used for a right upper lobe bronchus originating from trachea by Sandifort in 1785. However, currently the term is applied for a variety of anomalous bronchi that supply the upper lobe or its apical segment. The anomalous bronchi may originate from trachea or main bronchi (Figure 28)[38]. Patients are usually asymptomatic. However, in patients presenting with persistent/recurrent pneumonia or atelectasis of the upper lobe, a possibility of tracheal bronchus should be kept in mind.

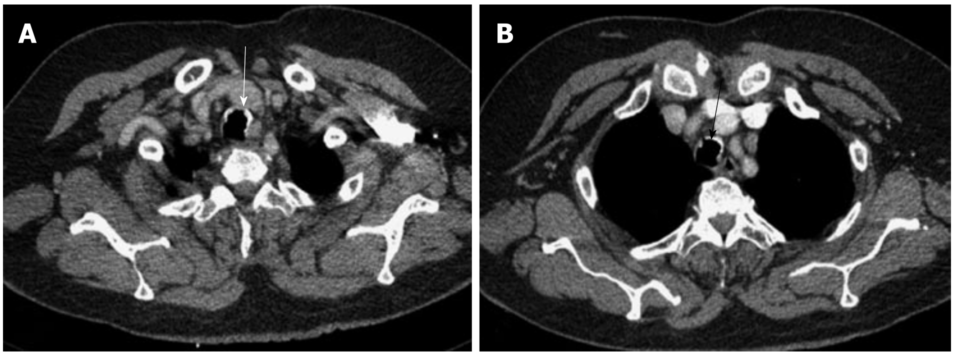

Figure 27 Tracheobronchopathia osteochondrodisplastica. Axial images of thorax (A and B) show irregular nodular thickening with foci of calcification involving the anterior and lateral walls of trachea (arrows). There is characteristic sparing of the posterior tracheal membrane.

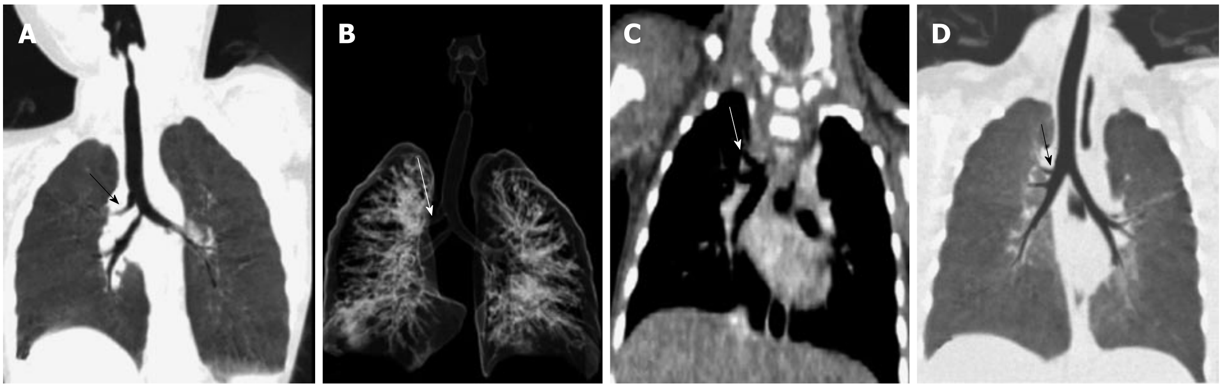

Figure 28 Displaced bronchus. Case 1: Coronal MinIP (A) and VRT (B) images show anomalous origin of right upper lobe bronchus from trachea-"Pig bronchus/ bronchus suis" (arrow). Case 2: Coronal MPR (C) and MinIP (D) images show anomalous origin of the right apical segment bronchus from right main bronchus (arrow). MPR: Multiplanar reformation; MinIP: Minimum intensity projection; VRT: Volume rendering technique.

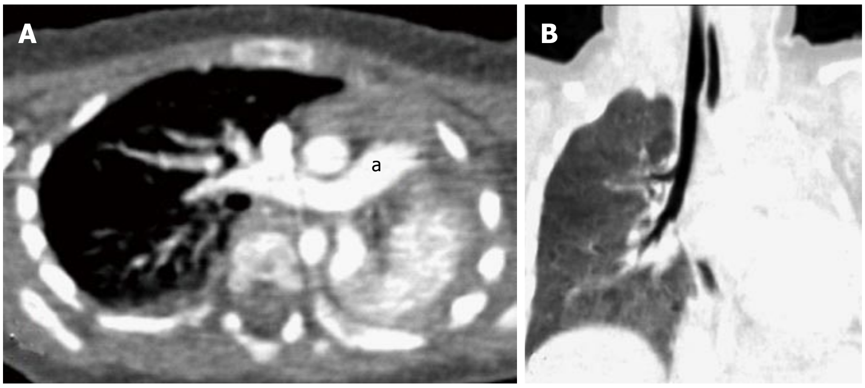

Figure 29 Bronchial agenesis. Axial (A) and coronal MinIP (B) images show absent left lung with left sided mediastinal shift and volume loss. Main pulmonary artery (a) continues as right pulmonary artery with absent left pulmonary artery. There is also associated absence of left main bronchus. MinIP: Minimum intensity projection.

Bronchial agenesis

Bronchial agenesis is always associated with congenital absence of lung, *i.e.*, pulmonary agenesis and absence of its vascular supply[54]. Bilateral lung agenesis is always fatal in antenatal or immediate postnatal period. Infants with unilateral agenesis usually survive, but they may have associated congenital heart disease, trachea-esophageal atresia, spinal and renal anomalies[39]. These neonates usually present with respiratory distress. They can also be discovered incidentally in older children and adults. MDCT is the modality of choice as it can easily diagnose the absence of lung parenchyma, bronchus and pulmonary vessels (Figure 29).

CONCLUSION

MDCT is a rapid and non-invasive investigation for evaluation of patients with suspected airway pathology. It is highly accurate in evaluating intraluminal obstruction, extraluminal vascular anomalies and airway wall defects. The entire extra luminal anatomy anatomy is clearly delineated and any associated finding within the mediastinum or lung parenchyma is also clearly depicted. Therefore, it provides a comprehensive information about the extent of disease process including the luminal and extraluminal components. In addition, VB can also help access sites beyond a proximal stenosis which cannot be seen on conventional bronchoscopy due to the inability of bronchoscope to negotiate through a proximal occlusive lesion. Therefore MDCT has an immense potential to emerge as a non-invasive, rapidly reproducible investigation tool which can provide information about primary airway disease as well as extraluminal pathologies affecting the airway.

REFERENCES

1 **Burke AJ**, Vining DJ, McGuirt WF, Postma G, Browne JD. Evaluation of airway obstruction using virtual endoscopy. *Laryngoscope* 2000; **110**: 23-29 [PMID: 10646710 DOI: 10.1097/00005537-200001000-00005]

2 **Stern RL**, Cline HE, Johnson GA, Ravin CE. Three-dimensional imaging of the thoracic cavity. *Invest Radiol* 1989; **24**: 282-288 [PMID: 2745007 DOI: 10.1097/00004424-198904000-00005]

3 **Hu H**, He HD, Foley WD, Fox SH. Four multidetector-row helical CT: image quality and volume coverage speed. *Radiology* 2000; **215**: 55-62 [PMID: 10751468 DOI: 10.1148/radiology.215.1.r00ap3755]

4 **Rydberg J**, Buckwalter KA, Caldemeyer KS, Phillips MD, Conces DJ, Aisen AM, Persohn SA, Kopecky KK. Multisection CT: scanning techniques and clinical applications. *Radiographics* 2000; **20**: 1787-1806 [PMID: 11112829 DOI: 10.1148/radiographics.20.6.g00nv071787]

5 **Ravenel JG**, McAdams HP, Remy-Jardin M, Remy J. Multidimensional imaging of the thorax: practical applications. *J Thorac Imaging* 2001; **16**: 269-281 [PMID: 11685092 DOI: 10.1097/00005382-200110000-00008]

6 **Boiselle PM**, Reynolds KF, Ernst A. Multiplanar and three-dimensional imaging of the central airways with multidetector CT. *AJR Am J Roentgenol* 2002; **179**: 301-308 [PMID: 12130424 DOI: 10.2214/ajr.179.2.1790301]

7 **Remy-Jardin M**, Remy J, Artaud D, Fribourg M, Naili A. Tracheobronchial tree: assessment with volume rendering--technical aspects. *Radiology* 1998; **208**: 393-398 [PMID: 9680565 DOI: 10.1148/radiology.208.2.9680565]

8 **Higgins WE**, Ramaswamy K, Swift RD, McLennan G, Hoffman EA. Virtual bronchoscopy for three--dimensional pulmonary image assessment: state of the art and future needs. *Radiographics* 1998; **18**: 761-778 [PMID: 9599397 DOI: 10.1148/radiographics.18.3.9599397]

9 **Kay CL**, Evangelou HA. A review of the technical and clinical aspects of virtual endoscopy. *Endoscopy* 1996; **28**: 768-775 [PMID: 9007432 DOI: 10.1055/s-2007-1005603]

10 **Holbert JM**, Strollo DC. Imaging of the normal trachea. *J Thorac Imaging* 1995; **10**: 171-179 [PMID: 7674430 DOI: 10.1097/00005382-199522000-00003]

11 **Boiselle PM**, Lee KS, Ernst A. Multidetector CT of the central airways. *J Thorac Imaging* 2005; **20**: 186-195 [PMID: 16077334 DOI: 10.1097/01.rti.0000171624.84951.f2]

12 **Gamsu G**, Webb WR. Computed tomography of the trachea: normal and abnormal. *AJR Am J Roentgenol* 1982; **139**: 321-326 [PMID: 6979885 DOI: 10.2214/ajr.139.2.321]

13 **Naidich DP**, Webb WR. Introduction to imaging methodology and airway anatomy. In: Naidich DP, Webb WR, Grenier PA, Gefter WB, Harkin TJ, editor. Imaging of the Airways Functional and Radiologic Correlations. Philadelphia: Lippincott Williams and Wilkins, 2005: 1-28

14 **Ngo AV**, Walker CM, Chung JH, Takasugi JE, Stern EJ, Kanne JP, Reddy GP, Godwin JD. Tumors and tumorlike conditions of the large airways. *AJR Am J Roentgenol* 2013; **201**: 301-313 [PMID: 23883210 DOI: 10.2214/AJR.12.9043]

15 **Jemal A**, Siegel R, Xu J, Ward E. Cancer statistics, 2010. *CA Cancer J Clin* 2010; **60**: 277-300 [PMID: 20610543 DOI: 10.3322/caac.20073]

16 **Hartman TE**, Tazelaar HD, Swensen SJ, Müller NL. Cigarette smoking: CT and pathologic findings of associated pulmonary diseases. *Radiographics* 1997; **17**: 377-390 [PMID: 9084079 DOI: 10.1148/radiographics.17.2.9084079]

17 **Travis WD**. Pathology of lung cancer. *Clin Chest Med* 2002; **23**: 65-81, viii [PMID: 11901921 DOI: 10.1016/S0272-5231(03)00061-3]

18 **Pearlberg JL**, Sandler MA, Lewis JW, Beute GH, Alpern MB. Small-cell bronchogenic carcinoma: CT evaluation. *AJR Am J Roentgenol* 1988; **150**: 265-268 [PMID: 2827450 DOI: 10.2214/ajr.150.2.265]

19 **Rady PL**, Schnadig VJ, Weiss RL, Hughes TK, Tyring SK. Malignant transformation of recurrent respiratory papillomatosis associated with integrated human papillomavirus type 11 DNA and mutation of p53. *Laryngoscope* 1998; **108**: 735-740 [PMID: 9591556 DOI: 10.1097/00005537-199805000-00021]

20 **Park CM**, Goo JM, Lee HJ, Kim MA, Lee CH, Kang MJ. Tumors in the tracheobronchial tree: CT and FDG PET features. *Radiographics* 2009; **29**: 55-71 [PMID: 19168836 DOI: 10.1148/rg.291085126]

21 **Jeong SY**, Lee KS, Han J, Kim BT, Kim TS, Shim YM, Kim J. Integrated PET/CT of salivary gland type carcinoma of the lung in 12 patients. *AJR Am J Roentgenol* 2007; **189**: 1407-1413 [PMID: 18029878 DOI: 10.2214/AJR.07.2652]

22 **Hartman TE**, Primack SL, Lee KS, Swensen SJ, Müller NL. CT of bronchial and bronchiolar diseases. *Radiographics* 1994; **14**: 991-1003 [PMID: 7991828 DOI: 10.1148/radiographics.14.5.7991828]

23 **Gustafsson BI**, Kidd M, Chan A, Malfertheiner MV, Modlin IM. Bronchopulmonary neuroendocrine tumors. *Cancer* 2008; **113**: 5-21 [PMID: 18473355 DOI: 10.1002/cncr.23542]

24 **Marom EM**, Goodman PC, McAdams HP. Focal abnormalities of the trachea and main bronchi. *AJR Am J Roentgenol* 2001; **176**: 707-711 [PMID: 11222209 DOI: 10.2214/ajr.176.3.1760707]

25 **Chang CH**, Wang HC, Wu MT, Lu JY. Virtual bronchoscopy for diagnosis of recurrent respiratory papillomatosis. *J Formos Med Assoc* 2006; **105**: 508-511 [PMID: 16801040]

26 **Kozower BD**, Javiden-Nejad C, Lewis JS, Safdar S, Cooper JD, Patterson GA. Clinical-pathologic conference in general thoracic surgery: malignant transformation of recurrent respiratory papillomatosis. *J Thorac Cardiovasc Surg* 2005; **130**: 1190-1193 [PMID: 16214538 DOI: 10.1016/j.jtcvs.2005.06.036]

27 **Taha MS**, Mostafa BE, Fahmy M, Ghaffar MK, Ghany EA. Spiral CT virtual bronchoscopy with multiplanar reformatting in the evaluation of post-intubation tracheal stenosis: comparison between endoscopic, radiological and surgical findings. *Eur Arch Otorhinolaryngol* 2009; **266**: 863-866 [PMID: 19002699 DOI: 10.1007/s00405-008-0854-y]

28 **Lee KS**, Yoon JH, Kim TK, Kim JS, Chung MP, Kwon OJ. Evaluation of tracheobronchial disease with helical CT with multiplanar and three-dimensional reconstruction: correlation with bronchoscopy. *Radiographics* 1997; **17**: 555-567; discussion 568-570 [PMID: 9153696 DOI: 10.1148/radiographics.17.3.9153696]

29 **Koşucu P**, Ahmetoğlu A, Koramaz I, Orhan F, Ozdemir O, Dinç H, Okten A, Gümele HR. Low-dose MDCT and virtual bronchoscopy in pediatric patients with foreign body aspiration. *AJR Am J Roentgenol* 2004; **183**: 1771-1777 [PMID: 15547227 DOI: 10.2214/ajr.183.6.01831771]

30 **Applegate KE**, Dardinger JT, Lieber ML, Herts BR, Davros WJ, Obuchowski NA, Maneker A. Spiral CT scanning technique in the detection of aspiration of LEGO foreign bodies. *Pediatr Radiol* 2001; **31**: 836-840 [PMID: 11727016 DOI: 10.1007/s002470100001]

31 **Karakoç F**, Karadağ B, Akbenlioğlu C, Ersu R, Yildizeli B, Yüksel

M, Dağli E. Foreign body aspiration: what is the outcome? *Pediatr Pulmonol* 2002; **34**: 30-36 [PMID: 12112794 DOI: 10.1002/ppul.10094]

32 **Khan MF**, Herzog C, Ackermann H, Wagner TO, Maataoui A, Harth M, Abolmaali ND, Jacobi V, Vogl TJ. Virtual endoscopy of the tracheo-bronchial system: sub-millimeter collimation with the 16-row multidetector scanner. *Eur Radiol* 2004; **14**: 1400-1405 [PMID: 15133710 DOI: 10.1007/s00330-004-2325-1]

33 **Slim MS**, Yacoubian HD. Complications of foreign bodies in the tracheobronchial tree. *Arch Surg* 1966; **92**: 388-393 [PMID: 5906833 DOI: 10.1001/archsurg.1966.01320210068013]

34 **Zerella JT**, Dimler M, McGill LC, Pippus KJ. Foreign body aspiration in children: value of radiography and complications of bronchoscopy. *J Pediatr Surg* 1998; **33**: 1651-1654 [PMID: 9856887 DOI: 10.1016/S0022-3468(98)90601-7]

35 **Seo JB**, Song KS, Lee JS, Goo JM, Kim HY, Song JW, Lee IS, Lim TH. Broncholithiasis: review of the causes with radiologic-pathologic correlation. *Radiographics* 2002; **22** Spec No: S199-S213 [PMID: 12376611 DOI: 10.1148/radiographics.22.suppl_1.g02oc07s199]

36 **Moriwaki Y**, Sugiyama M, Matsuda G, Toyoda H, Kosuge T, Uchida K, Fukuyama H, Iwashita M, Morimura N, Suzuki J, Yamamoto T, Suzuki N. Usefulness of the 3-dimensionally reconstructed computed tomography imaging for diagnosis of the site of tracheal injury (3D-tracheography). *World J Surg* 2005; **29**: 102-105 [PMID: 15599743 DOI: 10.1007/s00268-004-7433-1]

37 **Turner A**, Gavel G, Coutts J. Vascular rings--presentation, investigation and outcome. *Eur J Pediatr* 2005; **164**: 266-270 [PMID: 15666159 DOI: 10.1007/s00431-004-1607-6]

38 **Berrocal T**, Madrid C, Novo S, Gutiérrez J, Arjonilla A, Gómez-León N. Congenital anomalies of the tracheobronchial tree, lung, and mediastinum: embryology, radiology, and pathology. *Radiographics* 2004; **24**: e17 [PMID: 14610245 DOI: 10.1148/rg.e17]

39 **Lee EY**, Boiselle PM, Cleveland RH. Multidetector CT evaluation of congenital lung anomalies. *Radiology* 2008; **247**: 632-648 [PMID: 18487532 DOI: 10.1148/radiol.2473062124]

40 **Kimura-Hayama ET**, Meléndez G, Mendizábal AL, Meave-González A, Zambrana GF, Corona-Villalobos CP. Uncommon congenital and acquired aortic diseases: role of multidetector CT angiography. *Radiographics* 2010; **30**: 79-98 [PMID: 20083587 DOI: 10.1148/rg.301095061]

41 **Schanker HM**, Rachelefsky G, Siegel S, Katz R, Spector S, Rohr A, Rodriquiz C, Woloshin K, Papanek PJ. Immediate and delayed type hypersensitivity to malathion. *Ann Allergy* 1992; **69**: 526-528 [PMID: 1471787]

42 **Aktoğu S**, Yuncu G, Halilçolar H, Ermete S, Buduneli T. Bronchogenic cysts: clinicopathological presentation and treatment. *Eur Respir J* 1996; **9**: 2017-2021 [PMID: 8902460 DOI: 10.1183/09031936.96.09102017]

43 **McAdams HP**, Kirejczyk WM, Rosado-de-Christenson ML, Matsumoto S. Bronchogenic cyst: imaging features with clinical and histopathologic correlation. *Radiology* 2000; **217**: 441-446 [PMID: 11058643 DOI: 10.1148/radiology.217.2.r00nv19441]

44 **Williams HJ**, Johnson KJ. Imaging of congenital cystic lung lesions. *Paediatr Respir Rev* 2002; **3**: 120-127 [PMID: 12297058 DOI: 10.1016/S1526-0550(02)00006-9]

45 **Torres de Amorim e Silva CJ**, Fink AM. Case 137: Pneumonia and bronchiectasis secondary to unrecognized peanut impaction. *Radiology* 2008; **248**: 1080-1082 [PMID: 18710997 DOI: 10.1148/radiol.2483050725]

46 **Urkin J**, Bar-David Y. Respiratory distress secondary to esophageal foreign body: a case report. *ScientificWorldJournal* 2006; **6**: 16-19 [PMID: 16432624 DOI: 10.1100/tsw.2006.08]

47 **Edlavitch SA**, Crow R, Burke GL, Huber J, Prineas R, Blackburn H. The effect of the number of electrocardiograms analyzed on cardiovascular disease surveillance: the Minnesota Heart Survey (MHS). *J Clin Epidemiol* 1990; **43**: 93-99 [PMID: 2319286 DOI: 10.1002/ppul.22728]

48 **Grenier PA**, Beigelman-Aubry C, Brillet PY. Nonneoplastic tracheal and bronchial stenoses. *Radiol Clin North Am* 2009; **47**: 243-260 [PMID: 19249454 DOI: 10.1016/j.rcl.2008.11.011]

49 **Trigaux JP**, Hermes G, Dubois P, Van Beers B, Delaunois L, Jamart J. CT of saber-sheath trachea. Correlation with clinical, chest radiographic and functional findings. *Acta Radiol* 1994; **35**: 247-250 [PMID: 8192961 DOI: 10.1177/028418519403500310]

50 **Shin MS**, Jackson RM, Ho KJ. Tracheobronchomegaly (Mounier-Kuhn syndrome): CT diagnosis. *AJR Am J Roentgenol* 1988; **150**: 777-779 [PMID: 3258088 DOI: 10.2214/ajr.150.4.777]

51 **Jain P**, Dave M, Singh DP, Kumawat DC, Babel CS. Mounier-Kuhn syndrome. *Indian J Chest Dis Allied Sci* 2002; **44**: 195-198 [PMID: 12206481]

52 **Chroneou A**, Zias N, Gonzalez AV, Beamis JF. Tracheobronchopathia osteochondroplastica. An underrecognized entity? *Monaldi Arch Chest Dis* 2008; **69**: 65-69 [PMID: 18837419]

53 **Zack JR**, Rozenshtein A. Tracheobronchopathia osteochondroplastica: report of three cases. *J Comput Assist Tomogr* 2002; **26**: 33-36 [PMID: 11801902 DOI: 10.1097/00004728-200201000-00006]

54 **Ghaye B**, Szapiro D, Fanchamps JM, Dondelinger RF. Congenital bronchial abnormalities revisited. *Radiographics* 2001; **21**: 105-119 [PMID: 11158647 DOI: 10.1148/radiographics.21.1.g01ja06105]

P- Reviewer: Chow J, Yazdi HR **S- Editor**: Gong ZM **L- Editor**: A
E- Editor: Wu HL

WJR World Journal of Radiology

Submit a Manuscript: http://www.wjgnet.com/esps/
Help Desk: http://www.wjgnet.com/esps/helpdesk.aspx
DOI: 10.4329/wjr.v7.i12.475

World J Radiol 2015 December 28; 7(12): 475-483
ISSN 1949-8470 (online)

MINIREVIEWS

Amyloid positron emission tomography and cognitive reserve

Matteo Bauckneht, Agnese Picco, Flavio Nobili, Silvia Morbelli

Matteo Bauckneht, Silvia Morbelli, Nuclear Medicine Unit, Department of Health Science, University of Genoa and IRCCS AOU San Martino-IST, 16132 Genoa, Italy

Agnese Picco, Flavio Nobili, Clinical Neurology Unit, Department of Neuroscience, University of Genoa and IRCCS AOU San Martino-IST, 16132 Genoa, Italy

Author contributions: Morbelli S designed the reivew; Bauckneht M performed literature search and draft the manuscript; Picco A, Nobili F and Morbelli S made critical revisions related to important intellectual content of the manuscript; Morbelli S have given final approval of the version of the article to be published; all authors read and approved the final manuscript.

Conflict-of-interest statement: The authors have no conflict of interest to declare.

Correspondence to: Silvia Morbelli, MD, PhD, Nuclear Medicine Unit, Department of Health Science, University of Genoa and IRCCS AOU San Martino-IST, Largo R. Benzi 10, 16132 Genoa,
Italy. silviadaniela.morbelli@hsanmartino.it
Telephone: +39-10-5552027
Fax: +39-10-5556911

Received: July 28, 2015
Peer-review started: July 29, 2015
First decision: August 14, 2015
Revised: September 1, 2015
Accepted: October 16, 2015
Article in press: October 19, 2015
Published online: December 28, 2015

Abstract

Alzheimer's disease (AD) is characterized by a non-linear progressive course and several aspects influence the relationship between cerebral amount of AD pathology and the clinical expression of the disease. Brain cognitive reserve (CR) refers to the hypothesized capacity of an adult brain to cope with brain damage in order to minimize symptomatology. CR phenomenon contributed to explain the disjunction between the degree of neurodegeneration and the clinical phenotype of AD. The possibility to track brain amyloidosis (Aβ) *in vivo* has huge relevance for AD diagnosis and new therapeutic approaches. The clinical repercussions of positron emission tomography (PET)-assessed Aβ load are certainly mediated by CR thus potentially hampering the prognostic meaning of amyloid PET in selected groups of patients. Similarly, amyloid PET and cerebrospinal fluid amyloidosis biomarkers have recently provided new evidence for CR. The present review discusses the concept of CR in the framework of available neuroimaging studies and specifically deals with the reciprocal influences between amyloid PET and CR in AD patients and with the potential consequent interventional strategies for AD.

Key words: Cognitive reserve; Amyloid positron emission tomography; Mild cognitive impairment; Alzheimer disease; Brain

Core tip: Given the large population of aging individuals and the consequent huge, progressive Alzheimer's disease (AD)-related healthcare costs, it is critical to find effective therapeutic strategies to mitigate the AD cognitive dysfunction. Accordingly, understanding the neurobiological mechanisms underlying cognitive reserve (CR) is of utmost importance. Instead, Amyloid

positron emission tomography (PET) has recently improved our knowledge in the field of CR. The present review discusses the concept of CR in the framework of available neuroimaging studies and specifically deals with the reciprocal influences between Amyloid PET and CR in AD patients and with the potential consequent interventional strategies for AD.

Bauckneht M, Picco A, Nobili F, Morbelli S. Amyloid positron emission tomography and cognitive reserve. *World J Radiol* 2015; 7(12): 475-483 Available from: URL: http://www.wjgnet.com/1949-8470/full/v7/i12/475.htm DOI: http://dx.doi.org/10.4329/wjr.v7.i12.475

INTRODUCTION

Alzheimer's disease (AD) is the most common neurodegenerative cause of dementia and affects around 10% of individuals over age 65 and up to 40% of individuals over age 85[1]. In 2010 it has been estimated that 4.7 million individuals aged 65 years or older were affected by AD in the United States with the total number of people with AD dementia projected to be 13.8 million in 2050[1]. AD is characterized by a progressive deterioration in memory and other cognitive abilities as well as in capability for independent living. The course of AD is variable[2], but symptoms tend to develop over the same general steps: Mild cognitive impairment (MCI) (which in typical forms begin with episodic memory impairment), slow, progressive affection of other cognitive domains and, eventually, dementia[3]. Amyloid deposition and tau pathology (neurofibrillary tangles) within the cerebral cortex are the neuropathological hallmarks of AD[4]. Several lines of evidence, demonstrated that AD is characterized by a non-linear progressive course and that several aspects may influence the relationship between cerebral amount of AD pathology and its clinical expression[3,5,6]. In fact, it has been shown that at least 20% of elderly people who are cognitively normal before death show postmortem findings sufficient to fulfill neuropathological criteria for AD[7,8]. On the other hand, several studies showed that biological factors such as the age of onset and the expression of Apolipoprotein E genotype, can be associated with a faster cognitive decline[9,10]. Similarly, increasing evidence has highlighted the role of oxidative stress in AD, because of the increased production of reactive oxygen species and the influence of oxidative stress on brain energy metabolism[11].

Accordingly clinical expression of AD is critically affected by the resilience of the individual brain to molecular mechanisms and neuropathology[12]. These complex mechanisms have been historically referred to as Brain Cognitive Reserve phenomenon (CR[13]). CR refers to the hypothesized capacity of an adult brain to cope with brain damage in order to minimize symptomatology[13]. Individuals with high reserve are thought to have either higher number of neurons and synapses ("brain reserve"), and/or a better ability to put in place alternative strategies or compensatory mechanisms ("cognitive reserve") than individuals with low reserve[12,14]. Therefore, CR phenomenon may also at least partially explain the disjunction between the degree of neurodegeneration and the clinical phenotype of AD.

In this framework it has been hypothesized that not only duration of formal education, but also the quality of performance throughout the years can influence CR and the general brain reaction to AD pathology in clinical terms[12]. First evidence for CR date back to the 80's, when neuropathological studies highlighted the existence of subgroups of cognitively intact subjects matching criteria for AD at autopsy[7]. In the following decades, structural [magnetic resonance imaging (MRI)] and functional (MRI, SPECT and PET) studies have confirmed the existence of CR and allowed a better comprehension and anatomical localization of this phenomenon. In more recent years, the availability of new molecular probes sensitive to amyloid-beta (Aβ) deposition have allowed the *in vivo* demonstration of amyloid load by means of PET (Amy-PET)[15-18]. The possibility to track Aβ pathology *in vivo* has huge relevance for AD diagnosis and clinical trials. The oldest and more extensively studied PET tracer for Amy-PET is the Carbon11 labeled pittsburgh compound B (PiB)[15]. More recently three fluorine18 labeled compounds have been developed. Following multicenter phase 3 trials, they were all approved both in the United States and Europe to *in vivo* image amyloid plaques[18-20]. Accordingly, appropriate use criteria have been now proposed for the use of Amy-PET[21]. Although obtaining *in vivo* information about the presence of amyloid pathology allowed a greater accuracy in the work up of patients with suspected AD, the clinical repercussions of PET-assessed Aβ load are certainly mediated by CR. In fact CR can potentially hamper the prognostic meaning of Amy-PET at least in selected groups of patients. On the other side CR phenomenon itself has gained renovated interest from the possibility of knowing and *in vivo* localizing Aβ load by means of PET thus providing further evidence for a more etiopathological effect of CR[22,23]. Therefore on the one side, Amy-PET [and cerebrospinal fluid (CSF) amyloidosis biomarkers] provide new evidence for CR, on the other side, CR has clinical and pathophysiological repercussion for the study of AD, especially now, in the era of brain amyloidosis biomarkers. The present review discusses the concept of CR in the framework of available neuroimaging studies and specifically deals with the reciprocal influences between Amy-PET and CR in AD patients and with the potential consequent interventional strategies for AD.

CONCEPT OF COGNITIVE RESERVE: PIONEERING STUDIES

Historically the first model proposed to explain CR was referred to quantitative measures of head circumference, brain size[24], and synaptic or neuronal count[25]. According to this approach, individuals with more neurons required more brain damage to reach a threshold of clinically evident dementia (passive model of CR). However, since the first studies on CR, subjects with either greater brain size, quantities of neurons or synapses were demonstrated to have different epidemiological/demographic features that can be responsible for CR and thus can serve as proxies for reserve. These factors include measures of educational attainment and socioeconomic status, such as income or occupational attainment. Similarly, physical activity and cognitive activity even during midlife have been associated with a reduced risk of AD[26,27]. However, since the first studies education has probably been the most widely used proxy for CR. In fact level of education is relatively easy to ascertain. Moreover, proposed model fitted to the epidemiological evidence that higher incidence of AD and other dementia was observed among elder populations with low levels of education[27]. However, this epidemiological approach lacks of anatomic localization and produces only indirect (based on neuropsychology) evidence about brain functional damage and networking[28].

CONRIBUTION OF NEUROIMAGING TO THE UNDERSTANDING OF CR

Due to these limitations many groups turned to functional neuroimaging approach, which is able to provide a more precise proxy measure about CR *in vivo*, thus allowing a more comprehensive understanding and localization of this phenomenon. In fact, while neuropsychological test results are influenced by the cognitive ability of the patient and his/her motivation to perform the tests, the imaging-assessed brain impairment more closely reflects the underlying brain damage (*i.e.,* neurodegeneration). In this line, functional neuroimaging supported the idea that even when neurodegeneration is higher in educated individuals, the clinical phenotype of AD may be similar to those in patients with lower education and less pathology[14]. Based on this integrated approach, CR can be defined as the difference between an individual's expected (based on neuroimaging) and actual (assessed by neuropsychology) cognitive performance.

To elucidate these mechanisms, several imaging studies have originally used resting regional cerebral blood flow (rCBF) PET measurement as a surrogate of AD pathology[29]. In these studies correlation between rCBF on one side and education and life-time activities score on the other was tested and an inverse correlation with rCBF in temporal-parietal-occipital areas was demonstrated in AD patients[29].

Similar results were obtained by means of 3D MRI analysis demonstrating that education increases regional cortical thickness in healthy controls, while it is inversely correlated with regional cortical thicknesses in temporal, parietal and occipital regions in AD patients[30]. Finally, FDG-PET studies demonstrated that reserve mechanism are already at work in patients with amnestic mild cognitive impairment (aMCI) and prodromal Alzheimer's disease (pAD) patients[14,31]. In fact, even in this early stages, AD patients with higher education showed more severe and extended "posterior" AD typical brain hypometabolism with respect to poorly educated patients expressing the same level of cognitive symptoms[14,31]. This means that in early stage of disease CR may have meaningful repercussions for the clinical diagnosis of AD as highly educated prodromal AD patients can clinically hide the disease for a longer period of time. Accordingly, new lines of research focused on the mechanism(s) specifically allowing highly educated AD to cope with their greater brain damage. These mechanisms, evaluated by means of functional MRI and H215O PET activation studies as well with resting FDG PET, allowed to develop the so-called "active model" of CR[29,32]. As CR allows maintenance of effective function across a wide range of activities despite the presence of brain pathology, it can be hypothesized that a specific network (or multiple integrated networks) are able to sustain CR and thus patients' cognitive function and independent activities of daily leaving[33,34]. To investigate this hypothesis, Stern's group[35] carried out a fMRI study by scanning young and elder subjects while performing two different tasks underlying two different cognitive domains and activations were regressed onto putative CR variables. A common network was actually identified including bilateral superior and medial frontal gyri thus suggesting a central role of the frontal cortex in CR-mediating mechanism[35]. Another possible strategy to identify a specific CR network is the so-called metabolic connectivity analysis of brain ^{18}F-FDG PET studies[36]. In fact by calculating correlation coefficients -or pattern of intercorrelations- between values of FDG uptake, it is possible to estimate the functional association between cerebral areas[36]. Therefore interregional correlations of metabolic glucose rates can be regarded in terms of "traffic (metabolic-functional connectivity) in the anatomical 'roads' present in the brain" which, by contrast, can be investigated by other neuroimaging methods such as diffusion tensor imaging[37,38]. Morbelli *et al*[14] investigated functional mechanisms underling CR in 64 early stage AD patients and 90 healthy controls who underwent brain ^{18}F-FDG PET. Highly and poorly educated subjects were compared bidirectionally and with age and education-matched controls. It was indeed demonstrated that although AD-typical damage is more prominent in highly educated subjects, highly educated pAD have also a relatively higher metabolic levels with respect to poorly educated patients in the right inferior, middle, and superior frontal gyri with respect to less educated AD subjects.

These regions, which corresponded to the right dorsolateral prefrontal cortex (DLFC), were then included as covariates in the subsequent metabolic connectivity analysis in highly and poorly educated AD patients. As the results, in highly educated AD patients, metabolism of the DLFC correlated significantly with that of several cortical areas in both hemispheres, while it was basically only auto correlated in poorly educated AD. Accordingly this metabolic connectivity analysis supports the existence of a network mediating CR and is anatomically consistent with a crucial role of lateral frontal cortex in CR-mediating mechanism. However, all these analyses did not completely elucidate whether these functional networks are due to preserved functional connections that are physiologically present in more educated subjects (*i.e.*, the brain reserve component of cognitive reserve) or to the recruitment of alternative neural networks able to support cognitive function just in the presence of disease related damage elsewhere (*i.e.,* the brain compensation component of cognitive reserve)[33]. To specifically address this aspect, the same analysis was extended to the control groups and demonstrated that the large bilateral fronto-temporal-limbic metabolic network related to CR was actually present and topographically similar in highly educated controls. However this network was quantitatively less pronounced with respect to highly educated AD patients thus demonstrating that CR in early AD patients with a high level of education is a result of both neural reserve and neural compensation[14]. The importance of reinforcement in brain connectivity in healthy elders was further confirmed in a multimodal imaging study involving 36 healthy elders presenting normal cognition and a negative florbetapir-PET scan[39]. In fact, seed connectivity analyses of resting state fMRI showed that education was positively related to the magnitude of functional connectivity between the anterior cingulate cortex and the hippocampus as well as the inferior frontal lobe, posterior cingulate cortex and angular gyrus.

IMPLICATION OF CR FOR CLINICAL USE

AMYLOID IMAGING

Amy-PET offers great promise to facilitate the evaluation of patients in a clinical setting, to improve our understanding of AD pathophysiology and to advance the development of effective therapy.

In vivo PET studies have shown an increased uptake of amyloid ligand 11C-labeled Pittsburgh Compound B ([11C]PIB) and fluorinated Amy-PET tracers in AD and mild cognitive impairment patients, especially in the frontal, parietal, and temporal cortices and in the posterior cingulate, which indicates an increased amyloid accumulation in these areas[40,41]. However, in agreement with reports that significant Aβ deposits can be found in the brain of cognitively normal elderly individuals at autopsy, Amy-PET studies revealed that 20%-40% of cognitively unimpaired individuals over the age of 65 years can have brain uptake above a predetermined threshold for AD in at least one region of interest[42,43]. This evidence can be at least partially linked to CR phenomenon. In fact it was further demonstrated that even in patients with AD, the well-known greater posterior hypometabolism present in highly educated pAD is paralleled by a greater Amy-PET tracer's uptake especially in the ventrolateral frontal cortex[44]. While only longitudinal evaluation of Amy-PET positive cognitively normal subjects can allow to access their long term outcome, this evidence have important diagnostic repercussion. In fact as CR is influenced by several (often measurable) epidemiological and social factors, these factors could be taken into account to support the final diagnosis of probable AD by means of Amy-PET or CSF amyloidosis biomarkers. Kemppainen *et al*[44] tested this hypothesis by assessing whether factors thought to influence the association of AD pathology and dementia help to accurately identify dementia of the Alzheimer type when considered together with Amy-PET. They generated receiver operating characteristic curves to compare the predictive accuracy of using Amy-PET alone or Amy-PET together with the above mentioned factors with the aim to tell apart AD patients from subjects with normal cognition. In this study, factors reported to influence associations between AD pathology and dementia demonstrated to improve the predictive accuracy of amyloid imaging for the identification of symptomatic AD. In fact, if a scan is performed and found positive (*i.e.,* in depressed patients with concurrent cognitive impairment), the risk of incidental brain amyloidosis must be taken into consideration when defining probable diagnosis and planning subsequent management[45]. In this scenario high prognostic value of Amy-PET is present in case of a negative scan thus virtually excluding AD and encouraging a more vigorous evaluation of alternative diagnoses and treatment (for example when differential diagnosis was defined with respect to depression)[45]. By contrast to exclude the presence of "incidental" positivity of Amy-PET the use of different biomarkers (*i.e.,* biomarkers of neurodegeneration) can be proposed to support a diagnosis of AD. In fact glucose hypometabolism as assessed by means of ^{18}F-FDG PET as well as brain atrophy are more directly associated with neurodegeneration and thus with concurrent cognitive function[46]. Noteworthy, if CR phenomenon is at work, PET-assessed hypometabolism might be markedly reduced even in presence of a mild cognitive impairment. The validity of this approach have been recently confirmed by a large retrospective multicenter study showing that, in clinical setting, the combined use of both amyloid and neuronal injury markers offers the most accurate prognosis in MCI patients[47]. Besides underlying the importance of integrating Amy-PET with neurodegeneration biomarkers, the issue of positive Amy-PET in cognitive normal subjects further supports the need of a standardized approach

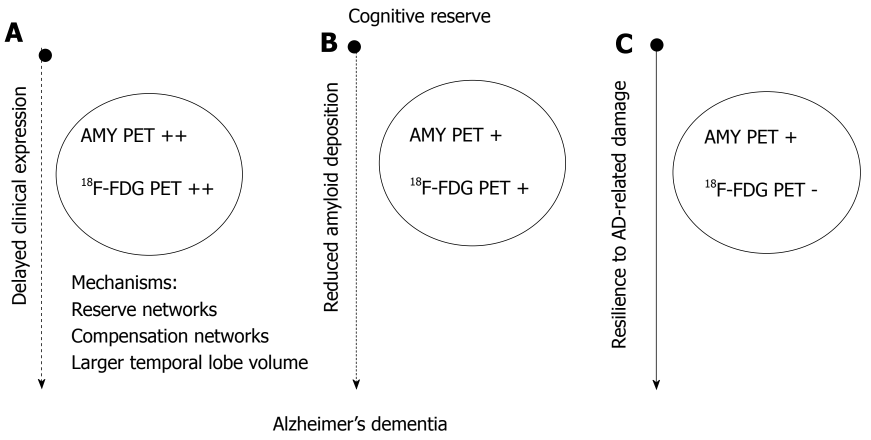

Figure 1 Schematic representation of the possible mechanisms mediating the effect of cognitive reserve on the onset of Alzheimer's dementia and corresponding expected results on ^{18}F-FDG and amyloid positron emission tomography. According to hypothesis (A) cognitive reserve (CR) would simply delay the clinical expression of the disease. In fact despite amyloid positron emission tomography (PET) and FDG PET marked positivity patients are able to delay symptoms thanks to compensative functional networks and/or structural features such as larger temporal lobe volume[14,51]. Hypothesis (B) admits an opposite scenario in which, CR would prevent/delay amyloid deposition and Alzheimer's dementia (AD) pathology and thus neuronal damage and dementia onset[17]. Finally hypothesis (C) could coexist with either of the first two and would explain the effect of CR as a sort of brain resilience despite AD pathology thus allowing a relatively preserved ^{18}F-FDG PET scan for a longer period of time[59]. Amy-PET: Amyloid PET; ++: Markedly positive scan; +: Positive scan; -: Negative/relatively preserved scan.

to Amy-PET quantification. In fact, to date there's still considerable variability in the numbers reported as quantitative outcome measures of tracer retention. Many international efforts are ongoing to address the problem of Amy-PET quantification[48]. Besides the increased accuracy and consistency potentially provided by tracer binding quantification, a further possible benefit would be related to the possibility of defining three ranges of amyloid deposition: (1) the amyloid-negative range; (2) the "AD-like" range; and (3) the "just-positive" range[48,49]. A greater comprehension of this latter range may be of interest to better differentiated "incidental" amyloid load from amyloid load in the AD-like range in cognitively intact subjects with greater CR.

IMPLICATION OF AMYLOID IMAGING FOR COMPREHENSION OF CR

Many implications have been derived from CR for the clinical use of Amy-PET. Similarly, CR has gained new evidence and new interest from the availability of Amy-PET. As mentioned, patients with mild AD dementia and higher education (*i.e.,* 15 or more years of education) were found to have higher uptake of amyloid PET tracers in the frontal cortex compared with patients with lower education (*i.e.,* 6 years of education)[6]. These results confirm that highly educated individuals manifest mild AD later on in the clinical course of the disease when more Aβ pathology is present thus supporting CR hypothesis.

However the availability of this information during life and the possibility to correlate this finding with other biomarkers have provided novel evidence for CR. This information can be relevant for AD model approach and biomarkers cascade in more comprehensive way. In fact, Chételat *et al*[50] correlated Amy-PET and brain structure data and cognitive performance in subjects with and without memory complaints. They demonstrated that Amy-PET positive subjects without memory complaints had larger temporal lobes and better verbal learning performance than Amy-PET negative controls. On the opposite, Amy-PET positive subjects with subjective memory complaints had smaller regional brain volumes and worse global cognition than Amy-PET with memory complaints. Altogether these finding allow to propose a general model of interpretation. In fact the larger temporal lobes may have been crucial for Amy-PET positive subjects to maintain their cognitive ability while Amy-PET positive subjects with memory complaints might originally have less gray matter than those without memory complaints, and therefore had less CR[50,51] (Figure 1). Accordingly the availability of Amy-PET and this multi-biomarker approach provided *in vivo* evidence that improving brain structure (*i.e.,* through cognitive or physical activity) may help compensate for AD related damage.

NEW PERSPECTIVE ON AMYLOID PET AND CR

Given the large population of aging individuals and the consequent huge, progressive AD-related Healthcare Costs, it is critical to find effective therapeutic strategies to mitigate the AD cognitive dysfunction. Understanding the neurobiological mechanisms underlying CR is thus of utmost importance. First studies trying to simulate, measure and possibly influence the effect of CR on AD were performed in animal models. Environmental enrichment paradigms has been developed in rodents by manipulating the complexity of their social, cognitive, and sensorial environments[52]. These models are ideal to experimentally measure the effect of environmental stimulation on cognitive reserve. In addition, previous studies demonstrated that environmental enrichment triggers structural and biochemical modification on neurons[53], stimulates hippocampal neurogenesis in adult animals[54] and attenuate cognitive decline in transgenic models of familial AD[55]. Animal models may also serve to better define the specific age and time-frame in which exposure to environmental enrichment can still trigger functional compensation and mitigate memory dysfunction. Finally, the effect of environmental stimulation on neuropathological hallmarks of AD can be assessed *ex vivo* for example in mouse model of the disease. In this framework, Verret *et al*[22] examined whether exposure of a Tg2576 transgenic mouse model of AD to environmental enrichment at a specific period during the amyloidogenic process favored the establishment of a cognitive reserve. They demonstrated that environmental stimulation during early adulthood of mice - before amyloidogenesis has started - reduced the severity of AD-related cognitive deficits more efficiently than exposure later in life, when the pathology is already present. More importantly they highlighted *ex vivo* that, early-life environmental stimulation, slightly reduced forebrain surface covered by amyloid plaques (while not significantly impact remodeling in the hippocampus). These findings may open new scenarios related to the effect of CR in AD patients as they might suggest that cognitive activity may even modify amyloid deposition, rather than just compensating for it[51]. Amy-PET and CSF biomarkers may allow to test this hypothesis *in vivo* in humans. In this framework, Landau *et al*[17] aimed to assess the association between lifestyle practices (cognitive and physical activity) and β-amyloid deposition, measured with positron emission tomography using carbon [11C]PIB, in healthy elderly. Greater participation in cognitively stimulating activities across the lifespan, but particularly in early and middle life, was associated with reduced [11C]PIB uptake (taken into account age, sex, and education). Moreover, among older controls, those who were more involved in cognitively stimulating activities across the lifespan (especially during young and middle age) had brain amyloid levels comparable to young controls, while those who were poorly cognitively active had amyloid levels similar to AD patients. Other studies reported that CR-related factors such as physical exercise correlated with less Aβ accumulation, however results are not always consistent. In fact in some cases those effects reached significance only in ApoE4 carriers[56] and in other studies no evidence was highlighted concerning an effect of lifetime cognitive stimulation on the level of Aβ accumulation regardless of ApoE genotype[57].

Accordingly is still a matter of debate if cognitive/physical stimulation can really modify the underlying pathology of AD or if CR just gives a resilience to it (as in the original definition of CR[13]). However even in this latter case the availability of amyloidosis and neurodegeneration AD biomarkers can further clarify and possibly localize mechanism of resistance to AD-related damage. In other words: Should we just define CR as the use of pre-existing and/or compensative network or can we hypothesized that brains/neurons in subjects with higher CR may be less damaged by AD-related pathology and thus may demonstrate less neurodegeneration? A first answer to this question has been provided by Almeida *et al*[58] who aimed to measure whether cognitive reserve could weaken the relationship between age and AD biomarker levels. A cross-sectional cohort of 268 individuals (211 cognitively normal and 57 cognitively impaired subjects; average age 62 years) was evaluated with respect to Aβ42, t-tau, and p-tau immunoassays. The authors found that the difference in CSF phosphorylated tau (p-tau) and total tau (t-tau) between younger and older people was larger in subgroup of subjects with less than 16 years of education than it was in the subgroups with at least 16 years of schooling. These findings suggest that education could attenuate age-related increment in CSF p-tau and t-tau and might suggest a more general effect on age-related neurodegeneration. However, although raising interesting possibility and stimulating new interventional strategies in AD patients, this evidence need to be further tested especially with respect to its relevance for the future onset of dementia. In the next future, the availability not only of Amy-PET but also of Tau imaging (and thus the possibility to quantify and anatomically localize neurodegeneration[59]) will allow to track and localize the pathological biomarkers cascade of AD in earlier stage of the illness (Figure 1). In fact, given models in which molecular pathologic changes (β-amyloid deposition) may temporarily precede neurodegeneration by a substantial of time period[60], evaluation of just one of these two types of biomarkers do not allow to direct measure resilience to AD-related damage. Once entity, time-frame and individual peculiarity of this resilience will be identified, a more precise model of CR and its consequences on AD clinics will be defined thus finally elucidating (and selecting patients) for CR-related interventional approaches.

REFERENCES

1 **Hebert LE**, Weuve J, Scherr PA, Evans DA. Alzheimer disease in the United States (2010-2050) estimated using the 2010 census. *Neurology* 2013; **80**: 1778-1783 [PMID: 23390181 DOI: 10.1212/WNL.0b013e31828726f5]

2 **Tschanz JT**, Corcoran CD, Schwartz S, Treiber K, Green RC, Norton MC, Mielke MM, Piercy K, Steinberg M, Rabins PV, Leoutsakos JM, Welsh-Bohmer KA, Breitner JC, Lyketsos CG. Progression of cognitive, functional, and neuropsychiatric symptom domains in a population cohort with Alzheimer dementia: the Cache County Dementia Progression study. *Am J Geriatr Psychiatry* 2011; **19**: 532-542 [PMID: 21606896 DOI: 10.1097/JGP.0b013e3181faec23]

3 **Grober E**, Hall CB, Lipton RB, Zonderman AB, Resnick SM, Kawas C. Memory impairment, executive dysfunction, and intellectual decline in preclinical Alzheimer's disease. *J Int Neuropsychol Soc* 2008; **14**: 266-278 [PMID: 18282324 DOI: 10.1017/S1355617708080302]

4 **Hardy J**, Selkoe DJ. The amyloid hypothesis of Alzheimer's

disease: progress and problems on the road to therapeutics. *Science* 2002; **297**: 353-356 [PMID: 12130773]

5 **Cummings JL**, Vinters HV, Cole GM, Khachaturian ZS. Alzheimer's disease: etiologies, pathophysiology, cognitive reserve, and treatment opportunities. *Neurology* 1998; **51**: S2-S17; discussion S65-S67 [PMID: 9674758]

6 **Mungas D**, Reed BR, Jagust WJ, DeCarli C, Mack WJ, Kramer JH, Weiner MW, Schuff N, Chui HC. Volumetric MRI predicts rate of cognitive decline related to AD and cerebrovascular disease. *Neurology* 2002; **59**: 867-873 [PMID: 12297568]

7 **Katzman R**, Terry R, DeTeresa R, Brown T, Davies P, Fuld P, Renbing X, Peck A. Clinical, pathological, and neurochemical changes in dementia: a subgroup with preserved mental status and numerous neocortical plaques. *Ann Neurol* 1988; **23**: 138-144 [PMID: 2897823]

8 **Bennett DA**, Schneider JA, Arvanitakis Z, Kelly JF, Aggarwal NT, Shah RC, Wilson RS. Neuropathology of older persons without cognitive impairment from two community-based studies. *Neurology* 2006; **66**: 1837-1844 [PMID: 16801647]

9 **Kim EJ**, Cho SS, Jeong Y, Park KC, Kang SJ, Kang E, Kim SE, Lee KH, Na DL. Glucose metabolism in early onset versus late onset Alzheimer's disease: an SPM analysis of 120 patients. *Brain* 2005; **128**: 1790-1801 [PMID: 15888536]

10 **Mosconi L**, Perani D, Sorbi S, Herholz K, Nacmias B, Holthoff V, Salmon E, Baron JC, De Cristofaro MT, Padovani A, Borroni B, Franceschi M, Bracco L, Pupi A. MCI conversion to dementia and the APOE genotype: a prediction study with FDG-PET. *Neurology* 2004; **63**: 2332-2340 [PMID: 15623696]

11 **Picco A**, Polidori MC, Ferrara M, Cecchetti R, Arnaldi D, Baglioni M, Morbelli S, Bastiani P, Bossert I, Fiorucci G, Brugnolo A, Dottorini ME, Nobili F, Mecocci P. Plasma antioxidants and brain glucose metabolism in elderly subjects with cognitive complaints. *Eur J Nucl Med Mol Imaging* 2014; **41**: 764-775 [PMID: 24297504 DOI: 10.1007/s00259-013-2638-x]

12 **Ewers M**, Frisoni GB, Teipel SJ, Grinberg LT, Amaro E, Heinsen H, Thompson PM, Hampel H. Staging Alzheimer's disease progression with multimodality neuroimaging. *Prog Neurobiol* 2011; **95**: 535-546 [PMID: 21718750 DOI: 10.1016/j.pneurobio.2011.06.004]

13 **Stern Y**. What is cognitive reserve? Theory and research application of the reserve concept. *J Int Neuropsychol Soc* 2002; **8**: 448-460 [PMID: 11939702]

14 **Morbelli S**, Perneczky R, Drzezga A, Frisoni GB, Caroli A, van Berckel BN, Ossenkoppele R, Guedj E, Didic M, Brugnolo A, Naseri M, Sambuceti G, Pagani M, Nobili F. Metabolic networks underlying cognitive reserve in prodromal Alzheimer disease: a European Alzheimer disease consortium project. *J Nucl Med* 2013; **54**: 894-902 [PMID: 23591639 DOI: 10.2967/jnumed.112.113928]

15 **Klunk WE**, Engler H, Nordberg A, Wang Y, Blomqvist G, Holt DP, Bergström M, Savitcheva I, Huang GF, Estrada S, Ausén B, Debnath ML, Barletta J, Price JC, Sandell J, Lopresti BJ, Wall A, Koivisto P, Antoni G, Mathis CA, Långström B. Imaging brain amyloid in Alzheimer's disease with Pittsburgh Compound-B. *Ann Neurol* 2004; **55**: 306-319 [PMID: 14991808]

16 **Villemagne VL**, Mulligan RS, Pejoska S, Ong K, Jones G, O'Keefe G, Chan JG, Young K, Tochon-Danguy H, Masters CL, Rowe CC. Comparison of 11C-PiB and 18F-florbetaben for Aβ imaging in ageing and Alzheimer's disease. *Eur J Nucl Med Mol Imaging* 2012; **39**: 983-989 [PMID: 22398958 DOI: 10.1007/s00259-012-2088-x]

17 **Landau SM**, Marks SM, Mormino EC, Rabinovici GD, Oh H, O' Neil JP, Wilson RS, Jagust WJ. Association of lifetime cognitive engagement and low β-amyloid deposition. *Arch Neurol* 2012; **69**: 623-629 [PMID: 22271235]

18 **Curtis C**, Gamez JE, Singh U, Sadowsky CH, Villena T, Sabbagh MN, Beach TG, Duara R, Fleisher AS, Frey KA, Walker Z, Hunjan A, Holmes C, Escovar YM, Vera CX, Agronin ME, Ross J, Bozoki A, Akinola M, Shi J, Vandenberghe R, Ikonomovic MD, Sherwin PF, Grachev ID, Farrar G, Smith AP, Buckley CJ, McLain R, Salloway S. Phase 3 trial of flutemetamol labeled with radioactive fluorine 18 imaging and neuritic plaque density. *JAMA Neurol* 2015; **72**: 287-294 [PMID: 25622185 DOI: 10.1001/jamaneurol.2014.4144]

19 **Clark CM**, Schneider JA, Bedell BJ, Beach TG, Bilker WB, Mintun MA, Pontecorvo MJ, Hefti F, Carpenter AP, Flitter ML, Krautkramer MJ, Kung HF, Coleman RE, Doraiswamy PM, Fleisher AS, Sabbagh MN, Sadowsky CH, Reiman EP, Zehntner SP, Skovronsky DM. Use of florbetapir-PET for imaging beta-amyloid pathology. *JAMA* 2011; **305**: 275-283 [PMID: 21245183 DOI: 10.1001/jama.2010.2008]

20 **Sabri O**, Sabbagh MN, Seibyl J, Barthel H, Akatsu H, Ouchi Y, Senda K, Murayama S, Ishii K, Takao M, Beach TG, Rowe CC, Leverenz JB, Ghetti B, Ironside JW, Catafau AM, Stephens AW, Mueller A, Koglin N, Hoffmann A, Roth K, Reininger C, Schulz-Schaeffer WJ. Florbetaben PET imaging to detect amyloid beta plaques in Alzheimer's disease: phase 3 study. *Alzheimers Dement* 2015; **11**: 964-974 [PMID: 25824567 DOI: 10.1016/j.jalz.2015.02.004]

21 **Johnson KA**, Minoshima S, Bohnen NI, Donohoe KJ, Foster NL, Herscovitch P, Karlawish JH, Rowe CC, Hedrick S, Pappas V, Carrillo MC, Hartley DM. Update on appropriate use criteria for amyloid PET imaging: dementia experts, mild cognitive impairment, and education. Amyloid Imaging Task Force of the Alzheimer's Association and Society for Nuclear Medicine and Molecular Imaging. *Alzheimers Dement* 2013; **9**: e106-e109 [PMID: 23809369 DOI: 10.1016/j.jalz.2013.06.001]

22 **Verret L**, Krezymon A, Halley H, Trouche S, Zerwas M, Lazouret M, Lassalle JM, Rampon C. Transient enriched housing before amyloidosis onset sustains cognitive improvement in Tg2576 mice. *Neurobiol Aging* 2013; **34**: 211-225 [PMID: 22727275 DOI: 10.1016/j.neurobiolaging.2012.05.013]

23 **Landau SM**, Lu M, Joshi AD, Pontecorvo M, Mintun MA, Trojanowski JQ, Shaw LM, Jagust WJ. Comparing positron emission tomography imaging and cerebrospinal fluid measurements of β-amyloid. *Ann Neurol* 2013; **74**: 826-836 [PMID: 23536396 DOI: 10.1002/ana.23908]

24 **Katzman R**. Education and the prevalence of dementia and Alzheimer's disease. *Neurology* 1993; **43**: 13-20 [PMID: 8423876]

25 **Yodlowski EH**, Mortimer JT. The relationship between receptor occlusion and the frequency sweep electromyogram during competitive neuromuscular blockade. *Anesthesiology* 1981; **54**: 23-28 [PMID: 6257148]

26 **Friedland RP**, Fritsch T, Smyth KA, Koss E, Lerner AJ, Chen CH, Petot GJ, Debanne SM. Patients with Alzheimer's disease have reduced activities in midlife compared with healthy control-group members. *Proc Natl Acad Sci USA* 2001; **98**: 3440-3445 [PMID: 11248097]

27 **Stern Y**, Gurland B, Tatemichi TK, Tang MX, Wilder D, Mayeux R. Influence of education and occupation on the incidence of Alzheimer's disease. *JAMA* 1994; **271**: 1004-1010 [PMID: 8139057]

28 **Reed BR**, Mungas D, Farias ST, Harvey D, Beckett L, Widaman K, Hinton L, DeCarli C. Measuring cognitive reserve based on the decomposition of episodic memory variance. *Brain* 2010; **133**: 2196-2209 [PMID: 20591858 DOI: 10.1093/brain/awq154]

29 **Scarmeas N**, Zarahn E, Anderson KE, Habeck CG, Hilton J, Flynn J, Marder KS, Bell KL, Sackeim HA, Van Heertum RL, Moeller JR, Stern Y. Association of life activities with cerebral blood flow in Alzheimer disease: implications for the cognitive reserve hypothesis. *Arch Neurol* 2003; **60**: 359-365 [PMID: 12633147]

30 **Liu Y**, Julkunen V, Paajanen T, Westman E, Wahlund LO, Aitken A, Sobow T, Mecocci P, Tsolaki M, Vellas B, Muehlboeck S, Spenger C, Lovestone S, Simmons A, Soininen H. Education increases reserve against Alzheimer's disease--evidence from structural MRI analysis. *Neuroradiology* 2012; **54**: 929-938 [PMID: 22246242 DOI: 10.1007/s00234-012-1005-0]

31 **Garibotto V**, Borroni B, Kalbe E, Herholz K, Salmon E, Holtoff V, Sorbi S, Cappa SF, Padovani A, Fazio F, Perani D. Education and occupation as proxies for reserve in aMCI converters and AD: FDG-PET evidence. *Neurology* 2008; **71**: 1342-1349 [PMID: 18936426 DOI: 10.1212/01.wnl.0000327670.62378.c0]

32 **Springer MV**, McIntosh AR, Winocur G, Grady CL. The relation between brain activity during memory tasks and years of education in young and older adults. *Neuropsychology* 2005; **19**: 181-192 [PMID: 15769202]

33 **Stern Y**. Cognitive reserve. *Neuropsychologia* 2009; **47**: 2015-2028 [PMID: 19467352 DOI: 10.1016/j.neuropsychologia.2009.03.004]

34 **Morbelli S**, Nobili F. Cognitive reserve and clinical expression of Alzheimer's disease: evidence and implications for brain PET imaging. *Am J Nucl Med Mol Imaging* 2014; **4**: 239-247 [PMID: 24795838]

35 **Stern Y**, Zarahn E, Habeck C, Holtzer R, Rakitin BC, Kumar A, Flynn J, Steffener J, Brown T. A common neural network for cognitive reserve in verbal and object working memory in young but not old. *Cereb Cortex* 2008; **18**: 959-967 [PMID: 17675368]

36 **Morbelli S**, Arnaldi D, Capitanio S, Picco A, Buschiazzo A, Nobili F. Resting metabolic connectivity in Alzheimer's disease. *Clin Transl Imaging* 2013; **1**: 271-278 [DOI: 10.1007/s40336-013-0027-x]

37 **Lee DS**, Kang H, Kim H, Park H, Oh JS, Lee JS, Lee MC. Metabolic connectivity by interregional correlation analysis using statistical parametric mapping (SPM) and FDG brain PET; methodological development and patterns of metabolic connectivity in adults. *Eur J Nucl Med Mol Imaging* 2008; **35**: 1681-1691 [PMID: 18491089 DOI: 10.1007/s00259-008-0808-z]

38 **Morbelli S**, Drzezga A, Perneczky R, Frisoni GB, Caroli A, van Berckel BN, Ossenkoppele R, Guedj E, Didic M, Brugnolo A, Sambuceti G, Pagani M, Salmon E, Nobili F. Resting metabolic connectivity in prodromal Alzheimer's disease. A European Alzheimer Disease Consortium (EADC) project. *Neurobiol Aging* 2012; **33**: 2533-2550 [PMID: 22365486 DOI: 10.1016/j.neurobiolaging.2012.01.005]

39 **Arenaza-Urquijo EM**, Landeau B, La Joie R, Mevel K, Mézenge F, Perrotin A, Desgranges B, Bartrés-Faz D, Eustache F, Chételat G. Relationships between years of education and gray matter volume, metabolism and functional connectivity in healthy elders. *Neuroimage* 2013; **83**: 450-457 [PMID: 23796547 DOI: 10.1016/j.neuroimage.2013.06.053]

40 **Kemppainen NM**, Aalto S, Wilson IA, Någren K, Helin S, Brück A, Oikonen V, Kailajärvi M, Scheinin M, Viitanen M, Parkkola R, Rinne JO. Voxel-based analysis of PET amyloid ligand [11C]PIB uptake in Alzheimer disease. *Neurology* 2006; **67**: 1575-1580 [PMID: 16971697]

41 **Kemppainen NM**, Aalto S, Wilson IA, Någren K, Helin S, Brück A, Oikonen V, Kailajärvi M, Scheinin M, Viitanen M, Parkkola R, Rinne JO. PET amyloid ligand [11C]PIB uptake is increased in mild cognitive impairment. *Neurology* 2007; **68**: 1603-1606 [PMID: 17485647 DOI: 10.1212/01.wnl.0000260969.94695.56]

42 **Aizenstein HJ**, Nebes RD, Saxton JA, Price JC, Mathis CA, Tsopelas ND, Ziolko SK, James JA, Snitz BE, Houck PR, Bi W, Cohen AD, Lopresti BJ, DeKosky ST, Halligan EM, Klunk WE. Frequent amyloid deposition without significant cognitive impairment among the elderly. *Arch Neurol* 2008; **65**: 1509-1517 [PMID: 19001171 DOI: 10.1001/archneur.65.11.1509]

43 **Lister-James J**, Pontecorvo MJ, Clark C, Joshi AD, Mintun MA, Zhang W, Lim N, Zhuang Z, Golding G, Choi SR, Benedum TE, Kennedy P, Hefti F, Carpenter AP, Kung HF, Skovronsky DM. Florbetapir f-18: a histopathologically validated Beta-amyloid positron emission tomography imaging agent. *Semin Nucl Med* 2011; **41**: 300-304 [PMID: 21624563 DOI: 10.1053/j.semnuclmed.2011.03.001]

44 **Kemppainen NM**, Aalto S, Karrasch M, Någren K, Savisto N, Oikonen V, Viitanen M, Parkkola R, Rinne JO. Cognitive reserve hypothesis: Pittsburgh Compound B and fluorodeoxyglucose positron emission tomography in relation to education in mild Alzheimer's disease. *Ann Neurol* 2008; **63**: 112-118 [PMID: 18023012]

45 **Rowe CC**, Villemagne VL. Brain amyloid imaging. *J Nucl Med Technol* 2013; **41**: 11-18 [PMID: 23396994 DOI: 10.2967/jnumed.110.076315]

46 **Ossenkoppele R**, van der Flier WM, Verfaillie SC, Vrenken H, Versteeg A, van Schijndel RA, Sikkes SA, Twisk J, Adriaanse SM, Zwan MD, Boellaard R, Windhorst AD, Barkhof F, Scheltens P, Lammertsma AA, van Berckel BN. Long-term effects of amyloid, hypometabolism, and atrophy on neuropsychological functions. *Neurology* 2014; **82**: 1768-1775 [PMID: 24748672 DOI: 10.1212/WNL.0000000000000432]

47 **Vos SJ**, Verhey F, Frölich L, Kornhuber J, Wiltfang J, Maier W, Peters O, Rüther E, Nobili F, Morbelli S, Frisoni GB, Drzezga A, Didic M, van Berckel BN, Simmons A, Soininen H, Kłoszewska I, Mecocci P, Tsolaki M, Vellas B, Lovestone S, Muscio C, Herukka SK, Salmon E, Bastin C, Wallin A, Nordlund A, de Mendonça A, Silva D, Santana I, Lemos R, Engelborghs S, Van der Mussele S, Freund-Levi Y, Wallin ÅK, Hampel H, van der Flier W, Scheltens P, Visser PJ. Prevalence and prognosis of Alzheimer's disease at the mild cognitive impairment stage. *Brain* 2015; **138**: 1327-1338 [PMID: 25693589 DOI: 10.1093/brain/awv029]

48 **Klunk WE**, Koeppe RA, Price JC, Benzinger TL, Devous MD, Jagust WJ, Johnson KA, Mathis CA, Minhas D, Pontecorvo MJ, Rowe CC, Skovronsky DM, Mintun MA. The Centiloid Project: standardizing quantitative amyloid plaque estimation by PET. *Alzheimers Dement* 2015; **11**: 1-15.e1-1-15.e4 [PMID: 25443857 DOI: 10.1016/j.jalz.2014.07.003]

49 **Mormino EC**, Brandel MG, Madison CM, Rabinovici GD, Marks S, Baker SL, Jagust WJ. Not quite PIB-positive, not quite PIB-negative: slight PIB elevations in elderly normal control subjects are biologically relevant. *Neuroimage* 2012; **59**: 1152-1160 [PMID: 21884802 DOI: 10.1016/j.neuroimage.2011.07.098]

50 **Chételat G**, Villemagne VL, Pike KE, Baron JC, Bourgeat P, Jones G, Faux NG, Ellis KA, Salvado O, Szoeke C, Martins RN, Ames D, Masters CL, Rowe CC. Larger temporal volume in elderly with high versus low beta-amyloid deposition. *Brain* 2010; **133**: 3349-3358 [PMID: 20739349 DOI: 10.1093/brain/awq187]

51 **Braskie MN**, Thompson PM. Understanding cognitive deficits in Alzheimer's disease based on neuroimaging findings. *Trends Cogn Sci* 2013; **17**: 510-516 [PMID: 24029445 DOI: 10.1016/j.tics.2013.08.007]

52 **Nithianantharajah J**, Hannan AJ. Enriched environments, experience-dependent plasticity and disorders of the nervous system. *Nat Rev Neurosci* 2006; **7**: 697-709 [PMID: 16924259]

53 **Escorihuela RM**, Fernández-Teruel A, Tobeña A, Vivas NM, Mármol F, Badia A, Dierssen M. Early environmental stimulation produces long-lasting changes on beta-adrenoceptor transduction system. *Neurobiol Learn Mem* 1995; **64**: 49-57 [PMID: 7582812]

54 **van Praag H**, Kempermann G, Gage FH. Running increases cell proliferation and neurogenesis in the adult mouse dentate gyrus. *Nat Neurosci* 1999; **2**: 266-270 [PMID: 10195220]

55 **Costa DA**, Cracchiolo JR, Bachstetter AD, Hughes TF, Bales KR, Paul SM, Mervis RF, Arendash GW, Potter H. Enrichment improves cognition in AD mice by amyloid-related and unrelated mechanisms. *Neurobiol Aging* 2007; **28**: 831-844 [PMID: 16730391]

56 **Head D**, Bugg JM, Goate AM, Fagan AM, Mintun MA, Benzinger T, Holtzman DM, Morris JC. Exercise Engagement as a Moderator of the Effects of APOE Genotype on Amyloid Deposition. *Arch Neurol* 2012; **69**: 636-643 [PMID: 22232206]

57 **Vemuri P**, Lesnick TG, Przybelski SA, Machulda M, Knopman DS, Mielke MM, Roberts RO, Geda YE, Rocca WA, Petersen RC, Jack CR. Association of lifetime intellectual enrichment with cognitive decline in the older population. *JAMA Neurol* 2014; **71**: 1017-1024 [PMID: 25054282 DOI: 10.1001/jamaneurol.2014.963]

58 **Almeida RP**, Schultz SA, Austin BP, Boots EA, Dowling NM, Gleason CE, Bendlin BB, Sager MA, Hermann BP, Zetterberg H, Carlsson CM, Johnson SC, Asthana S, Okonkwo OC. Effect of Cognitive Reserve on Age-Related Changes in Cerebrospinal Fluid Biomarkers of Alzheimer Disease. *JAMA Neurol* 2015; **72**: 699-706 [PMID: 25893879 DOI: 10.1001/jamaneurol.2015.0098]

59 **Cook CN**, Murray ME, Petrucelli L. Understanding biomarkers of neurodegeneration: Novel approaches to detecting tau pathology. *Nat Med* 2015; **21**: 219-220 [PMID: 25742457 DOI: 10.1038/

nm.3809]
60 **Jack CR**, Knopman DS, Jagust WJ, Shaw LM, Aisen PS, Weiner MW, Petersen RC, Trojanowski JQ. Hypothetical model of dynamic biomarkers of the Alzheimer's pathological cascade. *Lancet Neurol* 2010; **9**: 119-128 [PMID: 20083042 DOI: 10.1016/S1474-4422(09)70299-6]

P- Reviewer: Gupta SK, Vinh-Hung V **S- Editor**: Tian YL
L- Editor: A **E- Editor**: Wu HL

WJR World Journal of Radiology

Submit a Manuscript: http://www.wjgnet.com/esps/
Help Desk: http://www.wjgnet.com/esps/helpdesk.aspx
DOI: 10.4329/wjr.v7.i12.484

World J Radiol 2015 December 28; 7(12): 484-493
ISSN 1949-8470 (online)

MINIREVIEWS

Three-dimensional imaging of the uterus: The value of the coronal plane

Lufee Wong, Nikki White, Jayshree Ramkrishna, Edward Araujo Júnior, Simon Meagher, Fabricio Da Silva Costa

Lufee Wong, Nikki White, Jayshree Ramkrishna, Simon Meagher, Fabricio Da Silva Costa, Monash Ultrasound for Women, Clayton, Victoria 3168, Australia

Lufee Wong, Department of Obstetrics and Gynaecology, Monash Medical Centre, Southern Health, Clayton, Victoria 3168, Australia

Edward Araujo Júnior, Department of Obstetrics, Paulista School of Medicine - Federal University of São Paulo (EPM-UNIFESP), São Paulo, CEP 05303-000, Brazil

Author contributions: Wong L performed the research; White N, Ramkrishna J, Meagher S and Da Silva Costa F contributed to the images; Wong L and Da Silva Costa F wrote the manuscript; Araujo Júnior E reviewed the manuscript.

Conflict-of-interest statement: The authors declare no conflict of interest.

Correspondence to: Edward Araujo Júnior, PhD, Professor, Department of Obstetrics, Paulista School of Medicine - Federal University of São Paulo (EPM-UNIFESP), Rua Belchior de Azevedo, 156, apto. 111 Torre Vitoria, São Paulo, CEP 05303-000, Brazil. araujojred@terra.com.br
Telephone: +55-11-37965944
Fax: +55-11-37965944

Received: July 9, 2015
Peer-review started: July 14, 2015
First decision: August 25, 2015
Revised: October 10, 2015
Accepted: November 3, 2015
Article in press: November 4, 2015
Published online: December 28, 2015

Abstract

Advent in three-dimensional (3D) imaging technology has seen 3D ultrasound establish itself as a useful adjunct complementary to traditional two-dimensional imaging of the female pelvis. This advantage largely arises from its ability to reconstruct the coronal plane of the uterus, which allows further delineation of many gynecological disorders. 3D imaging of the uterus is now the preferred imaging modality for assessing congenital uterine anomalies and intrauterine device localization. Newer indications include the diagnosis of adenomyosis. It can also add invaluable information to delineate other endometrial and myometrial pathology such as fibroids and endometrial polyps.

Key words: Three-dimensional ultrasound; Coronal view; Pelvis; Uterus; Uterine anomalies

Core tip: Three-dimensional ultrasound imaging of the female pelvis is a useful adjunct to conventional two-dimensional imaging. By acquiring a set volume which is stored, volumetric acquisitions allow the offline review, manipulation and analysis of saved images to obtain the maximum information from a study. Recent literature has suggested this imaging approach is rapidly realizing widespread use in the assessment of a variety of gynecological disorders including uterine anomalies, intrauterine device localization, endometrial disorders and fibroids. Recent advances have also suggested it may be useful in diagnosing disorders of the endometrial-myometrial interface, such as adenomyosis.

Wong L, White N, Ramkrishna J, Araujo Júnior E, Meagher S, Da Silva Costa F. Three-dimensional imaging of the uterus: The value of the coronal plane. *World J Radiol* 2015; 7(12): 484-493 Available from: URL: http://www.wjgnet.com/1949-8470/full/v7/i12/484.htm DOI: http://dx.doi.org/10.4329/wjr.v7.i12.484

INTRODUCTION

Three-dimensional (3D) ultrasound imaging of the female pelvis is a useful adjunct to conventional two-dimensional (2D) imaging. By acquiring a set volume which is stored, volumetric acquisitions allow the offline review, manipulation and analysis of saved images to obtain the maximum information from a study. Recent literature has suggested this imaging approach is rapidly realizing widespread use in the assessment of a variety of gynecological disorders including uterine anomalies, intrauterine device (IUD) localization, endometrial disorders and fibroids[1]. Recent advances have also suggested it may be useful in diagnosing disorders of the endometrial-myometrial interface, such as adenomyosis[2].

While 2D imaging provides information through axial and sagittal planes, it is limited by accessibility to assess pathology in the coronal plane. One of the main advantages of 3D imaging of the uterus, on the other hand, is the capacity to reconstruct the coronal plane. Particularly when the 2D imaging is abnormal, it offers the ability to better define some uterine anomalies. Andreotti *et al*[3] reported that out of 49 patients with abnormal findings on 2D ultrasound, 3D ultrasound provided additional information in 26 (53%) of these patients. These included uterine anomalies, improved endometrium delineation, more accurate visualization of endometrial polyps, fibroids and location of IUD. In another study, Benacerraf *et al*[4] showed 3D ultrasound provided additional information in 16 out of 66 patients. When 2D imaging is normal, it is a less useful adjunct but still offers the ability to occasionally detect unsuspected anomalies in some circumstances, such as arcuate uteri. The improved visualization with 3D ultrasound is particularly evident when the endometrium thickness is greater than 5 mm, since there is greater contrast with the more hypoechoic myometrium[4].

This article aims to illustrate the applicability of 3D imaging of the uterus, particularly some of the newer advances of 3D imaging in the assessment of myometrial disorders.

OBTAINING A 3D CORONAL IMAGE OF THE UTERUS

Volume acquisition for 3D ultrasound requires specialized ultrasound systems and transducers. A transvaginal, compared to the transabdominal, approach is generally preferred, due to the higher frequency of the probe and the proximity to the pelvic organs, which improve image resolution[1]. An adequately enlarged mid-sagittal or transverse section of the uterine body is obtained, although a mid-sagittal plane is preferred since under optimal circumstances, this allows the visualization of the entire length of the endometrial cavity as well as the endocervical canal. Depending on the machine, an automatic or manual sweep is performed to obtain a volume of the region of interest. Upon acquisition of the 3D volume, examination of the volume is performed in the standardized multi-planar view by adjusting the slice through the three orthogonal planes separately (Figure 1). This standardized multi-planar view reduces inter-observer variation and may be achieved by the "Z-rotation" technique (Table 1)[5-7]. This information could be stored, which allows the user to manipulate and analyze the images offline. This may also facilitate the retrospective analysis of these images to give a second opinion by another examiner if required[1].

Table 1 Steps for the application of the "Z-rotation" technique

Step 1: Position the reference marker/dot et the level of the mid-cavity over the endometrial stripe in the sagittal plane (Figure 1A)
Step 2: Use the Z rotation to align the long axis of the endometrial stripe along the horizontal axis in the sagittal plane of the uterus
Step 3: Position the reference marker/dot et the level of the of the midcavity over the endometrial stripe in the transverse plane (Figure 1B)
Step 4: Use the Z rotation to align the endometrial stripe with the horizontal axis in the transverse plane of the uterus
Step 5: Following step 4, the coronal plane of the uterus will be displayed in plane C (Figure 1C); use the Z rotation on plane C to display the midcoronal plane in the conventional orientation (Figure 1D)

Data from "The Z Technique: an easy approach to the display of the midcoronal plane of the uterus in volume sonography". *J Ultrasound Med* 2006; 25: 607-612.

Multiple features for image optimization and post-processing functions are available, including surface rendering and volume contrast imaging (VCI) (Figure 2). VCI increases the contrast of images by refining the slices through the images. This improves depth perception and thus improves the visualization of finer detail. This is particularly useful for improving assessment of the junctional zone (JZ)[2,8]. Rendering is a technique that mimics the concept of placing a "drape" over the organ of interest. It is particularly applicable to visualizing the surface, such as over the external serosal contour of the uterus. However, the disadvantage of this method is that while the surface display is optimized, the sonographic information within the object is not displayed[9].

LIMITATIONS OF 3D ULTRASOUND OF THE UTERUS

Like 2D ultrasound, 3D ultrasound is subject to the same limitations of ultrasound physics. One of the main underlying prerequisites to a quality 3D image is a good 2D image. Volume acquisition in 3D imaging relies on reconstruction of a series of images processed during a sweep with a single elevation focus where the resolution of images beyond the focal zone is diminished[1]. Hence, it is quintessential that imaging settings are optimized to enhance 3D imaging. Artifacts in 3D reconstructions can be less readily recognizable and have the potential to distort an image enough to alter the diagnosis. In

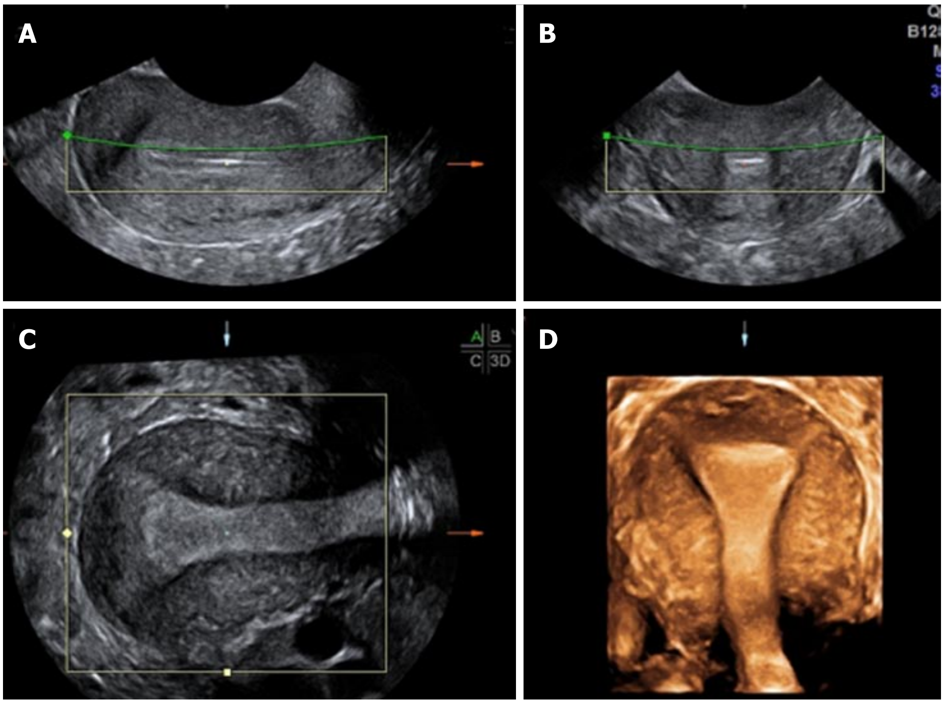

Figure 1 Multiplanar and rendering modes of the uterus. Multiplanar reconstructions from 3D ultrasound show a normal uterus in sagittal (A), transverse (B) and true coronal (C) planes. Surface rendering reconstructed image in a coronal plane of the uterus demonstrating a normal uterine fundal contour (D). 3D: Three-dimensional.

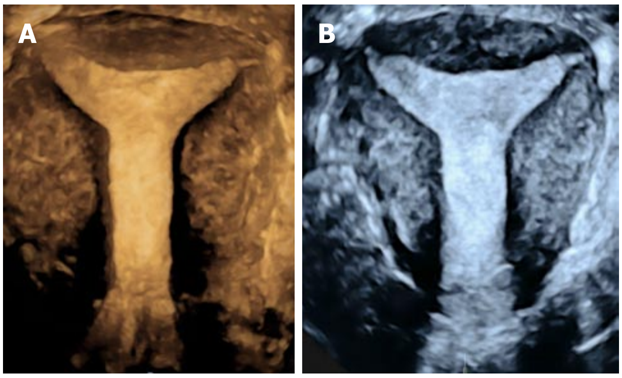

Figure 2 Examples of post-processing functions include surface render and volume contrast imaging. A: Three-dimensional (3D) ultrasound with surface rendering of a normal uterus in the coronal plane; B: 3D ultrasound with volume contrast imaging of the same uterus.

fact, artifacts can be compounded within a volume and not be immediately apparent. Thus, it is important to review the image in the acquisition plane to identify these artifacts[6]. Another potential disadvantage is the considerable "learning curve" associated with the manipulation of 3D ultrasound by the examiner. Various settings, which are machine-dependent, are available to the operator and optimizing the image through the manipulation of settings require training and time[1]. Machines and probes with 3D capability often come at an additional cost, which may limit its availability and accessibility although it is likely that with increasing popularity and acceptance, this will be less prohibitive since it also has proven cost effectiveness[10].

PRACTICAL APPLICATIONS

Mullerian duct anomalies

Congenital uterine anomalies are associated with an increased risk of infertility, recurrent miscarriages and other obstetric complications. It is estimated to have a prevalence of 17% in the population with recurrent miscarriages, compared to 6% in the general population[11]. Following a proposed classification by Buttram *et al*[12] of Mullerian duct anomalies in 1979, the American Society for Reproductive Medicine (formerly the American Fertility Society) subsequently adapted this classification for use in 1988, and this remains the most widely accepted over the last 25 years[12,13]. Traditionally, screening for uterine cavity anomalies has relied on hysterosalpingography, an image modality that is disadvantaged by potential contrast medium hypersensitivity and radiation exposure. If an anomaly was suspected, further investigations involving a hysteroscopy was considered the gold standard for diagnosing uterine cavity shape anomalies under direct vision, and laparoscopy could be used to assess the external fundal contour. The advances in magnetic resonance imaging (MRI), has increasingly gained popularity as an alternative modality for diagnosing congenital uterine anomalies since it has the potential to illustrate both the uterine cavity as well as external fundal contour. However, widespread uptake of MRI has been limited by its higher cost and lower patient acceptance. As 3D ultrasound gained validity, there has been shown to be a high degree of concordance between 3D ultrasound and MRI in defining uterine

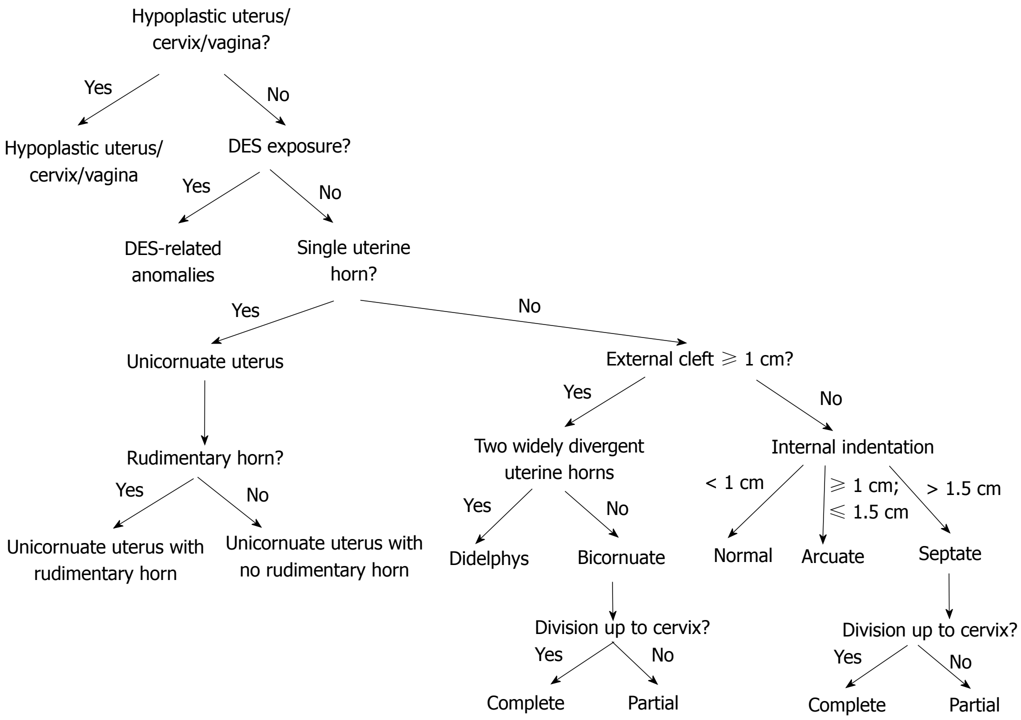

Figure 3 Algorithm for distinguishing between Mullerian duct anomalies. Modified to include morphology criteria by Ludwin *et al*[17], Bermejo *et al*[14] and Salim *et al*[17,18].

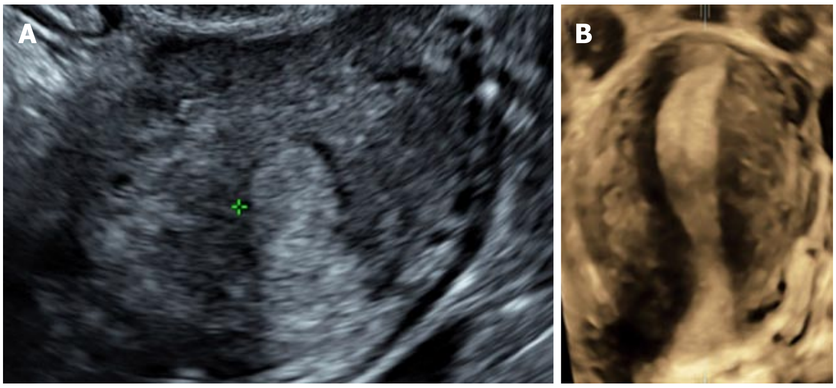

Figure 4 Unicornuate uterus with no rudimentary horn. A: Transverse 2D ultrasound image shows a single endometrial cavity; B: Coronal 3D (with VCI) ultrasound image of the unicornuate uterus showing a single uterine horn with no divergence of the endometrium towards both ostia and absence of a rudimentary horn. 3D: Three-dimensional; 2D: Two-dimensional; VCI: Volume contrast imaging.

anomalies[14]. While 2D transvaginal ultrasonography has an accurate diagnosis rate of 60%-82% for uterine malformation depending on different studies, 3D ultrasound was superior with a diagnostic accuracy of 88%-100%[15,16].

Uterine anomalies can be broadly classified into 3 broad categories: Fusion (didelphys and bicornuate uteri), septal resorption (arcuate and septate uteri) and hypoplasia/agenesis abnormalities. In 2D sonography, these abnormalities can present with a common feature: 2 endometrial cavities are seen. To distinguish between these various abnormalities, a coronal plane would be useful in demonstrating their distinguishing features. Although there no universally-accepted criteria for the classification of Mullerian duct anomalies, Ludwin *et al*[17], Bermejo *et al*[14] and Salim *et al*[18,19] described distinguishing features involving the external cleft of the fundal contour and internal cavity indentation, measured from a horizontal line drawn across the two uterine horns of the uterine cavity. Using this criterion, an algorithm for distinguishing between uterine anomalies is proposed (Figure 3). Hypoplastic uterus, cervix, vagina can be related to the Mayer-Rokitansky-Kuster-Hauser syndrome whereby the uterus, cervix and vagina are hypoplastic or absent. The classic anomaly associated with Diethylstilboestrol exposure is the T-shaped uterus which includes a widened lower uterine segment, a hypoplastic uterus, and a narrowed fundal endometrial cavity. A single uterine horn distinguishes a unicornuate uterus from the remaining ano-

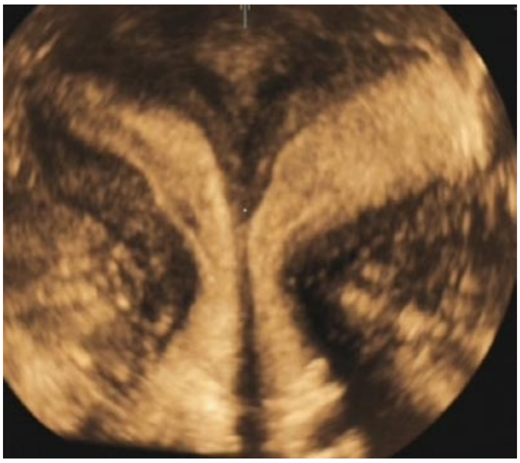

Figure 5 Uterine didelphys. Coronal 3D ultrasound image of a didelphys uterus show two widely divergent uterine horns separated by a deep external cleft ⩾ 1 cm. 3D: Three-dimensional.

malies, although a rudimentary horn can sometimes be present (Figure 4). The distinguishing feature of fusion anomalies (didelphys or bicornuate uteri) from resorption anomalies is the external contour. Should the external cleft be greater than or equal to 1 cm, the degree of separation of the two horns will distinguish an uterine didelphys (Figure 5) from a bicornuate uterus (Figure 6). Uterine didelphys has 2 widely separated uterine horns, while a bicornuate uterus has a single uterine body with internal indentation greater than or equal to 1.5 cm. In the event that the external cleft is less than 1 cm, the depth of internal indentation will distinguish the septate (greater than 1.5 cm) (Figure 7) from the arcuate (between 1 and 1.5 cm) (Figure 8), and from normal uteri (less than 1 cm). Note that normal uteri can have either a straight or convex contour, or an external contour of less than 1 cm (Figure 3).

In several series, arcuate uteri was the commonest anomaly detected in 3D ultrasound when 2D ultrasound was normal[3,4]. While arcuate uteri is generally thought to be a normal variant with no reproductive consequences, there is some limited evidence that arcuate uteri can be associated with recurrent fetal loss[20]. It is particularly important to distinguish a septate uterus from fusion abnormalities since a septate uterus is amenable to hysteroscopic septoplasty to respect the residual septum while surgery is not an option for fusion abnormalities.

While septate and fusion anomalies are usually recognized on 2D ultrasound due to the presence of 2 uterine cavities, a unicornuate uterus (Figure 4) is more likely to be undetected given that the presence of a rudimentary horn can be very small and be masked by surrounding bowel. This anomaly has potentially severe consequences since besides the associations with miscarriage and premature delivery, the rudimentary horn can harbor a developing pregnancy and result in late uterine rupture and potentially life-threatening consequences[21].

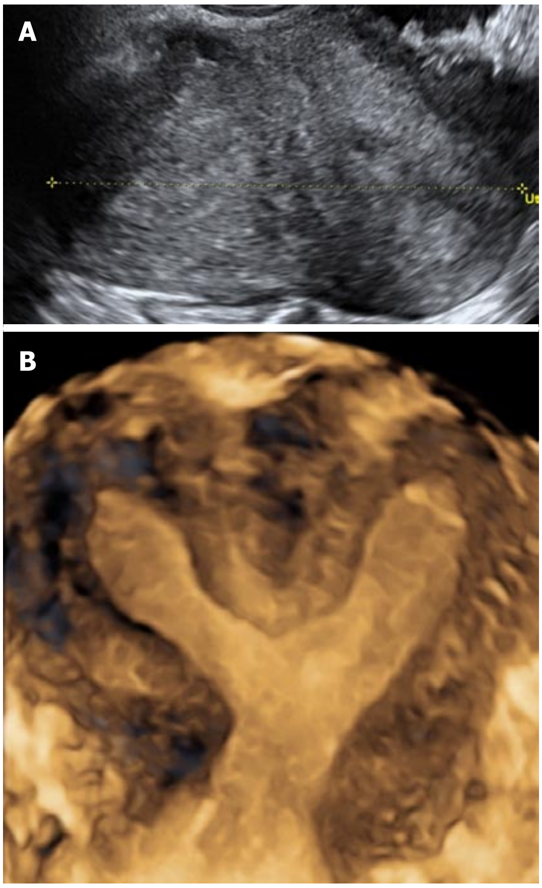

Figure 6 Bicornuate uterus. A: Transverse 2D ultrasound image of a bicornuate uterus showing the presence of 2 endometrial cavities; B: Coronal 3D ultrasound image of a bicornuate uterus showing external cleft ⩾ 1 cm and internal indentation ⩾ 1.5 cm. Note the presence of fundal soft tissue separating the 2 uterine cavities, which distinguishes it from uterine didelphys. 3D: Three-dimensional; 2D: Two-dimensional.

IUDs

While 2D transvaginal sonography has traditionally been used to assess the placement of IUDs, it is not able to demonstrate the entire IUD. 3D reconstructions in the coronal plane have the added advantage of demonstrating the complete IUD including shaft and arms. Lee *et al*[22] reported that by using the coronal plane, simultaneous visualization of the TCu380A IUD in its entirety was possible in 95% of 96 cases, while keeping examination time to a minimum. This can improve the detection rate of IUDs that have embedded in the myometrium since this can be a significant source of pelvic pain and abnormal bleeding for patients post IUD insertion (Figure 9)[23]. When assessing for IUD location, it should not extend past the endometrial cavity into the myometrium or cervix.

Fibroids and endometrial polyps

Fibroids are benign smooth muscle tumors of the uterus. While they are commonly asymptomatic, they can result in heavy menstrual bleeding, particularly when they are submucosal and distort the endometrial cavity (Figure 10)[24]. However, while fibroids can be

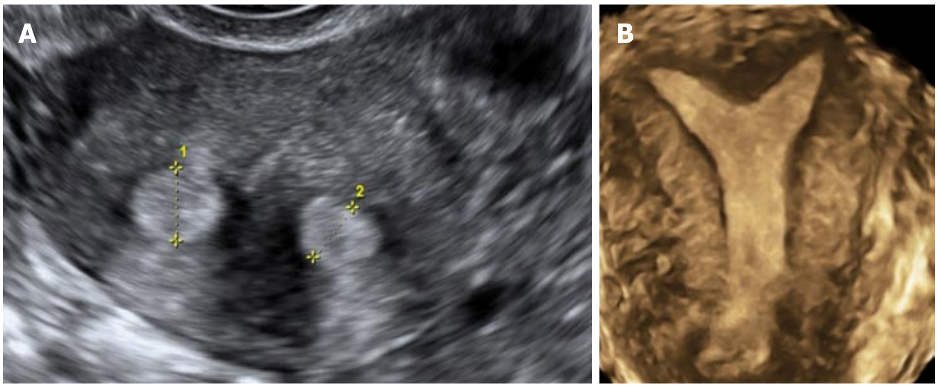

Figure 7 Septate uterus. A: Transverse 2D ultrasound image of a septate uterus showing the presence of 2 endometrial cavities; B: Coronal 3D ultrasound image of a partial septate uterus with the external cleft < 1 cm but internal indentation > 1.5 cm. 3D: Three-dimensional; 2D: Two-dimensional.

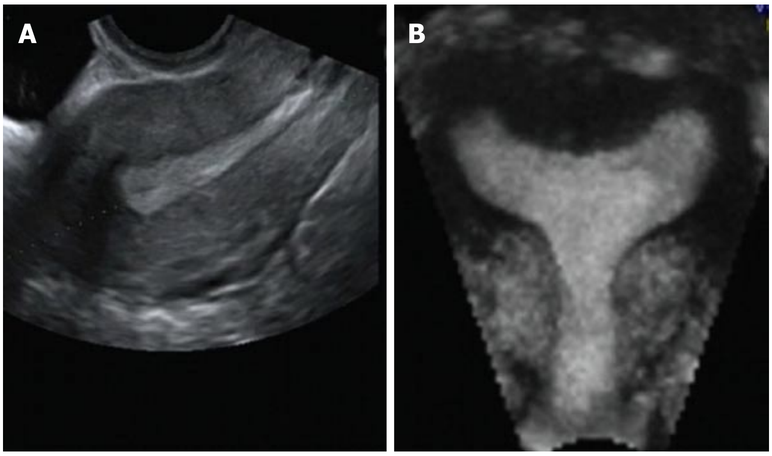

Figure 8 Arcuate uterus. A: Sagittal 2D ultrasound image of an arcuate uterus; B: Coronal 3D ultrasound image of an arcuate uterus with a smooth external contour and internal indentation ⩾ 1 cm but ⩽ 1.5 cm. 3D: Three-dimensional; 2D: Two-dimensional.

assessed on standard 2D imaging, their exact location in relation to the endometrial cavity and serosal contour can be difficult to determine due to shadowing artifacts. These difficulties can be overcome on a coronal plane since it allows the demonstration of the exact location of the fibroids, such as cavity distortion by submucosal fibroids and the planning of management options. Benacerraf *et al*[4] demonstrated that the 3D coronal view was useful in more accurately determining the specific location of fibroids (*i.e.*, submucous *vs* intramural) in 24% of patients using the coronal view.

Endometrial polyps are benign growths that are generally rounded, well-circumscribed echogenic masses seen within the endometrial cavity. Accurate imaging in 2D generally relies on the demonstration of a feeding vessel on color Doppler as demonstrated in Figure 11. As an adjunct, a coronal 3D imaging provides an opportunity to delineate the polyp more accurately since nearly the entire endometrial cavity can be seen in the same plane. However, the importance of the surrounding contrasting endometrium must not be overlooked. Indeed, Benacerraf *et al*[4] demonstrated that the width of the endometrium was an important predictor of whether the reconstructed coronal view would be helpful. Endometrium thickness of greater than 5 mm allowed a more confident diagnosis compared to patients whose endometrium was less than 5 mm[4].

Adenomyosis

Myometrial disorders are increasingly recognized as a cause for infertility and miscarriages, as well as subsequent obstetric complications[25,26]. The endometrium and the myometrial JZ, which is a highly-specialized inner third of the myometrium that together with its overlying endometrium, are key areas fundamental to the process of implantation and subsequently placentation. Consequently, any endometrial or myometrial disorders in the uterus that disrupt the transformation of these layers in early pregnancy can potentially interfere with the implantation and subsequent placentation, leading to various complications, such as miscarriage, pre-eclampsia and fetal growth restriction (Figure 12)[25]. Changes in the JZ have been thought to explain the pathogenesis behind why myometrial disorders such as adenomyosis can contribute to infertility[26].

Adenomyosis refers to the presence of ectopic endometrial glands and stroma within the myometrium, and

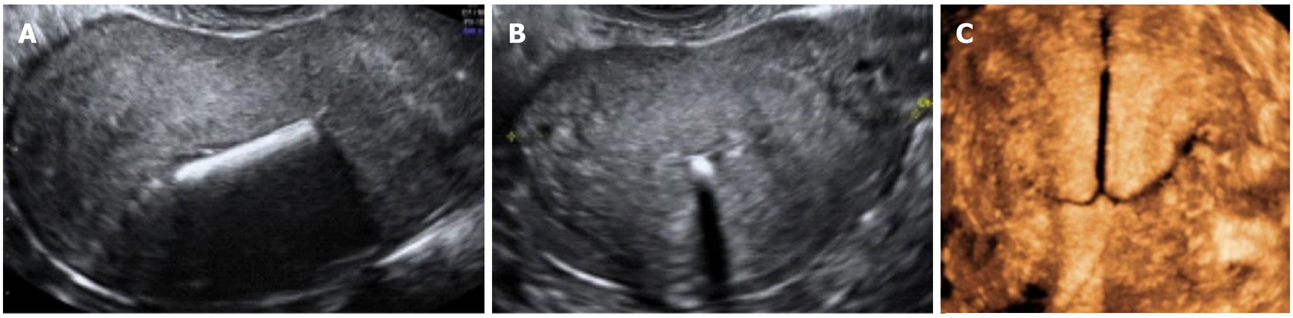

Figure 9 Malposition of an intrauterine device. Sagittal (A) and transverse (B) 2D ultrasound image showing the shaft within the endometrial cavity; C: Coronal 3D ultrasound image showing the IUD lying inverted with both arms embedded within the myometrium. 3D: Three-dimensional; 2D: Two-dimensional; IUD: Intrauterine device.

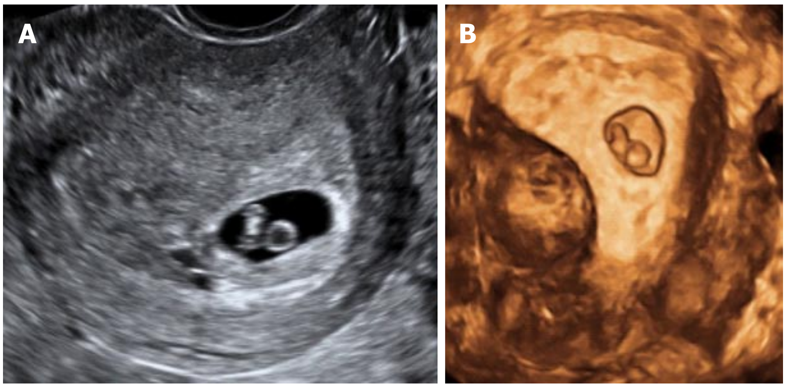

Figure 10 Intramural fibroid with an intrauterine pregnancy. A: Transverse 2D ultrasound image showing an intrauterine gestation sac positioned towards the left endometrial cavity; B: 3D coronal ultrasound image showing an intramural fibroid distorting the endometrial cavity, thus deviating the intrauterine pregnancy towards the left endometrial cavity. 3D: Three-dimensional; 2D: Two-dimensional.

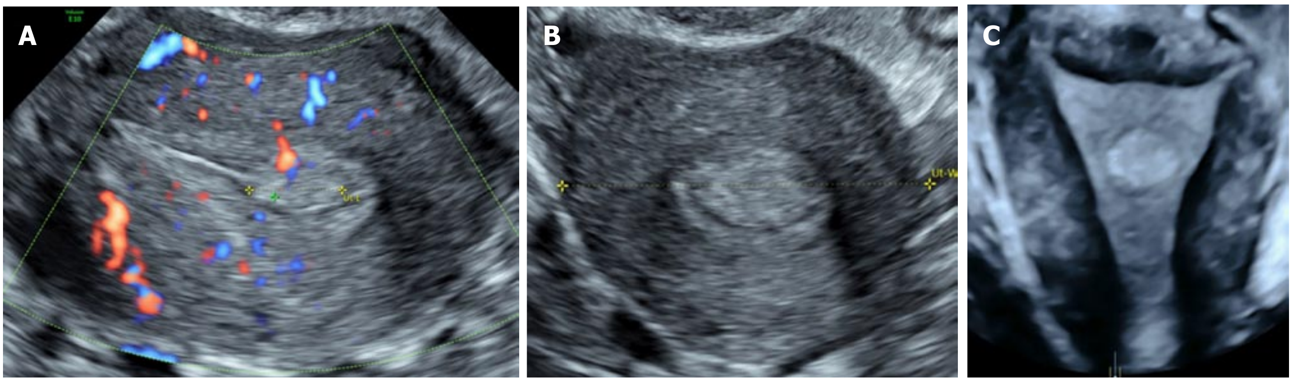

Figure 11 Endometrial polyp. A: Sagittal 2D ultrasound image of an endometrial polyp as identified by a vascular pedicle; B: Transverse 2D ultrasound image of the echogenic endometrial polyp; C: 3D coronal (VCI) ultrasound image showing the endometrial polyp better delineated as an echogenic mass. 3D: Three-dimensional; 2D: Two-dimensional; VCI: Volume contrast imaging.

is often classified as either diffuse or focal[27]. Rarely, it can present as a large adenomyotic cyst[28]. In assessing for changes due to adenomyosis, assessment of both the myometrium, as well as the JZ, are important features of diagnosing adenomyosis. In fact, in a recent consensus statement[28] describing ultrasound features of myometrial pathology, ultrasound features considered to be typical of adenomyosis include asymmetrical thickening, cysts, hyperechoic islands, fan shaped shadowing, echogenic subendometrial lines and buds, translesional vascularity, irregular JZ and interrupted JZ. While most of these features can be demonstrated on 2D ultrasound or colour Doppler, 3D ultrasound can be particularly useful for assessing the JZ in the coronal plane.

The JZ may be regular, irregular, interrupted, not visible, not assessable, or may manifest more than one feature, as classified by a recent consensus[28]. Although detailed morphological assessment and measurement of the JZ is currently predominantly for research pur-

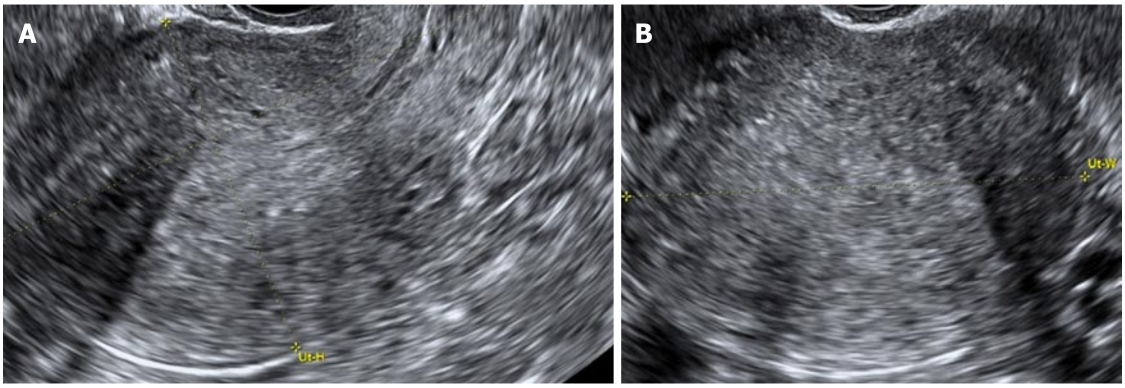

Figure 12 Adenomyosis with loss of the endometrial-myometrial junction. Sagittal (A) and transverse (B) 2D ultrasound images show the classic "venetian blind" shadowing of diffuse adenomyosis with loss of the endometrial-myometrial junction; B: 3D coronal ultrasound image (with VCI) showing the irregular endometrial-myometrial junction. Note the left lateral intramural fibroid. 3D: Three-dimensional; 2D: Two-dimensional; VCI: Volume contrast imaging.

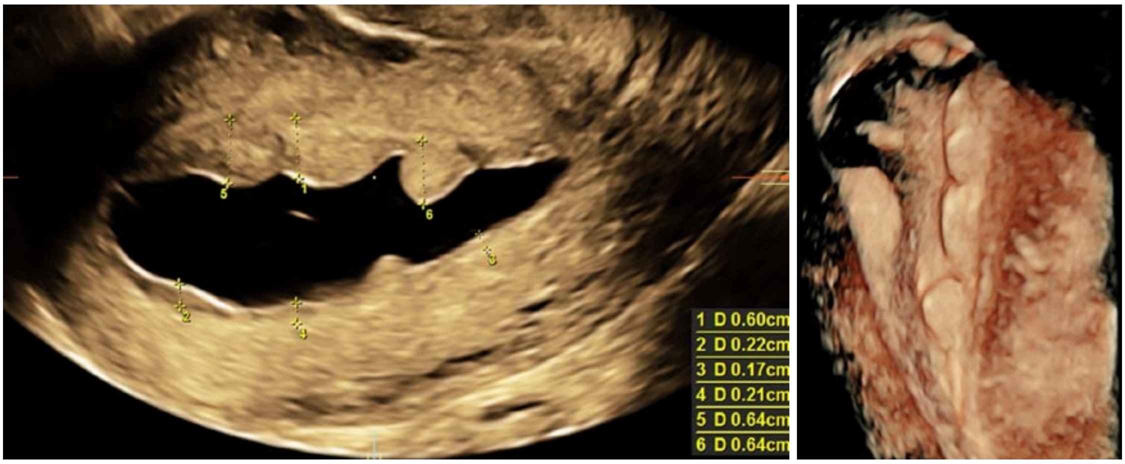

Figure 13 Saline infusion sonohysterography. A: 3D (VCI) A-plane image showing a thickened polypoid anterior endometrium upon distension with saline; B: 3D coronal image showing delineation of the polypoid endometrium on SIS. SIS: Saline infusion sonohysterography; 3D: Three-dimensional; VCI: Volume contrast imaging.

poses, broadly categorizing the JZ as either normal, or abnormal (irregular/interrupted), or not visible/not assessable will give an indication of the likelihood of JZ disorders[28].

Both MRI and 3D ultrasonography have been used to diagnose adenomyosis. In a systematic review by Champaneria *et al*[29] comparing the accuracy of the two imaging modalities, both TVUS and MRI were shown to have sufficiently high diagnostic accuracy although the study did not distinguish between 2D and 3D ultrasound. As on T2-weighted MR images, the JZ on 3D ultrasound appear as hypoechoic zone underlying the endometrium. 3D reconstruction of coronal sections of the uterine cavity has made it possible to assess minor changes in the lateral and fundal aspects of the JZ, which are impossible to delineate using standard 2D ultrasound. In additional, processing modalities such as VCI further enhance visualization of the hypoechoic JZ in comparison to that using 2D imaging[2,30,31]. Thus, 3D technology has made it possible to accurately assess and grade changes in the JZ architecture such as thickening, disruption and protrusion of the endometrium in to the inner myometrium. Exacoustos *et al*[2] correlated 2D and 3D transvaginal ultrasound imaging with histopathological features of adenomyosis in a total of 72 premenopausal patients. The most specific 2D-transvaginal ultrasound feature for the diagnosis of adenomyosis was presence of myometrial cysts (98% specificity; 78% accuracy), whereas a heterogeneous myometrium was most sensitive (88% sensitivity; 75% accuracy). On 3D-transvaginal ultrasound, the best markers were JZ difference ≥ 4 mm and JZ infiltration and distortion (both 88% sensitivity; 85% and 82% accuracy, respectively)[2].

Uterine synechiae

Uterine synechiae or adhesions have a significant adverse effect on fertility. 2D ultrasound may present a diagnostic clue to adhesions within the endometrial cavity through the presence of bands seen within the endometrial echo, particularly with the aid of sonohysterography. However, the true narrowing or "bands" adherent across the cavity is usually well delineated on the coronal plane on 3D imaging. Knopman *et al*[32] demonstrated that the sensitivity of detection with 3D ultrasound was higher compared to hysterosalpingogram and that 3D ultrasound predicted adhesions and cavity damage with greater accuracy than hysterosalpingogram in patients with suspected Asherman's syndrome.

3D reconstructions with saline-instilled sonohysterography

Saline-instilled sonohysterography (SIS) involves injection of sterile saline into the endometrial cavity *via* a catheter (Figure 13). The main purpose is to allow for assessment of the endometrial cavity for possible distortion of the endometrial cavity due to submucosal fibroids or endometrial polyps, congenital uterine anomalies or synechiae after distension of the cavity. Besides 2D SIS, 3D SIS to assess this data in the coronal plane is also helpful. 3D SIS may have the advantages over 2D SIS because by injection of saline, it will enhance the contrast of the endometrial-myometrial junction. It will also allow the collection of volume data which can then be manipulated and analysed offline, hence potentially decreasing the time taken to perform the study[1].

CONCLUSION

Advent in 3D imaging technology has seen 3D ultrasound establish itself as a useful adjunct complementary to traditional 2D imaging of the female pelvis. This advantage largely arises from its ability to reconstruct the coronal plane of the uterus, which allows further delineation of many gynecological disorders. 3D imaging of the uterus is now the preferred imaging modality for assessing congenital uterine anomalies and IUD localization. Newer indications include the diagnosis of adenomyosis. It can also add invaluable information to delineate other endometrial and myometrial pathology such as fibroids and endometrial polyps.

REFERENCES

1 **Andreotti RF**, Fleischer AC. Practical applications of 3D sonography in gynecologic imaging. *Radiol Clin North Am* 2014; **52**: 1201-1213 [PMID: 25444101 DOI: 10.1016/j.rcl.2014.07.001]

2 **Exacoustos C**, Brienza L, Di Giovanni A, Szabolcs B, Romanini ME, Zupi E, Arduini D. Adenomyosis: three-dimensional sonographic findings of the junctional zone and correlation with histology. *Ultrasound Obstet Gynecol* 2011; **37**: 471-479 [PMID: 21433167 DOI: 10.1002/uog.8900]

3 **Andreotti RF**, Fleischer AC, Mason LE. Three-dimensional sonography of the endometrium and adjacent myometrium: preliminary observations. *J Ultrasound Med* 2006; **25**: 1313-1319 [PMID: 16998104]

4 **Benacerraf BR**, Shipp TD, Bromley B. Which patients benefit from a 3D reconstructed coronal view of the uterus added to standard routine 2D pelvic sonography? *AJR Am J Roentgenol* 2008; **190**: 626-629 [PMID: 18287431 DOI: 10.2214/AJR.07.2632]

5 **Martins WP**, Raine-Fenning NJ, Leite SP, Ferriani RA, Nastri CO. A standardized measurement technique may improve the reliability of measurements of endometrial thickness and volume. *Ultrasound Obstet Gynecol* 2011; **38**: 107-115 [PMID: 21465609 DOI: 10.1002/uog.9016]

6 **Armstrong L**, Fleischer A, Andreotti R. Three-dimensional volumetric sonography in gynecology: an overview of clinical applications. *Radiol Clin North Am* 2013; **51**: 1035-1047 [PMID: 24210443 DOI: 10.1016/j.rcl.2013.07.005]

7 **Abuhamad AZ**, Singleton S, Zhao Y, Bocca S. The Z technique: an easy approach to the display of the mid-coronal plane of the uterus in volume sonography. *J Ultrasound Med* 2006; **25**: 607-612 [PMID: 16632784]

8 **Exacoustos C**, Luciano D, Corbett B, De Felice G, Di Feliciantonio M, Luciano A, Zupi E. The uterine junctional zone: a 3-dimensional ultrasound study of patients with endometriosis. *Am J Obstet Gynecol* 2013; **209**: 248.e1-248.e7 [PMID: 23770466 DOI: 10.1016/j.ajog.2013.06.006]

9 **Steiner H**, Staudach A, Spitzer D, Schaffer H. Three-dimensional ultrasound in obstetrics and gynaecology: technique, possibilities and limitations. *Hum Reprod* 1994; **9**: 1773-1778 [PMID: 7836537]

10 **Bocca SM**, Oehninger S, Stadtmauer L, Agard J, Duran EH, Sarhan A, Horton S, Abuhamad AZ. A study of the cost, accuracy, and benefits of 3-dimensional sonography compared with hysterosalpingography in women with uterine abnormalities. *J Ultrasound Med* 2012; **31**: 81-85 [PMID: 22215773]

11 **Saravelos SH**, Cocksedge KA, Li TC. Prevalence and diagnosis of congenital uterine anomalies in women with reproductive failure: a critical appraisal. *Hum Reprod Update* 2008; **14**: 415-429 [PMID: 18539641 DOI: 10.1093/humupd/dmn018]

12 **Buttram VC**, Gibbons WE. Müllerian anomalies: a proposed classification. (An analysis of 144 cases). *Fertil Steril* 1979; **32**: 40-46 [PMID: 456629]

13 The American Fertility Society classifications of adnexal adhesions, distal tubal occlusion, tubal occlusion secondary to tubal ligation, tubal pregnancies, müllerian anomalies and intrauterine adhesions. *Fertil Steril* 1988; **49**: 944-955 [PMID: 3371491]

14 **Bermejo C**, Martínez Ten P, Cantarero R, Diaz D, Pérez Pedregosa J, Barrón E, Labrador E, Ruiz López L. Three-dimensional ultrasound in the diagnosis of Müllerian duct anomalies and concordance with magnetic resonance imaging. *Ultrasound Obstet Gynecol* 2010; **35**: 593-601 [PMID: 20052665 DOI: 10.1002/uog.7551]

15 **Ghi T**, Casadio P, Kuleva M, Perrone AM, Savelli L, Giunchi S, Meriggiola MC, Gubbini G, Pilu G, Pelusi C, Pelusi G. Accuracy of three-dimensional ultrasound in diagnosis and classification of congenital uterine anomalies. *Fertil Steril* 2009; **92**: 808-813 [PMID: 18692833 DOI: 10.1016/j.fertnstert.2008.05.086]

16 **Moini A**, Mohammadi S, Hosseini R, Eslami B, Ahmadi F. Accuracy of 3-dimensional sonography for diagnosis and classification of congenital uterine anomalies. *J Ultrasound Med* 2013; **32**: 923-927 [PMID: 23716512 DOI: 10.7863/ultra.32.6.923]

17 **Ludwin A**, Ludwin I. Comparison of the ESHRE-ESGE and ASRM classifications of Müllerian duct anomalies in everyday practice. *Hum Reprod* 2015; **30**: 569-580 [PMID: 25534461 DOI: 10.1093/humrep/deu344]

18 **Salim R**, Regan L, Woelfer B, Backos M, Jurkovic D. A comparative study of the morphology of congenital uterine anomalies in women with and without a history of recurrent first trimester miscarriage. *Hum Reprod* 2003; **18**: 162-166 [PMID: 12525460]

19 **Salim R**, Woelfer B, Backos M, Regan L, Jurkovic D. Reproducibility of three-dimensional ultrasound diagnosis of congenital uterine anomalies. *Ultrasound Obstet Gynecol* 2003; **21**: 578-582 [PMID: 12808675 DOI: 10.1002/uog.127]

20 **Woelfer B**, Salim R, Banerjee S, Elson J, Regan L, Jurkovic D. Reproductive outcomes in women with congenital uterine anomalies detected by three-dimensional ultrasound screening. *Obstet Gynecol* 2001; **98**: 1099-1103 [PMID: 11755560]

21 **Jurkovic D**, Mavrelos D. Catch me if you scan: ultrasound diagnosis of ectopic pregnancy. *Ultrasound Obstet Gynecol* 2007; **30**: 1-7 [PMID: 17587215 DOI: 10.1002/uog.4077]

22 **Lee A**, Eppel W, Sam C, Kratochwil A, Deutinger J, Bernaschek G. Intrauterine device localization by three-dimensional transvaginal sonography. *Ultrasound Obstet Gynecol* 1997; **10**: 289-292 [PMID: 9383883 DOI: 10.1046/j.1469-0705.1997.10040289.x]

23 **Benacerraf BR**, Shipp TD, Bromley B. Three-dimensional ultrasound

detection of abnormally located intrauterine contraceptive devices which are a source of pelvic pain and abnormal bleeding. *Ultrasound Obstet Gynecol* 2009; **34**: 110-115 [PMID: 19565532 DOI: 10.1002/uog.6421]

24 **Sehgal N**, Haskins AL. The mechanism of uterine bleeding in the presence of fibromyomas. *Am Surg* 1960; **26**: 21-23 [PMID: 14444585]

25 **Brosens I**, Derwig I, Brosens J, Fusi L, Benagiano G, Pijnenborg R. The enigmatic uterine junctional zone: the missing link between reproductive disorders and major obstetrical disorders? *Hum Reprod* 2010; **25**: 569-574 [PMID: 20085913 DOI: 10.1093/humrep/dep474]

26 **Campo S**, Campo V, Benagiano G. Adenomyosis and infertility. *Reprod Biomed Online* 2012; **24**: 35-46 [PMID: 22116070 DOI: 10.1016/j.rbmo.2011.10.003]

27 **Meredith SM**, Sanchez-Ramos L, Kaunitz AM. Diagnostic accuracy of transvaginal sonography for the diagnosis of adenomyosis: systematic review and metaanalysis. *Am J Obstet Gynecol* 2009; **201**: 107.e1-107.e6 [PMID: 19398089 DOI: 10.1016/j.ajog.2009.03.021]

28 **Van den Bosch T**, Dueholm M, Leone FP, Valentin L, Rasmussen CK, Votino A, Van Schoubroeck D, Landolfo C, Installé AJ, Guerriero S, Exacoustos C, Gordts S, Benacerraf B, D'Hooghe T, De Moor B, Brölmann H, Goldstein S, Epstein E, Bourne T, Timmerman D. Terms, definitions and measurements to describe sonographic features of myometrium and uterine masses: a consensus opinion from the Morphological Uterus Sonographic Assessment (MUSA) group. *Ultrasound Obstet Gynecol* 2015; **46**: 284-298 [PMID: 25652685 DOI: 10.1002/uog.14806]

29 **Champaneria R**, Abedin P, Daniels J, Balogun M, Khan KS. Ultrasound scan and magnetic resonance imaging for the diagnosis of adenomyosis: systematic review comparing test accuracy. *Acta Obstet Gynecol Scand* 2010; **89**: 1374-1384 [PMID: 20932128 DOI: 10.3109/00016349.2010.512061]

30 **Abdallah Y**, Naji O, Saso S, Pexsters A, Stalder C, Sur S, Raine-Fenning N, Timmerman D, Brosens JJ, Bourne T. Ultrasound assessment of the peri-implantation uterus: a review. *Ultrasound Obstet Gynecol* 2012; **39**: 612-619 [PMID: 21910147 DOI: 10.1002/uog.10098]

31 **Naftalin J**, Jurkovic D. The endometrial-myometrial junction: a fresh look at a busy crossing. *Ultrasound Obstet Gynecol* 2009; **34**: 1-11 [PMID: 19565525 DOI: 10.1002/uog.6432]

32 **Knopman J**, Copperman AB. Value of 3D ultrasound in the management of suspected Asherman's syndrome. *J Reprod Med* 2007; **52**: 1016-1022 [PMID: 18161399]

P- Reviewer: Peitsidis P, Tirumani SH **S- Editor**: Ji FF **L- Editor**: A
E- Editor: Wu HL

World Journal of
Radiology

Submit a Manuscript: http://www.wjgnet.com/esps/
Help Desk: http://www.wjgnet.com/esps/helpdesk.aspx
DOI: 10.4329/wjr.v7.i12.494

World J Radiol 2015 December 28; 7(12): 494-500
ISSN 1949-8470 (online)

ORIGINAL ARTICLE

Retrospective Study

Recovery of serum testosterone following neoadjuvant and adjuvant androgen deprivation therapy in men treated with prostate brachytherapy

Hideyasu Tsumura, Takefumi Satoh, Hiromichi Ishiyama, Shuhei Hirano, Ken-ichi Tabata, Shinji Kurosaka, Kazumasa Matsumoto, Tetsuo Fujita, Masashi Kitano, Shiro Baba, Kazushige Hayakawa, Masatsugu Iwamura

Hideyasu Tsumura, Takefumi Satoh, Shuhei Hirano, Ken-ichi Tabata, Shinji Kurosaka, Kazumasa Matsumoto, Tetsuo Fujita, Shiro Baba, Masatsugu Iwamura, Department of Urology, Kitasato University School of Medicine, Sagamihara 252-0374, Japan

Hiromichi Ishiyama, Masashi Kitano, Kazushige Hayakawa, Department of Radiation Oncology, Kitasato University School of Medicine, Sagamihara 252-0374, Japan

Author contributions: Tsumura H performed the majority of the work including collecting, analyzing, and interpreting the data and writing the report; Ishiyama H, Hirano S, Kurosaka S and Kitano M contributed to collecting the data; Tabata K, Matsumoto K and Fujita T were participated in analyzing and interpreting the data; Satoh T, Baba S, Hayakawa K and Iwamura M designed and coordinated the study.

Institutional review board statement: The study was reviewed and approved by the Institutional Review Board of Kitasato University School of Medicine and Kitasato University Hospital (B14-21).

Informed consent statement: This retrospective study was performed under IRB approval, all data is de-identified for statistical analysis. Therefore, we think that a waiver of informed consent may be justifiable under this situation.

Conflict-of-interest statement: Dr. Tsumura received honoraria for lecture fees from Nihon Medi-Physics Co, Ltd. Astellas Pharma Inc, and Takeda Pharmaceutical Co, Ltd. Drs Satoh, Ishiyama and Hayakawa received honoraria for lecture fees from Medicon Co, Ltd, and Nihon Medi-Physics Co, Ltd.

Data sharing statement: No additional data are available.

Correspondence to: Hideyasu Tsumura, MD, Department of Urology, Kitasato University School of Medicine, 1-15-1 Kitasato Minami-ku, Sagamihara 252-0374,
Japan. tsumura@med.kitasato-u.ac.jp
Telephone: +81-42-7789091
Fax: +81-42-7789374

Received: May 8, 2015
Peer-review started: May 9, 2015
First decision: July 27, 2015
Revised: August 13, 2015
Accepted: October 12, 2015
Article in press: October 12, 2015
Published online: December 28, 2015

Abstract

AIM: To investigate the time course of testosterone (T) recovery after cessation of androgen deprivation therapy (ADT) in patients treated with brachytherapy.

METHODS: One-hundred and seventy-four patients treated between June 1999 and February 2009 were studied. Patients were divided into a short-term usage group ($\leqslant$ 12 mo, *n* = 91) and a long-term usage group ($\geqslant$ 36 mo, *n* = 83) according to the duration of gonadotropin-releasing hormone agonist therapy. Median follow-up was 29 mo in the short-term group and was 60 mo in the long-term group.

RESULTS: Cumulative incidence rates of T recovery to normal and supracastrate levels at 24 mo after cessation were 28.8% and 74.6%, respectively, in the long-term usage group, whereas these values were 96.4% and 98.8% in the short-term usage group. T recovery to normal and supracastrate levels occurred significantly more rapidly in the short-term than in the long-term usage group (P < 0.001 and P < 0.001, respectively). Five years after cessation, 22.6% of patients maintained a castrate T level in the long-term usage group. On multivariate analysis, lower T levels (< 10 ng/dL) at cessation of ADT was significantly associated with prolonged T recovery to supracastrate levels in the long-term usage group (P = 0.002).

CONCLUSION: Lower T levels at cessation of ADT were associated with prolonged T recovery in the long-term usage group. Five years after cessation of long-term ADT, approximately one-fifth of patients still had castrate T levels. When determining the therapeutic effect, especially biochemical control, we should consider this delay in T recovery.

Key words: Androgen deprivation; Gonadotropin-releasing hormone agonist; Prostate brachytherapy; Prostate cancer; Testosterone

Core tip: We evaluated the time course of testosterone recovery and the prognostic factors associated with prolonged testosterone recovery after the cessation of long-term (⩾ 36 mo) androgen deprivation therapy in patients treated with brachytherapy. Five years after cessation, 22.6% of patients maintained a castrate testosterone level. We should consider this delay when determining therapeutic effects. Lower testosterone levels at cessation were significantly associated with prolonged testosterone recovery.

Tsumura H, Satoh T, Ishiyama H, Hirano S, Tabata K, Kurosaka S, Matsumoto K, Fujita T, Kitano M, Baba S, Hayakawa K, Iwamura M. Recovery of serum testosterone following neoadjuvant and adjuvant androgen deprivation therapy in men treated with prostate brachytherapy. *World J Radiol* 2015; 7(12): 494-500 Available from: URL: http://www.wjgnet.com/1949-8470/full/v7/i12/494.htm DOI: http://dx.doi.org/10.4329/wjr.v7.i12.494

INTRODUCTION

Gonadotropin-releasing hormone (GnRH) agonists are widely used in various radiotherapies for the management of prostate cancer. The intended purpose and duration of hormonal therapy vary depending on the local extent of the cancer and the type of radiotherapy[1-3]. According to several randomized controlled studies, the use of 6 to 36 mo of hormonal therapy with external beam radiotherapy (EBRT) contributed to overall survival or cancer-specific survival in men with locally advanced or localized unfavorable-risk prostate cancer compared with radiotherapy alone[4-7]. After the cessation of androgen deprivation therapy (ADT), serum testosterone (T) levels usually recover from castrate levels to normal levels. However, some patients maintain the castrate T levels for several years after cessation, especially if hormonal manipulation is used for prolonged periods. In these cases, clinicians cannot assess whether radiotherapy controls prostate-specific antigen (PSA) levels because there is a possibility that prolonged effects of ADT simply control the disease. Thus, clinicians should assess the recovery of T levels after cessation of ADT when they interpret PSA relapse-free survival rates. Although some studies have documented the time course of recovery of T levels after cessation of long-term ADT, these studies were intended for patients who had received less than 36 mo of continuous GnRH agonist therapy or who were observed for shorter follow-up periods[8,9].

In this retrospective study, we estimated the time course of recovery of T levels after cessation of long-term use (⩾ 36 mo) of ADT and short-term use (⩽ 12 mo) of ADT in patients treated with prostate brachytherapy. In addition, the factors associated with T recovery were analyzed to determine which patients have the potential for prolonged time until recovery to supracastrate and/or normal T levels after cessation of ADT.

MATERIALS AND METHODS

Patients

There were 216 candidates for this study who received either ^{192}Ir high-dose rate (HDR) brachytherapy or ^{125}I permanent low-dose rate (LDR) brachytherapy for prostate cancer with neoadjuvant hormonal therapy (NHT) or adjuvant hormonal therapy (AHT) using GnRH agonists between June 1999 and February 2009 at our institution. Patients were divided into two groups according to the duration of GnRH agonist therapy: short-term (neoadjuvant) usage group (duration 3 to 12 mo) and long-term (neoadjuvant and adjuvant) usage group (⩾ 36 mo). A normal level of T and a castrate T level were defined as ⩾ 207 ng/dL and ⩽ 50 ng/dL, respectively. A T level of > 50 ng/dL was defined as a supracastrate level. Both supracastrate and normal levels were used for the definition of T recovery.

The T level of each patient was measured 1 mo before the cessation of GnRH agonist therapy (baseline levels) and until it recovered to a normal level. A follow-up examination after the cessation of ADT was scheduled every 3 mo for the first year, and then every 6 mo thereafter. Patients were removed from the study if PSA failure was observed during AHT because they needed to continue the administration of GnRH agonist therapy to maintain the castrate T level. All patients underwent a complete history and physical examination at the time of brachytherapy, including

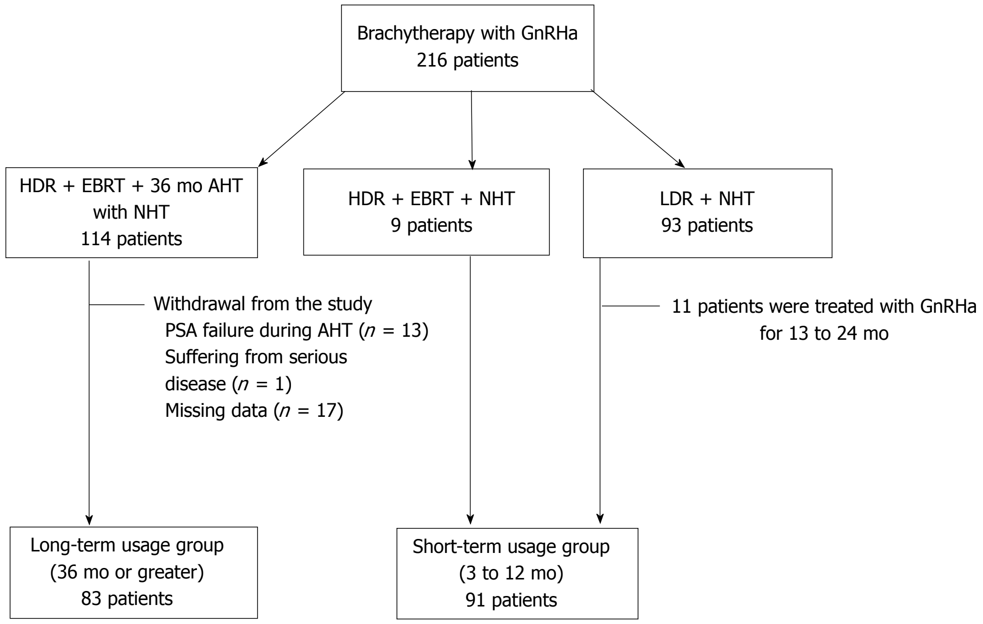

Figure 1 Characteristics of the 216 candidates considered for the study. GnRHa: Gonadotropin-releasing hormone agonist therapy; HDR: High-dose rate brachytherapy; EBRT: External beam radiotherapy; AHT: Adjuvant hormonal therapy; NHT: Neoadjuvant hormonal therapy; LDR: Low-dose rate brachytherapy; PSA: Prostate-specific antigen.

body mass index and the presence or absence of diabetes and hypertension. ADT consisted of GnRH agonist as a 1-mo or 3-mo formulation with or without an oral anti-androgen. Either flutamide (375 mg/d) or bicalutamide (80 mg) was used as the nonsteroidal anti-androgen agent. Either goserelin (3.6 or 10.8 mg) or leuprorelin (3.75 or 11.25 mg) was administrated as the GnRH agonist. Serum T levels were measured by immunoradiometric assay. Approval was granted by the ethics committee of our institution. Median follow-up times from cessation were 29 and 60 mo for the short-term and long-term groups, respectively.

LDR brachytherapy and hormonal therapy

Patients with low-risk or intermediate-risk prostate cancer were candidates for LDR brachytherapy. The prescribed dose to the periphery of the prostate was 145 Gy using a prostate implant technique that was described previously[10,11]. Patients who had large glands or who were at intermediate risk were treated with combined androgen blockade for 3 to 12 mo as NHT. Neither EBRT nor AHT was administered.

HDR brachytherapy and hormonal therapy

We previously mentioned about our protocol and procedure for HDR brachytherapy and hormonal therapy in high-risk prostate cancer[12,13]. Briefly, the mean dose to 90% of the planning target volume was 6.3 Gy/fraction of ^{192}Ir HDR brachytherapy. After five fractions of HDR treatment, EBRT with 10 fractions of 3 Gy was administered. Patients received EBRT using a dynamic-arc conformal technique, administered with high-energy photons comprising 10-MV X-rays. The radiation field was limited to the prostate gland with or without proximal seminal vesicles with a 7-mm leaf margin using multileaf collimators. Testicular dose was not computed. All patients initially underwent 6 mo or more of neoadjuvant ADT. In patients who had high-risk cancer, adjuvant ADT was continued for 36 mo after EBRT. Low-risk or intermediate-risk patients were treated without adjuvant ADT D'Amico criteria were used for risk group stratification[14].

Statistical analysis

The Kaplan-Meier method was used to estimate the cumulative incidence of T recovery. A Log-Rank test was performed to compare these estimates. Multivariate Cox regression models were created based on the covariates that were significant in univariate analysis. Differences were regarded as statistically significant at $P < 0.05$. Analyses were performed using SPSS version 11.0 for Windows (SPSS, Inc., Chicago, IL, United States), GraphPad Prism, version 5 (GraphPad Software, Inc., CA, United States), and Microsoft Excel (Microsoft, Redmond, WA, United States).

RESULTS

Patient characteristics

Figure 1 provides the characteristics of the 216 patients who were candidates for the present study. Data for the 174 who were eligible for inclusion in the efficacy analysis were analyzed, and 42 patients (19.4%) were removed for reasons detailed in Figure 1: PSA failure during AHT (*n* = 13), severe disease (*n* = 1), missing data (*n* = 17), and ADT duration deviation from study protocol (*n* = 11). All patients reached castrate T levels at cessation of ADT. Table 1 shows the patient

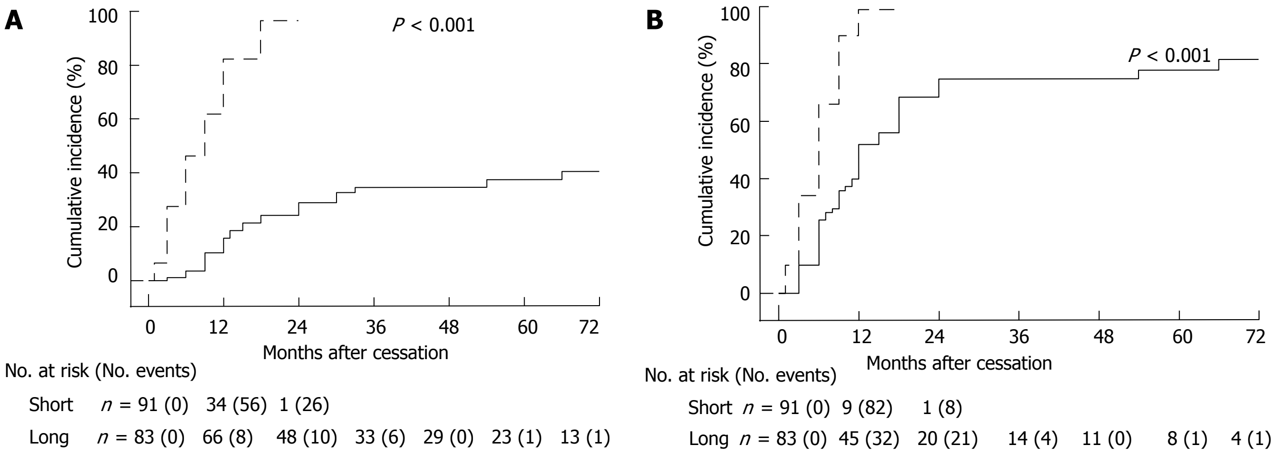

Figure 2 Cumulative incidence of testosterone recovery to normal levels (A) and supracastrate levels (B) according to duration of gonadotropin-releasing hormone agonist therapy. Significance ($P < 0.05$) was determined according to a Log-Rank test.

Table 1 Patient background data

	Short-term usage group (n = 91)		Long-term usage Group (n = 83)	
	Median	Range	Median	Range
Age at cessation (yr)	69	54-78	73	53-90
Body mass index	24.1	18.6-32.5	24.3	17.1-32.5
Duration of GnRHa (mo)	6	3-12	47	36-66
Follow-up duration from cessation of GnRHa (mo)	29	3-52	60	3-94
	n	%	*n*	%
Diabetes, yes	10	10.9	8	9.6
Hypertension, yes	36	39.5	33	39.7

GnRHa: Gonadotropin-releasing hormone agonist therapy.

Table 2 Univariate and multivariate analyses of factors associated with testosterone recovery to supracastrate levels in the long-term usage group

Factor	Univariate analysis			Multivariate analysis		
	HR	95%CI	*P* value	HR	95%CI	*P* value
At brachytherapy						
Body mass index						
< 25	1.249	0.733-2.130	0.413	-	-	-
≥ 25	1.000	(reference)		-	-	-
Diabetes						
No	1.262	0.505-3.156	0.687	-	-	-
Yes	1.000	(reference)		-	-	-
Hypertension						
No	0.959	0.572-1.608	0.873	-	-	-
Yes	1.000	(reference)		-	-	-
At cessation						
Age						
< 73 yr	1.98	1.182-3.317	0.009	2.020	1.190-3.429	0.009
≥ 73 yr	1.000	(reference)		1.000	(reference)	
T level at baseline[1]						
< 10 ng/dL	1.000	(reference)		1.000	(reference)	
≥ 10 ng/dL	2.261	1.316-3.883	0.003	2.327	1.354-4.000	0.002
Drug formulation						
Duration of activity						
1 mo	1.000	(reference)		-	-	-
3 mo	1.419	0.821-2.454	0.209	-	-	-
Material						
Goserelin	0.973	0.579-1.635	0.917	-	-	-
Leuprorelin	1.000	(reference)		-	-	-

[1] Testosterone level at baseline was measured 1 mo before the cessation of androgen deprivation therapy. Statistical significance was assessed at $P < 0.05$. T: Testosterone.

background data for the short-term and long-term usage groups (n = 91 and n = 83, respectively).

Cumulative incidence of T recovery

We compared the cumulative incidence of T recovery to normal levels (Figure 2A) and to supracastrate levels (Figure 2B) between the short-term and long-term usage groups. A Log-Rank test showed that T recovery to normal levels occurred significantly more rapidly in the short-term than in the long-term usage group (HR = 9.180; 95%CI: 5.883-14.32; $P < 0.001$). T recovery to supracastrate levels also occurred significantly more rapidly in the short-term than in the long-term usage group (HR = 5.051; 95%CI: 3.346-7.624; $P < 0.001$). Cumulative incidences of T recovery to normal and supracastrate levels at 24 mo after cessation were 28.8% and 74.6%, respectively, in the long-term usage group, whereas these values were 96.4% and 98.8% in the short-term usage group. Five years after cessation, 22.6% of patients maintained a castrate T level in the long-term usage group.

Factors associated with T recovery

Table 2 provides the univariate and multivariate results of factors that may influence T recovery to supracastrate levels in the long-term usage group. Age 73 years or older at cessation (n = 47; 57%) was significantly associated with slower recovery to supracastrate levels in the long-term usage group (multivariate analysis, P = 0.009). T level < 10 ng/dL at baseline (n = 39; 47%)

was also significantly associated with slower recovery to supracastrate levels in this group (multivariate analysis, $P = 0.002$). Both age 73 years or older at cessation and T level < 10 ng/dL at baseline were also significantly associated with slower recovery to normal levels in the long-term usage group on multivariate analysis ($P = 0.005$ and $P = 0.001$, respectively). There were no significant factors associated with slower T recovery in the short-term usage group (data not shown).

Influence of different GnRH agonist agents on T recovery

To examine the influence of different GnRH agonist agents on T recovery in the long-term usage group, patients were divided into two groups according to drug material: Goserelin ($n = 34$; 41%) and leuprorelin ($n = 49$; 59%). Patients were also divided into two groups according to the duration of drug activity: 1-mo formulation ($n = 34$; 41%) and 3-mo formulation ($n = 35$; 42%). Fourteen patients (17%) were switched from the 1-mo formulation to the 3-mo formulation for various reasons and were removed from this analysis. There was no significant difference regarding the time course of T recovery to supracastrate levels between goserelin and leuprorelin (univariate analysis, $P = 0.917$). The 1-mo formulation was not significantly associated with more rapid recovery to supracastrate levels, nor was the 3-mo formulation (univariate analysis, $P = 0.209$).

DISCUSSION

In the present study, we estimated the time course of recovery of T levels after cessation of long-term use (≥ 36 mo) of ADT in high-risk prostate cancer patients treated with brachytherapy. More than half the patients who received long-term ADT did not experience recovery to normal T levels at 5 years after cessation. In addition, approximately one-fifth of the patients who received long-term ADT still had castration levels at 5 years after cessation. In these cases, we have difficulty judging whether cure is attributable to radiotherapy, to sustained castration, or to both.

Several studies showed that the longer the ADT treatment, the more time that was required for T recovery[8,15-17]; some studies reported prolonged sustainment of castrate T levels after cessation of long-term ADT. Giberti *et al*[18] performed testicular biopsies in seven patients who received long-term ADT. This revealed impaired Leydig cell masses with tubular derangement and fibrosis. The findings suggested that long-term ADT induces not only functional inhibition of testicular androgenesis but also anatomical testicular damage that is likely irreversible. We previously investigated the changes in serum T and luteinzing hormone (LH) levels after withdrawal of long-term ADT in patents with intermittent endocrine therapy. Patients who maintained castrate T levels after long-term follow-up had above-normal LH levels[16]. This indicated that the feedback system of the hypothalamo-pituitary responded normally to the low levels of T after cessation. Thus, the prolonged sustainment of castrate T levels after cessation of long-term ADT may be attributable to the testicular damage, which is likely irreversible.

Shahidi *et al*[19] reported serum T levels were restored to normal levels in the majority of patients (88%) after short-term (3 to 6 mo) GnRH agonist administration and radiotherapy. Murthy *et al*[20] found that T was maintained at normal levels 5 years after the combination of a short course of GnRH agonist therapy (median, 97 d; range, 28-167 d) and EBRT. Our findings also suggest that the suppression of T levels after short-term ADT is reversible, because the majority of men who underwent prostate brachytherapy had T that recovered to normal levels. Although prolonged sustainment of castrate T levels after cessation of ADT is of little concern for the short-term usage group (≤ 12 mo), this sustainment occurred in approximately 20% of patients in the long-term usage group (≥ 36 mo) in the present study. Yoon *et al*[9] reported that approximately 10% of patients maintained castrate T levels after cessation of long-term use (2 years) of ADT. The rates of prolonged sustainment have a tendency to increase with the duration of the use of ADT. The longer the ADT treatment, the more patients were unlikely to recover from castrate T levels. The use of more than 2 years of ADT is likely to increase the incidence of this prolonged sustainment of castrate T levels.

The prolonged sustainment of castrate T levels not only could affect the biochemical control rates in patients treated with prostate radiotherapy but also could maintain the adverse long-term effects in patients. This could put some men at risk for cardiovascular events, diabetes, and osteoporotic fracture[21-23]. Fracture rates increased with increasing cumulative GnRH dose. The osteoporotic fracture caused by long-term ADT could affect the prognosis in prostate cancer patients, and the mortality rate doubled for men experiencing a fracture after their diagnosis compared with that for men who did not experience a fracture[24]. Thus, the management of bone health and T recovery is important in those patients[21,25].

In accordance with our findings, previous studies reported that older age was a significant factor associated with slower T recovery when GnRH agonist therapy was used for at least 24 mo[9,17,26]. The production of T decreases with age[27,28]. This decline might also be related to later T recovery in older men treated with long-term ADT[9].

The present study has certain shortcomings. Previous studies suggested the impact of scatter radiation on T levels and Leydig cell function in men treated with EBRT[29,30]. It is still unclear how HDR or LDR brachytherapy influences T levels. Thus, the cumulative incidence of T recovery might be incommensurable among men undergoing different kinds of radiotherapy. Unlike previous studies[9,17], we could not evaluate the impact of pre-ADT T levels on T recovery because some patients had already received ADT when they began treatment at our institution. In addition, we did not investigate how the prolonged sustainment of castrate T levels had an impact on patient quality of life. However, the present study is the first to find that a lower T level at cessation of ADT (⩽ 10 ng/dL) is one significant factor that affected the slower T recovery to supracastrate levels in patients treated with long-term GnRH agonist therapy.

In men treated with long-term ADT, 22.6% of the patients maintained castrate T levels at 5 years after cessation. When determining the therapeutic effects, especially biochemical control, we should consider this delay in time to T recovery. Older age (73 years or older) and lower T levels (< 10 ng/dL) at ADT cessation were significantly associated with slower T recovery to supracastrate levels in men treated with long-term ADT.

COMMENTS

Background

Some patients maintain the castrate testosterone (T) levels for several years after cessation of androgen deprivation therapy (ADT), especially if hormonal manipulation is used for prolonged periods. In these cases, clinicians cannot assess whether radiotherapy controls prostate-specific antigen (PSA) levels because there is a possibility that prolonged effects of ADT simply control the disease. Thus, clinicians should assess the recovery of T levels after cessation of ADT when they interpret PSA relapse-free survival rates.

Research frontiers

Some studies have documented the time course of recovery of T levels after cessation of long-term ADT. These studies were intended for patients who had received less than 36 mo of continuous gonadotropin-releasing hormone (GnRH) agonist therapy. The present study is the first to evaluate the time course of recovery of T levels after cessation of ⩾ 36 mo use of ADT.

Innovations and breakthroughs

Previous studies reported that older age was a significant factor associated with slower T recovery when GnRH agonist therapy was used for at least 24 mo. The present study is the first to find that a lower T level at cessation of ADT (⩽ 10 ng/dL) is one significant factor that affected the slower T recovery to supracastrate levels in patients treated with long-term GnRH agonist therapy.

Applications

Five years after cessation of long-term ADT (⩾ 36 mo), approximately one-fifth of patients still had castrate T levels. When determining the therapeutic effect of radiotherapy, especially biochemical control, researchers should consider this delay in T recovery.

Terminology

ADT: Prostate cancer usually requires androgen hormones such as T. GnRH agonists are widely used as ADT for the management of prostate cancer. GnRH agonists reduce the levels of serum T.

Peer-review

Very well written paper and the authors provided the important and clear message that GnRHa hormone therapy might cause long lasting androgen suppression.

REFERENCES

1 **Monroe AT**, Faricy PO, Jennings SB, Biggers RD, Gibbs GL, Peddada AV. High-dose-rate brachytherapy for large prostate volumes (& gt; or =50cc)-Uncompromised dosimetric coverage and acceptable toxicity. *Brachytherapy* 2008; **7**: 7-11 [PMID: 18299109 DOI: 10.1016/j.brachy.2007.10.005]

2 **Bittner N**, Merrick GS, Butler WM, Galbreath RW, Lief J, Adamovich E, Wallner KE. Long-term outcome for very high-risk prostate cancer treated primarily with a triple modality approach to include permanent interstitial brachytherapy. *Brachytherapy* 2012; **11**: 250-255 [PMID: 22436516 DOI: 10.1016/j.brachy.2012.02.002]

3 **Zumsteg ZS**, Spratt DE, Pei X, Yamada Y, Kalikstein A, Kuk D, Zhang Z, Zelefsky MJ. Short-term androgen-deprivation therapy improves prostate cancer-specific mortality in intermediate-risk prostate cancer patients undergoing dose-escalated external beam radiation therapy. *Int J Radiat Oncol Biol Phys* 2013; **85**: 1012-1017 [PMID: 22981709 DOI: 10.1016/j.ijrobp.2012.07.2374]

4 **Bolla M**, Collette L, Blank L, Warde P, Dubois JB, Mirimanoff RO, Storme G, Bernier J, Kuten A, Sternberg C, Mattelaer J, Lopez Torecilla J, Pfeffer JR, Lino Cutajar C, Zurlo A, Pierart M. Long-term results with immediate androgen suppression and external irradiation in patients with locally advanced prostate cancer (an EORTC study): a phase III randomised trial. *Lancet* 2002; **360**: 103-106 [PMID: 12126818]

5 **Horwitz EM**, Bae K, Hanks GE, Porter A, Grignon DJ, Brereton HD, Venkatesan V, Lawton CA, Rosenthal SA, Sandler HM, Shipley WU. Ten-year follow-up of radiation therapy oncology group protocol 92-02: a phase III trial of the duration of elective androgen deprivation in locally advanced prostate cancer. *J Clin Oncol* 2008; **26**: 2497-2504 [PMID: 18413638 DOI: 10.1200/JCO.2007.14.9021]

6 **Denham JW**, Steigler A, Lamb DS, Joseph D, Mameghan H, Turner S, Matthews J, Franklin I, Atkinson C, North J, Poulsen M, Christie D, Spry NA, Tai KH, Wynne C, Duchesne G, Kovacev O, D'Este C. Short-term androgen deprivation and radiotherapy for locally advanced prostate cancer: results from the Trans-Tasman Radiation Oncology Group 96.01 randomised controlled trial. *Lancet Oncol* 2005; **6**: 841-850 [PMID: 16257791 DOI: 10.1016/S1470-2045(05)70348-X]

7 **D'Amico AV**, Chen MH, Renshaw AA, Loffredo M, Kantoff PW. Androgen suppression and radiation vs radiation alone for prostate cancer: a randomized trial. *JAMA* 2008; **299**: 289-295 [PMID: 18212313 DOI: 10.1001/jama.299.3.289]

8 **Pickles T**, Agranovich A, Berthelet E, Duncan GG, Keyes M, Kwan W, McKenzie MR, Morris WJ. Testosterone recovery following prolonged adjuvant androgen ablation for prostate carcinoma. *Cancer* 2002; **94**: 362-367 [PMID: 11900222 DOI: 10.1002/cncr.10219]

9 **Yoon FH**, Gardner SL, Danjoux C, Morton G, Cheung P, Choo R. Testosterone recovery after prolonged androgen suppression in patients with prostate cancer. *J Urol* 2008; **180**: 1438-1443; discussion 1443-1444 [PMID: 18710743 DOI: 10.1016/j.juro.2008.06.029]

10 **Ishiyama H**, Kitano M, Satoh T, Niibe Y, Uemae M, Fujita T, Baba S, Hayakawa K. Difference in rectal dosimetry between pre-plan and post-implant analysis in transperineal interstitial brachytherapy for prostate cancer. *Radiother Oncol* 2006; **78**: 194-198 [PMID: 16414135 DOI: 10.1016/j.radonc.2005.12.008]

11 **Sekiguchi A**, Ishiyama H, Satoh T, Tabata K, Komori S, Tsumura H, Kawakami S, Soda I, Iwamura M, Hayakawa K. 125Iodine monotherapy for Japanese men with low- and intermediate-risk prostate cancer: outcomes after 5 years of follow-up. *J Radiat Res* 2014; **55**: 328-333 [PMID: 24105711 DOI: 10.1093/jrr/rrt113]

12 **Ishiyama H**, Kitano M, Satoh T, Kotani S, Uemae M, Matsumoto K, Okusa H, Tabata K, Baba S, Hayakawa K. Genitourinary toxicity after high-dose-rate (HDR) brachytherapy combined with Hypofractionated External beam radiotherapy for localized prostate cancer: an analysis to determine the correlation between dose-volume histogram parameters in HDR brachytherapy and severity of toxicity. *Int J Radiat Oncol Biol Phys* 2009; **75**: 23-28 [PMID: 19243900 DOI: 10.1016/j.ijrobp.2008.11.006]

13 **Ishiyama H**, Satoh T, Kitano M, Tabata K, Komori S, Ikeda M, Soda I, Kurosaka S, Sekiguchi A, Kimura M, Kawakami S, Iwamura M, Hayakawa K. High-dose-rate brachytherapy and hypofractionated external beam radiotherapy combined with long-

term hormonal therapy for high-risk and very high-risk prostate cancer: outcomes after 5-year follow-up. *J Radiat Res* 2014; **55**: 509-517 [PMID: 24222312 DOI: 10.1093/jrr/rrt128]

14 **D'Amico AV**, Whittington R, Malkowicz SB, Schultz D, Blank K, Broderick GA, Tomaszewski JE, Renshaw AA, Kaplan I, Beard CJ, Wein A. Biochemical outcome after radical prostatectomy, external beam radiation therapy, or interstitial radiation therapy for clinically localized prostate cancer. *JAMA* 1998; **280**: 969-974 [PMID: 9749478]

15 **Nejat RJ**, Rashid HH, Bagiella E, Katz AE, Benson MC. A prospective analysis of time to normalization of serum testosterone after withdrawal of androgen deprivation therapy. *J Urol* 2000; **164**: 1891-1894 [PMID: 11061874]

16 **Egawa S**, Okusa H, Matsumoto K, Suyama K, Baba S. Changes in prostate-specific antigen and hormone levels following withdrawal of prolonged androgen ablation for prostate cancer. *Prostate Cancer Prostatic Dis* 2003; **6**: 245-249 [PMID: 12970730 DOI: 10.1038/sj.pcan.4500675]

17 **Kaku H**, Saika T, Tsushima T, Ebara S, Senoh T, Yamato T, Nasu Y, Kumon H. Time course of serum testosterone and luteinizing hormone levels after cessation of long-term luteinizing hormone-releasing hormone agonist treatment in patients with prostate cancer. *Prostate* 2006; **66**: 439-444 [PMID: 16329145 DOI: 10.1002/pros.20341]

18 **Giberti C**, Barreca T, Martorana G, Truini M, Franceschini R, Rolandi E, Giuliani L. Hormonal pattern and testicular histology in patients with prostatic cancer after long-term treatment with a gonadotropin-releasing hormone agonist analogue. *Eur Urol* 1988; **15**: 125-127 [PMID: 2975220]

19 **Shahidi M**, Norman AR, Gadd J, Huddart RA, Horwich A, Dearnaley DP. Recovery of serum testosterone, LH and FSH levels following neoadjuvant hormone cytoreduction and radical radiotherapy in localized prostate cancer. *Clin Oncol* (R Coll Radiol) 2001; **13**: 291-295 [PMID: 11554629 DOI: 10.1007/s001740170058]

20 **Murthy V**, Norman AR, Barbachano Y, Parker CC, Dearnaley DP. Long-term effects of a short course of neoadjuvant luteinizing hormone-releasing hormone analogue and radical radiotherapy on the hormonal profile in patients with localized prostate cancer. *BJU Int* 2007; **99**: 1380-1382 [PMID: 17537213 DOI: 10.1111/j.1464-410X.2007.06843.x]

21 **Zhumkhawala AA**, Gleason JM, Cheetham TC, Niu F, Loo RK, Dell RM, Jacobsen SJ, Chien GW. Osteoporosis management program decreases incidence of hip fracture in patients with prostate cancer receiving androgen deprivation therapy. *Urology* 2013; **81**: 1010-1015 [PMID: 23490521 DOI: 10.1016/j.urology.2012.11.066]

22 **Keating NL**, O'Malley AJ, Smith MR. Diabetes and cardiovascular disease during androgen deprivation therapy for prostate cancer. *J Clin Oncol* 2006; **24**: 4448-4456 [PMID: 16983113 DOI: 10.1200/JCO.2006.06.2497]

23 **Keating NL**, O'Malley A, Freedland SJ, Smith MR. Diabetes and cardiovascular disease during androgen deprivation therapy: observational study of veterans with prostate cancer. *J Natl Cancer Inst* 2012; **104**: 1518-1523 [PMID: 23210129]

24 **Beebe-Dimmer JL**, Cetin K, Shahinian V, Morgenstern H, Yee C, Schwartz KL, Acquavella J. Timing of androgen deprivation therapy use and fracture risk among elderly men with prostate cancer in the United States. *Pharmacoepidemiol Drug Saf* 2012; **21**: 70-78 [PMID: 22114014 DOI: 10.1002/pds.2258]

25 **Skolarus TA**, Caram MV, Shahinian VB. Androgen-deprivation-associated bone disease. *Curr Opin Urol* 2014; **24**: 601-607 [PMID: 25144145 DOI: 10.1097/MOU.0000000000000101]

26 **Wilke DR**, Parker C, Andonowski A, Tsuji D, Catton C, Gospodarowicz M, Warde P. Testosterone and erectile function recovery after radiotherapy and long-term androgen deprivation with luteinizing hormone-releasing hormone agonists. *BJU Int* 2006; **97**: 963-968 [PMID: 16542340 DOI: 10.1111/j.1464-410X.2006.06066.x]

27 **Plymate SR**, Tenover JS, Bremner WJ. Circadian variation in testosterone, sex hormone-binding globulin, and calculated non-sex hormone-binding globulin bound testosterone in healthy young and elderly men. *J Androl* 1989; **10**: 366-371 [PMID: 2592266]

28 **Morley JE**, Kaiser FE, Perry HM, Patrick P, Morley PM, Stauber PM, Vellas B, Baumgartner RN, Garry PJ. Longitudinal changes in testosterone, luteinizing hormone, and follicle-stimulating hormone in healthy older men. *Metabolism* 1997; **46**: 410-413 [PMID: 9109845 DOI: 10.1016/S0026-0495(97)90057-3]

29 **Izard MA**. Leydig cell function and radiation: a review of the literature. *Radiother Oncol* 1995; **34**: 1-8 [PMID: 7792393]

30 **Zagars GK**, Pollack A. Serum testosterone levels after external beam radiation for clinically localized prostate cancer. *Int J Radiat Oncol Biol Phys* 1997; **39**: 85-89 [PMID: 9300743]

P- Reviewer: Vinh-Hung V **S- Editor**: Tian YL **L- Editor**: A
E- Editor: Wu HL

WJR World Journal of Radiology

Submit a Manuscript: http://www.wjgnet.com/esps/
Help Desk: http://www.wjgnet.com/esps/helpdesk.aspx
DOI: 10.4329/wjr.v7.i12.501

World J Radiol 2015 December 28; 7(12): 501-508
ISSN 1949-8470 (online)

ORIGINAL ARTICLE

Retrospective Study

Common bile duct diameter in an asymptomatic population: A magnetic resonance imaging study

Rong Peng, Ling Zhang, Xiao-Ming Zhang, Tian-Wu Chen, Lin Yang, Xiao-Hua Huang, Ze-Ming Zhang

Rong Peng, Ling Zhang, Ze-Ming Zhang, Department of Radiology, Medical Imaging Center, Panzhihua Central Hospital, Panzhihua 617000, Sichuan Province, China

Xiao-Ming Zhang, Tian-Wu Chen, Lin Yang, Xiao-Hua Huang, Sichuan Key Laboratory of Medical Imaging, Department of Radiology, Affiliated Hospital of North Sichuan Medical College, Nanchong 637000, Sichuan Province, China

Author contributions: Peng R and Zhang XM contributed equally to this work; Peng R, Zhang L, Zhang XM, Chen TW, Yang L, Huang XH and Zhang ZM designed research; Peng R, Zhang L and Zhang XM performed research; Peng R, Chen TW and Zhang ZM analyzed the data; Peng R and Zhang XM wrote the paper.

Institutional review board statement: This study was reviewed and approved by Ethics Committee of Affiliated Hospital of North Sichuan Medical College.

Informed consent statement: Through consideration by the Ethics Committee, the experimental design and the program of the study will not cause harm and risk to the subjects. Due to the retrospective nature of this study and the actual medical condition of Nanchong, it's difficult to get informed consent from all patients involved in the study. The data collected were analyzed anonymously. So Ethics Committee of our Hospital waived the need for written informed consent from the all participants.

Conflict-of-interest statement: We have no financial relationships to disclose.

Data sharing statement: No additional data are available.

Correspondence to: Xiao-Ming Zhang, MD, PhD, Sichuan Key Laboratory of Medical Imaging, Department of Radiology, Affiliated Hospital of North Sichuan Medical College, Wenhua Road 63, Nanchong 637000, Sichuan Province, China. cjr.zhxm@vip.163.com
Telephone: +86-817-2262218
Fax: +86-817-2222856

Received: June 12, 2015
Peer-review started: June 15, 2015
First decision: October 21, 2015
Revised: November 11, 2015
Accepted: December 8, 2015
Article in press: December 11, 2015
Published online: December 28, 2015

Abstract

AIM: To measure the common bile duct (CBD) diameter by magnetic resonance cholangiopancreatography (MRCP) in a large asymptomatic population and analyze its some affecting factors.

METHODS: This study included 862 asymptomatic subjects who underwent MRCP. The CBD diameter was measured at its widest visible portion on regular end-expiration MRCP for all subjects. Among these 862 subjects, 221 volunteers also underwent end-inspiration MRCP to study the effect of respiration on the CBD diameter. The age, sex, respiration, body length, body weight, body mass index (BMI), portal vein diameter (PVD), length of the extrahepatic duct and CBD, cystic junction radial orientation and location were recorded. The subjects were divided into 7 groups according to age. All of the above factors were compared with the CBD diameter on end-expiration MRCP.

RESULTS: Among the 862 subjects, the CBD diameter was 4.13 ± 1.11 mm (range, 1.76-9.45 mm) and was correlated with age (r = 0.484; P < 0.05), with a dilation of 0.033 mm per year. The upper limit of the 95% reference range was 5.95 mm, resulting in a reasonable upper limit of 6 mm for the asymptomatic population. Respiration and other factors, including sex, body length, body weight, BMI, PVD, length of the extrahepatic duct and CBD, cystic junction radial orientation and location, were not related to the CBD diameter.

CONCLUSION: We established a reference range for the CBD diameter on MRCP for an asymptomatic population. The CBD diameter is correlated with age. Respiration did not affect the non-dilated CBD diameter.

Key words: Adult; Biliary tract; Common bile duct; Magnetic resonance imaging

Core tip: We measured the common bile duct (CBD) diameter by magnetic resonance cholangiopancreatography (MRCP) for a large asymptomatic population and suggested the normal upper limit of the duct be set at 6 mm on MRCP. The CBD diameter was correlated with age, and gradually dilates 0.033 mm per year. Respiration didn't effect on the non-dilated CBD diameter on MRCP. The significant changes of CBD diameter between inspiration and expiration may suggest a dilation of CBD.

Peng R, Zhang L, Zhang XM, Chen TW, Yang L, Huang XH, Zhang ZM. Common bile duct diameter in an asymptomatic population: A magnetic resonance imaging study. *World J Radiol* 2015; 7(12): 501-508 Available from: URL: http://www.wjgnet.com/1949-8470/full/v7/i12/501.htm DOI: http://dx.doi.org/10.4329/wjr.v7.i12.501

INTRODUCTION

A dilated common bile duct (CBD) suggests obstructive causes, which may require invasive imaging or remedial procedures[1]. However, an accurate reference range for CBD size remains debatable[1-9]. Thus, to determine whether a spontaneous abnormality or atypical dilation is important, there needs to be a reference range such that CBD diameters exceeding the upper limit can be classified as abnormal.

With the widespread use of cross-sectional imaging and improvements in cross-sectional imaging technology, the diameter of the CBD is being detected incidentally with increasing frequency when using ultrasound, computed tomography (CT) and magnetic resonance cholangiopancreatography (MRCP)[1-9]. MRCP is a technique that uses T2 sequence magnetic resonance imagery to perform a noninvasive evaluation of the anatomy and pathology of the pancreatobiliary system[10]. MRCP can be used to measure the diameter of the CBD[11]. MRCP is the principal diagnostic modality that determines whether endoscopic retrograde cholangiopancretography is needed, particularly when ultrasound findings are equivocal[12]. Chen *et al*[1] measured the normal CBD diameter in 187 patients by MRCP and found that the CBD diameter was significantly correlated only with age.

The diameter of the CBD changes in response to various factors, including age[1-3], cholecystectomy[2,3], measurement location[4], respiration[5], and body mass index (BMI, which was calculated as weight in kilograms divided by the square of height in meters)[3]. For some of these factors, such as age and gender, the effect on the CBD is not clear. More than 30 years ago, Wu *et al*[6] utilized ultrasound to determine that the CBD diameter increases by 1 mm every decade. Later, other studies supported this observation[1-4,9]. However, Horrow *et al*[7] obtained controversial results by ultrasound; they found that age was not associated with the size of the extrahepatic bile duct in 258 asymptomatic adults. Some studies[1,3,8] have suggested that gender has no significant effect on CBD diameter by ultrasound and MRCP, but Matcuk *et al*[9] reported that the extrahepatic bile duct was larger in females after performing an ultrasound on 1484 normal individuals. There has been only one study[3] concerning the effect of BMI on the CBD diameter. The anomalous junction of the cystic duct with the common bile duct may cause stagnation of bile[13]. Cystic duct anatomic variants (such as the cystic junction radial orientation variant) can be a source of confusion during surgery if unrecognized[14]. Low-junction patients with a short CBD experience several complications, including congenital dilation of the cystic duct[13]. Choledochocele is a cystic or diverticular dilatation of the lower bile duct and is sometimes associated with cholangitis or pancreatitis[15]. To the best of our knowledge, there is no report concerning the relationship between the diameter and length of the extrahepatic duct and the CBD, the cystic junction radial orientation or the cystic junction location.

The purpose of our study was to evaluate the CBD diameter in a large cohort of asymptomatic patients using MRCP and to determine the normal size range of the CBD in this population. In addition, this study aimed to determine the effects of age, sex, respiration, body length, body weight, BMI, portal vein diameter (PVD), extrahepatic duct and CBD length, cystic junction radial orientation and cystic junction location on the CBD diameter as measured by MRI.

MATERIALS AND METHODS

Patients

This retrospective study was approved by our institutional review board. Patient informed consent was waived. During the period of January 2010 to March 2014, we recruited all the patients who underwent an abdominal MRI in our hospital for our study. We recorded the age, sex, medical history, list of medications, total serum cholesterol, liver function tests, and hepatitis status of each patient. In addition, body length, body weight and BMI were recorded for the volunteers.

The following search criteria were used: (1) normal abdomen; (2) hepatic cysts; (3) hepatic or splenic hemangiomas; and (4) renal cysts.

The exclusion criteria were the following: (1) preexisting hepatobiliary and pancreatic surgery; (2) intra- or retroperitoneal tumors, inflammation or hemorrhagic diseases; (3) biliary tract stones; (4) cholecystitis; (5) cirrhosis of the liver; (6) ascites; (7) abnormal liver function tests (total bilirubin, aspartate aminotransferasea, alanine aminotransferase); (8) current use of medication that causes relaxation of smooth muscle (*e.g.*, calcium blockers and papaverine hydrochloride); and (9) abnormal total serum cholesterol.

We identified 5792 patients who underwent abdominal MR imaging at our hospital. Of these patients, 167 were excluded because of artifacts. A total of 4763 patients met the exclusion criteria and were not included in the study. The final study cohort consisted of 862 consecutive patients, including 450 male and 412 female patients aged 5 to 87 years (mean age ± SD, 46.10 ± 16.38 years). Among these 862 people, 221 were volunteers, including 108 males and 113 females aged 17 to 80 years (mean age ± SD, 37.80 ± 17.77 years).

The patients were divided into 7 groups according to their age: Group Ⅰ, ⩽ 20 years; Group Ⅱ, 21-30 years; Group Ⅲ, 31-40 years; Group Ⅳ, 41-50 years; Group Ⅴ, 51-60 years; Group Ⅵ, 61-70 years; and Group Ⅶ, > 70 years.

The patients were divided into normal weight (BMI < 25 kg/m^2), overweight (25 kg/m^2 $\leqslant$ BMI < 28 kg/m^2) and obesity (BMI $\geqslant 28$ kg/m^2) groups according to their BMI[16,17].

MR imaging technique

MR imaging was performed on the patients after an overnight fast of at least 8 h prior to the MR examination. All the examinations were performed with a 1.5-T MR scanner with 38 mT/M gradients and a 120 mT/M-per-second slope (Signa Excite; GE Medical Systems, Milwaukee, WI, United States) using a phased-array torso-pelvis coil. The imaging sequences, including two-dimensional coronal and axial single-shot fast spin-echo (SSFSE) T2-weighted imaging, axial respiratory gating fast-recovery fast-spin echo (FRFSE) T2-weighted imaging with fat suppression, fast-spoiled gradient-echo T1-weighted imaging with fat suppression, axial spoiled dual gradient-echo T1-weighted in- and out-of-phase MR imaging, axial slab three-dimensional (3D) spoiled gradient-echo dynamic contrast-enhanced MR imaging with fat suppression, and SSFSE radial series slab MRCP, were performed when all the patients were at the end of expiration and were holding their breath. End-expiration MRCP was considered conventional MRCP for each patient. The volunteers also underwent MRCP at the end of inspiration.

Coronal and axial SSFSE T2-weighted images were obtained during breath-holding with the following parameters: echo time (TE) = 90-100 ms; 2 s between slice acquisitions; section thickness = 5 mm; intersection gap = 0.5 mm; matrix = 384 × 224; one-half signal acquired; and field of view (FOV) = 33 cm × 33 cm. FRFSE T2-weighted images were obtained with the following parameters: repetition time (TR) ms/TE ms = 10000-12000/90-100, with TR determined by the frequency of respiration; section thickness = 5 mm; intersection gap = 0.5 mm; matrix = 256 × 192; number of signals acquired (NSA) = 3; and FOV = 34 cm × 34 cm. The acquisitions were completed in approximately 3-4 min.

Radial oblique slab SSFSE images were obtained for end-expiration and end-inspiration MRCP with the following parameters: TE = 1300 ms; 6 s between image acquisitions; section thickness = 40 mm; matrix = 384 × 224; one-half signal acquired; and FOV = 30 cm × 30 cm.

All of the other routine sequences mentioned above were not used in the analysis presented in this article; thus, we have not listed the parameters for those sequences.

It took approximately 30 min to complete all of the non-contrast MRI sequences and 35 min to complete the contrast-enhanced MR imaging.

MR image analysis

The original MRI data were loaded onto a workstation (GE, AW 4.1, Sun Microsystems, Palo Alto, CA, United States) for review. Two observers (with 4 and 6 years of experience interpreting abdominal MR images) retrospectively and individually reviewed the coronal and transverse T2-weighted and MRCP images to evaluate the CBD.

The widest diameter of the CBD was measured by placing an electronic caliper perpendicular to the long axis at the widest visible portion of the CBD on end-expiration MRCP for all the patients (Figure 1A). To study the effect of breath on the diameter of the CBD, the volunteers also underwent end-inspiration MRCP. The measurements on end-inspiration MRCP were taken at the same location as those on end-expiration. Because the CBD frequently exhibits a tortuous or serpentine course, the length of the extrahepatic bile duct is the sum of the length from the hepatic hilum to the tortuous portion and from the tortuous portion to the ampulla (Figure 1B). Similarly, the length of the CBD is the sum of the length from the cystic duct insertion to the tortuous portion and from the tortuous portion to the ampulla (Figure 1C). The anteroposterior diameters of the portal vein were measured by placing the electronic caliper at the splenic veins into the portal vein on T2-weighted images (Figure 1D). The radial orientation of the cystic junction was defined as lateral (insertion diagonally from the right), medial (insertion into the left

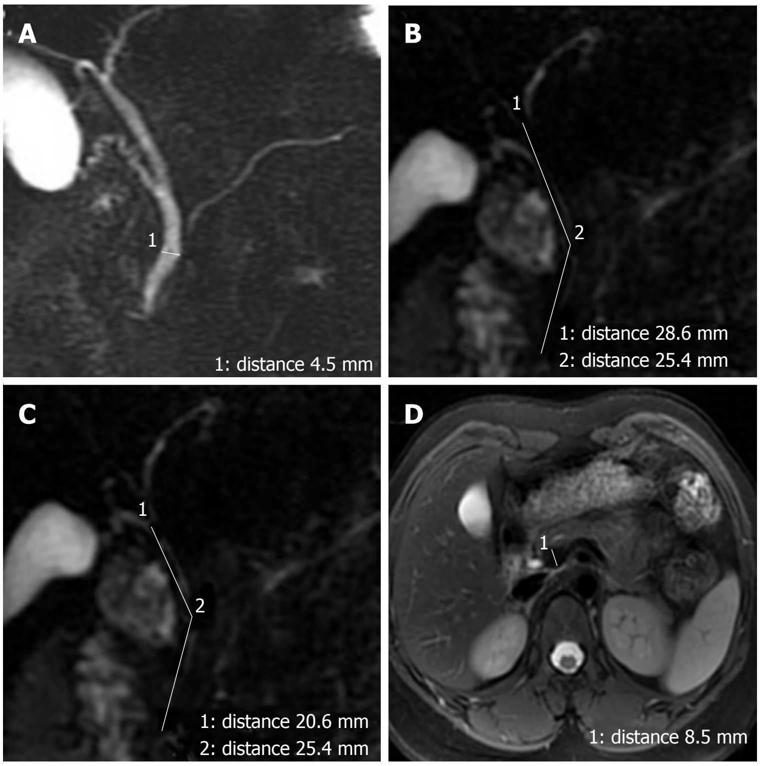

Figure 1 The measurement method. A: Measurement of the common bile duct (CBD) diameter by placing an electronic caliper at the widest visible portion of the CBD on magnetic resonance cholangiopancreatography (MRCP); B: Measurement of the length of the extrahepatic bile duct on MRCP. It is the sum of the length from the hepatic hilum to the tortuous portion and from the tortuous portion to the ampulla; C: Measurement of the length of the CBD on MRCP. It is the sum of the length from the cystic duct insertion to the tortuous portion and from the tortuous portion to the ampulla; D: Measurement of the portal vein anteroposterior diameters by placing the electronic caliper at the splenic veins into the portal vein on T2-weighted images.

Figure 2 The cystic junction radial orientation. An FRFSE T2-weighted image (A) shows lateral insertion of the cystic duct (arrow). A coronal SSFSE T2-weighted image (B) shows medial insertion of the cystic duct (arrow). An FRFSE T2-weighted image (C) shows posteroanterior insertion of the cystic duct (arrow). SSFSE: Single-shot fast spin-echo; FRFSE: Fast-recovery fast-spin echo.

side of the common hepatic duct), or posteroanterior (overlap of the junction with the bile duct in the postero-anterior view)[14] (Figure 2). Proximal, middle and low insertion of the cystic duct into the bile duct was defined when the cystic junction was detected in the proximal, middle or distal third, respectively, of the bile duct between the hepatic hilum and the ampulla of Vater (Figure 3).

Statistical analysis

Data derived from the MR images were expressed as the average of the two observers' findings. Any discrepancies in the discrete data were discussed by the two observers until a consensus was reached.

The inter-rater agreement for the prevalence of the cystic junction radial orientation and cystic junction location was assessed using the kappa (κ) statistic. This statistic is generally interpreted as follows: A κ value equal to or greater than 0.81 indicates very good agreement, a κ value ranging from 0.80 to 0.61 indicates good agreement, a kappa value ranging from 0.60 to 0.41 indicates moderate agreement, and a κ value of less than 0.41 indicates poor agreement.

The results of the CBD diameter, body length, body

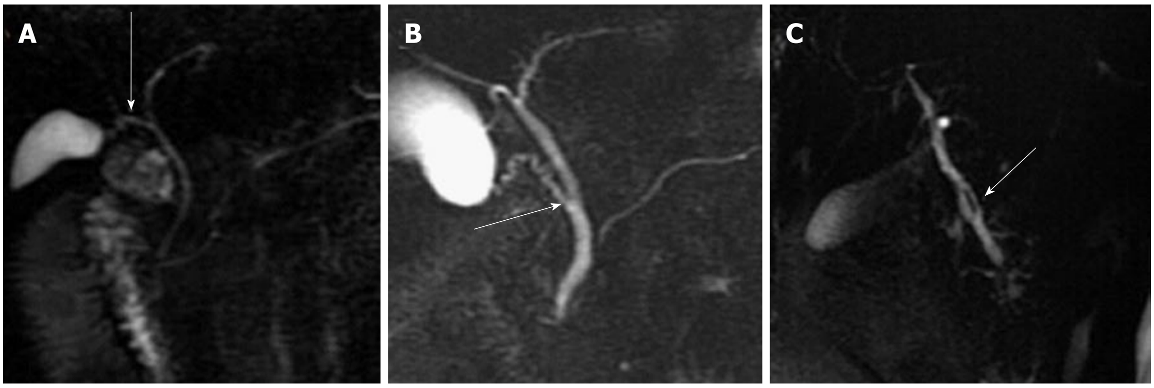

Figure 3 The cystic junction location. Magnetic resonance cholangiopancreatography shows proximal (A), middle (B) and distal (C) third conjunction of the cystic duct with the common bile duct (arrow).

Table 1 Common bile duct diameters in each age group

Group number	Age (yr)	Patient number	Common bile duct diameter Mean ± SD (mm)
I	≤ 20	42	3.23 ± 0.77
II	21-30	123	3.45 ± 0.67
III	31-40	137	3.80 ± 0.97
IV	41-50	234	4.01 ± 0.89
V	51-60	155	4.50 ± 1.11
VI	61-70	113	4.83 ± 1.18
VII	> 70	58	5.12 ± 1.10

weight, BMI, PVD, and extrahepatic duct and CBD length were expressed as the mean ± SD. The upper limit of the 95% reference range for the CBD diameter was defined as the mean + 1.64 SD.

The independent t test was used to compare the CBD diameter between patients younger and older than 60 years and between genders. CBD diameters were analyzed based on age, body length, body weight, PVD, and extrahepatic duct and CBD length using Pearson correlations. The CBD diameters in the end-inspiration and end-expiration phases were analyzed using paired t tests. Analysis of variance (ANOVA) was used to compare the diameter by BMI, cystic junction radial orientation and cystic junction location. Linear regressions were used to confirm the relationships between the CBD diameters and age.

The data analysis was performed using Statistical Package for Social Sciences (SPSS) for Windows (Version 13.0, Chicago, IL, United States). P values ≤ 0.05 were considered statistically significant.

RESULTS

Agreement between the two radiologists was good regarding the prevalence of the cystic junction location ($\kappa = 0.79$) and moderate concerning the prevalence of the cystic junction radial orientation ($\kappa = 0.53$).

Among the 862 subjects, the mean diameter of the CBD on end-expiration MRCP was 4.13 ± 1.11 mm (1.76-9.45 mm). There was a significant correlation between the CBD diameter and age ($r = 0.484$, $P < 0.05$; Figure 4). According to the linear periodic model, the regression equation for diameter was as follows: 0.033 × age + 2.624. Thus, the duct gradually dilated by 0.033 mm per year. Table 1 lists the mean CBD diameters of the subjects in each group. The upper limit of the 95% reference range for the CBD diameter was 5.95 mm, resulting in the reasonable upper limit of 6 mm for the asymptomatic population. The CBD diameter in people older than 61 years of age (4.93 ± 1.15 mm) was significantly different than that in subjects younger than 60 years of age (3.93 ± 0.99 mm; $t = -11.364$, $P = 0.000$).

In the cohort of 862 subjects, the mean CBD diameter in females was slightly larger than that in males (4.18 ± 1.09 mm *vs* 4.09 ± 1.13 mm), although this difference was not statistically significant ($t = -1.252$, $P = 0.211$).

Among the 221 volunteers, the mean CBD diameter was slightly larger on end- inspiration MRCP (3.90 ± 0.96 mm) than on end-expiration MRCP (3.88 ± 0.96 mm), but the difference was not statistically significant ($t = -0.896$, $P = 0.371$) (Figure 5).

In the cohort of 221 volunteers, the normal weight subjects (83.7%; 185/221) had a CBD diameter of 3.85 ± 0.95 mm, the overweight subjects (14.5%; 32/221) had a CBD diameter of 4.09 ± 1.00 mm, and the obese subjects (1.8%; 4/221) had a CBD diameter of 3.61 ± 1.14 mm. The CBD diameters are not significantly different among the normal weight, overweight and obese groups ($F = 1.034$, $P = 0.357$).

In the 221 volunteers, the mean CBD diameters were not significantly related to body length or body weight (Table 2). In the 862 subjects, the mean CBD diameters were not significantly related to the PVD, extrahepatic bile duct length or CBD length (Table 2).

Based on the different cystic junction radical orientations, subjects (74.8%; 645/862) with a lateral junction had a CBD diameter of 4.09 ± 1.10 mm, subjects with a medial junction (7.9%; 68/862) had a CBD diameter of 4.25 ± 1.30 mm, and subjects with a posteroanterior junction (17.3%; 149/862) had a CBD diameter of 4.24 ± 1.03 mm. The CBD diameters were not significantly different between the subjects grouped based on cystic

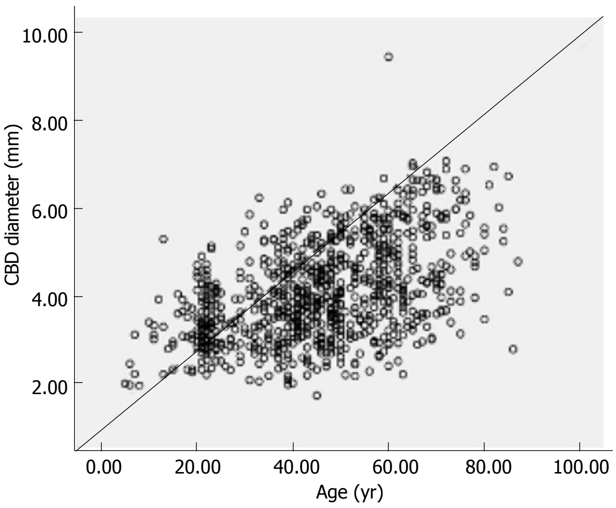

Figure 4 Pearson correlation between the diameter of the common bile duct and age (r = 0.484, P = 0.000).

junction radial orientation (F = 1.559, P = 0.211). Based on the cystic junction location, subjects with a proximal insertion (23.5%; 203/862) had a CBD diameter of 4.04 ± 1.17 mm, subjects with a middle insertion (73.8%; 636/862) had a CBD diameter of 4.30 ± 1.08 mm, and subjects with a low insertion (2.7%; 23/862) had a CBD diameter of 4.16 ± 1.08 mm. The CBD diameters were not significantly different among the groups based on cystic junction location (F = 1.683, P = 0.186).

DISCUSSION

In this study, we found that the mean diameter of the CBD on end-expiration MRCP was 4.13 ± 1.11 mm, with a range of 1.76 to 9.45 mm. The CBD diameters were significantly different between patients younger and older than 60 years of age (P < 0.05). The CBD diameter was correlated with age (r = 0.484; P < 0.05) and gradually dilated 0.033 mm per year. We suggest that the normal upper limit of the duct should be set at 6 mm. The CBD diameters were not significantly related to gender, body length, body weight, BMI, PVD, the length of the extrahepatic duct or the CBD, the cystic junction radial orientation or location. Respiration did not affect the non-dilated CBD diameter. Our results established a reference range for the CBD diameter on MRCP in an asymptomatic population that will be useful for evaluating suspected biliary tract disease.

Previous studies have shown that the mean diameter of the CBD is between 3.4 and 7.39 mm, with a range of 1.0 to 15.0 mm[1,2,4-8,18,19], and our results were well within the reported range. In our study, the upper limit of the 95% reference range for the CBD diameter was 5.95 mm, and the upper limit was 6 mm; these values are comparable to those from ultrasound[4] and CT[2]. The upper limit in our study was lower than that reported by Chen *et al*[1], possibly because of the larger population and wider age range in our study.

Table 2 Pearson correlation coefficients between the common bile duct diameters and their relationship to different parameters

	Patient number	Mean ± SD	R value	P value
Body length (m)	221	1.60 ± 0.07	-0.067	0.325
Body weight (kg)	221	57.01 ± 9.17	0.041	0.548
Portal vein diameter (mm)	862	8.79 ± 0.91	0.034	0.318
Length of the extrahepatic bile duct (mm)	862	63.75 ± 9.07	0.045	0.185
Length of the CBD (mm)	862	47.53 ± 10.44	0.003	0.922

CBD: Common bile duct.

A few reports have considered the important age-dependent variations in the CBD diameter[1-4,6,8,9,18,19]. Some studies have revealed a slight increase in duct diameter with advancing age[6,9]. It has also been shown that the CBD diameter is directly proportional to age after patients were divided into two groups with 65 years as the cut-off age[1]. Park *et al*[18] reported that the CBD diameter by CT in people older than 51 years of age was significantly different than that in subjects younger than 50 years of age. Additionally, Kaim *et al*[19] reported that the CBD diameter in asymptomatic elderly subjects (> 75 years) was considerably higher compared with the recommended borderline values in the ultrasound literature. However, Horrow *et al*[7] found no increase in the size of the extrahepatic bile duct with increasing age in an adult population, and their data do not support the rule of a 1-mm-per-decade increase in the size of the bile duct by ultrasound. In this study, we found that the CBD diameter increases with age and gradually dilates 0.033 mm per year. CBD diameters are significantly different between patients who are younger or older than 60 years of age, perhaps because longitudinal smooth muscle bands and their intervening connective tissue fragments with increasing age accompanied by the loss of the reticulo-endothelial network of the ductal wall[20], resulting in age-related biliary dilatation of the CBD.

Some previous studies have reported that gender has no significant effect on the CBD diameter[1,3,8]. However, Matcuk *et al*[9] found that the extrahepatic bile duct increases with female sex by ultrasound. Our studies support the notion that gender has no significant effect on the CBD diameter.

Wachsberg[5] demonstrated that the maximal bile duct measurement can increase during deep inspiration by ultrasonography. However, their study included thirty subjects with a maximal anteroposterior CBD diameter of 5 mm or greater, some of whom presented with biliary obstruction. An MRCP study[21] found that the mean maximal diameter of the extrahepatic bile duct was significantly larger on end-inspiratory MRCP in the group of subjects with an extrahepatic bile duct diameter of less than 10 mm. However, their study included 102 patients

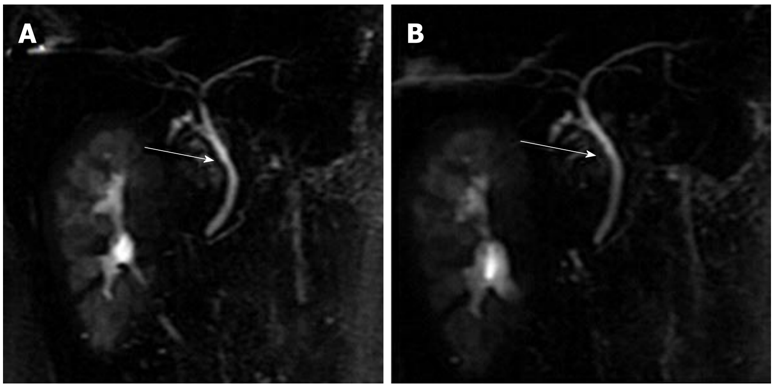

Figure 5 Deep respiratory magnetic resonance cholangiopancreatography obtained in a 32-year-old female volunteer. Breath-hold magnetic resonance cholangiopancreatography obtained during end-expiration (A) or end-inspiration (B) provides an overview of the common bile duct (arrow). There is no obvious change in the common bile duct diameter.

with suspected biliary abnormalities by ultrasonography or computed tomography. Our results showed that the mean CBD diameters between end-inspiratory MRCP and end-expiratory MRCP were not statistically different. Our study is unique in that MRCP was used to evaluate the effect of respiration on the "normal" diameter of the CBD. Our results indicate that respiration does not affect the non-dilated CBD diameter. We speculate that the significant changes in the CBD diameter between inspiration and expiration[5,21] may suggest dilation of the CBD.

Previous studies have suggested that body length and body weight have no significant effect on the CBD diameter[3,8]. Our studies support these observations. Daradkeh *et al*[3] reported that the CBD diameter was correlated with BMI by ultrasound. In this study, we found that BMI had no significant effect on the CBD diameter, perhaps because ultrasound has limitations regarding overweight persons[22]. In our study, 14% (32/221) of the patients were overweight, and 1.8% (4/221) were obese. Ultrasound may have certain limitations in measuring the CBD diameter in these 15.8% of the patients, thereby resulting in measureable differences.

In our study, we also found that the PVD was not associated with the CBD diameter on MRCP, a finding that is similar to that reported by Chen *et al*[1].

The most common or "normal" way of entry (up to 65%) involves draining the cystic duct from the right lateral position[23]; however, in other series, a lateral junction was observed in only 31.8% of the cases[14]. In our study, lateral insertion of the cystic duct was detected in 74.8% of the cases, whereas medial and posteroanterior insertions accounted for the remainder. Our study of the cystic junction radial orientation supports the report by Turner *et al*[23]. The cystic duct usually joins the common hepatic duct about halfway between the porta hepatis and the ampulla of Vater (in 75% of cases)[23]. We found that the cystic duct joins the common hepatic duct about halfway between the porta hepatis and the ampulla of Vater in 73.8% of cases, a rate similar to that reported by Turner *et al*[23]. We found no relationships among the diameter and length of the extrahepatic duct, length of the CBD, cystic junction radial orientation or cystic junction location.

There are some limitations to this retrospective study. First, the variation in the depth of individual patient inspiration may have affected the length and maximal diameter of the extrahepatic bile duct during respiratory MRCP, although all of the patients were instructed before the examinations to take a deep breath or to completely exhale. Second, there were only a few patients older than 70 (6.7%) or younger than 20 (4.9%) years. This may have introduced bias regarding the imaging review and analysis.

In conclusion, in this study, we established a reference range for the CBD diameter on MRCP for an asymptomatic population. The CBD diameter is correlated with age, and its normal upper limit can be set at 6 mm. Respiration and other factors, such as gender, body length, body weight, BMI, PVD, extrahepatic duct and CBD length, and the cystic junction radial orientation and location, do not affect the non-dilated CBD diameter. The significant changes in the CBD diameter between inspiration and expiration may suggest dilation of the CBD. This is a useful reference for evaluating suspected biliary tract disease.

COMMENTS

Background

A dilated common bile duct (CBD) suggests obstructive. An accurate reference range for CBD size remains debatable. Magnetic resonance cholangiopancreatography (MRCP) can be used to measure the diameter of the CBD.

Research frontiers

An accurate reference for CBD size on imaging.

Innovations and breakthroughs

To measurement the CBD diameter in a large cohort of asymptomatic patients (862) using MRCP.

Applications

The CBD diameter is correlated with age, and its normal upper limit can be set at 6 mm. Respiration and other factors, such as gender, body length, body weight, body mass index, portal vein diameter, extrahepatic duct and CBD length, and the cystic junction radial orientation and location, do not affect the non-dilated CBD diameter.

Peer-review

This work is alright to publish. However, more relationships of diameter other than age should be presented. Relationships of diameter and say, gender, patient weight and height are suggested.

REFERENCES

1 **Chen T**, Hung CR, Huang AC, Lii JM, Chen RC. The diameter of the common bile duct in an asymptomatic Taiwanese population: measurement by magnetic resonance cholangiopancreatography. *J Chin Med Assoc* 2012; **75**: 384-388 [PMID: 22901722 DOI: 10.1016/j.jcma.2012.06.002]

2 **Senturk S**, Miroglu TC, Bilici A, Gumus H, Tekin RC, Ekici F, Tekbas G. Diameters of the common bile duct in adults and postcholecystectomy patients: a study with 64-slice CT. *Eur J Radiol* 2012; **81**: 39-42 [PMID: 21144686 DOI: 10.1016/j.ejrad.2010.11.007]

3 **Daradkeh S**, Tarawneh E, Al-Hadidy A. Factors affecting common bile duct diameter. *Hepatogastroenterology* 2005; **52**: 1659-1661 [PMID: 16334751]

4 **Bowie JD**. What is the upper limit of normal for the common bile duct on ultrasound: how much do you want it to be? *Am J Gastroenterol* 2000; **95**: 897-900 [PMID: 10763933]

5 **Wachsberg RH**. Respiratory variation of extrahepatic bile duct diameter during ultrasonography. *J Ultrasound Med* 1994; **13**: 617-621 [PMID: 7933030]

6 **Wu CC**, Ho YH, Chen CY. Effect of aging on common bile duct diameter: a real-time ultrasonographic study. *J Clin Ultrasound* 1984; **12**: 473-478 [PMID: 6436325]

7 **Horrow MM**, Horrow JC, Niakosari A, Kirby CL, Rosenberg HK. Is age associated with size of adult extrahepatic bile duct: sonographic study. *Radiology* 2001; **221**: 411-414 [PMID: 11687684]

8 **Mahour GH**, Wakim KG, Ferris DO. The common bile duct in man: its diameter and circumference. *Ann Surg* 1967; **165**: 415-419 [PMID: 6019316]

9 **Matcuk GR**, Grant EG, Ralls PW. Ultrasound measurements of the bile ducts and gallbladder: normal ranges and effects of age, sex, cholecystectomy, and pathologic states. *Ultrasound Q* 2014; **30**: 41-48 [PMID: 24901778 DOI: 10.1097/RUQ.0b013e3182a80c98]

10 **Uysal F**, Obuz F, Uçar A, Seçil M, Igci E, Dicle O. Anatomic variations of the intrahepatic bile ducts: analysis of magnetic resonance cholangiopancreatography in 1011 consecutive patients. *Digestion* 2014; **89**: 194-200 [PMID: 24732700 DOI: 10.1159/000358558]

11 **Chiu NC**, Chiou YY. Role of MRCP in the measurement of the CBD diameter. *J Chin Med Assoc* 2012; **75**: 423-424 [PMID: 22989536 DOI: 10.1016/j.jcma.2012.06.013]

12 **Shanmugam V**, Beattie GC, Yule SR, Reid W, Loudon MA. Is magnetic resonance cholangiopancreatography the new gold standard in biliary imaging? *Br J Radiol* 2005; **78**: 888-893 [PMID: 16177010]

13 **Uetsuji S**, Okuda Y, Komada H, Yamamura M, Kamiyama Y. Clinical evaluation of a low junction of the cystic duct. *Scand J Gastroenterol* 1993; **28**: 85-88 [PMID: 8430277]

14 **Tsitouridis I**, Lazaraki G, Papastergiou C, Pagalos E, Germanidis G. Low conjunction of the cystic duct with the common bile duct: does it correlate with the formation of common bile duct stones? *Surg Endosc* 2007; **21**: 48-52 [PMID: 16960679]

15 **Kamisawa T**, Yoshiike M, Egawa N, Tsuruta K, Okamoto A, Matsukawa M. Classification of choledochocele. *Hepatogastroenterology* 2005; **52**: 29-32 [PMID: 15782987]

16 **Salas-Salvadó J**, Rubio MA, Barbany M, Moreno B. SEEDO 2007 Consensus for the evaluation of overweight and obesity and the establishment of therapeutic intervention criteria. *Med Clin* (Barc) 2007; **128**: 184-196; quiz 1 p following 200 [PMID: 17298782]

17 **Adeboye B**, Bermano G, Rolland C. Obesity and its health impact in Africa: a systematic review. *Cardiovasc J Afr* 2012; **23**: 512-521 [PMID: 23108519 DOI: 10.5830/CVJA-2012-040]

18 **Park JS**, Lee DH, Jeong S, Cho SG. Determination of Diameter and Angulation of the Normal Common Bile Duct using Multidetector Computed Tomography. *Gut Liver* 2009; **3**: 306-310 [PMID: 20431765 DOI: 10.5009/gnl.2009.3.4.306]

19 **Kaim A**, Steinke K, Frank M, Enriquez R, Kirsch E, Bongartz G, Steinbrich W. Diameter of the common bile duct in the elderly patient: measurement by ultrasound. *Eur Radiol* 1998; **8**: 1413-1415 [PMID: 9853225]

20 **Kialian GP**, Aznaurian AV. The age-related characteristics of the muscular layer of the common bile duct in man. *Morfologiia* 1995; **108**: 10-12 [PMID: 7550906]

21 **Ito K**, Shimizu A, Tanabe M, Matsunaga N. Respiratory variation of the extrahepatic bile duct: evaluation with deep inspiratory and expiratory MRCP. *Magn Reson Imaging* 2012; **30**: 579-582 [PMID: 22387023 DOI: 10.1016/j.mri.2011.12.024]

22 **Ongoïba N**, Sissoko F, Ouologuem I, Bérété S, Diop AK, Sidibé S, Touré M, Kéita AD, Koumaré AK. The size of the bile duct by echograph. A study. *Morphologie* 2012; **96**: 7-11 [PMID: 22445527 DOI: 10.1016/j.morpho.2012.01.003]

23 **Turner MA**, Fulcher AS. The cystic duct: normal anatomy and disease processes. *Radiographics* 2001; **21**: 3-22; questionnaire 288-294 [PMID: 11158640]

P- Reviewer: Chow J **S- Editor**: Wang JL **L- Editor**: A
E- Editor: Wu HL

WJR World Journal of Radiology

Submit a Manuscript: http://www.wjgnet.com/esps/
Help Desk: http://www.wjgnet.com/esps/helpdesk.aspx
DOI: 10.4329/wjr.v7.i12.509

World J Radiol 2015 December 28; 7(12): 509-520
ISSN 1949-8470 (online)

ORIGINAL ARTICLE

Observational Study

Combined value of apparent diffusion coefficient-standardized uptake value max in evaluation of post-treated locally advanced rectal cancer

Davide Ippolito, Davide Fior, Chiara Trattenero, Elena De Ponti, Silvia Drago, Luca Guerra, Cammillo Talei Franzesi, Sandro Sironi

Davide Ippolito, Davide Fior, Chiara Trattenero, Elena De Ponti, Silvia Drago, Luca Guerra, Cammillo Talei Franzesi, Sandro Sironi, School of Medicine, University of Milano-Bicocca, 20126 Milan, Italy

Davide Ippolito, Davide Fior, Chiara Trattenero, Silvia Drago, Cammillo Talei Franzesi, Sandro Sironi, Department of Diagnostic Radiology, H S.Gerardo Monza, 20052 Milan, Italy

Luca Guerra, Department of Nuclear Medicine and PET Unit-Molecular Bioimaging Centre, San Gerardo Hospital, 20052 Monza, Italy

Elena De Ponti, Department of Medical Physics, San Gerardo Hospital, 20052 Monza, Italy

Author contributions: Ippolito D was the guarantor of integrity of entire study and contributed to study concepts; Ippolito D, Fior D and Trattenero C contributed to study design; Drago S and Franzesi CT contributed to literature research; Ippolito D and Guerra L contributed to clinical studies; Ippolito D, Fior D and Guerra L contributed to data acquisition; Ippolito D, Fior D, Trattenero C and De Ponti E contributed to data analysis/interpretation; De Ponti E contributed to statistical analysis; Ippolito D, Fior D, Trattenero C and Drago S contributed to manuscript preparation; Ippolito D and Sironi S contributed to manuscript definition of intellectual content and manuscript editing; all the authors contributed to manuscript revision/review; Ippolito D gave the manuscript final version approval.

Institutional review board statement: No ethical approval is needed, because the used data have been generated as part of the routine work of our organization.

Informed consent statement: This prospective study was approved by our institutional review board, and informed consent was obtained from all patients.

Conflict-of-interest statement: No Conflict-of-interest. Authors declare no competing financial interests in relation to the work described.

Data sharing statement: No additional data are available.

Correspondence to: Davide Ippolito, MD, Department of Diagnostic Radiology, H S.Gerardo Monza, Via Pergolesi 11, 20052 Milan, Italy. davide.atena@tiscalinet.it
Fax: +39-039-2333463

Received: January 25, 2015
Peer-review started: January 26, 2015
First decision: March 6, 2015
Revised: July 1, 2015
Accepted: November 3, 2015
Article in press: November 4, 2015
Published online: December 28, 2015

Abstract

AIM: To assess the clinical diagnostic value of functional imaging, combining quantitative parameters of apparent diffusion coefficient (ADC) and standardized uptake value (SUV)max, before and after chemo-radiation therapy, in prediction of tumor response of patients with rectal cancer, related to tumor regression grade at histology.

METHODS: A total of 31 patients with biopsy proven diagnosis of rectal carcinoma were enrolled in our study. All patients underwent a whole body ^{18}FDG positron emission tomography (PET)/computed tomography

(CT) scan and a pelvic magnetic resonance (MR) examination including diffusion weighted (DW) imaging for staging (PET1, RM1) and after completion (6.6 wk) of neoadjuvant treatment (PET2, RM2). Subsequently all patients underwent total mesorectal excision and the histological results were compared with imaging findings. The MR scanning, performed on 1.5 T magnet (Philips, Achieva), included T2-weighted multiplanar imaging and in addition DW images with b-value of 0 and 1000 mm²/s. On PET/CT the SUVmax of the rectal lesion were calculated in PET1 and PET2. The percentage decrease of SUVmax (ΔSUV) and ADC (ΔADC) values from baseline to presurgical scan were assessed and correlated with pathologic response classified as tumor regression grade (Mandard's criteria; TRG1 = complete regression, TRG5 = no regression).

RESULTS: After completion of therapy, all the patients were submitted to surgery. According to the Mandard's criteria, 22 tumors showed complete (TRG1) or subtotal regression (TRG2) and were classified as responders; 9 tumors were classified as non responders (TRG3, 4 and 5). Considering all patients the mean values of SUVmax in PET 1 was higher than the mean value of SUVmax in PET 2 ($P < 0.001$), whereas the mean ADC values was lower in RM1 than RM2 ($P < 0.001$), with a ΔSUV and ΔADC respectively of 60.2% and 66.8%. The best predictors for TRG response were SUV2 (threshold of 4.4) and ADC2 (1.29×10^{-3} mm^2/s) with high sensitivity and specificity. Combining in a single analysis both the obtained median value, the positive predictive value, in predicting the different group category response in related to TRG system, presented R^2 of 0.95.

CONCLUSION: The functional imaging combining ADC and SUVmax in a single analysis permits to detect changes in cellular tissue structures useful for the assessment of tumour response after the neoadjuvant therapy in rectal cancer, increasing the sensitivity in correct depiction of treatment response than either method alone.

Key words: Advanced rectal cancer; Functional imaging; FDG-PET/CT; Magnetic resonance imaging; Apparent diffusion coefficient; Neoadjuvant treatment; Tumor regression grade

Core tip: In our study we evaluated the combination of changes of glucose metabolism values expressed as SUVmax and the changes of apparent diffusion coefficient (ADC map) values, before and after neoadjuvant therapy, in patients with advanced rectal cancer in order to predict, *in vivo*, the therapy response. The importance of this work consist of the possibility to offer, in the era of positron emission tomography (PET)/magnetic resonance imaging scanner, a new advanced tool that allows the non-invasive evaluation of response to neoadjuvant chemotherapy treatment in patients with rectal cancer, by adding quantitative value information on diffusion weighted images and on PET/computed tomography imaging.

Ippolito D, Fior D, Trattenero C, De Ponti E, Drago S, Guerra L, Franzesi CT, Sironi S. Combined value of apparent diffusion coefficient-standardized uptake value max in evaluation of post-treated locally advanced rectal cancer. *World J Radiol* 2015; 7(12): 509-520 Available from: URL: http://www.wjgnet.com/1949-8470/full/v7/i12/509.htm DOI: http://dx.doi.org/10.4329/wjr.v7.i12.509

INTRODUCTION

The use of pre-operative chemoradiation treatment (CRT) induces downsizing and downstaging of primary rectal tumors, yielding a pathologic complete response (pCR) in up to 24% of patients[1]. A pCR is known to be associated with a favourable oncologic outcome, in regard to both recurrence and patients survival[2].

The trend in treatment of rectal cancer, although is still controversial, to date is toward a more conservative approach in patients identified as complete responders after CRT. Generally, a pCR is determined with histopathologic examination after surgery, but, if the determination of CR before surgery may influence the subsequent treatment decision, an accurate clinical assessment of response becomes essential[3-5].

Recently, diffusion weighted magnetic resonance imaging (DW-MR) after CRT has demonstrated to be more valuable than standard morphologic MR study in differentiation between a pCR and the presence of residual disease. On DW images, the viable neoplastic remnants are more easily defined, since they appear hyperintense in comparison to the low signal intensity (SI) of the surroundings not neoplastic tissues[6,7]. Promising results have been shown with quantitative DW imaging analysis by quantifying the apparent diffusion coefficient (ADC) in the evaluation of treatment response to CRT in patients having rectal cancer[8-14].

Even positron emission tomography (PET)/computed tomography (CT) has been suggested to be an accurate imaging modality in the staging of newly diagnosed or in detection of recurrent rectal cancer. Furthermore, qualitative and quantitative assessment of fluorodeoxyglucose-PET provide helpful information regarding treatment response and prognosis of patients with rectal cancer[15,16] .

Both DWI imaging and PET-CT imaging have been used separately in different fields of tumor evaluation, such as detection, characterization and CRT response assessment. As both ADC and standardized uptake value (SUV) have been associated with biological behaviour and treatment response in various tumors types a correlation between SUV values, which reflect metabolic activity and ADC values which reflect cellular density might be found[17].

To date, there have been few comparative studies between ADC and SUVmax to evaluate the tumour response to preoperative CRT in locally advanced rectal cancer (LARC). The aim of this study was, along with brief review of literature, to evaluate the accuracy of combined ADC and SUVmax values in prediction of tumor regression grade (TRG) complete responders in LARC patients, using histological tumor regression grade as standard reference.

MATERIALS AND METHODS

Patients

Between June 2009 and April 2012, 53 consecutive patients with diagnosis of rectal cancer were considered for eligibility. Inclusion criteria were: (1) histopathologically proved rectal adenocarcinoma (0 to 15 cm from anal verge, by means of endoscopic biopsy); (2) LARC staged by baseline MR imaging examination (⩾ T3 or positive lymph nodes); (3) absence of distant metastases; (4) neoadjuvant preoperative CRT. The exclusion criteria were: (1) previous CRT for primary rectal carcinoma or tumour in other organ; (2) contraindication to MR imaging study; (3) premature discontinuation of CRT; (4) delayed (more than 8 mo after CRT) or cancelled surgery; and (5) discontinued or non-diagnostic MR imaging examinations during therapy.

A total of 31 patients (22 men and 9 women, mean age of 64.5 years with a range of 42-80) met the study criteria.

This prospective study was approved by our institutional review board, and informed consent was obtained from all patients.

MR acquisition protocol

The baseline MR imaging examination (MR1) was performed within a mean of 4.8 wk (I-III quartile: 3.8-6.3 wk) before the treatment for tumour staging, while the second study (MR2) was performed within a mean of 6.6 wk (I-III quartile: 5.3-7.7 wk) after the completion of CRT and before surgery. MRI was performed using a 1.5 T magnet (Philips, Achieva 1.5 T, The Netherlands). The patients were positioned supine and feet first, and scan was performed by using a five-channel high resolution phased-array body coil.

The standard protocol included multiplanar T2- TSE-weighted sequences without fat suppression, applying the following parameters: Repetition time msec/echo time msec 4750/120; slice thickness: 3 mm; slices: 18; matrix: 256 × 256; number of signal acquired (NSA): 4; axial TSE T1-weighted axial sequence Turbo Spin-Echo (TSE) T1-weighted (slice thickness: 3 mm; slice: 20; gap: 3 mm; TR: 612 ms; TE: 14 ms; flip angle: 90°; Field of View (FOV): 180; RFOV: 85; matrix: 272 × 320; NSA: 4.

The images were obtained in three different planes: sagittal, coronal and transverse, with the latter two orientations angled perpendicularly to the long axis of the tumour according to sagittal images. At the end of the examination, DW images using a Multi-slice Spin Echo Eco-planar Single Shot (SE-EPI-SSh) sequence were obtained in the axial plane with the following parameters: Repetition time msec/echo time 3000/74; slice thickness: 6 mm; slices: 12; matrix: 240 × 256; NSA: 4; b values of 0 and 1000 mm^2/s; time: 1.30 min; SENSE factor 1.5.

No intravenous contrast medium was injected as part of our routine acquisition protocol for rectal cancer evaluation, according to recent guidelines about clinical management of rectal cancer patients with MRI (recommendations from ESGAR, 2012).

MR image analysis

MR images were analyzed and ADC measurements were made by one radiologist experienced in abdominal radiology (DI), and who was blinded to the therapeutic response and to the histological results (Figures 1 and 2).

On post-CRT ADC maps, the region of interest (ROIs) were manually drawn on the basis of visual analysis of focal areas of residual high SI on the high-b-value images within the location of the primary tumour site, by comparing pre-CRT examination if needed. When no remaining high SI area could be depicted on the post-CRT DW images, the ROIs were drawn on the rectal wall at the former location of the primary tumour, using pre-CRT DW and T2W images as reference. The lesions were manually contoured along their edge avoiding vessels distortion areas, vessels and motion artefacts. Then, the mean and standard deviation of the ADC values were automatically calculated.

The size of ROI of one section was not less than 20 voxels. Diffusion-weighted images were of diagnostic quality in all patients, and no patients were excluded from the study.

In order to determine percentage variation of ADC before and after CRT, the ADC values in the MR1 (ADC 1) and MR2 (ADC 2) were used also to define delta ADC (ΔADC) as follows: $\Delta ADC = [(ADC2 - ADC1)/ADC2] \times 100$.

^{18}F-FDG-PET/CT imaging technique

All patients were investigated by FDG-PET/CT prior to the onset of CRT (PET1) and 4 wk after the completion of the pre-operative treatment (PET2). All studies were performed on a PET scanner coupled with a 8-detector rows CT scanner (Discovery ST - GE Healthcare, Milwaukee, WI, United States), thus allowing one step acquisition of co-registered PET and CT images. According to the acquisition protocol, patients fasted for at least 6 h before the intravenous administration of 3.7 MBq/kg body weight of ^{18}F-FDG. Blood glucose levels were checked before tracer administration and patients with glucose level above 170 mg/dL were excluded from the study. All patients were orally hydrated (500 mL of water) during the FDG uptake period and were

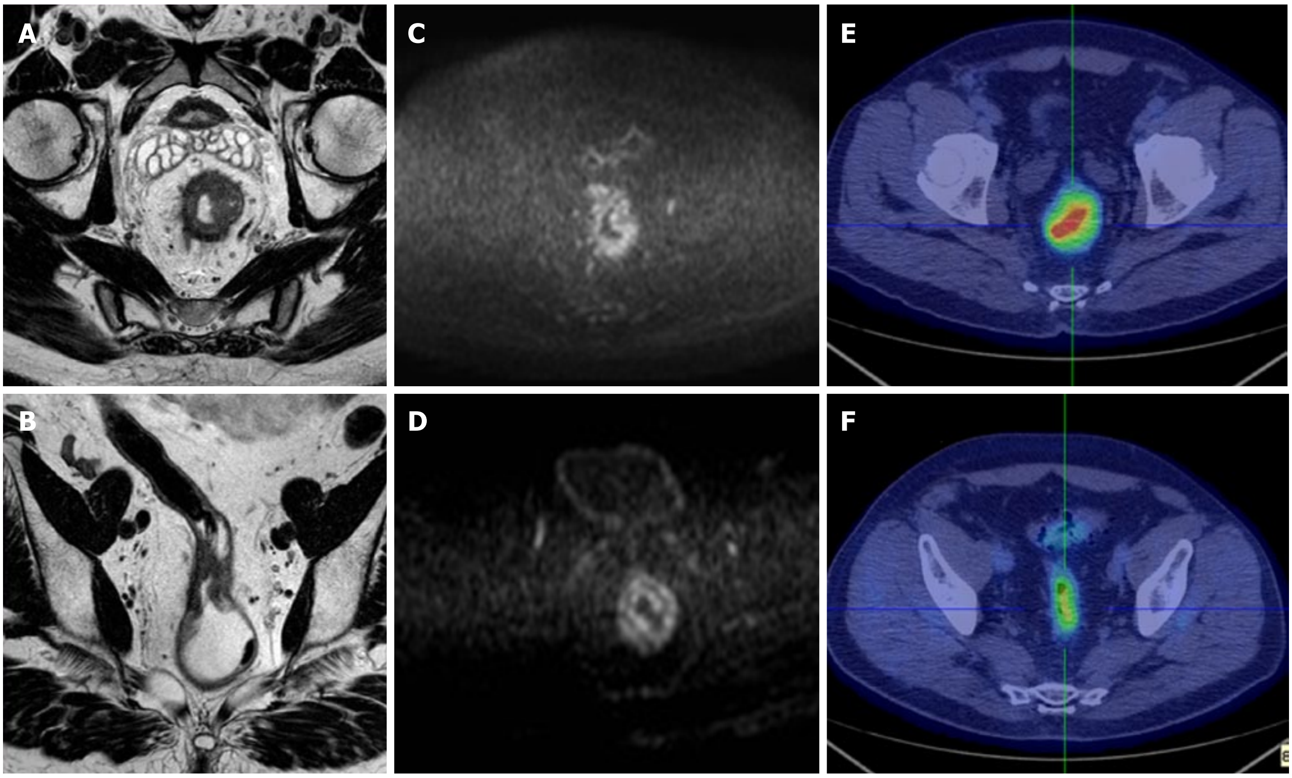

Figure 1 A 72-year-old man with pathologically proven proximal rectal cancer, classified as non-responder after chemoradiation treatment. A: Pre-CRT T2-weighted axial MR image shows a circumferential pathological rectal mass, with largest thickening from 12 to 6 o'clock position, narrowing rectal lumen and with corresponding mesorectal fat spread around; B: Post-CRT T2- weighted axial MR image shows incomplete decrease in rectal wall thickening, with irregular and inhomogeneous neoplastic tissue still determining lumen narrow; C: Pre-CRT DWI image shows the presence of hyperintense area at the corresponding level of tumor mass (ADC: 0.63 × 10^{-3} mm²/s); D: Post-CRT DWI image demonstrated partial response, with focal hyperintense area still detectable (ADC: 1.25 × 10^{-3} mm²/s); E: Pre-CRT axial pelvic scan examination image demonstrates a significant radiotracer uptake in the hight rectum, corresponding tumor region (SUVmax: 19.4); F: The partial metabolic response is also confirmed by CRT PET/CT scans, in particular a significant tumor uptake is still present (SUVmax: 4.3). CRT: Chemoradiation treatment; DWI: Diffusion weighted imaging; ADC: Apparent diffusion coefficient; SUV: Standardized uptake value.

asked to empty their bladder before positioning for the scan. Sixty ± ten minutes after the trace injection, PET/CT study was performed. Unenhanced low-dose CT (LD-CT) was acquired first with the following parameters: 120 kV, 60 mA, gantry rotation time of 0.8 s, section thickness of 3.75 mm and pitch of 1.65. PET emission scanning was performed immediately after LD-CT, with the same coverage volume. All PET studies were acquired in 3D mode, with acquisition time of 3 min per FOV. Images were reconstructed with ordered subsets expectation-maximization algorithm, 128 × 128 matrix size, attenuation, random, and scatter correction. Attenuation correction was performed on the basis of CT scan data. The CT pixel values measured in hounsfield units were transformed into linear attenuation coefficients for the 511-keV energy radiation. CT and PET images were then matched and fused into transaxial, coronal, and sagittal images.

Image analysis and quantification of PET data

PET, CT, and fused PET/CT images were displayed on Xeleris workstation (GE Medical Systems, Milwaukee, WI). Images were interpreted by one experienced nuclear medicine physicians (LG) without knowledge of clinical and histological data, but only of the presence of primary rectal cancer. Lesion uptake was identified as an area of pathologically increased ^{18}F-FDG uptake, excluding causes of nonspecific or physiologic accumulation of the radio- tracer (Figures 1 and 2). ROIs were drawn over the region of pathological uptake on the baseline scan (PET1) for the calculation of SUV1. At subsequent PET/CT (PET2) images were co-registered with the baseline study by means of the anatomical CT and the ROIs were drawn in the same positions of PET1 in order to calculate SUV2. SUV values were calculated using the maximum activity values within each ROI on the transaxial slices, normalized to the injected dose and patient's body weight, as per ADC values. The SUVmax values in the PET1 (SUV1) and PET2 (SUV2) were used to define ΔSUV in percentage as follows: $\Delta SUV1 = [(SUV1 - SUV2)/SUV1] \times 100$.

Histopathologic evaluation and TRG definition

Pathologic response was evaluated on resected specimens by a pathologist, with 15-year experience in gastrointestinal pathology. Each specimen was fixed in 10% buffered formalin for at least 48 h and inked. Serial transversal tissue blocks were cut at 5 mm intervals from the distal portion. Each block, consisting of full thickness of the rectal wall and the mesorectum,

Table 1 Summarizing table of mean values of standardized uptake value and apparent diffusion coefficient, before and after chemoradiation treatment, and their variation in the overall patients

Variable	Mean ± SD	*P* value (Wilcoxon paired)
SUV1	16.3 ± 8.6	< 0.0001
SUV2	4.5 ± 2.1	
ΔSUV (%)	66.8 ± 20.4	
ADC1	0.83 ± 0.15	< 0.0001
ADC2	1.33 ± 0.13	
ΔADC (%)	60.2 ± 23.2	

ADC: Apparent diffusion coefficient; SUV: Standardized uptake value.

Table 2 Responders (TRG1-2) *vs* non responders (TRG3-5)

Variable	Responders (Mean ± SD)	Not responders (Mean ± SD)	*P* value (Mann-Whitney *U* test)
SUV1	15.1 ± 8.0	19.5 ± 9.8	0.151
SUV2	3.6 ± 1.4	6.6 ± 2.1	0.0009
ΔSUV (%)	68.5 ± 23.2	62.8 ± 10.5	0.151
ADC1	0.88 ± 0.19	0.78 ± 0.09	0.076
ADC2	1.47 ± 0.22	1.19 ± 0.2	0.009
ΔADC(%)	72.6 ± 27.1	55.5 ± 18.5	0.0078

Mann-Whitney *U* test was used to calculate and compare obtained values between SUV1 and SUV2 and between ADC1 and ADC2. ADC: Apparent diffusion coefficient; SUV: Standardized uptake value.

was embedded in paraffin. Whole-mount sections were obtained and stained with hematoxylin and eosin. The TRG definition of Mandard *et al*[18] was adopted for clinical response classification. Patients with TRG1-2 scores were considered as responders, while patients with TRG3-5 were classified as non-responders.

Statistical analysis

Mean and SD of the SUV1, SUV2, ADC1 and ADC2 were calculated and the comparison between SUV1 and SUV2, and between ADC1 and ADC2 was done with Wilcoxon paired test (Table 1). The comparison of the same quantitative parameter was also performed between histopathologic responders and non responders patients with the non parametric Mann-Whitney *U* test (Table 2). The correlation between histological TRG in the resected specimen and the ADC and SUVmax values assessed before and after surgery was analysed with the Pearson correlation test. Multivariate regression model was evaluated including those parameters with significant correlation in univariate regression analysis (Figure 3). The final model incorporated ADC and SUVmax values measured after surgery (ADCpost - SUVpost). Model predictions of histological tumour regression were also compared with true patients' TRG and investigated with scatter diagram (Figure 4).

Receiver operating characteristic (ROC) analysis was performed to define the best accuracy of the metabolic parameters in predicting the response to treatment.

The sensitivity, specificity and overall diagnostic accuracy for each item were calculated under the optimal cut-off value.

Stata software 9.0 (Stata Corporation, College Station, Texas, United States) was used for performing statistical analysis and a $P < 0.05$ was deemed as statistical significant.

RESULTS

All patients underwent surgical excision within 8-10 wk after CRT completion, *i.e.*, low anterior resection ($n = 24$), abdominoperineal resection ($n = 6$) and extended resection ($n = 1$). The surgical approach was established considering the clinical response to CRT defined at conventional restaging.

ADC values analysis

In the whole sample of 31 patients, the mean tumor ADC before CRT in the responder group of 22 patients was 0.88×10^{-3} mm^2/s; while in the non-responder group (9 patients) was 0.78×10^{-3} mm^2/s. After CRT, the mean tumour ADC in the down-staged group was 1.47×10^{-3} mm^2/s, while in the nondown-staged group was 1.19×10^{-3} mm^2/s. ΔADC showed to be statistically relevant between responders and non responders ($P = 0.0078$), as shown in Table 2.

The regression analysis in comparing the ability of post-CRT ADC, ΔADC values in the identification of response to CRT demonstrates an optimal cut-off point of 1.294 for post-CRT measures [sensitivity = 86.4%, specificity = 66.7%, positive predictive value (PPV) = 86.4%, negative predictive value (NPV) = 66.7%], 0.500 for ΔADC (sensitivity = 63.4%, specificity = 66.7, PPV = 82.4%, NPV = 42.9%).

SUVmax analysis

The mean SUVmax and ΔSUV values of the rectal lesion for each PET/CT study are reported (Tables 1 and 2). SUV1 was found significantly higher than SUV2 ($P < 0.0001$). Figure 3 shows the results of univariate and multivariate linear regression analysis comparing metabolic parameters to TRG groups. In the univariate analysis, a statistically significant correlation was found for SUV2 ($P = 0.009$) with TRG (Table 2).

Considering the TRG1-2 patients as responder and TRG3-5 patients as non-responder, the highest accuracy in defining the response to treatment was obtained with a SUV2 cut-off value of 4.4. With this threshold, metabolic response evaluation was true positive in 17 patients, true negative in 8 patients, false positive in 1 patients and false negative in 5 patients, obtaining sensitivity, specificity, accuracy, PPV and NPV of 77.3%, 88.9%, 80.7%, 94.4% and 61.5%, respectively.

DISCUSSION

Recently, a more conservative treatment has been advocated in patients with rectal cancer showing a good or a complete response to neoadjuvant treatments. The

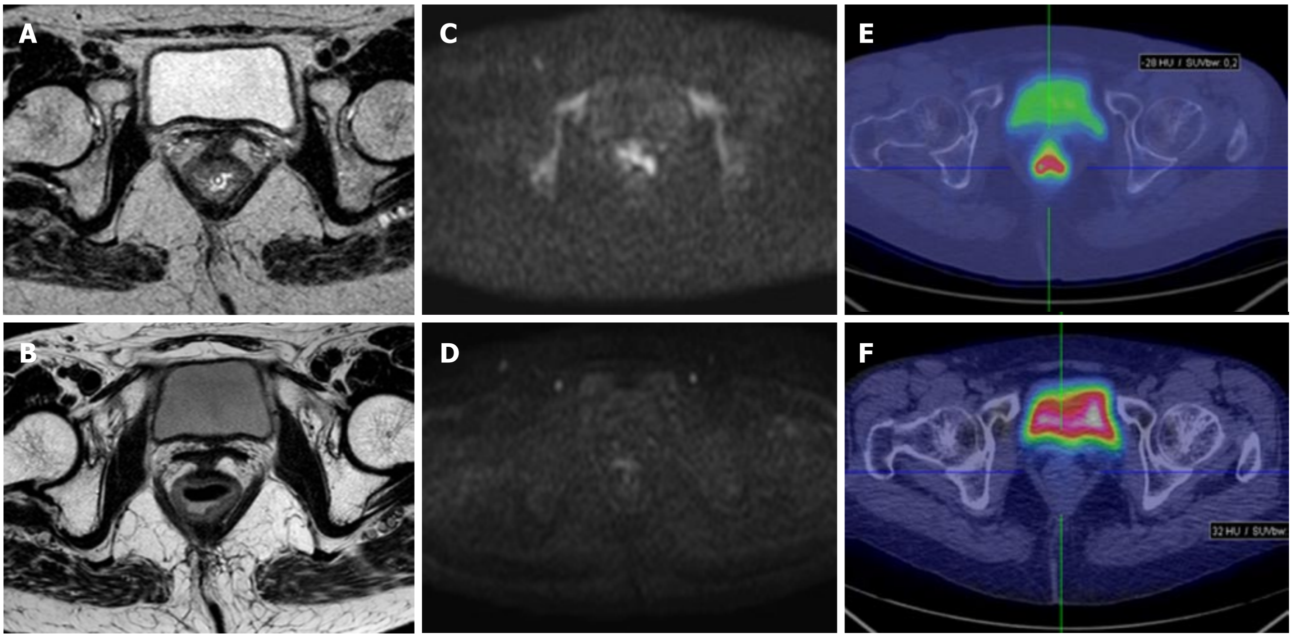

Figure 2 A 63-year-old woman with pathologically proven cancer in low rectum. It was difficult to evaluated correctly the response after CRT treatment by using only the T2 morphological information. After the additional reading of DWI images, the radiologist changed his evaluation and correctly classified the patient as responder. A: Pre-CRT T2-weighted axial MR image shows a ulcerative narrowing rectal neoplastic lesion from 11 to 3 o'clock position; B: Post-CRT T2-weighted axial MR image shows a residual homogeneous rectal wall thickening, isointense and not clearly definable as fibrotic tissue; C: Pre-CRT axial DWI image shows a focal hyperintense area in the corresponding site of rectal mass (ADC: 0.84 × 10^{-3} mm^2/s); D: Post-CRT axial DWI shows no residual hyperintense signal in the corresponding site of rectal wall (ADC: 1.39 × 10^{-3} mm²/s); E: Pre-CRT axial pelvic scan of PET/CT examination image demonstrated a significant focal radiotracer uptake in correspondence of rectal mass (SUVmax: 9.3); F: Post-CRT axial pelvic scan of PET/CT examination image shows no significant uptake (SUVmax: 2.6). CRT: Chemoradiation treatment; DWI: Diffusion weighted imaging; ADC: Apparent diffusion coefficient; SUV: Standardized uptake value.

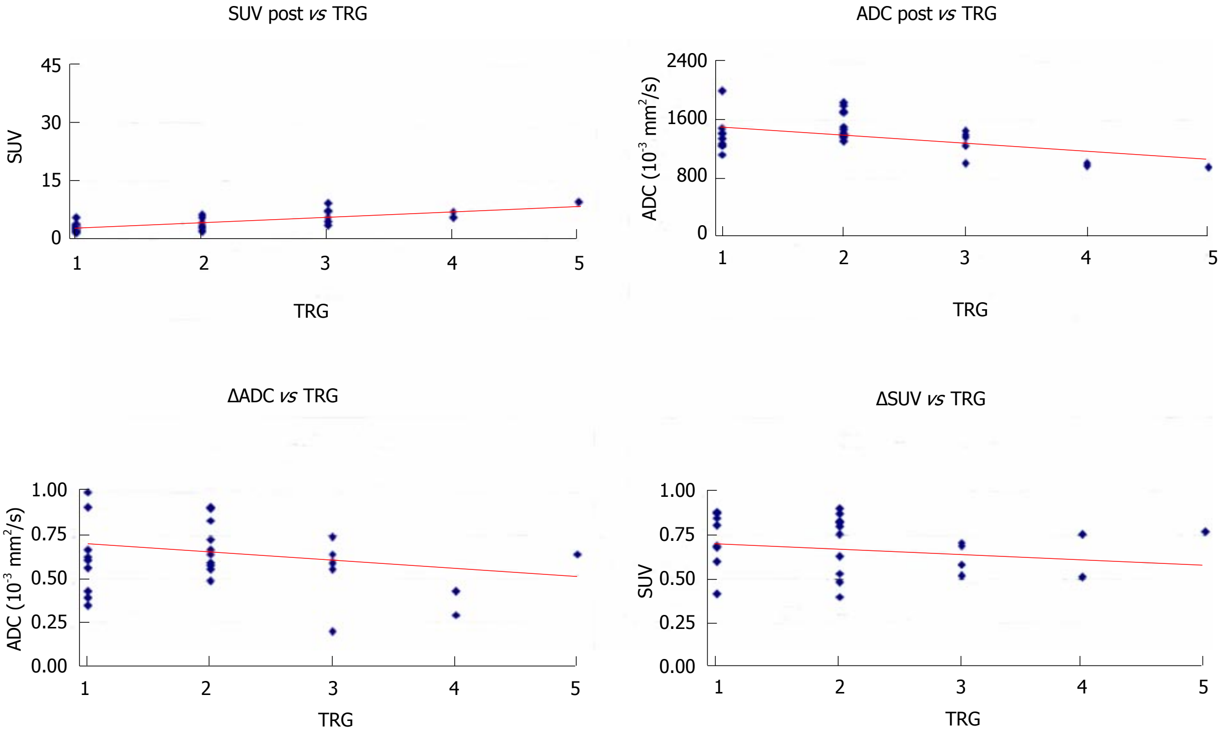

Figure 3 Univariate linear regression analysis comparing mean standardized uptake value post and apparent diffusion coefficient post with tumor regression grade. ADC: Apparent diffusion coefficient; SUV: Standardized uptake value; TRG: Tumor regression grade.

selection of true responders is essential and the role of imaging for restaging after CRT has been the subject of several recent studies, suggesting that neither MRI nor endorectal ultrasound or FDG-PET are enough accurate for identifying the true complete responders, with an overall PPV ranging from 17% to 50%[6,19-23].

Table 3 Overview of studies analysing mean standardized uptake value and delta standardized uptake value values of the rectal lesion for each PET/CT study

Ref.	No. of patients	Mean SUV 1	Mean SUV 2	Mean SUV 3	Sn (%)	Sp (%)	Late cut-off (%)	Sn (%)	Sp (%)	Delta SUV 1 R (%)	Delta SUV 1 NR (%)	Delta SUV 2 R (%)	Delta SUV 2 NR (%)
Bampo *et al*[31]	30	17.5		7.1								73.1	50.2
Cascini *et al*[24]	33	11.2	6	2.7	100	87				62	28		
Guerra *et al*[46]	31	16.3	8.1	4.3	63.2	55.6	60	77.3	55.6	51	43.1	68.5	62.8
Hermann *et al*[26]	28	9.5	5.2	3.1	74	50	45	63	100				
Janssen *et al*[25]	46	16.4	13										
Lambrecht *et al*[28]	22				100	75	76	100	75	59	25	90	63
Rosenberg *et al*[27]	30	9.5	5.5	3.5	74	70	57.5	79	70	44.3	29.6	66	48.3
Shanmugan *et al*[29]	70	10.8		3.8			63	60	84			74	56
Sun *et al*[30]	35	14.7		7.9								57.8	

R: Responders; NR: Non responders; SUV: Standardized uptake value; Sn: Sensibility; Sp: Specificity.

The correlation between therapy-related changes in FDG uptake and tumour response in rectal cancer has been previously reported by several groups. Despite the differences in study set-up, scan type, pathological and metabolic evaluation, the final metabolic response to CRT in rectal cancer with FDG-PET/CT have been demonstrated to correlate with the histopathological response and therefore to be a useful method for early assessment of treatment efficacy in rectal cancer. The different studies provided similar cut-off values, however the above mentioned differences make a direct comparison of the results not possible (Table 3).

Cascini *et al*[24] showed that early responder patients, evaluated with PET/CT 12 d after the beginning of therapy, had a higher decrease of SUV than non-responder patients (62% *vs* 28%, respectively; $P < 0.0001$). Conversely, the pre-surgical PET data did not demonstrate any statistically significant correlation between mean SUV late change and TRG findings ($P = 0.2$) obtaining a low correlation between overall changes and the TRG ($P = 0.63$).

Also Janssen *et al*[25] found an early significant decrease of the metabolic activity after the first week of CRT, both in SUVmean and SUVmax, that decreased from respectively 8.5 ± 2.8 (range: 4.0-15.1) and 16.4 ± 5.8 (range: 7.0-28.1) to 6.9 ± 2.2 (range: 4.3-12.7) ($P < 0.001$) and 13.0 ± 4.8 (range: 7.6-27.4) ($P < 0.001$) after the first week of combined treatment. More recently Herrmann *et al*[26] found in 28 patients a decrease of mean SUV uptake from 9.5 at baseline to 5.5 ($P < 0.001$) 14 d after the onset of preoperative radiochemotherapy and in the third PET scan (4 wk after completion of treatment), mean SUV decreased to 3.1 ($P < 0.001$).

Rosenberg *et al*[27] did not obtain the same result but reported that the percentage of early SUV reduction tended to be higher (44.3%) in responders than in non-responder patients (29.6%; $P = 0.085$). However after the completion of therapy, the reduction of FDG uptake was 66% in histopathologically responding tumors and 48.3% in non responding tumors ($P = 0.040$).

Similarly also Lambrecht *et al*[28] found, during CRT, a mean reduction in SUVmax of 59% in patients with histopathological complete response *vs* a mean reduction of SUVmax of 25% in patients without complete response ($P = 0.0036$). Additionally, 5 wk after the completion of CRT, a 90% SUVmax reduction in the first group *vs* 63% in second group ($P = 0.013$) was found.

Shanmugan *et al*[29] recently evaluated seventy patients that underwent pre- and post-CRT PET/CT followed by surgery and found that patients with pCR had a lower median post-CRT SUV compared with those without (2.7 *vs* 4.5, $P = 0.01$). Median SUV decrease was 63% (7.5%-95.5%) and predicted pCR ($P = 0.002$); the authors concluded that post-treatment SUV and %SUV decrease correlate with pCR.

Similar results were found by Sun *et al*[30] in a study group of 53 patients diagnosed with clinical T3- 4 and/or N+ rectal cancer and treated with CRT followed by radical surgery after 6-8 wk. A PET/CT scan was performed before (PET/CT1) beginning of treatment and a second scan (PET/CT2) was performed within 1 wk after the completion of CRT. Thirty-five out of 53 patients also underwent a third (PET/CT3) scan within 1 wk before surgery. When patients were regrouped as having a pCR and a non-pCR significant differences were found in the percentage difference between PET/CT1 and PET/CT3 in SUVmax [(Δ% SUVmax(1-3); 69.17% *vs* 57.77%)].

Also Bampo *et al*[31] evaluated the possible predictive role of late FDG-PET/CT for the assessment of pathological response in locally advanced rectal cancer following neoadjuvant chemoradiation in 30 patients; significant differences in late SUV value and response index were observed between complete and non-complete pathological responder ($P = 0.0006$ and 0.03). Furthermore, with receiver operating characteristic curve analysis, a SUV threshold of 5.4% had 81% sensitivity and 100% specificity, with 90% overall accuracy.

Nevertheless the optimal timing of the post-treatment PET scan, for a proper assessment of early response to CRT, is still unclear. Radiation-induced reduction in glucose intake occurs due to cell loss, which is a prolonged effect[32]. However, this can be confounded by two transient processes that occur soon after radio-

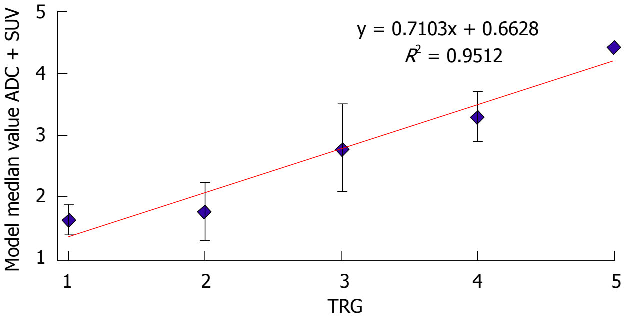

Figure 4 Univariate linear regression analysis of combined model with median value of standardized uptake value post and apparent diffusion coefficient post, in comparison with tumor regression grade. ADC: Apparent diffusion coefficient; SUV: Standardized uptake value; TRG: Tumor regression grade.

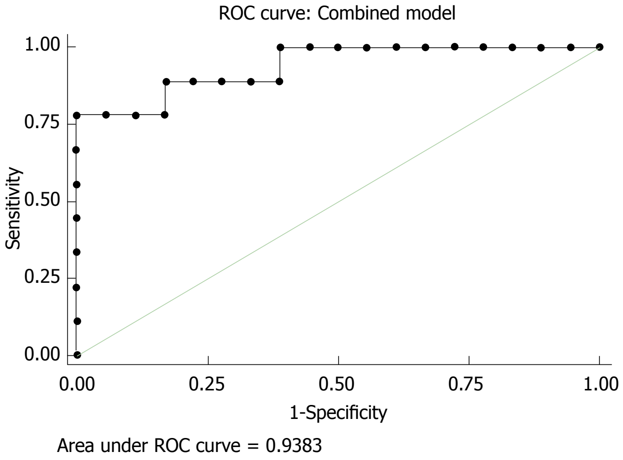

Figure 5 Receiver operating characteristic curve of combined model with median value of standardized uptake value post and apparent diffusion coefficient post, in comparison with tumor regression grade. ROC: Receiver operating characteristic.

chemotherapy. The first is defined as "stunning" of tumor cells and can lead to a transient reduction in glucose metabolism, increasing false negative results[33]. The second one is the possible increase in FDG uptake due to radiogenic inflammatory processes after radiotherapy and can lead to false positive results[34]. Increasing time interval between neoadjuvant treatment and PET scan should theoretically lead to a more accurate evaluation. Alternatively, ^{18}F-FLT PET has been tested to minimize the influence of radiation-induced inflammation[35]. In previous animal studies, FLT uptake has been shown to be in inflamed tissue as compared with FDG. However, it has not shown to be a valid tool for a proper CRT response assessment in rectal cancer patients[36].

In Lambrecht *et al*[28] study ROC curve analysis identified a threshold value for ΔSUVmax of 40%, for differentiating patients with a complete response after 2 wk, with a sensitivity of 100%, but a specificity of 75% and a PPV of 60%. Similarly using a threshold for ΔSUVmax of 76% after CRT and before surgery, is possible to identify complete responders with a sensitivity of 100%, a specificity of 75% and a PPV of 60%.

Considering our results, ROC curves analysis have shown that SUV2 has the best accuracy (80.7%) in predicting response to neoadjuvant treatment with a threshold value of 4.4. Interestingly, to note that in our study the PPV of SUV2 in predicting response was very high (94.4%) suggesting more conservative surgical approaches only in patients with evidence of lower glucose uptake at the end of neoadjuvant treatment.

While evaluating the correlation between the changes of ADC before and after CRT we found that before CRT, the mean tumour ADC in the responder group was (0.88 ± 0.19) × 10^{-3} mm^2/s, while that in the non-responder group was (0.78 ± 0.09) × 10^{-3} mm^2/s. At the end of combined chemoradiation therapy the mean tumor ADC value for responder patients was (1.47 ± 0.22) × 10^{-3} mm^2/s. For non-responder patients the mean ADC value after therapy was (1.19 ± 0.20) × 10^{-3} mm^2/s.

Our results are in line with the previously published by Jung *et al*[37]. Before neoadjuvant CRT, the mean ADC of responders and non-responders were (0.93 ± 0.09) × 10^{-3} mm^2/s and (1.03 ± 0.08) × 10^{-3} mm^2/s, respectively. After neoadjuvant CRT the mean post-CRT ADC in responders was higher than in non-responders (P = 0.009), being respectively (1.29 ± 0.13) × 10^{-3} mm^2/s and (1.18 ± 0.08) × 10^{-3} mm^2/s. Using a post-CRT ADC of 1.18 × 10^{-3} mm^2/s as cut-off value for discriminate between the responders and non-responders, the highest accuracy (77.1%) was obtained, with the following diagnostic predictive values: Sensitivity 91.3%, specificity 50.0%, positive predictive value 77.8%, and negative predictive value 75.0%.

Similarly Kim *et al*[6] reported that the mean ADC after CRT in the responders group [(1.62 ± 0.36) × 10^{-3} mm^2/s)] differed significantly from the one in the non-responders group [(1.04 ± 0.24) × 10^{-3} mm^2/s)]. Moreover, when an ADC value of 1.20 × 10^{-3} mm^2/s was used as cut-off, the authors obtained an accuracy of 85% with the following diagnostic predictive values: sensitivity 100%, specificity 79%, positive predictive value 65%, and negative predictive value 100%.

Recently, other studies[38-40] revealed similar data. Ha *et al*[38] comparing the mean post-CRT ADC for the RC group *vs* the non-CR group [(1.33 ± 0.25) × 10^{-3} mm^2/s *vs* (1.13 ± 0.32) × 10^{-3} mm^2/s] found a significant increased (P = 0.001) of ADC value. When a post-CRT ADC of 1.20 × 10^{-3} mm^2/s was used as a cut-off value for discriminating CR, the accuracy was 67%, sensitivity was 52.1%, specificity of 80.8%, positive predictive value of 71.4%, and negative predictive value of 64.6%.

Even the best timing to perform the follow-up MR study for the assessment of response to CRT is still debated. Some Authors performed the diffusion-MR also during the first 15 d of the combined treatment. Sun *et al*[12] evaluated the ADC only one week after the beginning of CRT. Before CRT the mean tumour ADC value in the down-staged group was lower than that in

Table 4 Overview of studies analysing mean apparent diffusion coefficient and delta apparent diffusion coefficient values of the rectal lesion for each MR study

Ref.	*n* of patients	Pre ADC mean R	Pre ADC mean NR	Post ADC mean R	Post ADC mean NR	ROC curve (highest accuracy)
Ippolito *et al*[45]	30	0.88 ± 0.19	0.78 ± 0.09	1.47 ± 0.22	1.19 ± 0.20	1.28 (80%)
Kim *et al*[41]	34	0.90 ± 0.06	0.94 ± 0.03			
Jung *et al*[37]	35	0.93 ± 0.09	1.03 ± 0.08	1.29 ± 0.13	1.18 ± 0.08	1.18 (77.1%)
Kim *et al*[6]	40			1.62 ± 0.36	1.04 ± 0.24	1.20 (85%)
Curvo Semedo *et al*[43]	50	1.07 ± 0.15	1.10 ± 0.19	1.39 ± 0.24	1.45 ± 0.28	1.41 (53%)
Ha *et al*[38]	100	0.59 ± 0.29	0.49 ± 0.22	1.33 ± 0.25	1.13 ± 0.32	1.20 (67%)
Genovesi[44]	28	1.01 ± 0.06	1.29 ± 0.02	1.79 ± 0.51	1.37 ± 0.43	29.5 (91.3%)
Cai *et al*[39]	15	0.659	0.885	0.713	1.027	
Birlik *et al*[40]	43	0.66 ± 0.10	0.72 ± 0.14	1.22 ± 0.26	0.95 ± 0.20	1.20 (60%)

R: Responders; NR: Non responders; ADC: Apparent diffusion coefficient.

the nondown-staged group (1.07 × 10^{-3} mm^2/s ± 0.13 *vs* 1.19 × 10^{-3} mm^2/s ± 0.15, $F = 6.91$, $P = 0.013$). At the end of the first week, the mean tumour ADC increased significantly to 1.32 × 10^{-3} mm^2/s ± 0.16 ($F = 37.63$, $P < 0.001$) in the down-staged group, while there was no significant ADC value increase in the nondown-staged group ($F = 1.18$, $P = 0.291$).

Also Kim *et al*[41] reported that the mean percentage of tumour ADC change in the responder group after 2 wk of CRT was higher in comparison with that of the non-responder group, even if not statistically significant. Seierstad *et al*[42] found an increase in tumour ADC values on day 11 after the beginning of CRT.

Cai *et al*[39] obtained an increase in the mean tumour ADC during the course of neoadjuvant CRT, especially at the 2nd week ($P = 0.004$), with a significant increase in the mean ADC at the 2nd week of neoadjuvant therapy in the T down-stage and tumour regression group ($P = 0.011$; 0.004). They also found a strong negative correlation between the mean pretreatment tumour ADC and tumour regression after neoadjuvant CRT ($P = 0.0021$).

Hypotizing that disrupted membranes increase the extracellular volume since they demonstrated higher permeability, Authors concluded that the ADC values changes in this early phase of CRT are probably the result of irreparable radiation induced DNA damage. However considering the variability among the results obtained in the recent literature (Table 4), actual evidence suggests that DWI-MR performed early after the beginning of therapy could not provide accurate and reproducible results for the evaluation of early tumour response to CRT. Hence the attention should be focused on ADC values obtained after the end of the treatment.

As well as for SUV values, in order to evaluate the prognostic value of pretreatment MR, several authors assessed[6,7,38-40,43,44] the pre-CRT ADC, obtaining controversial results. Curvo-Semedo *et al*[43] demonstrated that lower pre-CRT ADC values were associated with a more aggressive tumour profile: in their study mean ADCs were significantly different for mesorectal fascia tumour free (MRF) *vs* MRF-invaded ($P = 0.013$), mrN0 *vs* mrNþ ($P = 0.011$), and for the different tumour differentiation grades at histology ($P = 0.025$). Particularly tumours with involved MRFs, nodal-positive disease and those of less differentiated showed lower ADC values. Furthermore, a significant positive correlation ($r = 0.374$; $P = 0.019$) between ADC values and the distance of the tumour from the MRF was found.

Jung *et al*[37] recently reported that the mean pre-CRT ADC obtained with a 3 Tesla MR of responders was lower than that of non-responders ($P = 0.034$). Other authors[39,40], obtained similar results with 1.5 T MR. For instance, in the study of Birlik *et al*[40], before CRT the mean tumour ADC in the responder group was significantly lower than that in the nonresponder group ($P < 0.001$).

Other authors, however, reported that pre-treatment ADC values were not statistically different for responders and non-responders and that may be limited in predicting treatment outcome[6,38,41,44,45]. For instance, Kim *et al*[41] reported that, predicting the treatment outcome based on TRG, there were no significant differences among responder and non-responder groups when comparing pre-CRT ADCs and early tumour ADC increase rates: As the tumour responds to treatment, ADC values will probably rise at first, due the initial disruption of cell membranes, and then decrease at the end of the treatment, for the post-irradiation ingrowth of fibrosis restricting water mobility.

Considering these results and according to recent literature, the best reproducibility was obtained by studies that evaluated a post-treatment cut-off value of ADC and SUV; being the most promising and precise way of applying functional techniques in the clinical practice.

Moreover, as evaluated in our series of patients, combining in a single analysis the mathematical model of median values of ADC and of SUV values, the power of both functional technique improves, gaining a strictly and significant relationship with TRG system staging by linear regression analysis with R^2 of 0.95 (Figure 5).

In the era of PET/MRI scanner, the future approach should be represented by the combination of PET imaging with MRI not only to increase anatomical resolution but also for cell and molecular imaging, improving the accuracy in the assessment of tumour response. Moreover, the synchronous acquisition of both technique is critical in order to avoid differences in patient position, organ motion, and tumor growth.

In conclusion, the combined functional analysis of MRI and PET imaging, by the quantitative analysis of ADC map on DW-MR imaging and glucose uptake by ^{18}F-FDG-PET, can contribute to the management of patients with locally advanced rectal cancer increasing the overall accuracy and sensitivity for treatment response evaluation in one step, since they permit to detect changes in cellular tissue structures useful in prediction the different group category response in relation to TRG system.

COMMENTS

Background

The treatment of locally advanced rectal cancer has shifted in recent years toward a more conservative policy for patients identified as complete responders after chemoradiation treatment (CRT). Therefore the determination of CR before surgery would influence the subsequent treatment choice, an accurate clinical assessment of response becomes essential. Conventional imaging modalities cannot distinguish fibrosis or scar from viable tumour cells in residual masses after chemoradiotherapy; therefore, these methods have a negligible impact on the prediction of pathologic findings. For these reasons, in recent years, the functional imaging studies are increasingly being conducted to add information about changes in tumour pathophysiology.

Research frontiers

[^{18}F]fluorodeoxyglucose positron emission tomography (^{18}F-FDG PET) is a non-invasive tool to detect tumour metabolic activity and can be used to assess changes in tumour glucose metabolism after a CRT treatment. The semiquantitative assessment of glucose metabolism by evaluating the standardized uptake value (SUV) has been shown to have clinical relevance in several tumour types, since a strong relationship between ^{18}F-FDG SUV changes and pathological response has been proved in different types of cancer. DW-MRI enables noninvasive characterization of biologic tissues on the basis of their water diffusion properties (Brownian motion) microcirculation. Due to the restricted motion of water molecules, the diffusion coefficients obtained by quantitative DWI differ from the free diffusion values and are called apparent diffusion coefficients (ADC), and it can be measured. ADCs tend to decrease with increased tissue cellularity or cell density. Conversely, the cell density may be indicative of tumor aggressiveness; increased metastatic capacity of tumors with high cellularity.

Innovations and breakthroughs

The importance of this work consist of the possibility to offer, in the era of PET/MRI scanner, a new advanced quantitative tool that allows the non-invasive evaluation of response to neoadjuvant chemotherapy treatment in patients with rectal cancer, by adding quantitative value information on DW images and on PET/CT imaging, combined in a single analysis. Moreover in this manuscript the authors reviewed and commented the recent literature findings on this field by using the two different techniques modalities [*i.e.*, PET/CT and magnetic resonance imaging (MRI)].

Applications

Considering the variability among the results obtained in the recent literature, in rectal cancer post-therapy imaging assessment, the actual evidence suggests that DWI-MR and PET/CT performed early after the beginning of therapy could not provide accurate and reproducible results for the evaluation of early tumour response to CRT. Hence the attention should be focused on functional quantitative evaluation of ADC and SUVmax obtained after the end of the treatment.

Terminology

DWI: Diffusion MRI (or dMRI) is a MRI method which allows the mapping of the diffusion process of molecules, mainly water, in biological tissues, *in vivo* and non-invasively. Molecular diffusion in tissues is not free, but reflects interactions with many obstacles, such as macromolecules, fibers, and membranes. Water molecule diffusion patterns can therefore reveal microscopic details about tissue architecture, either normal or in a diseased state. ADC is a measure of the magnitude of diffusion (of water molecules) within tissue, and is commonly clinically calculated using MRI with diffusion weighted imaging, the extent of tissue cellularity and the presence of intact cell membrane help determine the impedance of water molecule diffusion. This impedance of water molecules diffusion can be quantitatively assessed using the ADC value. This assessment can be done using different b values *via* changing gradient amplitude. ADC values are calculated automatically by the software and then displayed as a parametric map that reflects the degree of diffusion of water molecules through different tissues. Then, by use of a dedicated workstation, ADC measurements are recorded for a given region by drawing regions of interest (ROIs) on the ADC map. SUVmax: The SUV is often used in PET imaging for a simple semiquantitative analysis. Its use is particularly common in the analysis of ^{18}F-FDG images of cancer patients. It can also be used with other PET agents especially when no arterial input function is available for more detailed pharmacokinetic modeling. The SUV represents the ratio of the image derived radioactivity concentration found in a selected part of the body at a certain time point, and as reference the radioactivity concentration in the hypothetical case of an even distribution of the injected radioactivity across the whole body.

Peer-review

This study is well designed and well described. The conclusion that MRI and PET imaging including the quantitative analysis of ADC map on DW-MR imaging and glucose uptake by ^{18}F-FDG-PET can contribute to the management of patients with locally advanced rectal cancer is helpful in clinical practice.

REFERENCES

1 **Curvo-Semedo L**, Lambregts DM, Maas M, Thywissen T, Mehsen RT, Lammering G, Beets GL, Caseiro-Alves F, Beets-Tan RG. Rectal cancer: assessment of complete response to preoperative combined radiation therapy with chemotherapy--conventional MR volumetry versus diffusion-weighted MR imaging. *Radiology* 2011; **260**: 734-743 [PMID: 21673229 DOI: 10.1148/radiol.11102467]

2 **Maas M**, Nelemans PJ, Valentini V, Das P, Rödel C, Kuo LJ, Calvo FA, García-Aguilar J, Glynne-Jones R, Haustermans K, Mohiuddin M, Pucciarelli S, Small W, Suárez J, Theodoropoulos G, Biondo S, Beets-Tan RG, Beets GL. Long-term outcome in patients with a pathological complete response after chemoradiation for rectal cancer: a pooled analysis of individual patient data. *Lancet Oncol* 2010; **11**: 835-844 [PMID: 20692872 DOI: 10.1016/S1470-2045(10)70172-8]

3 **Bujko K**, Kepka L, Nowacki MP. Chemoradiotherapy alone for rectal cancer: a word of caution. *Lancet Oncol* 2007; **8**: 860-862; author reply 862-863 [PMID: 17913654]

4 **O'Neill BD**, Brown G, Heald RJ, Cunningham D, Tait DM. Chemoradiotherapy alone for rectal cancer: a word of caution-author's reply [Letter]. *Lancet Oncol* 2007; **8**: 662-863

5 **O'Neill BD**, Brown G, Heald RJ, Cunningham D, Tait DM. Non-operative treatment after neoadjuvant chemoradiotherapy for rectal cancer. *Lancet Oncol* 2007; **8**: 625-633 [PMID: 17613424]

6 **Kim SH**, Lee JM, Hong SH, Kim GH, Lee JY, Han JK, Choi BI. Locally advanced rectal cancer: added value of diffusion-weighted MR imaging in the evaluation of tumor response to neoadjuvant chemo- and radiation therapy. *Radiology* 2009; **253**: 116-125 [PMID: 19789256 DOI: 10.1148/radiol.2532090027]

7 **Lambregts DM**, Vandecaveye V, Barbaro B, Bakers FC, Lambrecht M, Maas M, Haustermans K, Valentini V, Beets GL, Beets-Tan RG. Diffusion-weighted MRI for selection of complete responders after chemoradiation for locally advanced rectal cancer: a multicenter study. *Ann Surg Oncol* 2011; **18**: 2224-2231 [PMID: 21347783]

8 **Kim SH**, Lee JY, Lee JM, Han JK, Choi BI. Apparent diffusion

coefficient for evaluating tumour response to neoadjuvant chemoradiation therapy for locally advanced rectal cancer. *Eur Radiol* 2011; **21**: 987-995 [PMID: 20978768 DOI: 10.1007/s00330-010-1989-y]

9 **Hein PA**, Kremser C, Judmaier W, Griebel J, Pfeiffer KP, Kreczy A, Hug EB, Lukas P, DeVries AF. Diffusion-weighted magnetic resonance imaging for monitoring diffusion changes in rectal carcinoma during combined, preoperative chemoradiation: preliminary results of a prospective study. *Eur J Radiol* 2003; **45**: 214-222 [PMID: 12595106]

10 **DeVries AF**, Kremser C, Hein PA, Griebel J, Krezcy A, Ofner D, Pfeiffer KP, Lukas P, Judmaier W. Tumor microcirculation and diffusion predict therapy outcome for primary rectal carcinoma. *Int J Radiat Oncol Biol Phys* 2003; **56**: 958-965 [PMID: 12829130]

11 **Kremser C**, Judmaier W, Hein P, Griebel J, Lukas P, de Vries A. Preliminary results on the influence of chemoradiation on apparent diffusion coefficients of primary rectal carcinoma measured by magnetic resonance imaging. *Strahlenther Onkol* 2003; **179**: 641-649 [PMID: 14628131]

12 **Sun YS**, Zhang XP, Tang L, Ji JF, Gu J, Cai Y, Zhang XY. Locally advanced rectal carcinoma treated with preoperative chemotherapy and radiation therapy: preliminary analysis of diffusion-weighted MR imaging for early detection of tumor histopathologic downstaging. *Radiology* 2010; **254**: 170-178 [PMID: 20019139 DOI: 10.1148/radiol.2541082230]

13 **Dzik-Jurasz A**, Domenig C, George M, Wolber J, Padhani A, Brown G, Doran S. Diffusion MRI for prediction of response of rectal cancer to chemoradiation. *Lancet* 2002; **360**: 307-308 [PMID: 12147376]

14 **Roth Y**, Tichler T, Kostenich G, Ruiz-Cabello J, Maier SE, Cohen JS, Orenstein A, Mardor Y. High-b-value diffusion-weighted MR imaging for pretreatment prediction and early monitoring of tumor response to therapy in mice. *Radiology* 2004; **232**: 685-692 [PMID: 15215551]

15 **Amthauer H**, Denecke T, Rau B, Hildebrandt B, Hünerbein M, Ruf J, Schneider U, Gutberlet M, Schlag PM, Felix R, Wust P. Response prediction by FDG-PET after neoadjuvant radiochemotherapy and combined regional hyperthermia of rectal cancer: correlation with endorectal ultrasound and histopathology. *Eur J Nucl Med Mol Imaging* 2004; **31**: 811-819 [PMID: 14762698]

16 **Kalff V**, Duong C, Drummond EG, Matthews JP, Hicks RJ. Findings on 18F-FDG PET scans after neoadjuvant chemoradiation provides prognostic stratification in patients with locally advanced rectal carcinoma subsequently treated by radical surgery. *J Nucl Med* 2006; **47**: 14-22 [PMID: 16391182]

17 **Gu J**, Khong PL, Wang S, Chan Q, Law W, Zhang J. Quantitative assessment of diffusion-weighted MR imaging in patients with primary rectal cancer: correlation with FDG-PET/CT. *Mol Imaging Biol* 2011; **13**: 1020-1028 [PMID: 20872077 DOI: 10.1007/s11307-010-0433-7]

18 **Mandard AM**, Dalibard F, Mandard JC, Marnay J, Henry-Amar M, Petiot JF, Roussel A, Jacob JH, Segol P, Samama G. Pathologic assessment of tumor regression after preoperative chemoradiotherapy of esophageal carcinoma. Clinicopathologic correlations. *Cancer* 1994; **73**: 2680-2686 [PMID: 8194005]

19 **Janssen MH**, Ollers MC, Riedl RG, van den Bogaard J, Buijsen J, van Stiphout RG, Aerts HJ, Lambin P, Lammering G. Accurate prediction of pathological rectal tumor response after two weeks of preoperative radiochemotherapy using (18)F-fluorodeoxyglucose-positron emission tomography-computed tomography imaging. *Int J Radiat Oncol Biol Phys* 2010; **77**: 392-399 [PMID: 19646825 DOI: 10.1016/j.ijrobp.2009.04.030]

20 **Capirci C**, Rubello D, Chierichetti F, Crepaldi G, Carpi A, Nicolini A, Mandoliti G, Polico C. Restaging after neoadjuvant chemoradiotherapy for rectal adenocarcinoma: role of F18-FDG PET. *Biomed Pharmacother* 2004; **58**: 451-457 [PMID: 15464875]

21 **Kristiansen C**, Loft A, Berthelsen AK, Graff J, Lindebjerg J, Bisgaard C, Jakobsen A. PET/CT and histopathologic response to preoperative chemoradiation therapy in locally advanced rectal cancer. *Dis Colon Rectum* 2008; **51**: 21-25 [PMID: 17975715]

22 **Suppiah A**, Hunter IA, Cowley J, Garimella V, Cast J, Hartley JE, Monson JR. Magnetic resonance imaging accuracy in assessing tumour down-staging following chemoradiation in rectal cancer. *Colorectal Dis* 2009; **11**: 249-253 [PMID: 18513192 DOI: 10.1111/j.1463-1318.2008.01593.x]

23 **Vanagunas A**, Lin DE, Stryker SJ. Accuracy of endoscopic ultrasound for restaging rectal cancer following neoadjuvant chemoradiation therapy. *Am J Gastroenterol* 2004; **99**: 109-112 [PMID: 14687151]

24 **Cascini GL**, Avallone A, Delrio P, Guida C, Tatangelo F, Marone P, Aloj L, De Martinis F, Comella P, Parisi V, Lastoria S. 18F-FDG PET is an early predictor of pathologic tumor response to preoperative radiochemotherapy in locally advanced rectal cancer. *J Nucl Med* 2006; **47**: 1241-1248 [PMID: 16883000]

25 **Janssen MH**, Ollers MC, van Stiphout RG, Buijsen J, van den Bogaard J, de Ruysscher D, Lambin P, Lammering G. Evaluation of early metabolic responses in rectal cancer during combined radiochemotherapy or radiotherapy alone: sequential FDG-PET-CT findings. *Radiother Oncol* 2010; **94**: 151-155 [PMID: 20116114 DOI: 10.1016/j.radonc.2009.12.033]

26 **Herrmann K**, Bundschuh RA, Rosenberg R, Schmidt S, Praus C, Souvatzoglou M, Becker K, Schuster T, Essler M, Wieder HA, Friess H, Ziegler SI, Schwaiger M, Krause BJ. Comparison of different SUV-based methods for response prediction to neoadjuvant radiochemotherapy in locally advanced rectal cancer by FDG-PET and MRI. *Mol Imaging Biol* 2011; **13**: 1011-1019 [PMID: 20936364 DOI: 10.1007/s11307-010-0383-0]

27 **Rosenberg R**, Herrmann K, Gertler R, Künzli B, Essler M, Lordick F, Becker K, Schuster T, Geinitz H, Maak M, Schwaiger M, Siewert JR, Krause B. The predictive value of metabolic response to preoperative radiochemotherapy in locally advanced rectal cancer measured by PET/CT. *Int J Colorectal Dis* 2009; **24**: 191-200 [PMID: 19050900 DOI: 10.1007/s00384-008-0616-8]

28 **Lambrecht M**, Deroose C, Roels S, Vandecaveye V, Penninckx F, Sagaert X, van Cutsem E, de Keyzer F, Haustermans K. The use of FDG-PET/CT and diffusion-weighted magnetic resonance imaging for response prediction before, during and after preoperative chemoradiotherapy for rectal cancer. *Acta Oncol* 2010; **49**: 956-963 [PMID: 20586658 DOI: 10.3109/0284186X.2010.498439]

29 **Shanmugan S**, Arrangoiz R, Nitzkorski JR, Yu JQ, Li T, Cooper H, Konski A, Farma JM, Sigurdson ER. Predicting pathological response to neoadjuvant chemoradiotherapy in locally advanced rectal cancer using 18FDG-PET/CT. *Ann Surg Oncol* 2012; **19**: 2178-2185 [PMID: 22395978 DOI: 10.1245/s10434-012-2248-z]

30 **Sun W**, Xu J, Hu W, Zhang Z, Shen W. The role of sequential 18(F)-FDG PET/CT in predicting tumour response after preoperative chemoradiation for rectal cancer. *Colorectal Dis* 2013; **15**: e231-e238 [PMID: 23384167 DOI: 10.1111/codi.12165]

31 **Bampo C**, Alessi A, Fantini S, Bertarelli G, de Braud F, Bombardieri E, Valvo F, Crippa F, Di Bartolomeo M, Mariani L, Milione M, Biondani P, Avuzzi B, Chiruzzi C, Pietrantonio F. Is the standardized uptake value of FDG-PET/CT predictive of pathological complete response in locally advanced rectal cancer treated with capecitabine-based neoadjuvant chemoradiation? *Oncology* 2013; **84**: 191-199 [PMID: 23328390 DOI: 10.1159/000345601]

32 **Schiepers C**, Haustermans K, Geboes K, Filez L, Bormans G, Penninckx F. The effect of preoperative radiation therapy on glucose utilization and cell kinetics in patients with primary rectal carcinoma. *Cancer* 1999; **85**: 803-811 [PMID: 10091757]

33 **Denecke T**, Rau B, Hoffmann KT, Hildebrandt B, Ruf J, Gutberlet M, Hünerbein M, Felix R, Wust P, Amthauer H. Comparison of CT, MRI and FDG-PET in response prediction of patients with locally advanced rectal cancer after multimodal preoperative therapy: is there a benefit in using functional imaging? *Eur Radiol* 2005; **15**: 1658-1666 [PMID: 15806369]

34 **Haberkorn U**, Strauss LG, Dimitrakopoulou A, Engenhart R, Oberdorfer F, Ostertag H, Romahn J, van Kaick G. PET studies of fluorodeoxyglucose metabolism in patients with recurrent colorectal tumors receiving radiotherapy. *J Nucl Med* 1991; **32**: 1485-1490 [PMID: 1714497]

35 **van Waarde A**, Cobben DC, Suurmeijer AJ, Maas B, Vaalburg W, de Vries EF, Jager PL, Hoekstra HJ, Elsinga PH. Selectivity of 18F-FLT and 18F-FDG for differentiating tumor from inflammation in a rodent model. *J Nucl Med* 2004; **45**: 695-700 [PMID: 15073267]

36 **Wieder HA**, Geinitz H, Rosenberg R, Lordick F, Becker K, Stahl A, Rummeny E, Siewert JR, Schwaiger M, Stollfuss J. PET imaging with [18F]3'-deoxy-3'-fluorothymidine for prediction of response to neoadjuvant treatment in patients with rectal cancer. *Eur J Nucl Med Mol Imaging* 2007; **34**: 878-883 [PMID: 17195074]

37 **Jung SH**, Heo SH, Kim JW, Jeong YY, Shin SS, Soung MG, Kim HR, Kang HK. Predicting response to neoadjuvant chemoradiation therapy in locally advanced rectal cancer: diffusion-weighted 3 Tesla MR imaging. *J Magn Reson Imaging* 2012; **35**: 110-116 [PMID: 21989997 DOI: 10.1002/jmri.22749]

38 **Ha HI**, Kim AY, Yu CS, Park SH, Ha HK. Locally advanced rectal cancer: diffusion-weighted MR tumour volumetry and the apparent diffusion coefficient for evaluating complete remission after preoperative chemoradiation therapy. *Eur Radiol* 2013; **23**: 3345-3353 [PMID: 23812242 DOI: 10.1007/s00330-013-2936-5]

39 **Cai G**, Xu Y, Zhu J, Gu WL, Zhang S, Ma XJ, Cai SJ, Zhang Z. Diffusion-weighted magnetic resonance imaging for predicting the response of rectal cancer to neoadjuvant concurrent chemoradiation. *World J Gastroenterol* 2013; **19**: 5520-5527 [PMID: 24023496 DOI: 10.3748/wjg.v19.i33.5520]

40 **Birlik B**, Obuz F, Elibol FD, Celik AO, Sokmen S, Terzi C, Sagol O, Sarioglu S, Gorken I, Oztop I. Diffusion-weighted MRI and MR-volumetry--in the evaluation of tumor response after preoperative chemoradiotherapy in patients with locally advanced rectal cancer. *Magn Reson Imaging* 2015; **33**: 201-212 [PMID: 25460330 DOI: 10.1016/j.mri.2014.08.041]

41 **Kim YC**, Lim JS, Keum KC, Kim KA, Myoung S, Shin SJ, Kim MJ, Kim NK, Suh J, Kim KW. Comparison of diffusion-weighted MRI and MR volumetry in the evaluation of early treatment outcomes after preoperative chemoradiotherapy for locally advanced rectal cancer. *J Magn Reson Imaging* 2011; **34**: 570-576 [PMID: 21751285 DOI: 10.1002/jmri.22696]

42 **Seierstad T**, Folkvord S, Røe K, Flatmark K, Skretting A, Olsen DR. Early changes in apparent diffusion coefficient predict the quantitative antitumoral activity of capecitabine, oxaliplatin, and irradiation in HT29 xenografts in athymic nude mice. *Neoplasia* 2007; **9**: 392-400 [PMID: 17534444]

43 **Curvo-Semedo L**, Lambregts DM, Maas M, Beets GL, Caseiro-Alves F, Beets-Tan RG. Diffusion-weighted MRI in rectal cancer: apparent diffusion coefficient as a potential noninvasive marker of tumor aggressiveness. *J Magn Reson Imaging* 2012; **35**: 1365-1371 [PMID: 22271382 DOI: 10.1002/jmri.23589]

44 **Genovesi D**, Filippone A, Ausili Cèfaro G, Trignani M, Vinciguerra A, Augurio A, Di Tommaso M, Borzillo V, Sabatino F, Innocenti P, Liberatore E, Colecchia G, Tartaro A, Cotroneo AR. Diffusion-weighted magnetic resonance for prediction of response after neoadjuvant chemoradiation therapy for locally advanced rectal cancer: preliminary results of a monoinstitutional prospective study. *Eur J Surg Oncol* 2013; **39**: 1071-1078 [PMID: 23953231 DOI: 10.1016/j.ejso.2013.07.090]

45 **Ippolito D**, Monguzzi L, Guerra L, Deponti E, Gardani G, Messa C, Sironi S. Response to neoadjuvant therapy in locally advanced rectal cancer: assessment with diffusion-weighted MR imaging and 18FDG PET/CT. *Abdom Imaging* 2012; **37**: 1032-1040 [PMID: 22270580 DOI: 10.1007/s00261-011-9839-1]

46 **Guerra L**, Niespolo R, Di Pisa G, Ippolito D, De Ponti E, Terrevazzi S, Bovo G, Sironi S, Gardani G, Messa C. Change in glucose metabolism measured by 18F-FDG PET/CT as a predictor of histopathologic response to neoadjuvant treatment in rectal cancer. *Abdom Imaging* 2011; **36**: 38-45 [PMID: 20033405 DOI: 10.1007/s00261-009-9594-8]

P- Reviewer: Shen J, Yazdi HR **S- Editor**: Song XX **L- Editor**: A
E- Editor: Wu HL

World Journal of
Radiology

Submit a Manuscript: http://www.wjgnet.com/esps/
Help Desk: http://www.wjgnet.com/esps/helpdesk.aspx
DOI: 10.4329/wjr.v7.i12.521

World J Radiol 2015 December 28; 7(12): 521-530
ISSN 1949-8470 (online)

ORIGINAL ARTICLE

Prospective Study

Cavernosal nerve functionality evaluation after magnetic resonance imaging-guided transurethral ultrasound treatment of the prostate

Steffen Sammet, Ari Partanen, Ambereen Yousuf, Christina L Sammet, Emily V Ward, Craig Wardrip, Marek Niekrasz, Tatjana Antic, Aria Razmaria, Keyvan Farahani, Shunmugavelu Sokka, Gregory Karczmar, Aytekin Oto

Steffen Sammet, Ambereen Yousuf, Emily V Ward, Gregory Karczmar, Aytekin Oto, Department of Radiology, University of Chicago, Chicago, IL 60615, United States

Steffen Sammet, Gregory Karczmar, Committee on Medical Physics, University of Chicago, Chicago, IL 60615, United States

Ari Partanen, Shunmugavelu Sokka, Philips, Andover, MA 01810, United States

Christina L Sammet, Department of Medical Imaging, Lurie Children's Hospital, Chicago, IL 60611, United States

Craig Wardrip, Marek Niekrasz, Aria Razmaria, Department of Surgery, University of Chicago, Chicago, IL 60615, United States

Tatjana Antic, Department of Pathology, University of Chicago, Chicago, IL 60615, United States

Keyvan Farahani, National Cancer Institute, Bethesda, MD 60615, United States

Author contributions: Sammet S, Partanen A, Yousuf A, Farahani K, Sokka S, Karczmar G and Oto A designed the research; Sammet S, Partanen A, Karczmar G and Oto A developed the MRI protocols; Sammet S, Partanen A and Oto A performed the MRI and therapeutic ultrasound experiments; Antic T performed the histological analysis and the histological/radiological comparison; Oto A performed the radiological image analysis and the histological/radiological comparison; Sammet S, Wardrip C, Niekrasz M and Razmaria A monitored the animals during therapeutic ultrasound treatment and performed surgeries; Sammet S, Partanen A, Yousuf A, Ward EV, Sammet CL, and Oto A wrote the paper.

Supported by The National Cancer Institute Education and Career Development program R25 Cancer Nanotechnology in Imaging and Radiotherapy (5R25CA132822-04) in part; the Cancer Research Foundation; the University of Chicago Comprehensive Cancer Center; and Philips Healthcare.

Institutional review board statement: The study was reviewed and approved by the University of Chicago Institutional Animal Care and Use Committee.

Clinical trial registration statement: This study is not a registered clinical trial.

Informed consent statement: This study did not involve human subjects and therefore did not require informed consent.

Conflict-of-interest statement: Steffen Sammet, MD, PhD has received research funding from Philips Healthcare and fees as a consultant for Guerbet SA. Ari Partanen, PhD is an employee of Philips Healthcare. Shunmugavelu Sokka, PhD is an employee of Philips Healthcare. Aytekin Oto, MD has received research funding from Philips Healthcare and fees as a consultant for Guerbet SA.

Data sharing statement: No additional data are available.

Correspondence to: Steffen Sammet, MD, PhD, DABR, FAMP, Associate Professor and **Director** of Clinical MR Physics, Department of Radiology, University of Chicago, 5841 South Maryland Avenue, MC2026, Chicago, IL 60615, United States. ssammet@uchicago.edu
Telephone: +1-773-7023162
Fax: +1-773-7021161

Received: February 7, 2015
Peer-review started: February 8, 2015
First decision: May 19, 2015

Revised: October 19, 2015
Accepted: November 24, 2015
Article in press: November 25, 2015
Published online: December 28, 2015

Abstract

AIM: To evaluate the feasibility of using therapeutic ultrasound as an alternative treatment option for organ-confined prostate cancer.

METHODS: In this study, a trans-urethral therapeutic ultrasound applicator in combination with 3T magnetic resonance imaging (MRI) guidance was used for real-time multi-planar MRI-based temperature monitoring and temperature feedback control of prostatic tissue thermal ablation *in vivo*. We evaluated the feasibility and safety of MRI-guided trans-urethral ultrasound to effectively and accurately ablate prostate tissue while minimizing the damage to surrounding tissues in eight canine prostates. MRI was used to plan sonications, monitor temperature changes during therapy, and to evaluate treatment outcome. Real-time temperature and thermal dose maps were calculated using the proton resonance frequency shift technique and were displayed as two-dimensional color-coded overlays on top of the anatomical images. After ultrasound treatment, an evaluation of the integrity of cavernosal nerves was performed during prostatectomy with a nerve stimulator that measured tumescence response quantitatively and indicated intact cavernous nerve functionality. Planned sonication volumes were visually correlated to MRI ablation volumes and corresponding histo-pathological sections after prostatectomy.

RESULTS: A total of 16 sonications were performed in 8 canines. MR images acquired before ultrasound treatment were used to localize the prostate and to prescribe sonication targets in all canines. Temperature elevations corresponded within 1 degree of the targeted sonication angle, as well as with the width and length of the active transducer elements. The ultrasound treatment procedures were automatically interrupted when the temperature in the target zone reached 56 ℃. In all canines erectile responses were evaluated with a cavernous nerve stimulator post-treatment and showed a tumescence response after stimulation with an electric current. These results indicated intact cavernous nerve functionality. In all specimens, regions of thermal ablation were limited to areas within the prostate capsule and no damage was observed in periprostatic tissues. Additionally, a visual analysis of the ablation zones on contrast-enhanced MR images acquired post ultrasound treatment correlated excellent with the ablation zones on thermal dose maps. All of the ablation zones received a consensus score of 3 (excellent) for the location and size of the correlation between the histologic ablation zone and MRI based ablation zone. During the prostatectomy and histologic examination, no damage was noted in the bladder or rectum.

CONCLUSION: Trans-urethral ultrasound treatment of the prostate with MRI guidance has potential to safely, reliably, and accurately ablate prostatic regions, while minimizing the morbidities associated with conventional whole-gland resection or therapy.

Key words: Ultrasound therapy; Thermal tissue ablation; Prostate; Magnetic resonance imaging guided therapy; Intra-operative; Histology; Validation

Core tip: Therapeutic ultrasound is a promising treatment modality for minimally invasive thermal ablation of tissue. This study assessed a novel trans-urethral ultrasound therapy device with magnetic resonance imaging (MRI) guidance to ablate canine prostate tissue *in vivo*. Real-time temperature monitoring and thermotherapy feedback control was performed in a clinical 3T whole-body MR scanner. Post-treatment evaluation of cavernous nerve functionality was performed with a nerve stimulator. Treatment accuracy was assessed by correlation of treatment planning, thermal dose maps, and histopathological results. Regions of thermal ablation were limited to areas within the prostate capsule and no damage was observed in adjacent anatomical structures. These results indicate that MRI-guided transurethral ultrasound therapy can accurately ablate prostatic regions with minimal damage to surrounding tissue.

Sammet S, Partanen A, Yousuf A, Sammet CL, Ward EV, Wardrip C, Niekrasz M, Antic T, Razmaria A, Farahani K, Sokka S, Karczmar G, Oto A. Cavernosal nerve functionality evaluation after magnetic resonance imaging-guided transurethral ultrasound treatment of the prostate. *World J Radiol* 2015; 7(12): 521-530 Available from: URL: http://www.wjgnet.com/1949-8470/full/v7/i12/521.htm DOI: http://dx.doi.org/10.4329/wjr.v7.i12.521

INTRODUCTION

Cancer of the prostate is one of the most frequent malignant diseases and among the primary reasons of male cancer deaths in the United States[1]. Overtreatment is described as an unnecessary aggressive treatment of prostate cancer (Pca) including prostatectomy and radiation therapy and can lead to complications. The overtreatment of Pca is an important public health problem occurring in about 30%-40% of the cases[2]. Therefore, there is a need for the development of precise focal Pca treatment approaches to preserve continence and potency[3,4].

Ultrasound therapy is a novel, minimally invasive treatment option where an ultrasound transducer emits ultrasound waves with high acoustic intensities into the target regions. The deposited acoustic energy leads to temperature elevation and tissue destruction when the temperature exceeds ⩾ 56 ℃ within the focal area;

a phenomenon defined as thermo-ablation[4-8]. The ultrasound treatment can be guided with diagnostic ultrasound (US) or magnetic resonance imaging (MRI). MRI is superior to diagnostic US due to its ability to better detect real-time temperature changes in multiple planes. High resolution anatomical imaging sequences with superior soft tissues contrast and physiological protocols such as diffusion and perfusion MRI allow to evaluate the extent of tissue destruction post-ablation[9-11]. A combination of therapeutic ultrasound and MR guidance is particularly beneficial for focal and regional therapy of Pca[8]. Preliminary clinical trials utilizing trans-rectal and trans-urethral ultrasound for focal ablation of Pca have reported feasibility of these techniques[6,12]. One of the important unwanted side effects of whole gland treatment is erectile dysfunction. Even though focal therapy is expected to be safer in this regard, there is limited data in the literature to support this hypothesis.

This study utilized a novel transurethral ultrasound therapy system to ablate canine prostate tissue *in vivo* while simultaneously monitoring tissue temperature with multi-planar MRI. This dual modality system can assess temperature in real-time and is equipped with temperature feedback control[13]. The goal was *in vivo* evaluation of possible side-effects of this transurethral ultrasound therapy device. In addition to rectal damage, we specifically assessed the post-treatment functionality of the cavernosal nerves by analyzing the tumescence response qualitatively and quantitatively with a nerve stimulator during prostatectomy.

MATERIALS AND METHODS

Animals

In this Institutional Animal Care and Use Committee (IACUC) approved (University of Chicago, IACUC protocol number: 72317) MRI guided ultrasound treatment study, 8 canines (age range: 6 to 57 mo, average age: 26 mo; weight range 24 to 35.8 kg average weight: 27.9 kg) were treated with therapeutic ultrasound. All procedures took place in facilities that are United States Department of Agriculture registered, and AAALAC International (Association for Assessment and Accreditation of Laboratory Animal Care) accredited.

Pre-treatment procedures

A perineal urethrostomy was performed at least one week before the ultrasound treatment in all canines to better accommodate the ultrasound applicator in the incurvated penile urethra of the canines. A cephalic IV catheter was placed to induce anesthesia with either Propofol (5.5 mg/kg) or a combination of Buprenex (9 μg/kg), ketamine (3 mg/kg) and Dexdomitor (15 μg/kg) followed by an endotracheal intubation of the canines. A continuous inhalation of isoflurane (2%-4%) maintained the anesthesia during ultrasound treatment and subsequent MR imaging. A 6-French Foley catheter was inserted for bladder voiding until treatment. A 20-French rectal tube was placed before the ultrasound treatment to release gases from the rectum. The ultrasound applicator was manually carefully forwarded in the penile urethra to the prostate and the correct position within the prostate was verified with MR imaging. Experienced veterinarians and veterinary technologists monitored each canine throughout the procedure continuously. Monitoring included an electrocardiogram, blood pressure, blood oxygenation, in- and expired gases and physiological saline infusion.

MRI-guided ultrasound therapy system

A transurethral MR-guided ultrasound therapy prototype system (Philips, Vantaa, Finland) was utilized for administration of the ultrasound treatment on a clinical 3T MRI system (Achieva, Philips Healthcare, Best, The Netherlands). The ultrasound therapy system included a therapy workstation to plan and control the treatment, a radio-frequency generator, a water-cooled trans-urethral ultrasound system [5 mm (15 French) diameter] with eight transducer elements (4 mm × 5 mm/element) (Figure 1) and a motor to rotate the system (Figure 2). A clinical 8-channel cardiac receiver MR coil (Philips Healthcare, Best, The Netherlands) was used for MR imaging (Figure 3). The coil consisted of a 4-element anterior and a 4-element posterior part and was immobilized with straps around the canine and on the patient table (Figure 4).

Ultrasound treatment was performed at a frequency of 6.0 MHz in continuous wave mode. The motor rotated the applicator around its long axis and the ultrasound propagated through a 25 μm polyester membrane into the prostate tissue. Aqueous ultrasound gel was used to improve acoustic coupling. The urethras of the canines were cooled by pumping degassed water that circulated along the membrane and the transducer elements. Ablation depths from the urethra and ablation volumes were controlled by regulating the number of active transducer elements, output power of each element and the duration of sonication.

Ultrasound therapy planning, real-time MR thermometry, and post-therapy evaluation

MRI was used to localize the targets, plan ultrasound exposures, and to provide real-time intraprocedural temperature-monitoring during sonications. MRI images were also used to assess treatment outcome. Cumulative equivalent minutes at 43 ℃ (CEM_{43}) were used as a metric to quantify thermal tissue damage. Thermal doses in excess of 240 CEM_{43} were defined as ablative exposures[14]. MRI treatment planning included two-dimensional multi-slice T_2-weighted Turbo Spin Echo sequences in coronal, sagittal, and axial orientations. Seven slices were acquired in each dynamic in all orientations. Temporal resolution was 4.1 s/8 slices with spatial resolution of 1.5 mm × 1.5 mm in-plane and a 5 mm slice thickness. The MRI-guided ultrasound planning software allows the MRI slices to be automatically aligned with the ultrasound beam to monitor temperatures and to calculate thermal doses in the target region as

Figure 1 Trans-urethral ultrasound therapy probe. Rigid, water-cooled trans-urethral ultrasound applicator with 5 mm (15 French) diameter and eight transducer elements (4 mm × 5 mm/element).

Figure 2 Magnetic resonance imaging-compatible ultrasound therapy device. Set-up of the trans-urethral ultrasound applicator on the MRI patient table with control cables, and motor unit to control the rotation of the ultrasound transducer. MRI: Magnetic resonance imaging.

Figure 3 Equipment integration for magnetic resonance imaging-guided ultrasound therapy. Frontal oblique view of the 3T Philips MRI scanner with an 8-channel cardiac MR coil on the anterior part of the scanner table and ultrasound transducer on the posterior part of scanner table. MRI: Magnetic resonance imaging.

Figure 4 Canine positioning for magnetic resonance imaging-guided ultrasound therapy. Positioning of a canine in supine orientation on the patient table and preparation for the placement of the transurethral ultrasound transducer in the canine prostate.

well as in the peri-prostatic tissues. The MRI-based proton resonance frequency shift (PRFS = 0.0094 ppm/℃) method was used to calculate temperatures and thermal dose maps in real-time[15]. Color-coded temperature and thermal dose maps were displayed on top of anatomical MR images and updated in real time. Baseline temperature drift was accounted for by normalizing average apparent temperature changes in tissues outside the heated volumes.

Following ultrasound treatment, an axial T_2-weighted sequence was acquired in the same locations and orientation as the pre-treatment sequence. Diffusion weighted MR images (DWI) were acquired before a T_1-weighted fast-field echo sequence was used to monitor the inflow of an FDA approved gadolinium-chelate MRI contrast agent (Multihance, Bracco Diagnostics, 0.1 mmol/kg). The use of DWI and contrast-enhanced T_1-weighted MRI to visualize necrotic tissue were validated in previous studies[16,17].

Feedback control of thermal ablation

Before thermal ablations, a test-sonication (P_{ac} = 1.1 W of one active element, t = 12 s) was performed to verify sufficient acoustic coupling, the correct angle of the ultrasound transducer and the location of the heated volume. The rotation angle of the ultrasound transducer was modified with the control software if necessary to reach the target volume precisely, and a sonication was performed. A cool down period (> 5 min) was applied to allow the sonicated prostatic tissue to return to its baseline temperature. In each canine prostate this procedure was repeated in two discrete locations.

Treatment volumes were selected in different locations of the prostate and MRI-based temperature monitoring was used in each ablation location. A temperature feedback control volume of 5 voxels was selected at radial distances of 1.3 to 1.9 cm from the applicator. The acoustic power level ranged from 1.1 to 1.8 W per transducer element and it was kept constant during all independent treatments. The software stopped the sonications automatically once the mean temperature reached 56 ℃ in the control volume[18].

Evaluation of the integrity of cavernosal nerves post-treatment

Following the procedure, during the prostatectomy to

Figure 5 The CaverMap Surgical Aid nerve stimulator control unit. Device control unit with connectors for the stimulation needle, display of the applied current in mA, and light-emitting diode display (blue and red) to visualize tumescence response on an ordinal scale.

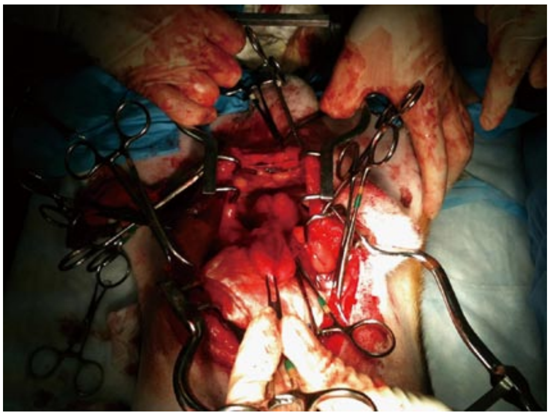

Figure 6 Surgical preparation of the canine prostate for nerve stimulation of the cavernosal nerves.

harvest the prostate, CaverMap Surgical Aid (Blue Torch Corporation, Norwood, MA) was used intra-operatively to identify and map the integrity of cavernosal nerves responsible for potency (Figure 5)[19]. The CaverMap Surgical Aid includes a nerve stimulator and an erectile response detection system. The CaverMap Surgical Aid has three major components: (1) A control unit with the electronics, connectors for the probe handle and disposable kit and a user interface to control the system; (2) A sterile and reusable probe handle for controlling the device during surgeries; and (3) A disposable kit including a probe tip that can be attached to the probe handle and a tumescence sensor. The electrical current is emitted by the probe tip.

The system applies a mild electrical stimulation for a measured tumescence response. The probe tip was inserted in close proximity to the cavernous nerves (Figures 6 and 7). A biphasic current pulse train with pulse duration of 800 μs and a current of 8 mA to 20 mA was applied for stimulation. The current was automatically increased every 20 s from 8 to 20 mA. Stimulating the cavernous nerves with the CaverMap Surgical Aid leads to an erectile response that can be measured in penile circumference changes in the tumescence sensor loop that is placed around the canine's penis. Stimulation with the probe tip produces a small erectile response that leads to an increased penile circumference. The integrity and functionality of the cavernous nerves after ultrasound therapy was evaluated by measuring erectile responses quantitatively by analyzing relative penile circumference changes with the tumescence sensor loop. Circumference changes of the sensor loop produced a change in the electric resistance in the mercury filled sensor. Tumescence changes of 0.5% produce a audible signal and a change of light-emitting diode scale (Figure 8).

Once an erectile response was measured, in a certain location of the neurovascular bundle, the position of stimulation was recorded and the probe tip was moved to another location[20].

Post-treatment procedures

Following treatment, post-treatment imaging, and cavermapping, canines were euthanized by injecting 150 mg/kg sodium pentobarbital IV followed by a prostatectomy. Potential thermal damage to periprostatic anatomical structures (*e.g.*, rectal wall, bladder wall) were also resected (Figure 9) for a detailed histological analysis (Figure 10).

Histopathological analysis

Following prostatectomies, the specimens were fixed in 10% formalin. The prostates were then sliced at 5 mm thickness parallel to the MRI axial slices and submitted for further processing. The processed paraffin blocks were cut at 4 μm and stained with haematoxylin and eosin stain. The immunohistochemical stain cytokeratin 8 (CK8) was used to analyze cell viability[21,22]. Photographs of the histological sections show visible lesions from the ultrasound treatment (Figure 10).

Ultrasound therapy analysis

The ultrasound therapy console allows the measurement of the mean temperature, the maximum temperature, and a calculation of thermal dose (> 240 CEM_{43}) volumes by using the Sapareto-Dewey equation[23].

An experienced genitourinary pathologist and a radiologist then visually correlated thermal dose (> 240 CEM_{43}) volumes, non-perfused volumes on immediate post-ablation contrast-enhanced MR images with whole-mount sections of the prostate. In each case, the correlation between MRI and pathology for location and size of the ablation zone was separately scored on a consensus scale of 3 (no correlation: 1; modest correlation: 2; and excellent correlation: 3).

RESULTS

MRI

MRI was performed in this study to plan the ultrasound treatment and to monitor temperature changes (Figure 11). The canine prostate was identified in the pre-treatment MR images and target locations were prescribed

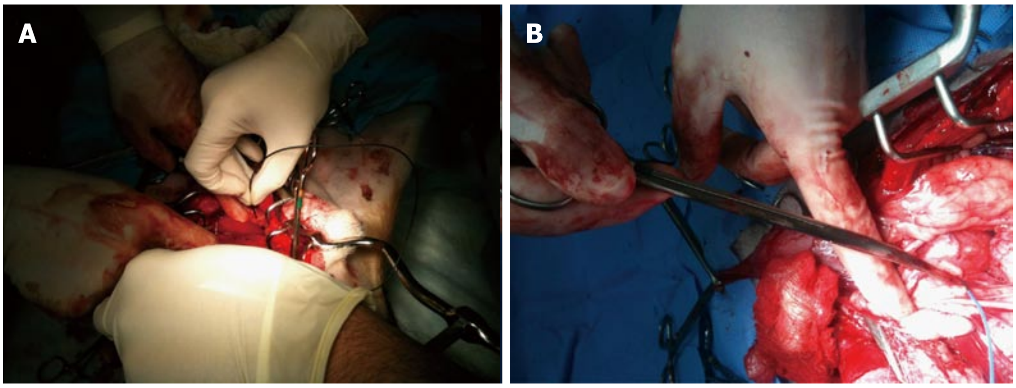

Figure 7 Placement of the CaverMap Surgical Aid nerve stimulator (A and B). Intrasurgical placement of the stimulation needle of the CaverMap Surgical Aid nerve stimulator close to the cavernosal nerves of the canine prostate.

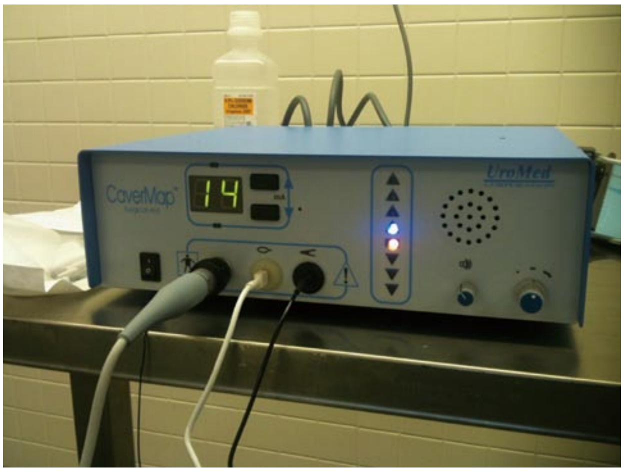

Figure 8 The CaverMap Surgical Aid nerve stimulator display. Control unit and display of the CaverMap Surgical Aid nerve stimulator to measure tumescence response on an ordinal scale intraoperatively. Below the digital display are the connectors for the probe handle, the tumescence sensor, and the lead for connecting the tumescence sensor to the control unit. The electric current for stimulation is emitted by the probe tip.

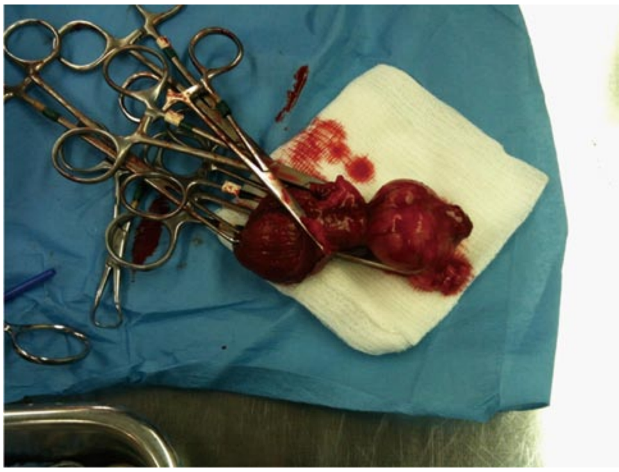

Figure 9 Explanted canine prostate and bladder after prostatectomy.

(Figure 11A, Figure 12A and B). Temperature elevations (Figure 11B and C) were in alignment of the direction of the transducer elements and corresponded to the element length and width. Figure 11D shows a corresponding histological slide of the canine prostate in haematoxylin and eosin staining to evaluate ultrasound treatment effects.

Feedback control of thermal ablation

A total of 16 sonications were performed in 8 canines. The ultrasound treatment procedures were automatically interrupted when the temperature in the target zone reached 56 ℃. The MRI-guided transurethral ultrasound therapy system provided multiplanar thermal maps of the prostate and periprostatic tissues, allowing for well-prescribed and controlled ablation of the selected targets.

Example temperature elevations in direction of the ultrasound beam propagation at the end of a sonication are shown in Figure 11B and C. The time period to reach the target mean temperature of 56 ℃ within the control volume was 1-3 min, and depended on the local tissue characteristics, control point distance, number of active elements, and acoustic power. The ultrasound treatment was stopped after reaching the target temperature. Tissue temperature dropped to their baseline values after approximately 5 min.

Thermal dose estimation, MR image evaluation, and histopathological evaluation

An exemplary T_2-weighted planning image, contrast-enhanced MR-image, temperature maps, and thermal dose maps are displayed in Figure 12. Contrast-enhanced-images were acquired in all canines after ultrasound treatment for visualization of non-perfused tissue (Figure 12G). Thermal dose assessments in the ablation zones are displayed in Figure 12E and F. In all specimens, regions of thermal ablation were limited to areas within the prostate capsule and no damage was observed in peri-prostatic tissues (Table 1).

In all canines erectile responses were evaluated with a cavernous nerve stimulator in average 5 d (range 0 to 15 d) post-treatment and showed tumescence responses ⩾ 2 on an ordinal scale ranging from + 2 to

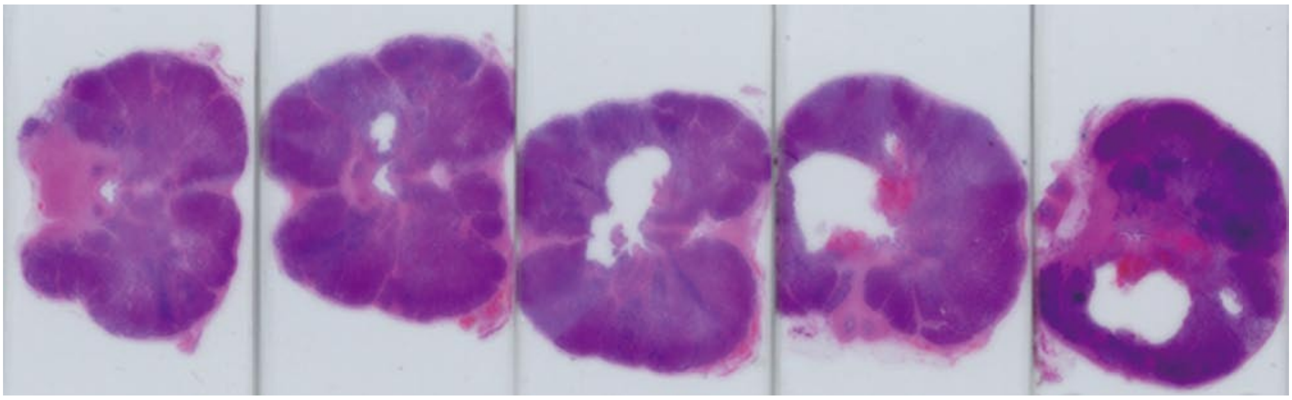

Figure 10 Histology of treated canine prostate. Series of histological slides of a canine prostate after H and E staining show ultrasound ablation zones and hemorrhage.

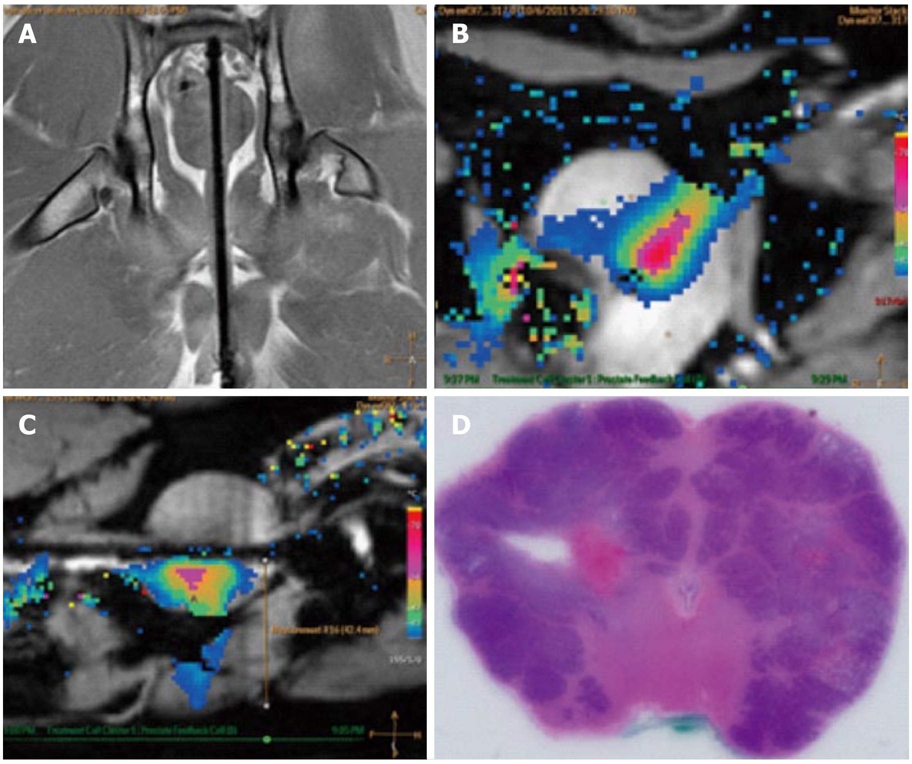

Figure 11 Example images of planning, treatment, and histological outcome. A: Coronal MR image of the intra-urethral catheter placement in the canine prostate for treatment planning with the canine in supine position: The ultrasound applicator is forwarded in the penile urethra to the prostate; B: Color-coded axial temperature map overlaid on the corresponding anatomical MR image demonstrates the typical temperature distribution post ultrasound treatment. Proton Resonance Frequency Shift measurements with a FFE-EPI imaging sequence were used for temperature monitoring and control; C: Sagittal temperature map during ultrasound treatment; D: Histological slide of the canine prostate in haematoxylin and eosin staining to evaluate ultrasound treatment effects. MR: Magnetic resonance; FFE: Fast-field echo.

+ 4 after a stimulation with a maximum current of 14 mA (Table 1). These results indicated intact cavernous nerve functionality.

Additionally, a visual analysis of the ablation zones on contrast-enhanced MR images acquired post ultrasound treatment correlated excellent with the ablation zones on thermal dose maps. All of the ablation zones received a consensus score of 3 (excellent) for the location and size of the correlation between the histologic ablation zone and MRI based ablation zone during the review of the lesions by a genitourinary pathologist and radiologist (Table 1). During the prostatectomy and histologic examination, no damage was noted in the bladder or rectum.

DISCUSSION

Image guided focal therapy of prostate cancer is a promising new technology that may provide high efficacy with reduced treatment-related morbidity. Focal therapy options to treat prostate cancer are laser ablation, electroporation, cryotherapy and ultrasound therapy[4]. Focal ultrasound therapy delivers ablative hyperthermia to the prostate and may be efficacious in

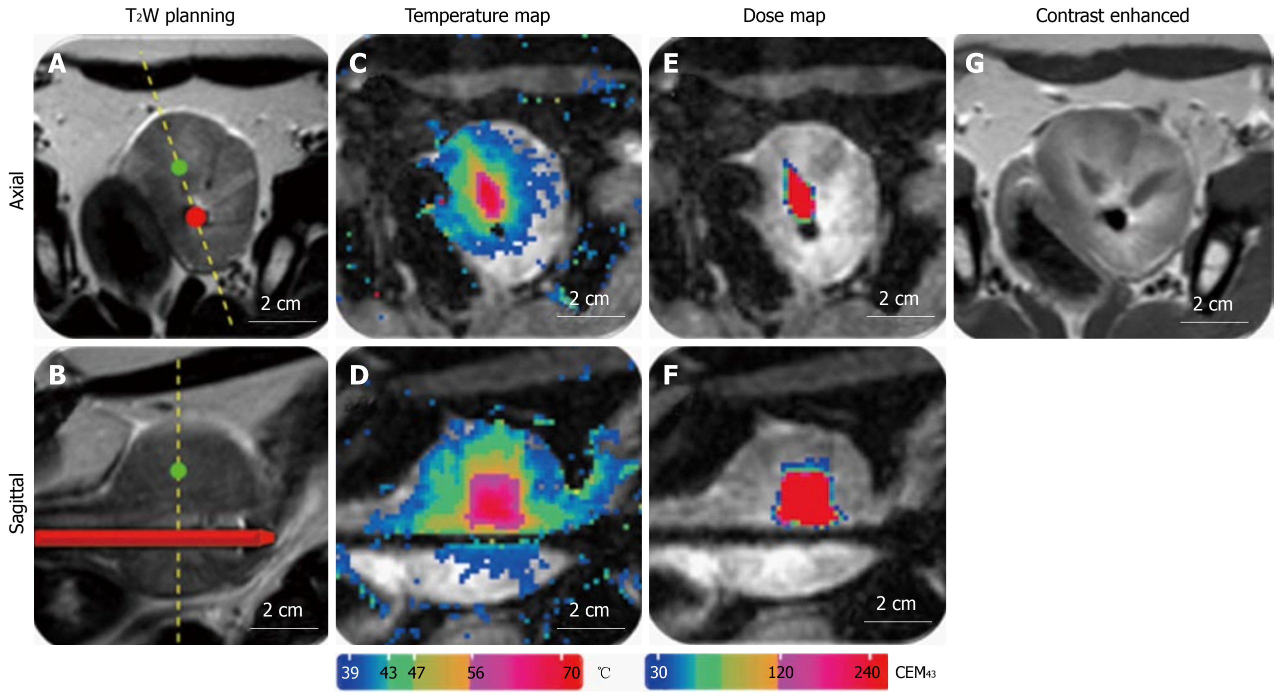

Figure 12 Representative images of magnetic resonance imaging-guidance. A: T_2-weighted image for positioning and treatment planning in axial and sagittal orientation (B); C: MR temperature map during ultrasound treatment in axial and sagittal orientation (D); E: MR dose map during ultrasound treatment in axial and sagittal orientation (F); G: Contrast enhanced T_1-weighted image after ultrasound treatment. MR: Magnetic resonance.

Table 1 Intra- and post-surgical evaluations after the treatment of eight canine prostates *in vivo* with magnetic resonance imaging-guided ultrasound therapy: Tumescence response on an ordinal scale, assessment of thermal damage to peri-prostatic tissues, and correlation between magnetic resonance imaging, thermal dose (> 240 CEM_{43}) volumes and pathology for location and size of the ablation zone

Canine	Tumescence response	Inspection of peri-prostatic tissues	Correlation between MRI, thermal dose (> 240 CEM_{43}) volumes and pathology for location and size of the ablation zone (no correlation: 1; modest correlation: 2; and excellent correlation: 3)
1	3	No damage	3
2	4	No damage	3
3	3	No damage	3
4	2	No damage	3
5	4	No damage	3
6	2	No damage	3
7	3	No damage	3
8	3	No damage	3

MRI: Magnetic resonance imaging.

the treatment of prostate cancer[4]. Multiple clinical trials have demonstrated the value of high intensity focused ultrasound to treat cancer[6,12,24,25].

Ultrasound therapy

Trans-rectal ultrasound therapy has been successfully applied as a focal prostate cancer treatment before[4,6,12], but limitations of trans-rectal ultrasound, imaging and trans-rectal biopsies have also been demonstrated[26]. It has been documented that multi-parametric MRI is superior to trans-rectal biopsy for detection of prostate carcinoma[27] with high specificity and sensitivity[28]. The combined use of multi-parametric MRI with trans-urethral ultrasound therapy could improve diagnosis and clinical outcomes in prostate cancer[13].

The results of this canine study demonstrate the feasibility of MR-guided trans-urethral ultrasound for the treatment of prostatic tissue. Our results suggest that focused ultrasound has sufficient spatial accuracy and precision to safely apply treatment of prostate tissue without damaging the neurovascular bundle or the surrounding organs. The nerves around the prostate responsible for erection remained functionally and anatomically intact following ultrasound treatment. We also demonstrated with MRI-based temperature monitoring that temperatures sufficient for ablation in target zones can be achieved while avoiding substantial increases in temperature in adjacent critical anatomical areas. Target locations in this study were located in different zones of the prostate and adequate depth of sonication could be achieved within the prostate. The ability to target diseased tissue in the prostate while avoiding thermal damage to periprostatic structure (especially to the neurovascular bundles) will be critical to the success of future clinical transurethral ultrasound ablation studies.

Although these pre-clinical results are promising, further investigations are needed to optimize trans-urethral MR-guided ultrasound therapy for use in humans with prostate cancer. In our feasibility study we chose not to rotate the applicator during ultrasound exposures.

Future experiments could explore the system's capability for regional or whole prostate treatments using this feature[29,30]. In particular, modifying the transducer orientation while sonicating may shorten the time it takes to treat the tissue[29,31]. Moreover, studies that employ a more flexible ultrasound applicator could facilitate urethral placement and improve tolerance of the therapy. Future research should also investigate the potential of this thermoablative therapy for the management of benign prostatic hypertrophy.

This study evaluated feasibility and precision of MRI-guided transurethral ultrasound in prostatic tissue *in vivo* and was therefore limited by not assessing the short-term or long-term outcomes of the therapy. As our canine subjects were cancer-free, we did not have a physiological target region. We instead defined a target region, applied only one ablation in this region, and assessed for correlation between planned targets and treatment. This may not adequately simulate clinical practice where several ablations may be required to treat the cancerous lesions. This study was also limited in its use of pre-pubertal canines. We recommend post-pubertal canines for future pre-clinical ultrasound therapy studies of the prostate to assure large enough prostate sizes for treatment of multiple locations.

In summary, a promising new dual-modality device which combines MRI guidance with a trans-urethral ultrasound therapy probe was able to precisely ablate canine prostate tissue while simultaneously providing accurate thermal maps of the prostate and periprostatic tissue. Real-time, multi-planar temperature mapping equipped with feed-back control allowed for well-targeted ablation of prescribed lesions. There was no impact of ablation on the function of the neurovascular bundle or surrounding organs such as rectum and bladder. Functionality of the cavernosal nerves after trans-urethral ultrasound therapy was confirmed with a nerve stimulator measuring the tumescence response. Results of the feasibility study reported here indicate that future research into the efficacy and functional outcomes of ultrasound therapy for prostate cancer should be explored.

ACKNOWLEDGMENTS

We would like to thank our MRI technologists Peters S and Jamison E as well as the certified veterinary technicians Vosicky J, Bruner M, Peterson K, McGrath J, and Zamora M for their outstanding support of this study and Dr. Mustafi D for providing degassed water.

COMMENTS

Background

Cancer of the prostate is one of the most common malignant diseases and among the leading reasons of male cancer deaths in the United States. There is a need for the development of precise focal Pca treatment approaches to preserve continence and potency. Ultrasound therapy is a novel, minimally invasive treatment option where an ultrasound probe emits a high intensity beam that can be used to destroy or "ablate" cancerous tissue. This study evaluated possible side-effects of prostate tissue ablation *in vivo* with an magnetic resonance imaging (MRI) guided transurethral ultrasound therapy system.

Research frontiers

In this study, an MRI guided transurethral ultrasound therapy system was tested in dogs. The authors evaluated the feasibility and safety of MRI-guided transurethral ultrasound to effectively and accurately ablate prostate tissue while minimizing the damage to surrounding tissues in canine prostates. In addition to assessing rectal and bladder damage, the authors specifically assessed the post-treatment functionality of the nerves by analyzing their response qualitatively and quantitatively with a nerve stimulator.

Innovations and breakthroughs

In this study, MRI was performed for treatment planning, ultrasound guidance and post-treatment evaluation in all canines. Prostate tissue was successfully ablated with the MRI-guided ultrasound therapy unit and regions of thermal ablation were limited to areas within the prostate capsule and no damage was observed in tissues surrounding the prostate. In all canines erectile responses were evaluated with a nerve stimulator post-treatment and indicated intact nerve functionality. No damage was noted in the bladder and rectum.

Applications

Image guided focal ultrasound therapy could help to treat prostate cancer with fewer side effects than standard treatment methods. The authors' results in a canine model suggest that MRI-guided trans-urethral focal ultrasound treatment is a safe and accurate approach to ablate prostatic tissue without damaging the neurovascular bundle and surrounding organs.

Terminology

Thermo-ablation: Energy absorption to increase in temperature for tissue destruction when the temperature exceeds ≥ 56 ℃ within the focal area. Thermocoagulation: The use of heat to bring about localized destruction and congealing of tissue. Transurethral: A medical procedure performed *via* the urethra. Neurovascular bundle: The nerves, arteries, veins and lymphatics that travel together in the body, specifically in this article, around the prostate. Cavernous Nerve: The nerves that facilitate penile erection.

Peer-review

This article is very good.

REFERENCES

1 **American Cancer Society**. Cancer Facts & Figures 2014. Atlanta: American Cancer Society, 2014. accessed 2014 Jun 12. Available from: URL: http://www.cancer.org/acs/groups/content/@research/documents/webcontent/acspc-042151.pdf

2 **Klotz L**. Prostate cancer overdiagnosis and overtreatment. *Curr Opin Endocrinol Diabetes Obes* 2013; **20**: 204-209 [PMID: 23609043 DOI: 10.1097/MED.0b013e328360332a]

3 **Hoang AN**, Volkin D, Yerram NK, Vourganti S, Nix J, Linehan WM, Wood B, Pinto PA. Image guidance in the focal treatment of prostate cancer. *Curr Opin Urol* 2012; **22**: 328-335 [PMID: 22647649 DOI: 10.1097/MOU.0b013e32835482cc]

4 **Lindner U**, Trachtenberg J, Lawrentschuk N. Focal therapy in prostate cancer: modalities, findings and future considerations. *Nat Rev Urol* 2010; **7**: 562-571 [PMID: 20842187 DOI: 10.1038/nrurol.2010.142]

5 **Hildebrandt B**, Wust P, Ahlers O, Dieing A, Sreenivasa G, Kerner T, Felix R, Riess H. The cellular and molecular basis of hyperthermia. *Crit Rev Oncol Hematol* 2002; **43**: 33-56 [PMID: 12098606]

6 **Ahmed HU**, Freeman A, Kirkham A, Sahu M, Scott R, Allen C, Van der Meulen J, Emberton M. Focal therapy for localized prostate cancer: a phase I/II trial. *J Urol* 2011; **185**: 1246-1254 [PMID: 21334018 DOI: 10.1016/j.juro.2010.11.079]

7 **Lindner U**, Lawrentschuk N, Weersink RA, Davidson SR, Raz O, Hlasny E, Langer DL, Gertner MR, Van der Kwast T, Haider MA, Trachtenberg J. Focal laser ablation for prostate cancer followed by radical prostatectomy: validation of focal therapy and imaging

accuracy. *Eur Urol* 2010; **57**: 1111-1114 [PMID: 20346578]
8 **Lukka H**, Waldron T, Chin J, Mayhew L, Warde P, Winquist E, Rodrigues G, Shayegan B. High-intensity focused ultrasound for prostate cancer: a systematic review. *Clin Oncol* (R Coll Radiol) 2011; **23**: 117-127 [PMID: 20932728 DOI: 10.1016/j.clon.2010.09.002]
9 **Soylu FN**, Eggener S, Oto A. Local staging of prostate cancer with MRI. *Diagn Interv Radiol* 2012; **18**: 365-373 [PMID: 22399364 DOI: 10.4261/1305-3825.DIR.4970-11.2]
10 **Jia G**, Abaza R, Williams JD, Zynger DL, Zhou J, Shah ZK, Patel M, Sammet S, Wei L, Bahnson RR, Knopp MV. Amide proton transfer MR imaging of prostate cancer: a preliminary study. *J Magn Reson Imaging* 2011; **33**: 647-654 [PMID: 21563248 DOI: 10.1002/jmri.22480]
11 **Wang S**, Peng Y, Medved M, Yousuf AN, Ivancevic MK, Karademir I, Jiang Y, Antic T, Sammet S, Oto A, Karczmar GS. Hybrid multidimensional T(2) and diffusion-weighted MRI for prostate cancer detection. *J Magn Reson Imaging* 2014; **39**: 781-788 [PMID: 23908146 DOI: 10.1002/jmri.24212]
12 **Ahmed HU**, Hindley RG, Dickinson L, Freeman A, Kirkham AP, Sahu M, Scott R, Allen C, Van der Meulen J, Emberton M. Focal therapy for localised unifocal and multifocal prostate cancer: a prospective development study. *Lancet Oncol* 2012; **13**: 622-632 [PMID: 22512844]
13 **Partanen A**, Yerram NK, Trivedi H, Dreher MR, Oila J, Hoang AN, Volkin D, Nix J, Turkbey B, Bernardo M, Haines DC, Benjamin CJ, Linehan WM, Choyke P, Wood BJ, Ehnholm GJ, Venkatesan AM, Pinto PA. Magnetic resonance imaging (MRI)-guided transurethral ultrasound therapy of the prostate: a preclinical study with radiological and pathological correlation using customised MRI-based moulds. *BJU Int* 2013; **112**: 508-516 [PMID: 23746198 DOI: 10.1111/bju.12126]
14 **Meshorer A**, Prionas SD, Fajardo LF, Meyer JL, Hahn GM, Martinez AA. The effects of hyperthermia on normal mesenchymal tissues. Application of a histologic grading system. *Arch Pathol Lab Med* 1983; **107**: 328-334 [PMID: 6687797]
15 **Ishihara Y**, Calderon A, Watanabe H, Okamoto K, Suzuki Y, Kuroda K, Suzuki Y. A precise and fast temperature mapping using water proton chemical shift. *Magn Reson Med* 1995; **34**: 814-823 [PMID: 8598808]
16 **Chen J**, Daniel BL, Diederich CJ, Bouley DM, van den Bosch MA, Kinsey AM, Sommer G, Pauly KB. Monitoring prostate thermal therapy with diffusion-weighted MRI. *Magn Reson Med* 2008; **59**: 1365-1372 [PMID: 18506801 DOI: 10.1002/mrm.21589]
17 **Jacobs MA**, Herskovits EH, Kim HS. Uterine fibroids: diffusion-weighted MR imaging for monitoring therapy with focused ultrasound surgery--preliminary study. *Radiology* 2005; **236**: 196-203 [PMID: 15987974 DOI: 10.1148/radiol.2361040312]
18 **Chopra R**, Tang K, Burtnyk M, Boyes A, Sugar L, Appu S, Klotz L, Bronskill M. Analysis of the spatial and temporal accuracy of heating in the prostate gland using transurethral ultrasound therapy and active MR temperature feedback. *Phys Med Biol* 2009; **54**: 2615-2633 [PMID: 19351975 DOI: 10.1088/0031-9155/54/9/002]
19 **Kim HL**, Mhoon DA, Brendler CB. Does the CaverMap device help preserve potency? *Curr Urol Rep* 2001; **2**: 214-217 [PMID: 12084267]
20 **Walsh PC**, Marschke P, Catalona WJ, Lepor H, Martin S, Myers RP, Steiner MS. Efficacy of first-generation Cavermap to verify location and function of cavernous nerves during radical prostatectomy: a multi-institutional evaluation by experienced surgeons. *Urology* 2001; **57**: 491-494 [PMID: 11248626]
21 **Makin CA**, Bobrow LG, Bodmer WF. Monoclonal antibody to cytokeratin for use in routine histopathology. *J Clin Pathol* 1984; **37**: 975-983 [PMID: 6206100]
22 **Van Leenders GJ**, Beerlage HP, Ruijter ET, de la Rosette JJ, van de Kaa CA. Histopathological changes associated with high intensity focused ultrasound (HIFU) treatment for localised adenocarcinoma of the prostate. *J Clin Pathol* 2000; **53**: 391-394 [PMID: 10889823]
23 **Sapareto SA**, Dewey WC. Thermal dose determination in cancer therapy. *Int J Radiat Oncol Biol Phys* 1984; **10**: 787-800 [PMID: 6547421]
24 **Foster RS**, Bihrle R, Sanghvi N, Fry F, Kopecky K, Regan J, Eble J, Hennige C, Hennige LV, Donohue JP. Production of prostatic lesions in canines using transrectally administered high-intensity focused ultrasound. *Eur Urol* 1993; **23**: 330-336 [PMID: 7683997]
25 **Gelet A**, Chapelon JY, Margonari J, Theillere Y, Gorry F, Cathignol D, Blanc E. Prostatic tissue destruction by high-intensity focused ultrasound: experimentation on canine prostate. *J Endourol* 1993; **7**: 249-253 [PMID: 8358423]
26 **Hwang SI**, Lee HJ. The future perspectives in transrectal prostate ultrasound guided biopsy. *Prostate Int* 2014; **2**: 153-160 [PMID: 25599070 DOI: 10.12954/PI.14062]
27 **Sciarra A**, Barentsz J, Bjartell A, Eastham J, Hricak H, Panebianco V, Witjes JA. Advances in magnetic resonance imaging: how they are changing the management of prostate cancer. *Eur Urol* 2011; **59**: 962-977 [PMID: 21367519 DOI: 10.1016/j.eururo.2011.02.034]
28 **Turkbey B**, Pinto PA, Mani H, Bernardo M, Pang Y, McKinney YL, Khurana K, Ravizzini GC, Albert PS, Merino MJ, Choyke PL. Prostate cancer: value of multiparametric MR imaging at 3 T for detection--histopathologic correlation. *Radiology* 2010; **255**: 89-99 [PMID: 20308447 DOI: 10.1148/radiol.09090475]
29 **Chopra R**, Colquhoun A, Burtnyk M, N'djin WA, Kobelevskiy I, Boyes A, Siddiqui K, Foster H, Sugar L, Haider MA, Bronskill M, Klotz L. MR imaging-controlled transurethral ultrasound therapy for conformal treatment of prostate tissue: initial feasibility in humans. *Radiology* 2012; **265**: 303-313 [PMID: 22929332 DOI: 10.1148/radiol.12112263]
30 **Diederich CJ**, Stafford RJ, Nau WH, Burdette EC, Price RE, Hazle JD. Transurethral ultrasound applicators with directional heating patterns for prostate thermal therapy: in vivo evaluation using magnetic resonance thermometry. *Med Phys* 2004; **31**: 405-413 [PMID: 15000627]
31 **Siddiqui K**, Chopra R, Vedula S, Sugar L, Haider M, Boyes A, Musquera M, Bronskill M, Klotz L. MRI-guided transurethral ultrasound therapy of the prostate gland using real-time thermal mapping: initial studies. *Urology* 2010; **76**: 1506-1511 [PMID: 20709381 DOI: 10.1016/j.urology.2010.04.046]

P- Reviewer: Soria F **S- Editor**: Ji FF **L- Editor**: A
E- Editor: Wu HL

World Journal of Radiology

Submit a Manuscript: http://www.wjgnet.com/esps/
Help Desk: http://www.wjgnet.com/esps/helpdesk.aspx
DOI: 10.4329/wjr.v7.i12.531

World J Radiol 2015 December 28; 7(12): 531-537
ISSN 1949-8470 (online)

SYSTEMATIC REVIEWS

Classifications of mandibular canal branching: A review of literature

Mauricio Augusto Aquino Castro, Manuel Oscar Lagravere-Vich, Tânia Mara Pimenta Amaral, Mauro Henrique Guimaraes Abreu, Ricardo Alves Mesquita

Mauricio Augusto Aquino Castro, Tânia Mara Pimenta Amaral, Ricardo Alves Mesquita, Department of Oral Surgery and Pathology, School of Dentistry, Federal University of Minas Gerais, Belo Horizonte MG 253 31270-901, Brazil

Manuel Oscar Lagravere-Vich, Graduate Orthodontic Program, University of Alberta, University of Alberta, Edmonton T6G1C9, Canada

Mauro Henrique Guimaraes Abreu, Department of Social and Preventive Dentistry, School of Dentistry, Federal University of Minas Gerais, Belo Horizonte MG 253 31270-901, Brazil

Author contributions: Castro MAA, Lagravere-Vich MO, Amaral TMP, Abreu MHG and Mesquita RA contributed equally to this work; all authors read and approved the final manuscript.

Supported by Grants from National Council for Scientific Technological Development (CNPq, #309209/2010-2).

Conflict-of-interest statement: All the authors declare that they have no competing interests.

Data sharing statement: The technical appendix and dataset are available from the corresponding author at ramesquita@ufmg.br.

Correspondence to: Ricardo Alves Mesquita, PhD, Department of Oral Surgery and Pathology, School of Dentistry, Federal University of Minas Gerais, Av. Antonio Carlos, 6627, Pampulha, Belo Horizonte MG 253 31270-010, Brazil. ramesquita@ufmg.br
Telephone: +55-31-34092499
Fax: +55-31-34092430

Received: May 29, 2015
Peer-review started: June 1, 2015
First decision: August 4, 2015
Revised: October 20, 2015
Accepted: November 3, 2015
Article in press: November 4, 2015
Published online: December 28, 2015

Abstract

AIM: To gather existing radiographic classifications of mandibular canals branching, considering the criteria on which these were based.

METHODS: The search for studies on mandibular canals based on imaging exams included literature reviews, epidemiological studies of prevalence, descriptive studies, or case reports. An electronic search in the MEDLINE (OvidSP), PubMed, EMBASE (OvidSP), Web of Science (Thompson Reuters), and Scopus (Elsevier) databases was performed, as well as a manual evaluation of the references of the selected articles. Combinations of key words were placed in each database. No restrictions were imposed regarding the year of publication or language. References collected in duplicate were removed by the authors. A table was drawn up, containing the included studies and respective interest data.

RESULTS: Six classifications of mandibular canals branching were selected for the present literature review. Four were based on two-dimensional radiographic exams, and two were performed based on three-dimensional tomographic exams. Three-dimensional classifications were determined based on the analysis found in the least number of exams, comparatively to two-dimensional studies. The prevalence of mandibular canal branching varied from 0% to 38.75% in the works based on two-dimensional exams, while those found in three-dimensional exams ranged from 15.6% to 65%. The studies were mostly referred to branches that began in the mandibular ramus. Just one classification considered the branches that began in the mandibular body region.

CONCLUSION: Three-dimensional exams appear to be the best method to view mandibular canal branching. Further studies are warranted to determine its true prevalence and questions concerning to associations.

Key words: Inferior alveolar nerve; Mandibular canal; Bifid mandibular canal; Dental radiography; Cone-beam computed tomography

Core tip: The identification of the mandibular canal and its branching are important for the planning of dental procedures. Due to the limitations of the two-dimensional exams, the three-dimensional view of the structures provided by computed tomography (CT) exams allowed for greater sensitivity for the detection and evaluation of mandibular canals. Nevertheless, some studies performed with CT exams continued to use the classifications based on two-dimensional exams. Given the variability of information on this aspect, this study aimed to gather existing information in an attempt to provide researchers and clinical professionals with a stronger basis for their studies and procedures.

Castro MAA, Lagravere-Vich MO, Amaral TMP, Abreu MHG, Mesquita RA. Classifications of mandibular canal branching: A review of literature. *World J Radiol* 2015; 7(12): 531-537 Available from: URL: http://www.wjgnet.com/1949-8470/full/v7/i12/531.htm DOI: http://dx.doi.org/10.4329/wjr.v7.i12.531

INTRODUCTION

Mandibular canals are intraosseous ducts, normally unique in each hemimandible. These begin in the mandibular foramen, located in the lingual surfaces of the mandibular bodies and stretch until they emerge in the mental foramen, in a vestibular direction in the pre-molar region. Located inside of these canals is the inferior alveolar neurovascular bundle, the largest ramus of the mandibular division of the trigeminal nerve, responsible for the innervation of the posterior teeth, of the surrounding bone structure, and of the mucosa of the tongue coating of the posterior region[1].

The identification of the mandibular canal is important for the planning of a wide range of dental procedures, especially surgical procedures. The insertion of implants, extraction of impacted teeth, surgical planning of biopsies, enucleations of pathologies, orthognathic surgeries, and the defining of differential diagnoses are only a few examples of the clinical importance of its localization[2-7]. The occurrence of anatomical branching in mandibular canals constitutes a complicating factor and requires care for the proper planning of such cases in order to avoid inferior alveolar neurovascular bundle lesions.

As this study treats intraosseous anatomic structures, imaging exams are recognized as the main diagnostic resource for their localization and evaluation. The radiographic study of human fetal mandibles, performed by Chávez-Lomeli *et al*[8], detected that bifid or trifid canals are the main anatomical branching of the mandibular canals. For this reason, radiographic classifications were developed according to conventional exams. These systems considered their origins, localization, aspect, and direction as core criteria[1,9-12]. Due to the limitation inherent to the two-dimensional exams, Langlais *et al*[11] contemplated the possibility of the existence of undetected or undescribed canals.

The three-dimensional view of the structures provided by computed tomography (CT) exams allowed for greater sensitivity for the detection and evaluation of mandibular canals, in addition to the three-dimensional classification of the mandibular canal. CT studies have presented different prevalence levels and other types of mandibular canal branches (Figure 1)[13-15]. Nevertheless, some studies performed with CT exams continued to use the classification of the variation of mandibular canals based on two-dimensional exams[14,16].

Bearing this finding in mind, the present review seeks to list the classifications and descriptions of the branching of existing mandibular canals, considering the applied diagnostic resources and the criteria on which these were based. Given the variability of information on this aspect, as well as the prevalence and classification, this study aimed to gather existing information in an attempt to provide researchers and clinical professionals with a stronger basis for their studies and procedures.

MATERIALS AND METHODS

Eligibility criteria

This literature review proposed the search for radiographic studies on mandibular canals in humans, based on conventional and digital two-dimensional exams and on CT exams. This work included literature reviews, epidemiological studies of prevalence, descriptive studies, or case reports. No letters to the editor, animal studies, abstracts, or personal opinions were included.

Sources

This study performed an electronic search in the PubMed, Embase, Web of Science (Thompson Reuters), and Scopus (Elsevier) databases. The references of the selected articles were also manually evaluated to detect relevant studies that might have been lost in the electronic search. A complementary search was also conducted using Google Search and Google Scholar

Figure 1 White arrow showing the origin of a mandibular canal branch in the mandibular body found by Rouas *et al*[13] (2007) on a computed tomography exam.

search tools.

Research strategy

Combinations of key words were placed in each database, using the following key words: Mandible, mandibular nerve, inferior alveolar nerve, mandibular canal, bifid mandibular canal, bifid canals, radiography, panoramic radiography, cone-beam computed tomography, dental implant, and anatomic variation. No restrictions were imposed regarding the year of publication or language. References collected in duplicate were removed by the authors.

Study selection

After having removed the duplicates, the abstracts of all of the chosen articles were read to verify the appropriateness of the theme. The main objective was to find articles that defined the classification of mandibular canal branching. After having selected the articles that met the eligibility criteria, these were read in full and incorporated into the present review.

Synthesis of the collected data

A table of the included studies was drawn up, containing the following data: Authors' names, year of publication, sample size, exam per image used in each study, prevalence of mandibular canal branching, and description of the defined classification, including the name adopted for the branches, the frequency of each type, the location of origin, aspect, direction, and end location.

RESULTS

Six radiographic classifications of the branching in mandibular canals were selected for the present literature review (Table 1)[1,9-12,14,15].

Within the listed classification, four were defined by evaluating the canals and their branching in two-dimensional radiographic exams[1,9-12], and two were performed based on three-dimensional CT exams. Two of the classifications based on two-dimensional evaluations also conducted dissections of the anatomical parts[10,12].

The classifications based on two-dimensional exams were carried out by analyzing the samples with the highest number of exams (9717 in total, with an average of 2429.25 exams). Nortjé *et al*[1,9] evaluated 3612 panoramic radiographs, while Langlais *et al*[11] evaluated 6000 exams. Three-dimensional classifications were determined based on the analysis found in the least number of exams (374 in total, with an average of 187 CT exams).

The prevalence of the mandibular canal branching varied from 0% to 38.75% in the works based on two-dimensional exams, with an average of 10.15%. The prevalence of branches found in CT exams ranged from 15.6% to 65%, with an average of 40.3%.

Only the classification defined by Kieser *et al*[12] considered the branches that began in the mandibular body. All others referred to those initiated in the mandibular ramus.

DISCUSSION

Radiographic studies of the prevalence branching in mandibular canals presents variability, ranging from 0.08%[17] to 38.75%[10] when based on two-dimensional exams, and from 15.6%[14] to 65%[15]. This variability is related to the use of different methods, including panoramic radiographic evaluations and CT exams.

Claeys *et al*[18] warned that, although panoramic radiographs offer diagnostic conditions, the recognition of the branching in mandibular canals is rare. The authors defined that the cross-sectional cuts of the mandibular bodies, made possible through CT exams, were the best method to identify and locate their route. In an attempt to establish a more efficient method, capable of detecting the real prevalence and localization of these alterations, the CT exam has truly sparked great progress and has proven to be better as regards the limitations presented by the panoramic radiographs[3,15,19]. For this reason, it is recommended as the method of choice for the planning of a wide range of surgical procedures in dentistry[20].

However, the comparison among the methods reaches beyond that referent to the absolute prevalence of the occurrence of anatomical branching in mandibular canals. The comparison of the prevalence of different types of canals detected in panoramic radiographs and in the three-dimensional exams is of outmost importance due to the highest and lowest clinical significance that each type can represent. Furthermore, this comparison is made more difficult by the lack of a standardization of the classifications adopted in the different studies. The classification of the branches detected through tomographic exams (Figure 2)[15,16,21,22], though similar to those from two-dimensional exams, presented some differences and some new criteria[1,10-12].

Table 1 Classifications of mandibular canal branching (1971-2010)

Ref.	Exam	Sample	Prevalence (mandibular canal branching)	Classification	Frequency of the types	Region of origin	Aspect	Direction	Local of termination
Carter *et al*[10] (1971)	Unilateral radiographs and dissection	80	38.75%	Type I	61.25%	Ramus region, from a single Mandibular Foramen	Single large structure with very short dental branches	Superior to the tips of molars roots	Mental arborization
				Type II	13.75% (types 1 or 2)	Ramus region, from a single Mandibular Foramen	Substantially lower down, with dental branches given off more posteriorly, longer and oblique	Oblique, toward the tips of molars roots	Mental arborization
				Type III	25% (types 2 or 3)	Ramus region, from a single Mandibular Foramen	Two large branches initiated posteriorly	Uppers like alveolar branches	Upper to the tips of the roots; Lower to mental forame
Nortjé *et al*[1] (1977)	Panoramic radiographs	3612	0.9	Type Ia	30.3% of duplication cases	Ramus region, from a single Mandibular Foramen	Two canals of a similar width (lower slightly narrower)	Inferior narrower	
				Type Ib		Ramus region, from a single Mandibular Foramen	Double (Superior narrower)	Anterior	
				Type II		Ramus region, from a single Mandibular Foramen	Duplo (Superior shorter)	Anterior	Superior: toward 2nd and 3rd molars and inferior: toward mental foramen
				Type III		Ramus region, from separated Mandibular Foramens	Double (Join in the molars region)	Anterior	Molars region
Nortjé *et al*[9] (1977)		3612		Type IV		Ramus region, from a single Mandibular Foramen	Double (Superior narrower than the main canal)	Anterior	Ramus region
Langlais *et al*[11] (1985)	Radiografias panorâmicas convencionais	6000	0.95	Type I	38.6%	Ramus region, from a single Mandibular Foramen	Double (Superior shorter)	Anterior	3rd molar and adjacente region
				Type II	54.4%	Ramus region, from a single Mandibular Foramen	Double (Joining anteriorly)	Anterior	Ramus or mandibular body regions
				Type III	3.5%	Ramus region, from a single Mandibular Foramen	Double (Combination of types II and III)	Anterior	Ramus, retromolar ou 3rd molar regions
				Type IV	3.5%	Ramus region, from separated Mandibular Foramens	Double (Joining anteriorly)	Inferior	Ramus region

Kieser *et al*[12] (2005)	Oclusal and unilateral radiographs and dissection	107 mandibles (25 radiographic exams)	0%	Type I (detected by mean of dissections and radiographs)		Ramus region, from a single Mandibular Foramen	Single, without branches	Anterior	Mental foramen region
				Type II (detectado em dissecações)		Mandibular body region	Series of individual branches	Superior	Alveolar process (Edentulous mandibles)
				Type III (detectado em dissecações)		Molars region	Molar plexus	Superior	Molar region (Edentulous mandibles)
				Type IV (detectado em dissecações)		Distal and proximal regions	Distal and proximal plexus	Distal plexus forward. Proximal plelxus toward superior	Alveolar process (Edentulous mandibles)
Naitoh *et al*[15] (2009)	CBCT	122	65%	Type I Retromolar	29.8%	Ramus region	Superior	Superior	Retromolar region
				Type II Dental Canal (3º molar)	7%	Ramus region	Superior	Anterior	Root Apex of the third molar
				Type II Dental Canal (2º molar)	1.8%	Ramus region	Superior	Anterior	Root Apex of the second molar
				Type III Forward Canal (with confluence)	4.5%	Ramus region	Superior (Joining to the main canal)	Anterior	Mandibular body
				Type III Forward Canal (without confluence)	55.3%	Ramus region	Superior	Anterior	Mandibular body
				Type IV Buccal or lingual canal	1.8%	Ramus region	Lateral	Inferior (Buccal or lingual)	Ramus region
Kuribayashi *et al*[14] (2010)	CBCT	301 unilateral exams from 252 patients	15.60%	Less than 50% of the diameter of the main canal	51%		Narrower (Less than 50% of the diameter of the main canal)		
				Equal or bigger than 50% of the diameter of the main canal	49%		Equal or bigger than 50% of the diameter of the main canal		

CBCT: Cone beam computed tomography.

In one three-dimensional exam, Kuribayashi *et al*[14], although they had defined an additional classification criterion by evaluating the diameter of the branches of the mandibular canals in relation to the main canal, primarily used the two-dimensional classification set forth by Nortjé *et al*[1] for detected canals. Their results pointed towards a greater prevalence of mandibular canal branching when compared to that found by Nortjé *et al*[1] Moreover, when compared to the diverse types of branches, a difference could also be observed regarding the most prevalent type of canal. While Nortjé *et al*[1] found greater prevalence for type I bifid canals (78.8%), Kuribayashi *et al*[14] found a greater prevalence of type II branches (13.2%).

Likewise, Correr *et al*[16] used the two-dimensional classification, as defined by Langlais *et al*[11], for a tomographic evaluation of mandibular canal branching. It was not possible to compare the prevalence of these studies, given that the samples evaluated by Correr *et al*[16] consisted, in its totality, of previously diagnosed exams referent to the occurrence of branches. However, as regards the proportion among the different types of branches, differences were observed. The type I standard was the most commonly detected in tomographic exams (72.6%), followed by the type II (19.3%), whereas the types I and II were detected in 38.6% and 54.4% of the panoramic radiographs, respectively. No type IV branches were detected in the scans.

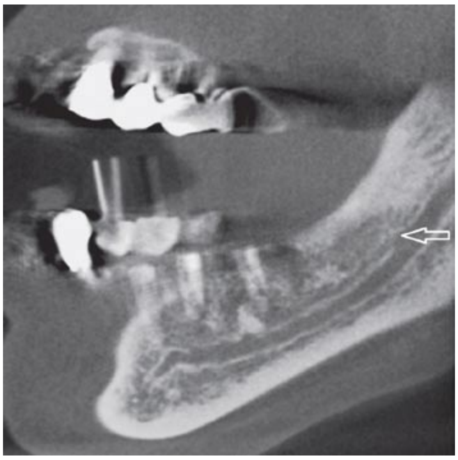

Figure 2 Cone bean computed tomography exam with a white arrow pointing the origin of a forward canal without confluence, bifurcated from the main mandibular canal in the ramus region, and classified as type 3 by Naitoh *et al*[15] (2009).

These results reveal the existence of differences in the diagnostic accuracy of the methods. Nevertheless, the analysis of the different two- and three-dimensional classifications calls attention to some other relevant differences. As regards the evaluation of the diameters of the branches referent to the main canals[14], this can contribute to the greater or lesser relevance of the findings. While higher caliber branches may represent a greater risk of injury, one must also bear in mind that the branches of a lesser volume may be referent to nutrient canals, such as that found in the dissections performed by Carter and Keen[10].

Another aspect to be considered refers to the direction of the branches. Whereas the two-dimensional classification includes the description of the direction only in the anteroposterior and superoinferior directions, the three-dimensional classification set forth by Naitoh *et al*[15] is also concerned with the situation of the branches in the vestibular-lingual direction. This is an important factor to be considered in the surgical planning of cases[2,6,23,24] thus contributing to improvements in the definition of the localization of the surgical access route as well as better estimations of the risk of injury to the surrounding anatomical structures.

In conclusion, the detection of mandibular canal branching is important to determine the proper conduct to be taken with patients with dental problems, and imaging exams represent the standard method to view these alterations. Three-dimensional exams appear to be the best method, however, further studies are warranted to determine the true prevalence these alterations, some possible associated factor, and other such questions concerning three-dimensional systems.

COMMENTS

Background

Mandibular canals are intraosseous ducts that contain the inferior alveolar neurovascular bundle, responsible for the innervation of the posterior teeth and of the surrounding structures of the posterior region. The identification of the mandibular canal is important for the planning of a wide range of dental surgical procedures. The occurrence of mandibular canals branching constitutes a complicating factor and requires care for the proper planning of the procedures in order to avoid neurovascular lesions. The present review seeks to list the classifications and descriptions of the mandibular canal branching, considering the applied diagnostic resources and the criteria on which these were based. Given the variability of information on this aspect, this study aimed to gather existing information in an attempt to provide researchers and clinical professionals with a stronger basis for their studies and procedures.

Research frontiers

Bifid or trifid canals are the main anatomical branching of the mandibular canals, according Chávez-Lomeli *et al* (1996). As the mandibular canals are intraosseous anatomic structures, imaging exams are recognized as the main diagnostic resource for their localization and evaluation. Radiographic classifications were mainly developed according to conventional exams. Due to the limitation of the two-dimensional exams, Langlais *et al* (1985) contemplated the possibility of the existence of undescribed canals.

Innovations and breakthroughs

The three-dimensional view of the structures provided by computed tomography (CT) exams allowed for greater sensitivity for the detection and evaluation of mandibular canals, in addition to the three-dimensional classification of the mandibular canal. CT studies have presented different prevalence levels and other types of mandibular canal branches. Nevertheless, some studies performed with CT exams continued to use the classification of the variation of mandibular canals based on two-dimensional exams.

Applications

This review suggests that three-dimensional exams appear to be the best method to view mandibular canal branching. Further studies are warranted to determine its true prevalence, new classifications and questions concerning to associations.

Terminology

Both cone beam computed tomography and CT exams were equally referred as the generic term CT in this study. These types of three-dimensional exams have greater sensitivity for the detection of mandibular canal branching in comparison to two-dimensional exams and a comparative evaluation of the sensitivity of these methods was not a goal of this review.

Peer-review

In this paper the authors conducted an internet based search on the different radiographic classifications as regards the identification of the mandibular canal and its branching. The review is concise and well written one.

REFERENCES

1 **Nortjé CJ**, Farman AG, Grotepass FW. Variations in the normal anatomy of the inferior dental (mandibular) canal: a retrospective study of panoramic radiographs from 3612 routine dental patients. *Br J Oral Surg* 1977; **15**: 55-63 [PMID: 268217 DOI: 10.1016/0007-117X(77)90008-7]

2 **Juodzbalys G**, Wang HL, Sabalys G. Injury of the Inferior Alveolar Nerve during Implant Placement: a Literature Review. *J Oral Maxillofac Res* 2011; **2**: e1 [PMID: 24421983 DOI: 10.5037/jomr.2011.2101]

3 **Kim TS**, Caruso JM, Christensen H, Torabinejad M. A comparison of cone-beam computed tomography and direct measurement in the examination of the mandibular canal and adjacent structures. *J Endod* 2010; **36**: 1191-1194 [PMID: 20630297 DOI: 10.1016/j.joen.2010.03.028]

4 **Hori M**, Sato T, Kaneko K, Okaue M, Matsumoto M, Sato H, Tanaka H. Neurosensory function and implant survival rate following implant placement with nerve transpositioning: a case study. *J Oral Sci* 2001; **43**: 139-144 [PMID: 11515599 DOI: 10.2334/josnusd.43.139]

5 **González-Santana H**, Peñarrocha-Diago M, Guarinos-Carbó

J, Balaguer-Martínez J. Pain and inflammation in 41 patients following the placement of 131 dental implants. *Med Oral Patol Oral Cir Bucal* 2005; **10**: 258-263 [PMID: 15876971]

6 **Mizbah K**, Gerlach N, Maal TJ, Bergé SJ, Meijer GJ. The clinical relevance of bifid and trifid mandibular canals. *Oral Maxillofac Surg* 2012; **16**: 147-151 [PMID: 21698363 DOI: 10.1007/s10006-011-0278-5]

7 **Simonton JD**, Azevedo B, Schindler WG, Hargreaves KM. Age- and gender-related differences in the position of the inferior alveolar nerve by using cone beam computed tomography. *J Endod* 2009; **35**: 944-949 [PMID: 19567312 DOI: 10.1016/j.joen.2009.04.032]

8 **Chávez-Lomeli ME**, Mansilla Lory J, Pompa JA, Kjaer I. The human mandibular canal arises from three separate canals innervating different tooth groups. *J Dent Res* 1996; **75**: 1540-1544 [PMID: 8906121 DOI: 10.1177/00220345960750080401]

9 **Nortjé CJ**, Farman AG, de V Joubert JJ. The radiographic appearance of the inferior dental canal: an additional variation. *Br J Oral Surg* 1977; **15**: 171-172 [PMID: 271020 DOI: 10.1016/0007-117X(77)90050-6]

10 **Carter RB**, Keen EN. The intramandibular course of the inferior alveolar nerve. *J Anat* 1971; **108**: 433-440 [PMID: 5575310]

11 **Langlais RP**, Broadus R, Glass BJ. Bifid mandibular canals in panoramic radiographs. *J Am Dent Assoc* 1985; **110**: 923-926 [PMID: 3860553 DOI: 10.14219/jada.archive.1985.0033]

12 **Kieser J**, Kieser D, Hauman T. The course and distribution of the inferior alveolar nerve in the edentulous mandible. *J Craniofac Surg* 2005; **16**: 6-9 [PMID: 15699637 DOI: 10.1097/00001665-200501000-00003]

13 **Rouas P**, Nancy J, Bar D. Identification of double mandibular canals: literature review and three case reports with CT scans and cone beam CT. *Dentomaxillofac Radiol* 2007; **36**: 34-38 [PMID: 17329586 DOI: 10.1259/dmfr/27374727]

14 **Kuribayashi A**, Watanabe H, Imaizumi A, Tantanapornkul W, Katakami K, Kurabayashi T. Bifid mandibular canals: cone beam computed tomography evaluation. *Dentomaxillofac Radiol* 2010; **39**: 235-239 [PMID: 20395465 DOI: 10.1259/dmfr/66254780]

15 **Naitoh M**, Nakahara K, Hiraiwa Y, Aimiya H, Gotoh K, Ariji E. Observation of buccal foramen in mandibular body using cone-beam computed tomography. *Okajimas Folia Anat Jpn* 2009; **86**: 25-29 [PMID: 19522303]

16 **Correr GM**, Iwanko D, Leonardi DP, Ulbrich LM, Araújo MR, Deliberador TM. Classification of bifid mandibular canals using cone beam computed tomography. *Braz Oral Res* 2013; **27**: 510-516 [PMID: 24346049 DOI: 10.1590/S1806-83242013000600011]

17 **Grover PS**, Lorton L. Bifid mandibular nerve as a possible cause of inadequate anesthesia in the mandible. *J Oral Maxillofac Surg* 1983; **41**: 177-179 [PMID: 6572228 DOI: 10.1016/0278-2391(83)90076-9]

18 **Claeys V**, Wackens G. Bifid mandibular canal: literature review and case report. *Dentomaxillofac Radiol* 2005; **34**: 55-58 [PMID: 15709108 DOI: 10.1259/dmfr/23146121]

19 **Muinelo-Lorenzo J**, Suárez-Quintanilla JA, Fernández-Alonso A, Marsillas-Rascado S, Suárez-Cunqueiro MM. Descriptive study of the bifid mandibular canals and retromolar foramina: cone beam CT vs panoramic radiography. *Dentomaxillofac Radiol* 2014; **43**: 20140090 [PMID: 24785820 DOI: 10.1259/dmfr.20140090]

20 **Tyndall DA**, Price JB, Tetradis S, Ganz SD, Hildebolt C, Scarfe WC. Position statement of the American Academy of Oral and Maxillofacial Radiology on selection criteria for the use of radiology in dental implantology with emphasis on cone beam computed tomography. *Oral Surg Oral Med Oral Pathol Oral Radiol* 2012; **113**: 817-826 [PMID: 22668710 DOI: 10.1016/j.oooo.2012.03.005]

21 **Orhan AI**, Orhan K, Aksoy S, Ozgül O, Horasan S, Arslan A, Kocyigit D. Evaluation of perimandibular neurovascularization with accessory mental foramina using cone-beam computed tomography in children. *J Craniofac Surg* 2013; **24**: e365-e369 [PMID: 23851871 DOI: 10.1097/SCS.0b013e3182902f49]

22 **Kang JH**, Lee KS, Oh MG, Choi HY, Lee SR, Oh SH, Choi YJ, Kim GT, Choi YS, Hwang EH. The incidence and configuration of the bifid mandibular canal in Koreans by using cone-beam computed tomography. *Imaging Sci Dent* 2014; **44**: 53-60 [PMID: 24701459 DOI: 10.5624/isd.2014.44.1.53]

23 **Tay AB**, Zuniga JR. Clinical characteristics of trigeminal nerve injury referrals to a university centre. *Int J Oral Maxillofac Surg* 2007; **36**: 922-927 [PMID: 17875382 DOI: 10.1016/j.ijom.2007.03.012]

24 **Miller CS**, Nummikoski PV, Barnett DA, Langlais RP. Cross-sectional tomography. A diagnostic technique for determining the buccolingual relationship of impacted mandibular third molars and the inferior alveolar neurovascular bundle. *Oral Surg Oral Med Oral Pathol* 1990; **70**: 791-797 [PMID: 2263343 DOI: 10.1016/0030-4220(90)90023-L]

P- Reviewer: Abdel-Salam OME, Stoetzer M **S- Editor**: Ji FF
L- Editor: A **E- Editor**: Wu HL

Published by **Baishideng Publishing Group Inc**
8226 Regency Drive, Pleasanton, CA 94588, USA
Telephone: +1-925-223-8242
Fax: +1-925-223-8243
E-mail: bpgoffice@wjgnet.com
Help Desk: http://www.wjgnet.com/esps/helpdesk.aspx
http://www.wjgnet.com